Title
The Photometric Properties of Extragalactic Globular Cluster Systems

Author
Jennings, Zachary Grove

Publication Date
2017

UNIVERSITY OF CALIFORNIA
SANTA CRUZ

THE PHOTOMETRIC PROPERTIES OF EXTRAGALACTIC GLOBULAR CLUSTER SYSTEMS

A dissertation submitted in partial satisfaction of the
requirements for the degree of

Doctor of Philosophy

in

ASTRONOMY & ASTROPHYSICS

by

Zachary Grove Jennings

June 2017

The Dissertation of Zachary Grove Jennings
is approved:

Professor Jean P. Brodie, Chair

Professor Aaron J. Romanowsky

Professor Puragra Guhathakurta

Tyrus Miller
Vice Provost and Dean of Graduate Studies

Table of Contents

List of Figures

/

List of Tables

Abstract

The Photometric Properties of Extragalactic Globular Cluster Systems

by

Zachary Grove Jennings

Globular Clusters (GCs) are powerful tools for understanding the formation of galaxies. GCs are located in the halos of galaxies and, due to their age and density, have borne witness to the major formation events of a galaxy's lifetime. One may study these objects using a wide array of techniques and datasets, including wide-field ground-based imaging, deep space-based imaging, and spectroscopy. All approaches involve tradeoffs, and in this work we consider a variety of ways to study GC systems in imaging data. We examine a wide-field *HST*/ACS mosaic of the nearby lenticular galaxy NGC 3115, selecting a high-quality GC sample using the superior resolution of the ACS data. We find strong color bimodality in the GC system of NGC 3115 and examine a number of trends in the properties of the GC system. Next, we consider the situation where one is limited to ground-based imaging, where contaminants to the GC population are a major concern. We detail a novel statistical methodology in which we treat the GC population and the contaminant population as a mixture model, and evaluate the model in a Bayesian context. We demonstrate the performance of the model on mock data, and note some areas where current analysis of GC systems may be missing information using traditional selection techniques. We also apply this Bayesian methodology to a subset of SLUGGS survey galaxies with high-quality photometry from either the MegaCam instrument on the Canada-France-Hawaii Telescope or the SuprimeCam instrument on the Subaru Telescope. In most cases, the mixture model recovers the GC system well, often finding the traditional bimodality and providing well-calibrated statistical uncertainties for the global parameters of the GC system. Finally, we examine the object NGC 3628 UCD1, a star cluster slightly more massive than the largest GCs. We identify that UCD1 is located in a stellar stream around the galaxy NGC 3628, and therefore is in the process of being accreted. We characterize UCD1 both in wide-field SuprimeCam imaging and in Keck/ESI spectroscopy, and identify a number of interesting parallels between UCD1 and ωCen, the largest Milky Way GC.

Acknowledgments

Graduate school is nothing if not a journey. In my five years at UC Santa Cruz, I've had the privilege of working professionally with many brilliant colleagues, and I've also had many fantastic friends to help me get through things.

I owe a great deal of thanks to Jean Brodie and Aaron Romanowsky, who have been invaluable advisors over the past five years. I look back on how little I knew as a first-year grad student, and am very thankful for their mentorship and patience. I also greatly appreciate their willingness to accept the career change I have made in the course of grad school, allowing me to work on projects and acquire skills which contributed to make that career change easier. Not all students are so fortunate as to have advisors so understanding and supportive of that decision. I also wish to thank all the extended members of the SAGES collaboration and SLUGGS surveys. It has been a pleasure getting to work with all of you on many various projects over the years. I appreciate the SAGES team being such a fun and supportive group.

There is no way I could have survived graduate school with an intact psyche without the support of all the amazing friends that I've met over the years. My cohort of Phil, Jieun, Alex, Camille, and Marie have been companions throughout all sorts of graduate school shared struggles. Claire, Katie, Chris, Alexa, and all the other friends that I've made in my time here have turned what can be a depressing drag into an enjoyable experience. And above all, I am thankful to Emily for being an amazing friend throughout, and for her unflinching support of me during my final year of school.

Finally, I am forever thankful for the continuous support of my parents and family through my schooling. While my dad will frequently state his amazement that I have been in school for 22 straight years without a break, I never would have embarked on this journey had a great curiosity about how things work not been instilled in me. My mom and dad are the reason for this, and their love and support, as well as that of the rest of my family, have been invaluable.

Paper Acknowledgments

The text of this dissertation includes reprints of the following published material by Jennings.

The contents of Jennings et al. (2014) make up Chapter 2. I was responsible for reducing the HST data and performing all analysis on the HST data. I also wrote all text and created all the figures of this paper. I would like to thank my coauthors Jay Strader, Aaron J. Romanowsky, Jean P. Brodie, Jacob A. Arnold, Dacheng Lin, Jimmy A. Irwin, Gregory R. Sivakoff, Ka-Wah Wong for their support and permission to include this work in my dissertation.

The contents of Jennings et al. (2015) make up Chapter 5. I was responsible for obtaining, reducing, and analyzing the SuprimeCam imaging of this galaxy. I was also responsible for all photometric analysis in the paper. All the text was written by me, along with Figs. 1 and 3. I would like to thank my coauthors Aaron J. Romanowsky, Jean P. Brodie, Joachim Janz, Mark A. Norris, Duncan A. Forbes, David Martinez-Delgado, Martina Fagioli, and Samantha J. Penny for their support and permission to include this work in my dissertation.

Science Acknowledgments

I gratefully acknowledge support from a Graduate Research Fellowship from the National Science Foundation, an ARCS fellowship from the ARCS foundation, and a UCSC President's Dissertation Fellowship. This research is based on observations made with the NASA/ESA *Hubble Space Telescope*, obtained from the data archive at the Space Telescope Science Institute. STScI is operated by the Association of Universities for Research in Astronomy, Inc. under NASA contract NAS 5-26555. Based in part on data collected at Subaru Telescope (operated by the National Astronomical Observatory of Japan) via a Gemini Observatory time exchange (GN-2008A-C-12), and also the 6.5 m Magellan Telescopes located at Las Campanas Observatory, Chile. Some of the data presented herein were obtained at the W. M. Keck Observatory, operated as a scientific partnership among the California Institute of Technology, the University of California and the National Aeronautics and Space Administration, and made possible by the generous financial support of the W. M. Keck Foundation. This material is based upon work supported in part by the National Science Foundation under Grants AST-1211995, AST-1109878, AST-1515084, and AST-1518294. This material is based upon work supported in part by HST-GO-12759.12-A. This research has made use of the NASA/IPAC Extragalactic Database (NED), which is operated by the Jet Propulsion Laboratory, California Institute of Technology, under contract with the National Aeronautics and Space Administration.

I would like to recognize and acknowledge the very significant cultural role and reverence that the summit of Mauna Kea has always had within the indigenous Hawaiian community. We are most fortunate to have the opportunity to conduct observations

from this mountain.

Chapter 1

INTRODUCTION

Globular clusters, or GCs, are among the oldest and most dense objects in the universe. Taken together, these two properties imply that GCs are powerful tool to probe the assembly histories of galaxies. Since GCs are predominantly old (the vast majority have ages greater than 10 Gyr), GCs have borne witness to most of the epochs of galaxy assembly. In addition, because of their high densities, GCs are capable of remaining gravitationally bound during merger events which would disrupt less-dense stellar systems. Furthermore, because they are so dense, GCs are also extremely easy to observe in extragalactic contexts where the light of galaxy field stars is far too faint. Understanding the origin and assembly of GC systems is akin to understanding the basics of how galaxies grow and assemble over their cosmic lifetimes. See Brodie & Strader (2006) for further discussion of the above points.

GCs have been used to infer information about galaxy formation at all sorts of different scales. For example, Forbes et al. (2011) examined GC color profiles as a function of radius in the galaxy NGC 1407. They interpreted flattening of color profiles at distance as indicative of two-phase galaxy formation, in which an inner gradient is formed in a dissipative collapse and outer flattening is created during steady accretion of other GC systems.

On the other hand, there is evidence of a link between GC system evolution and evolution on extremely small scales at the central supermassive black holes of galaxies. Strong correlations exist between the mass of a galaxy's central black hole and both the number of GCs, N_{gc} (e.g. Burkert & Tremaine 2010, but see also Harris et al. 2014) and the kinematics of the GC system Pota et al. (2013a). Explanations for these observations are still being made, but clearly understanding the global properties of GC systems ties directly in to understanding processes of galaxy evolution at all scales. GCs are also linked to galaxy properties at all scales in between, and it is clear that the GC systems of galaxies are evolutionarily related to all sorts of other galaxy properties.

Over the past decade, the Study of the Astrophysics of Globular Clusters in Extragalactic Systems (SAGES)[1] collaboration has undertaken the SAGES Legacy Unifying Globulars and Galaxies (SLUGGS)[2] Survey (Brodie et al., 2014). The SLUGGS survey has targeted a representative sample of 25 early-type galaxies spanning a wide-range in galaxy parameter spaces. The chief advantage of the SLUGGS survey is its combination of photometric and spectroscopic data.

Photometry has the advantage of probing much deeper detection thresholds and covering a much larger spatial area on the sky than spectroscopic data. Further-

---

[1] http://sages.ucolick.org/

[2] http://sluggs.swin.edu.au/Start.html

more, the acquisition of good quality photometry is what allows for target selection for spectroscopic follow-up. While this of course means that our imaging data must be acquired before our spectroscopic data, this also means that the imaging data is not subject to the same selection effects that must be employed to create a high-confidence spectroscopic target catalog.

Despite the difficulty in acquisition, spectroscopy has several advantages as well. First, a spectroscopic sample features essentially zero contamination; GC velocities in extragalactic systems are much greater than foreground stars in our own Milky Way, and much smaller than distant background galaxies. Spectroscopically-confirmed GCs thus offer a pristine sample of sources that one can perform analysis on. Furthermore, spectroscopy offers a much richer dataset than is available with photometry. Redshifts of GCs from spectra allow for extensive analysis of the kinematics of GC systems, providing information both about the potential well in which GCs exist as well as their potential infall channels into their host galaxies (e.g. Strader et al. 2011; Agnello et al. 2014; Pota et al. 2015).

1.1 Bimodality in GC Systems

One of the most striking features of GC systems is the fact that they exhibit color bimodality. When one examines the color distributions of extragalactic GC systems the distributions often clearly separate into two distributions, or at least what appear to be two distributions. This bimodality was first noticed in *HST* studies (e.g., Zepf & Ashman, 1993; Ostrov et al., 1993), where the precise photometry made this property stand out. Evidence for bimodality has since been found in many other studies in a wide range of GC contexts, including in the Milky Way.

This color bimodality has since been shown, in several systems, to also be seen in other parameter spaces. Blue GCs are frequently found to be more extended than red GCs, which tend to be more associated with the stellar light of the galaxy, (e.g. Foster et al. 2011; Strader et al. 2011; Blom et al. 2012b; Pota et al. 2013b, 2015). Red GCs also tend to have kinematics matched with the stellar kinematics of their galaxies, (e.g. Strader et al. 2011; Pota et al. 2015), and are typically more centrally-concentrated than the blue GCs.

It is unclear to what degree the bimodal models typically fit in the literature, usually bimodal normal distributions, are actually representative of the underlying distributions. Such distributions are typically chosen out of computational convenience. Some studies have found data that are inconsistent with such a simple bimodal model. Harris et al. (2017) examined distant GC systems in very massive galaxies using deep *HST* data. They found that, for these most massive systems, the GC color distributions appear much less distinct than a simple red and blue division. While unimodal normals are clearly poor fits to the data, other models may fit well without explicitly invoking a bimodal normal.

Other studies have found evidence that GC color distributions may be better-fit by trimodal distributions over unimodal distributions. For example, Blom et al. (2012b) found evidence for three populations in the galaxy NGC 4365, and Agnello et al. (2014) presented evidence for a very centrally-concentrated red population around NGC 4486.

Without a physically-motivated model for GC color distributions, linking these pieces of evidence to a physical third population is difficult. However, they do show that in some situations, the bimodal normal model may not do as effective job of fitting the data as other models. These difficulties in fitting motivate the development of more physically-motivated models.

Spectroscopicly measured metallicites, in systems where they exist, typically confirm that the GC bimodality is due to underlying differences in the metallicity of the different GC populations (Strader et al., 2007; Beasley et al., 2008; Brodie et al., 2011; Usher et al., 2012) (although others have proposed mechanisms by which non-linear color-metallicity relationships can produce the observed bimodality, c.f. Yoon et al. 2006, 2011). It is generally accepted that this underlying bimodality implies different channels by which the red and blue clusters have assembled. The simplest picture is one in which the red GC population is mostly formed from metal-enriched gas in more massive systems, while the metal poor GCs are predominantly formed from accretion of smaller dwarf systems with GCs which have been formed from their galaxy's more metal-poor gas.

1.2 Discussion of Bimodality Tests

Given the clarity with which bimodality has been observed in extragalactic GC systems, and the fact that it manifests itself in a wide range of measured parameters, it seems fairly reasonable that this bimodality is a real effect. However, it is important to clarify what is actually meant when one claims that a distribution is bimodal. Ashman et al. (1994) originally proposed a likelihood ratio test (LRT). The likelihood ratio compares likelihoods for both a mixture model with two normally-distributed distributions (with identical variances) and a model with a single normal distribution. This ratio can be shown to asymptotically approach a transformed χ^2_ν distribution, and therefore in the limit of infinite datapoints, can be assigned a probabilistic p-value in the typical frequentist approach to the problem.

Muratov & Gnedin (2010) proposed an updated version which allows for different variances in the proposed normal distributions, evaluating the chance of bimodality through bootstrapping algorithms. They also propose additional test-statistics including the relative difference of the bimodal distributions (scaled to the variances of the two distributions) and the measured kurtosis of the full distribution. They also note additional non-parametric means of detecting bimodality, such as the dip-test (see also Hartigan & Hartigan 1985; Gebhardt & Kissler-Patig 1999). Approaches from a Bayesian perspective, such as calculation of Bayes factors, have also been employed (Agnello et al. 2014, although see Gelman et al. 2013 for discussion of how Bayes factors can often lead to incorrect conlcusions).

However, an important caveat for all these methods (as noted by Muratov & Gnedin 2010) is that they mostly test whether the data are well-described by a single normal distribution, as opposed to definitively testing whether the data are likely to have been specifically drawn from two distributions. To put it another way, the standard LRT format of a test proposes a very specific alternative distribution, the bimodal normal, and then tests whether the single normal fails to describe the data relative to this alternative. One could imagine writing down all sorts of distributions (for example, a t-distribution with stronger tails) that might better describe the data. While the null distribution might not be a good descriptor of the data, this does not necessarily give strong evidence that the alternative is the ”correct” distribution.

Similar observations by Muratov & Gnedin (2010) motivate them to consider the additional test statistics, such as the measured kurtosis and the relative differences of the means. However, these test statistics still suffer from the above problems. Moreover, these additional test statistics are certainly not independent quantifications of bimodality; a dataset which is actually unimodal but which returns a significant result for bimodality under the LRT would also be expected to fail the other tests in a similar, although not identical, way.

Bayesian methods are not immune to this treatment; indeed, Bayes factors are typically very sensitive to priors, both on parameters and over the models themselves, and are often poorly-suited to problems featuring continuous data (Gelman et al., 2013). In general, it is a lot to ask from our data and our statistics that we are able to calculate a single number which can accurately compare the entire range of all possible “unimodal” distributions to the entire range of all “bimodal” distributions. Rather, we ought to look for areas where our current models perform well, and where it could be improved. It seems fairly convincing, from the evidence, that most GC color distributions are poorly described by single-mode normals. Making stronger conclusions than this requires additional treatment than is common in the literature. The general problem would benefit greatly from clear functional predictions from GC formation theories, which might then be fit using modern Bayesian techniques and checked to see how well they fit the data.

As a final point on this subject, we emphasize that, for ground-based photometry studies, unimodal normals are essentially guaranteed to be wrong due to the contamination present in ground-based data. We know that the “true” model of a GC system must account for this contamination. Otherwise, even a perfectly unimodal GC sample would have artificially- wide tails created by this contamination. Note that these wide tails will have have the same effect as a truly bimodal distribution in terms of rejecting a null, although the degree to which this will happen will depend on the amount of contamination relative to GCs.

1.3 ULTRA-COMPACT DWARF GALAXIES

Ultra-compact Dwarfs (UCDs) lie in a region of parameter space between the most massive GCs and the smallest dwarf galaxies, both in terms of total mass and in terms of angular size. A rough definition of a UCD is an object with an effective radius larger than 10 pc, with a luminosity of roughly $\mathrm{L_i} > 10^5 \mathrm{L}_\odot$ (Brodie et al., 2011).

The precise nature of UCDs is an open question. However, in the broadest sense, the primary point of interest is whether UCDs represent the largest star clusters or the smallest galaxies. This question essentially focuses on the formation channel by which most UCDs are created. Arguments have been put forward that UCDs may be formed within their galaxies (Fellhauer & Kroupa, 2002; Kissler-Patig et al., 2006; Murray, 2009), or they may be the central core remnants of dwarf galaxies that have fallen into the potential wells of larger galaxies and been disrupted (Bekki et al., 2001; Pfeffer & Baumgardt, 2013). Recent observations with adaptive optics instruments have confirmed that some UCDs contain embedded supermassive black holes (Seth et al., 2014; Ahn et al., 2017), essentially guaranteeing that at least some galaxies are stripped down to the sizes of large star clusters. Stellar population analysis has suggested that there may be a dividing line around $\sim 10^7$ $M_\odot$at which the formation channel for UCDs may become dominated by one process over the other (Janz et al., 2016).

A better understanding of the processes that create UCDs will have important implications both in understanding cluster formation physics, and in understanding the nature of galaxy accretion in a ΛCDM context.

1.4 OUTLINE

This work explores the photometric properties of GC systems using a wide range of data and methods. In Ch. 2, we explore the GC system of the galaxy NGC 3115 using a wide-field *HST*/ACS mosaic, which we supplement with ground-based Subaru/Suprime-Cam data. The use of *HST*/ACS data allows us to achieve a better target selection than is available in simple ground-based imaging. NGC 3115 is a prime target for study due to its nearby distance and its clearly bimodal GC system. We also investigate X-ray counterparts to likely GC candidates in the system. We explore this system in Ch. 2.

While *HST* imaging and spectroscopy are ideal datasets for investigating globular clusters, they are also typically biased (in spatial coverage and/or luminosity) and expensive to acquire. Wide-field ground based photometry is typically very efficient to acquire, at the cost of introducing potentially great levels of contamination from foreground stars in the MW and background galaxies. In Ch. 3, we consider a Bayesian mixture model formalism which attacks the problem of contamination in wide-field ground-based imaging. We demonstrate the method on mock data and verify that the inferences returned from the model are reliable. Following this, in Ch. 4, we apply the Bayesian mixture modeling to a selection of galaxies in the SLUGGS survey for which we have good-quality wide-field imaging. We present both our GC selection and our global parameter inference for each galaxy.

Finally, in Ch. 5, we switch gears somewhat and consider a UCD embedded in a stellar stream around the nearby spiral galaxy NGC 3628. We argue that this UCD represents the core of an infallng dwarf galaxy in the process of being disrupted in the potential well of NGC 3628. The combination of the stellar stream and this UCD allow us to establish an evolutionary link in parameter space between the infaling galaxy and this star cluster.

Chapter 2

The SLUGGS Survey: *HST*/ACS mosaic imaging of the NGC 3115 Globular Cluster System

2.1 INTRODUCTION

Globular clusters (GCs) serve a valuable role in the study of extragalactic systems. Due to their old ages, the properties of GCs trace the earliest stages of galaxy formation (see the review by Brodie & Strader 2006). In addition, due to their high luminosities, they are more easily observable than faint galaxy starlight, allowing for detailed inferences of galaxy formation and evolution in nearby systems at large galactocentric distances.

Extensive multi-wavelength investigation of nearby early-type galaxies has revealed a number of interesting properties in their GC systems. It has been well established for decades that early-type GC systems display clear color bimodality (e.g., Zepf & Ashman, 1993; Ostrov et al., 1993). It is generally accepted that this color bimodality corresponds to an underlying metallicity bimodality, with the red clusters metal-enhanced when compared to the blue clusters. This metallicity bimodality has been spectroscopically confirmed for a limited, but growing, number of systems (Puzia et al., 2002; Strader et al., 2007; Beasley et al., 2008; Alves-Brito et al., 2011; Usher et al., 2012; Brodie et al., 2012).

In addition, it is well established that a disproportionate number of low-mass X-ray binaries (LMXBs) in early-type systems are found in GCs (Fabbiano, 2006). The host GCs tend to be the most dense and compact clusters, where dynamical interactions are capable of creating LMXB systems. The exact properties of GCs that host these LMXBs are not well understood. It is generally established that the metal-rich subpopulation contains a significantly greater number of LMXBs, but it is not known how these properties may depend on other galaxy environmental factors (e.g., Sivakoff et al., 2007; Kundu et al., 2007).

In this paper, we investigate the GC system of the nearby S0 galaxy NGC 3115 with a six pointing *Hubble Space Telescope*/Advanced Camera for Surveys (*HST*/ACS) mosaic in the F475W and F850LP filters (hereafter g and z). *HST* observations of nearby GC systems have critical advantages over ground based imaging. The high resolution afforded by *HST* means that GCs will be partially resolved, allowing for measurements of their half-light radii (R_{h}). Extensive studies of partially-resolved GCs in *HST* imaging have revealed that red clusters are typically smaller than blue clusters, an observation that may be explained by either projection effects (Larsen & Brodie, 2003) or intrinsic differences (Jordán, 2004a).

However, while *HST* observations are powerful due to their resolution, they also feature a limited field of view. Ground based imaging is generally able to probe the halos of nearby galaxies out to many effective radii ($R_{\rm e}$), but *HST* requires multiple mosaiced images to achieve similar radial coverage. In general, while numerous studies have investigated GC properties in ACS imaging (e.g., Jordán et al. 2005, 2007a), there has been only limited exploration of GC trends out to several $R_{\rm e}$ (e.g Spitler et al., 2006; Forbes et al., 2006; Nantais et al., 2011; Blom et al., 2012b; Strader et al., 2012; Usher et al., 2013; Puzia et al., 2014). In particular, there have been few studies of the GC systems of lenticular galaxies in *HST*/ACS imaging, especially in non-cluster environments (e.g. Spitler et al., 2006; Cantiello et al., 2007; Harris & Zaritsky, 2009; Harris et al., 2010; Forbes et al., 2010). Finally, cluster size information has the added benefit of allowing us to search for ultra compact dwarf (UCD) candidates in our images.

NGC 3115 is of particular interest due both to its proximity and the properties of its GC system, and we are studying it as part of the SAGES Legacy Unifying Globulars and GalaxieS survey (SLUGGS; Brodie et al. 2014[3]). It is highly inclined and located at $D = 9.4$ Mpc (Tonry et al. 2001, with recommended correction of $(m - M) = -0.06$ from Mei et al. 2007). Both the galaxy as a whole, as well as its GCs, have seen previous discussion in the literature. Elson (1997) identified a color bimodality in the stellar halo of NGC 3115 in *HST*/WFPC2 data. Kundu & Whitmore

---

[3] `http://sluggs.ucolick.org`

(1998) subsequently analyzed the GCs seen in the WFPC2 data and identified a color bimodality in this population as well.

The GC system has also been analyzed spectroscopically. Puzia et al. (2002) identified a metallicity bimodality in the GC population using VLT/ISAAC spectroscopically, and found both populations consistent with being coeval, albeit with large uncertainties. Kuntschner et al. (2002) confirmed the GC bimodality in VLT/FORS2 spectroscopy of 24 GCs and found evidence for multiple formation epochs in the GC system. Brodie et al. (2012) demonstrated the metallicity bimodality to high confidence using a sample of 71 GCs with CaT-derived metallicities from DEIMOS spectra. Norris et al. (2006) found kinematic links between the NGC 3115 stellar spheroid component and the red GC population, as well as overall rotation in the GC population. Arnold et al. (2011) considered combined GC and stellar spectra and found that the properties of both the GC system and overall galaxy light favor a distinct 2-phase formation scenario wherein the halo of the galaxy is built through a series of minor mergers. The overall inferences from previous studies are that the color and metallicity bimodality in the GC systems are unambiguous, and that the GC system is clearly evolutionarily linked to the build up of the overall galaxy light. If there are intrinsic differences between the red and blue GC populations other properties (i.e. size or X-ray frequency), the NGC 3115 GC population is an ideal place to look.

For the remainder of this work, we adopt the $R_{\mathrm{e}} = 57''$ value for the bulge of NGC 3115 from Capaccioli et al. (1987) for consistency with Arnold et al. (2011), equivalent to ≈2.6 kpc projected distance. We also adopt the flattening value of $q = 0.5$

from Arnold et al. (2011) and a heliocentric recessional velocity of 663 km s^{-1} from Norris et al. (2006).

In §2.2, we discuss our methodology, particularly our methods for carrying out photometry and $R_{\rm h}$ measurements in our ACS images. In §2.3, we discuss our findings, including confirmation of color bimodality in the ACS data, the discovery of a "blue tilt," trends in color and $R_{\rm h}$ with galactocentric distance, and the results of a search for UCD candidates in our sample. In §2.4, we match our ACS catalog with *Chandra* X-ray detections and identify clusters with associated X-ray emission. Finally, in §2.5 we summarize our results.

2.2 DATA ANALYSIS

In this section, we discuss the methods employed to create our GC catalogs, consisting primarily of photometry and $R_{\rm h}$ measurements in our ACS mosaic. We also supplement our analysis with spectral catalogs of NGC 3115 GCs from Arnold et al. (2011) and Pota et al. (2013b), as well as a catalog of Subaru/Suprime-Cam g, r, and i photometry of the GC system initially analyzed in Arnold et al. (2011) but not fully published. We include the full catalog in this paper for reference.

2.2.1 Initial Data Reduction

The primary dataset analyzed in this work is the ACS/WFC mosaic of NGC 3115 from *HST* Program 12759 (PI: Jimmy Irwin). The mosaic consists of six pointings of the galaxy, extending out to $\sim 5R_{\rm e}$. Exposures are 824 s in g and 1170 s in z, with

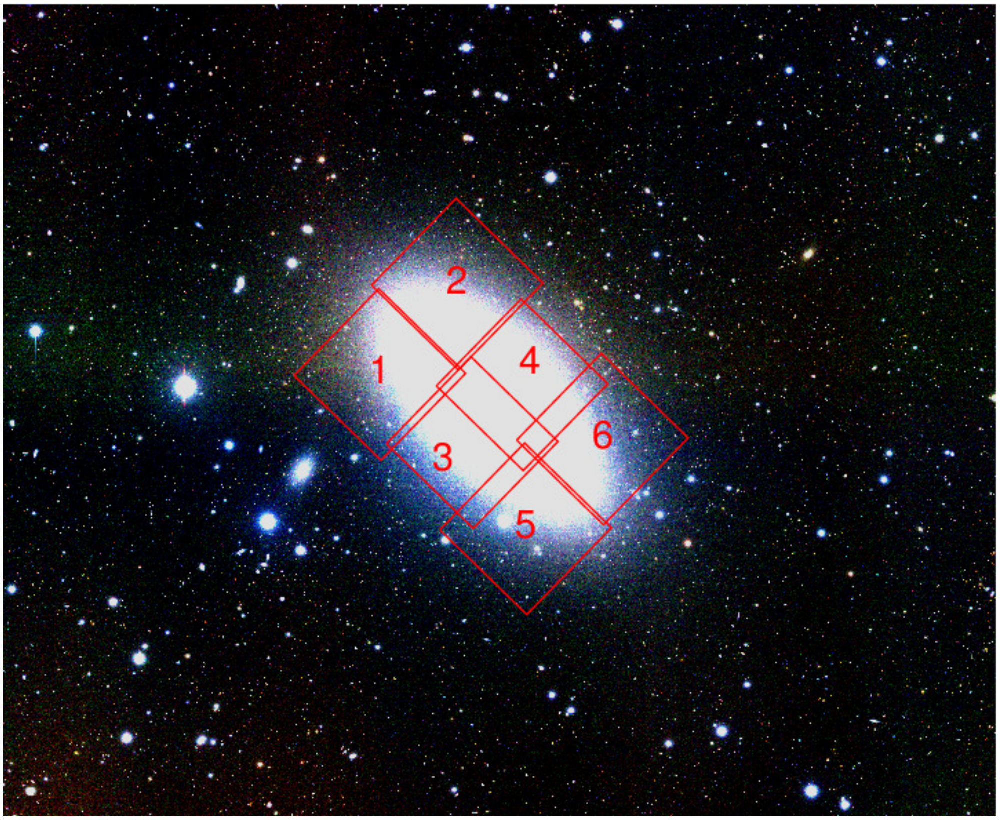

Figure 2.1: Combined g, r, and i Suprime-Cam image of NGC 3115. g is colored blue, r green, and i red. The locations of our six *HST*/ACS pointings are overlaid. North is up and east is left. Each box approximately represents the ACS field of view and is $200''$ on a side.

the exception of the POS-3 pointing (labelled 3 in Fig. 2.1), which was observed with exposures of 722 s in g and 1137 s in z. A simple line dither was used to cover the ACS chip gap, with 2 total exposures in g and 3 in z at each pointing. The two central pointings overlap significantly in the center in order to increase the signal-to-noise ratio (S/N) for the innermost GCs, where galaxy light adds additional noise. In Fig. 2.1, we overlay our six ACS pointings on the combined g, r, and i Subaru/Suprime-Cam mosaic.

We downloaded the *.flc* files of the exposures from the MAST website. These files have been flat-fielded and corrected for charge transfer efficiency problems in the ACS instrument. We then used the *astrodrizzle* [4] package to drizzle the separate images into distortion-corrected mosaics for each filter at each pointing. We performed a conservative CR rejection during the drizzling process to reject obvious cosmic rays.

2.2.2 Initial Photometry Measurements

We created our initial catalog for analysis using SExtractor (Bertin & Arnouts, 1996), selecting all candidates that were 3σ above background. We also required that each selection have at least 10 connected pixels. Photometric zeropoints were calculated using the ACS $PHOTPLAM$ and $PHOTFLAM$ keywords, placing the magnitudes on to the AB system. It is worth noting that while the *HST*/ACS filters are very close to the SDSS filters, they do not have precisely the same response functions, and slight systematic offsets are not unexpected.

We performed aperture photometry on this full list using the *daophot* package

---

[4] http://www.stsci.edu/hst/HST_overview/drizzlepac

in *IRAF*. We measured magnitudes within a 5 pixel ($0.25''$) aperture to maximize S/N, which we corrected to a 10 pixel ($0.5''$) aperture based on average photometric measurements of bright GCs in our data. The values of these corrections are 0.175 in g and 0.249 in z. Finally, we corrected these magnitudes to pseudo-infinite apertures ($5.5''$) using the values from Sirianni et al. (2005), who measured corrections of 0.095 is g and 0.117 in z. We also corrected for galactic foreground reddening using the Schlegel et al. (1998) reddening maps with updated calibrations from Schlafly & Finkbeiner (2011, $A_{\rm V} = 0.130$ for NGC 3115).

For the largest GCs in our sample, the above aperture corrections will systematically underestimate the final magnitudes due to additional light falling outside the 10-pixel corrected aperture. To correct for this, we employed size-dependent aperture corrections as described in §2.2.3. Based on the consistency of our photometry with matched Subaru/Suprime-Cam photometry (see §2.2.5), we conclude that our photometric methods are reasonable. It is worth noting that the size-dependent corrections are less well-constrained for the largest clusters due to the low S/N in the wings of the ACS PSF. As a result, while the size-dependent corrections are an appropriate first-order correction for the luminosities of the largest clusters, there will still be lingering systematic uncertainties.

None of our results depend strongly on the actual measured luminosities of the GCs, and systematic errors in the aperture corrections of GCs have little effect on the measured color of our sources. The latter point has also been emphasized in previous ACS studies of extragalactic GC systems (Jordán et al., 2009; Strader et al., 2012).

After photometry was performed, we pruned our catalog down to a list of reasonable GC candidates. First, we required that each object was detected in both filters by matching the coordinate lists within 2 pixels. We also rejected objects fainter than $g = 26$ or $z = 25$ to remove spurious noise detections and objects significantly fainter than we would expect for the GC population (typical turn-over magnitudes for GC populations will be $g \sim 22.5$ at the distance of NGC 3115, see Jordán et al. 2007b). Several of our pointings feature overlap, especially across the center of NGC 3115. We measured a simple astrometric shift to transform all pointings to the same WCS. We then matched sources across both pointings to within 3 pixels to combine photometry from sources imaged in multiple pointings. For all such sources, our final magnitudes are a weighted average of the separate photometric measurements. The median offset between sources detected in multiple images is 0.023 mag.

2.2.3 *ishape* R_h Measurements

The principal advantage of ACS GC imaging is the superior angular resolution of the instrument, which allows us to resolve the angular size of globular clusters. Throughout the paper, we quantify this size in terms of a half-light radius (R_{h}) and use the terms interchangeably. At the distance of NGC 3115, GCs of typical radius ($\sim$ 2–4 pc) will be partially resolved. The point spread function (PSF) of a partially resolved cluster is a convolution of the intrinsic PSF of the ACS instrument and the light profile for GCs, which we assume to be described by a King profile. We measured the PSF empirically using bright, unsaturated stars in the ACS field. The PSF was measured separately for each filter, but the same PSF was used across all pointings for each filter. We then used *ishape* (Larsen, 1999) to measure the FWHM of the King profile of the GC, which is easily converted to a half-light radius R_h using the relation $R_\mathrm{h} = 1.48(\mathrm{FWHM}_\mathrm{King30})$ (Larsen, 1999). The cluster concentration c (defined as $c \equiv\ r_\mathrm{t}/r_0$, where r_t is the tidal radius and r_0 is the core radius) cannot be measured reliably for most clusters; as a result, we adopted a King profile with a fixed value of $c = 30$ for all cluster measurements, consistent with other partially resolved GC studies (e.g., Harris & Zaritsky, 2009; Strader et al., 2012).

We made measurements of R_h using both filters. In Fig. 2.2, we plot the difference between sizes measured in both filters, $R_\mathrm{h,g} - R_\mathrm{h,z}$. We measure precisely zero median offset between the filter measurements. The standard deviation of the differences is 0.55 pc, indicating good agreement between the filters with some scatter in R_h measurements for the same source. In general, the scatter of the difference is larger both for more extended clusters and for fainter sources. Note that some clusters have exactly the same measurement in multiple filters due to internal resolution limits in ishape. For the remainder of the paper, we adopt the weighted average of the R_h value measured in the two filters. Previous studies of ACS-measured GC sizes have found systematic uncertainties on the level of ∼20%, or ∼0.4 pc for a typical cluster size of 2.0 pc, when measuring sizes with *ishape* (Spitler et al., 2006; Harris & Zaritsky, 2009).

Harris (2009a) argued that measurements of R_h are only reliable for candidates with S/N above 50, which roughly corresponds to limits of $g \sim 24$ and $z \sim 23$ in our data. While we measure sizes for all candidates in our sample, when we examine trends

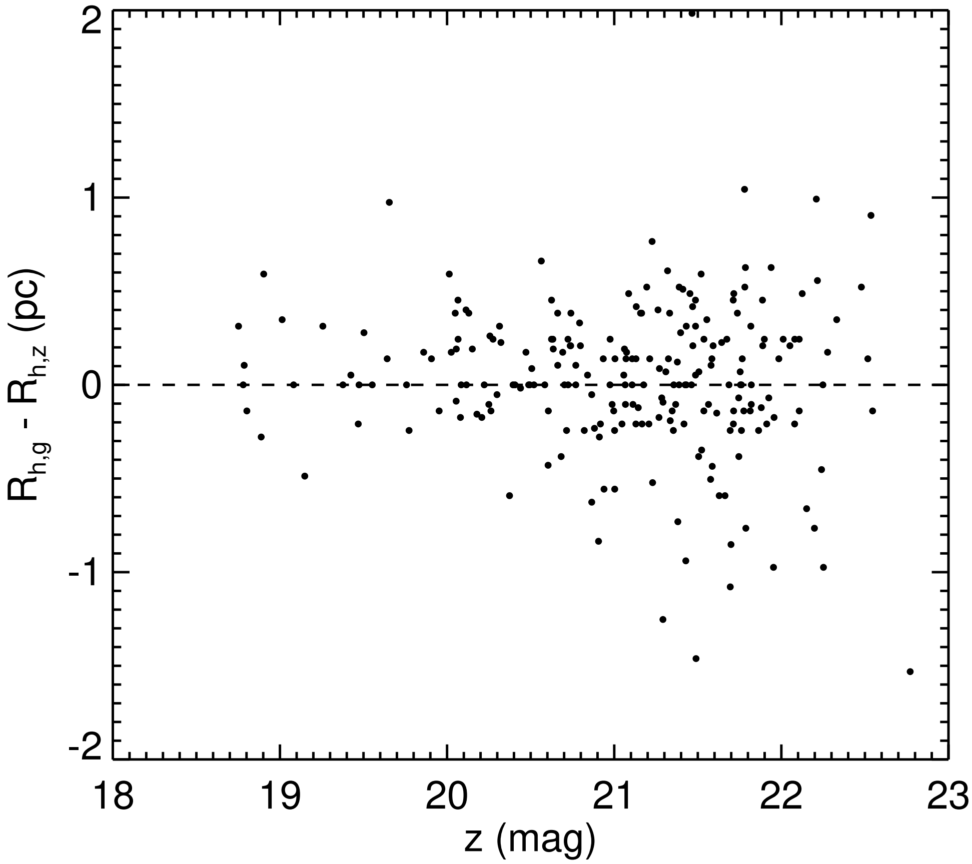

Figure 2.2: Plot of difference in R_{h} as measured in each of our two filters, g and z. We find a median offset of $(R_{\mathrm{h,g}} - R_{\mathrm{h,z}})_{med} = 0.00$ pc. The standard deviation of the differences is 0.55 pc. We interpret this as good agreement between the two filters, and use the weighted average of the two individual R_{h} measurements for the remainder of this work.

in the sizes of the GC subpopulations, we only consider those clusters with S/N above 50, around 65% of our sample.

Size-Dependent Aperture Corrections

To correct for additional light outside the 10 pixel aperture, we employed size-dependent aperture corrections for the full sample using a similar method to Strader et al. (2012). We convolved the empirically measured PSF from the ACS imaging with King profiles of fixed concentration 30, the same as used for the *ishape* measurements. We varied the FWHM of the King profile to create a series of fake clusters from $R_{\mathrm{h}} = 0$ pc out to $R_{\mathrm{h}} = 40$ pc. Using aperture photometry, we measured the light excess outside the 10 pixel aperture as a function of input cluster size, which we then used to correct our measured photometry. Representative corrections in g are 0.004 mag for $R_{\mathrm{h}} = 2$ pc, 0.30 mag for $R_{\mathrm{h}} = 10$ pc, and 0.94 mag for $R_{\mathrm{h}} = 30$ pc. These values are larger than those in Strader et al. (2012) because NGC 3115 is $\sim$ 7 Mpc closer than NGC 4649. As a result, clusters of similar size occupy a much larger angular area in the NGC 3115 data, requiring larger aperture corrections.

We performed corrections separately for the g and z filters, using the empirically measured PSF for both. However, since the excess light for large clusters is dominated by the King profile, the influence of the empirical PSF is minimal and thus the difference in the corrections between the two filters is small. As a result, the colors of the clusters are essentially unchanged by these corrections, as discussed in §2.2.2.

Note that uncertainties in the measured sizes of clusters are neglected in these photometric measurements. For GC-sized objects, these uncertainties are negligible given the small magnitudes of the corrections. However, for the larger objects in our sample, uncertainties in the measured sizes of objects can be large, especially for objects which are not actually well-parameterized by King profiles (i.e. background galaxies).

2.2.4 Catalog Selection

We performed *ishape*[5] (Larsen, 1999) measurements on the remaining ACS detected sources, as explained in §2.2.4. We considered any source with a measured size less than 0.3 pc a likely point source and removed it from the final GC candidate catalog. A color cut was applied to the catalog, selecting sources between $0.5 \leq (g-z) \leq 1.7$. We also performed a by-eye rejection of obvious background galaxies with visible features. Finally, we used our measured *ishape* sizes to remove extended objects, as described in §2.4.2. After all cuts, we were left with 360 GC candidates in our final catalog.

Table 1 summarizes the number of GC candidates in our various catalogs. We also list the number of GCs in the red and blue subpopulations, the division of which is explained in §2.3.1.

Use of $R_{\rm h}$ Measurements in Catalog Selection

Our use of *ishape* size measurements in pruning our final catalog merits further discussion. In any catalog cuts we may consider, we must make a trade-off between rejecting as much contamination as possible while preserving bona fide clusters. This motivates the use of different cuts in size for different scientific measurements of interest. We investigate three different catalogs in §2.3.

---

[5] http://baolab.astroduo.org/

Table 2.1: Summary of GC Catalogs Analyzed in this Work

Catalog	Total GCs	(With Spectra)	Blue GCs	(With Spectra)	Red GCs	(With Spectra)
ACS Detected GCs	360	(134)	191	(64)	169	(70)
Suprime-Cam Only	421	(42)	299	(24)	122	(18)
All GC Candidates	781	(176)	490	(88)	291	(88)

Note: Since spectroscopic data were acquired before the *HST*/ACS data,
no GCs unique to the ACS catalog have spectroscopically measured velocities.

First, for investigation of trends in cluster color and magnitude, we are chiefly interested in rejecting contaminating foreground stars and background galaxies that happen to fall in our GC color-magnitude space. As a result, we reject any source with a measured $R_{\rm h} < 0.3$ pc as being a point source, and therefore either a foreground star or background AGN. In addition, any source with a measured $R_{\rm h} > 8.0$ pc was rejected as being a possible background galaxy. While these cuts may also reject a few actual GCs from our sample, this rejection will simply increase random uncertainties from having fewer clusters. Note that, for these rejections, we still incorporate R_h measurements for clusters with S/N below 50. These are probably not very reliable for the larger sized objects, but there is no obvious selection bias introduced in the colors by their removal.

Many extended sources tend to be in the magnitude range where *ishape* is not as useful for rejection of galaxies. These sources will be extended, but with measured sizes that are still consistent with the largest GCs and luminosities that are consistent with the faint end of the globular cluster luminosity function (GCLF). To deal with such sources, we employ an aperture difference measurement: we reject any object with $g_{\rm 5pix} - g_{\rm 10pix} > 0.4$ as being extended, allowing us to cull down our final candidate list to a reasonable selection of GCs. We plot this selection criterion, which rejected 28 sources, in Fig. 2.3. We consider this catalog, containing 360 sources, as our final GC candidate list.

For §2.3.4, dealing with specific $R_{\rm h}$ measurements, we also reject all objects with a S/N below 50. For this analysis, we are interested in more precise measurements of GC $R_{\rm h}$, rather than crude rejection of point sources or highly extended objects. This

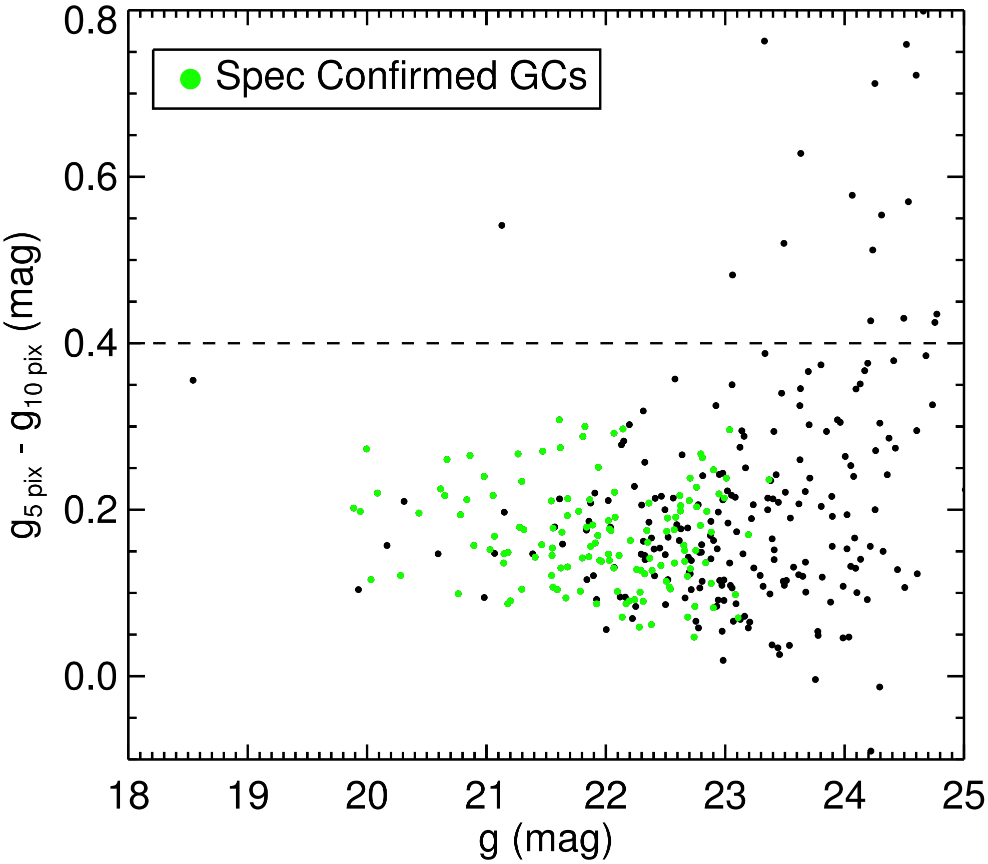

Figure 2.3: Illustration of our aperture-difference galaxy rejection method. We plot the difference in g as measured in 5 and 10 pixel apertures against the full corrected g value. We consider those clusters with $g_{5\mathrm{pix}} - g_{10\mathrm{pix}} > 0.4$ as being extended sources and remove them from our highest confidence GC catalog. Spectroscopically-confirmed GCs are plotted in green.

list of high S/N GCs contains 235 objects.

Finally, for §2.3.5, we are interested in finding ultra compact dwarf (UCD) candidates, as well as other clusters with sizes more extended than typical for GCs. As we are interested in reliably measured sizes for larger objects, we still require that the S/N of these candidates be greater than 50. However, as we are specifically interested in identifying sources with large R_h, we remove all constraints on the maximum size of the clusters, including both R_h measurement rejection and aperture difference rejection. This list of large UCD candidates contains 31 sources. Note that this list still discards objects rejected in our by-eye step that have obvious morphological features of galaxies.

2.2.5 Ground Based Photometry and Spectroscopy

To provide comparison with earlier work and improve our catalog selection, we supplement our ACS data with ground based imaging and spectroscopy. Arnold et al. (2011) presented a photometric and spectroscopic study of GCs around NGC 3115 using a combination of Subaru g, r, and i photometry and DEIMOS, LRIS, and IMACS spectroscopy. In this work, we publish the full catalog of Surpime-Cam(Miyazaki et al., 2002) photometry from the Arnold et al. (2011) study. The full spectroscopic sample was subsequently published in Pota et al. (2013b), and we include these velocities where available. The catalog includes 176 GCs with measured radial velocities consistent with NGC 3115 membership. In addition, there are 421 point-sources without measured velocities but with g, r, and i colors consistent with GCs. The color cuts adopted by

Arnold et al. (2011) correspond to

$$0.5 \leq (g-i)_0 \leq 1.4 \tag{2.1}$$

and

$$0.45 \times (g-i)_0 - 0.026 \leq (g-r)_0 \leq 0.45 \times (g-i)_0 - 0.08. \tag{2.2}$$

The Arnold et al. (2011) catalog also removes objects fainter than $i = 23$.

We display the color–color diagram in Fig. 2.4, with the entire point source catalog (~ 20000 objects) in black and those which passed the color–color cut in blue. In addition, we plot the location of GCs with ACS measured sizes in red and spectroscopically confirmed GCs in green. It is clear that color-color selections from ground based imaging reject a number of strong GC candidates, which is a necessary trade-off given the contamination of foreground and background sources away from the GC color-color sequence. Note that some spectroscopically confirmed GCs are outside the color-color selection as well. These GCs were placed on DEIMOS slitmasks as “low-confidence” GCs outside the main color selection, but ended up being confirmed regardless, further indicating the incompleteness of any sample selected with simply unresolved photometry.

Note that this catalog likely includes significant contamination from foreground stars and background galaxies, which are difficult to reject in ground-based imaging without measured radial velocities. We matched this GC catalog with our ACS data and identified 187 sources consistent with both catalogs.

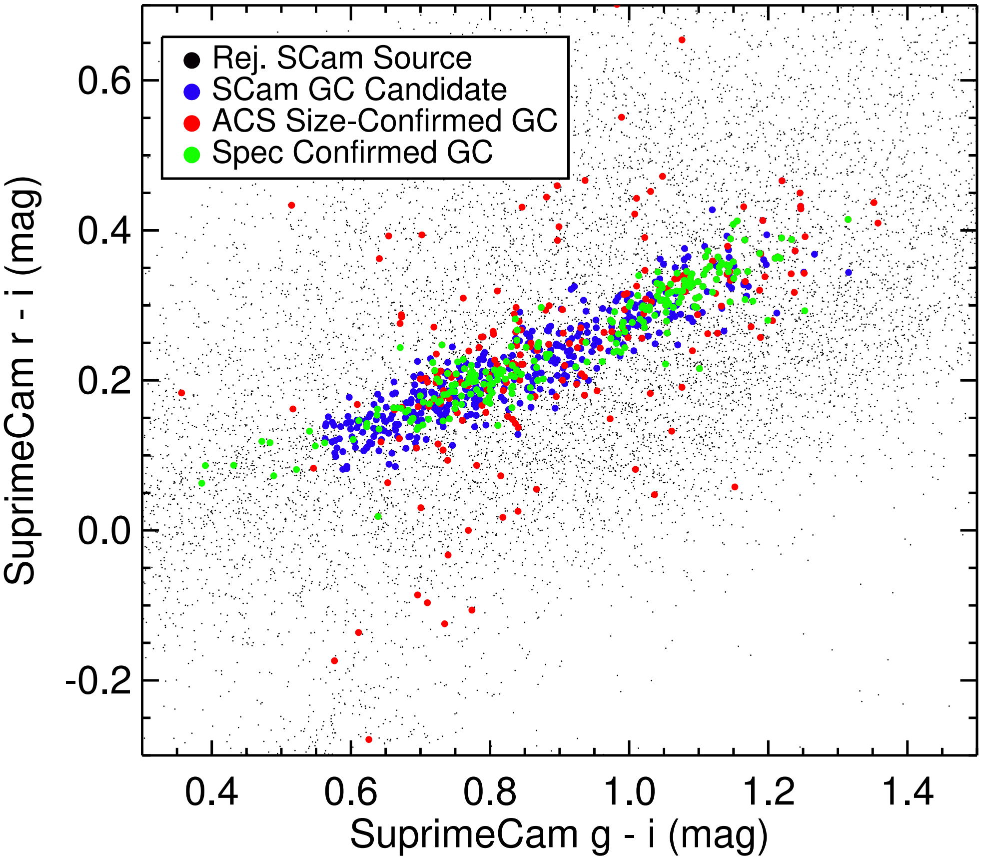

Figure 2.4: SuprimeCam $(g-i)_0$ vs. $(r-i)_0$ color–color diagram. All detected point sources are plotted in black, while those that pass our color–color and FWHM cuts are plotted in blue. We also plot GCs with ACS-measured sizes in red and spectroscopically confirmed GCs in green.

We did not use the Suprime-Cam catalog g, r, and i color–color photometry to reject any ACS objects that otherwise passed our ACS CMD and size cuts. While this would allow us to reduce background galaxy contamination in the ACS catalog, it would also introduce additional selection biases into our sample and reject a number of true GCs. We have greater confidence in ACS identified selections with consistent sizes than in non-spectroscopically confirmed Suprime-Cam color–color selections. However, we still include the measured Suprime-Cam photometry for these cases in our data table for reference.

Note that significant selection biases factor into which catalog a source will be found in. The Suprime-Cam catalog will be less complete very close to the nucleus of NGC 3115, and will also not reach as faint as the ACS catalog. In addition, brighter GCs were preferentially selected for spectroscopy due to observational constraints; it is difficult to get reliable spectra for GCs fainter than $i \sim 22$, and essentially impossible for objects fainter than $i \sim 23$. Finally, as the Suprime-Cam catalog was used to select spectral targets, no GCs unique to the ACS catalog have spectral confirmation.

It is worth noting that better selection can be achieved from color-color selections if NIR photometry is incorporated. Muñoz et al. (2014) demonstrated that incorporation of K-band photometry in color-color selections provides a much better discriminant between GCs and contaminants. There are still difficulties with identifying real GCs outside typical color-color selections. However, as more NIR photometric datasets of nearby galaxies become available (e.g. NGVS-IR), contamination of foreground and background objects in purely photometric GC studies can be significantly reduced.

We briefly detail our methods for Subaru/Suprime-Cam photometry below. Methodology for spectroscopic data analysis was presented in Arnold et al. (2011).

Subaru/Suprime-Cam Photometry

NGC 3115 was imaged in g, r and i-band filters on January 4th, 2008 using Suprime-Cam on the 8.2-m Subaru telescope. The camera's $34'$-by-$27'$ field-of-view consists of a mosaic of ten 2k-by-4k CCDs, separated by an average gap width of $16''$. A series of short exposures were taken with each filter (g: 5x40s, r: 5x15 s, i: 5x15 s) using a pre-defined 5-point dither pattern to account for bad pixels and to fill in chip gaps. Seeing varied between $0.5''$ and $0.7''$.

Suprime-Cam data were reduced using the *SDFRED1* pipeline[6]. Standard aperture Photometry was performed using IRAF, with zero points computed from SDSS sources in the field of view of a different galaxy observed the same night. This is necessary as NGC 3115 is not in the SDSS footprint. We also performed a color-correction to place our measurements onto the SDSS filter system[7]. Our apertures were selected to maximize the S/N. We then performed an aperture correction using a larger aperture and several bright stars located in the field. Astrometry was calibrated using the USNO-B catalog.

We compared our ACS measured g magnitudes to those from Subaru imaging. In Fig. 2.5, we plot $g_{\rm acs} - g_{\rm sub}$ against $g_{\rm acs}$. For GC candidates in both catalogs, we found a median difference of $g_{\rm acs} - g_{\rm sub} = -0.018$ with the standard deviation of the

---

[6] http://www.naoj.org/Observing/Instruments/SCam/sdfred/sdfred1.html.en

[7] http://www.sdss.org/dr7/algorithms/jeg_photometric_eq_dr1.html#usno2SDSS

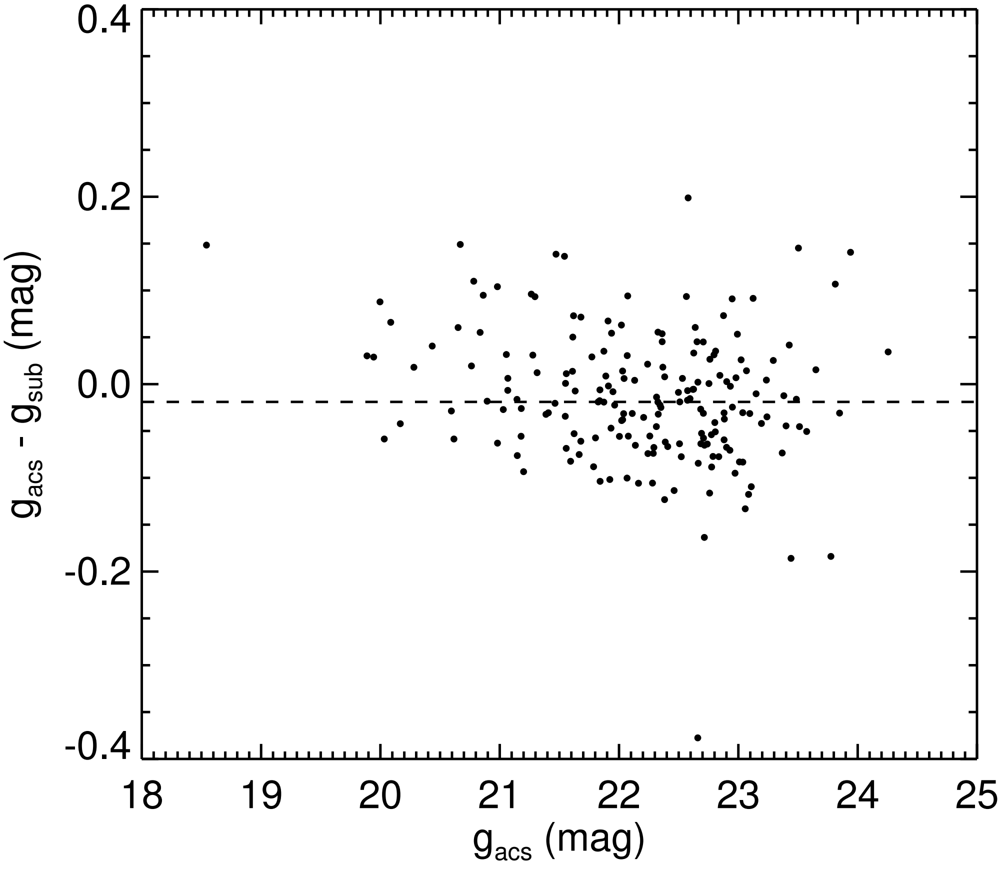

Figure 2.5: Difference between $g_{\rm acs}$ and $g_{\rm sub}$ for GC candidates common to both the ACS catalog and the Subaru Suprime-Cam catalog. The median offset between the photometry is 0.018 mag and the standard deviation of the differences is 0.078 mag, indicating good agreement.

differences being 0.078. Thus while there is some scatter in our measured photometry for a given source, in general g magnitudes can be compared without regard for any sizable systematic offset. Since GCs are unresolved point-sources in the Subaru photometry, a size-dependent aperture correction is not applicable to the Subaru imaging. ,

Use of Radial Velocities in Catalog Selections

For purposes of our catalog, we rejected any sources with measured radial velocities less than 350 km s^{-1} as being Milky Way foreground stars. While there will likely be a small amount of GCs with radial velocities smaller than this, Milky Way star contamination becomes dominant for velocities below this. For reference, the systematic radial velocity of NGC 3115 is 663 km s^{-1}, with a typical rotational velocity of ∼240 km s^{-1} and a dispersion of ∼100 km s^{-1} (Norris et al., 2006). Naturally, the latter two quantities vary with radius. We did not use radial velocities to reject background objects. Only six of our photometrically selected GCs have measured radial velocities greater than 1000 km s^{-1}, the highest of which is 1210 km s^{-1}. As there are no objects with velocities drastically inconsistent with NGC 3115 measurement, we included all these objects in our GC catalog. Inclusion of these six objects ultimately makes no difference to our overall conclusions.

2.2.6 Globular Cluster Luminosity Function

As a check on the reasonableness of our catalog selection criteria, we plot and fit the measured g-band GCLF for GC candidates observed for our ACS sample in Fig 2.6. We recover a reasonably well-defined GCLF. A Gaussian fit returns a peak

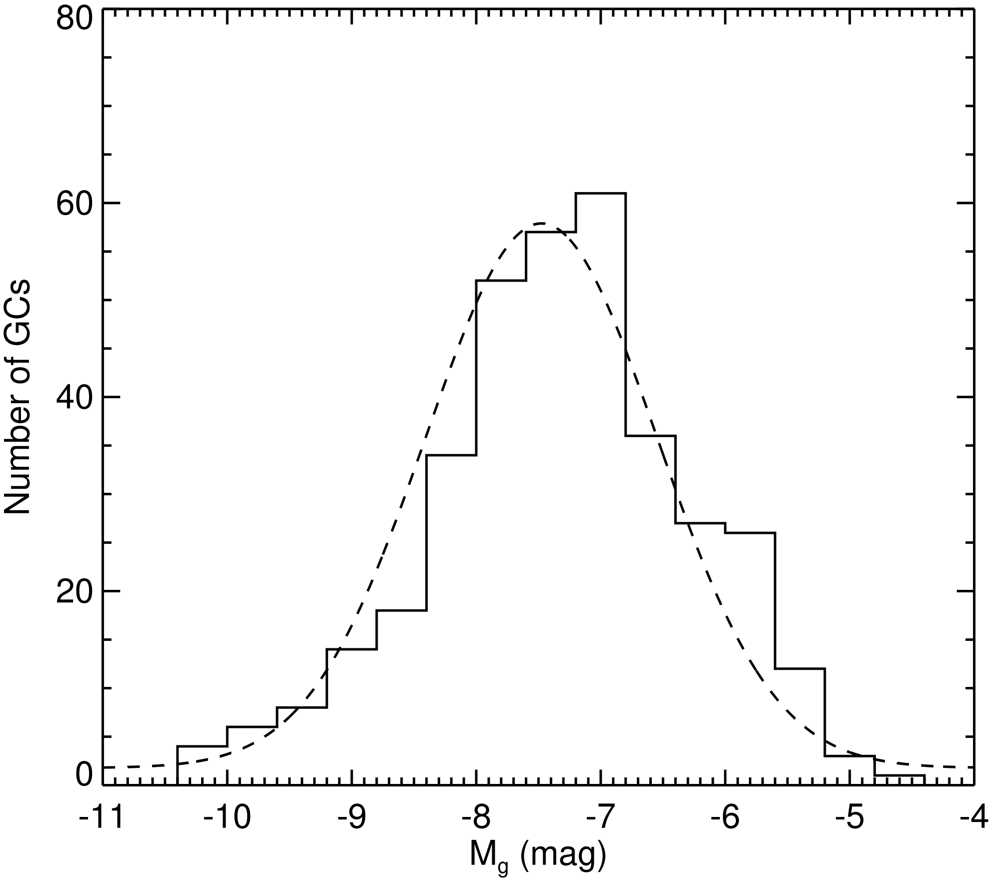

Figure 2.6: Histogram of GC candidate absolute magnitudes, with Gaussian fit plotted. The luminosity function peaks at $M_{\mathrm{g}} = -7.4$, consistent with studies of the GCLF around other early-type galaxies. We take this as evidence that our selection criteria produce a reasonable GC catalog, and that our data are reasonably complete down to the faintest magnitudes at which we would expect to find GCs. The poor fit at low luminosities is indicative of the level at which background contamination sets in (roughly $g \sim 23$ in apparent magnitude).

located at $M_{\rm g} = -7.4, \sigma_{\rm g} = 0.97$, which is consistent with that observed in ACS studies of other early-type galaxies (Jordán et al., 2007b). As we recover reasonable parameters for GCLF, we conclude that our catalog selection criteria produce a well-selected GC candidate list. Note that we have neglected any sort of contamination or completeness correction in the fitting of the GCLF. The ACS mosaic is deep, so it is likely that we are quite complete down to low luminosities. However, the GCLF fits more poorly at lower luminosities. This is an indication of the level at which contamination of the sample by background galaxies sets in, around roughly $g \sim 23$ in apparent magnitude.

It is worth noting that the selection biases in the Suprime-Cam catalog and the ACS catalog are different. In color-color space, background galaxies overlap little with GCs, and as a result the 3-filter Suprime-Cam catalog offers an effective means of background galaxy rejection. However, foreground star contamination is still prevalent in this catalog. Since GCs are partially resolved in ACS images, it is fairly easy to differentiate between unresolved foreground stars and partially resolved GCs in the ACS catalog. However, background galaxy rejection is somewhat ambiguous in the ACS data (although still reasonably achieved with color and size selections).

2.2.7 X-Ray Observations

The *HST*/ACS mosaic examined in this study was acquired to provide companion optical photometry to a ~ 1 Msec *Chandra* observation of NGC 3115. The full details of the *Chandra* data analysis are presented in Lin et al. (2015a). In this work, we match the observed X-ray sources from this catalog to GC candidates in the ACS mosaic to find GCs which may harbor LMXBs. To treat uncertainty on the position, we adopt the 3-σ uncertainty on the X-ray position source position; we assume that the uncertainties on the ACS-measured positions are small in comparison to the uncertainties on the X-ray-measured positions. A more thorough investigation of the choice of selection annulus will be included in the companion paper. Typical values of this uncertainty are $\sim 0.4''$. If any ACS GC candidates are found within the 3-σ uncertainty of the X-ray detection, we classify the closest ACS GC candidate as having an X-ray match. We did not encounter any situations in the ACS data where multiple GCs were within the 3-σ radius.

For Suprime-Cam detections far from the center of the *Chandra* pointing, the *Chandra* PSF is large, and there are a handful of *Chandra* sources where the 3-σ uncertainty overlaps with multiple Suprime-Cam sources. As we do not perform any analysis of the Suprime-Cam/X-ray matches in this work, we do not attempt to resolve these ambiguities further in this work and simply associate the single nearest source to the X-ray centroid as matching the X-ray detection. We briefly comment on apparent features of those GCs that hosts X-ray sources, specifically the coincidence fractions, in §2.4.

2.3 RESULTS AND DISCUSSION

In this section, we examine the photometry and sizes measured for our GC candidates. To explore trends in these values as a function of galactocentric radius, we adopt an equivalent "elliptical radius", defined as

$$R_{\rm g} = \sqrt{qX^2 + Y^2/q}, \tag{2.3}$$

where $q = 1 - b/a = 0.5$ is the flattening parameter for NGC 3115 and X and Y are cartesian coordinates measured along the major and minor axes of an ellipse centered on NGC 3115. While magnitudes of various gradients do change slightly (as would be expected) if we instead parameterize our radial trends using a simple circular radius, none of our overall conclusions are changed. Unless otherwise noted, $R_{\rm g}$ is measured in kiloparsecs for the remainder of the paper. We adopt the same P.A.= 43.5° as Arnold et al. (2011). Unless otherwise noted, we quote 1 σ uncertainties on any fitted relations.

In a few sections, we will discuss GC masses in place of luminosities. For these conversions, we must naturally use a mass-to-light ratio. We adopt a constant $M/L = 1.45$ from the arguments presented in Sivakoff et al. (2007) for all such conversions in the remainder of the paper.

In Table 2, we list a sample of our full catalog. *HST*/ACS objects are listed first, with objects only detected in Subaru Suprime-Cam imaging following. The entire catalog is available online in a machine readable format.

2.3.1 Color Bimodality

In Fig. 2.7 we present the measured ACS color-magnitude diagram (CMD) of the GC system in NGC 3115. The color bimodality of the NGC 3115 system, while well established, is particularly obvious in the ACS catalog. Using Gaussian Mixture

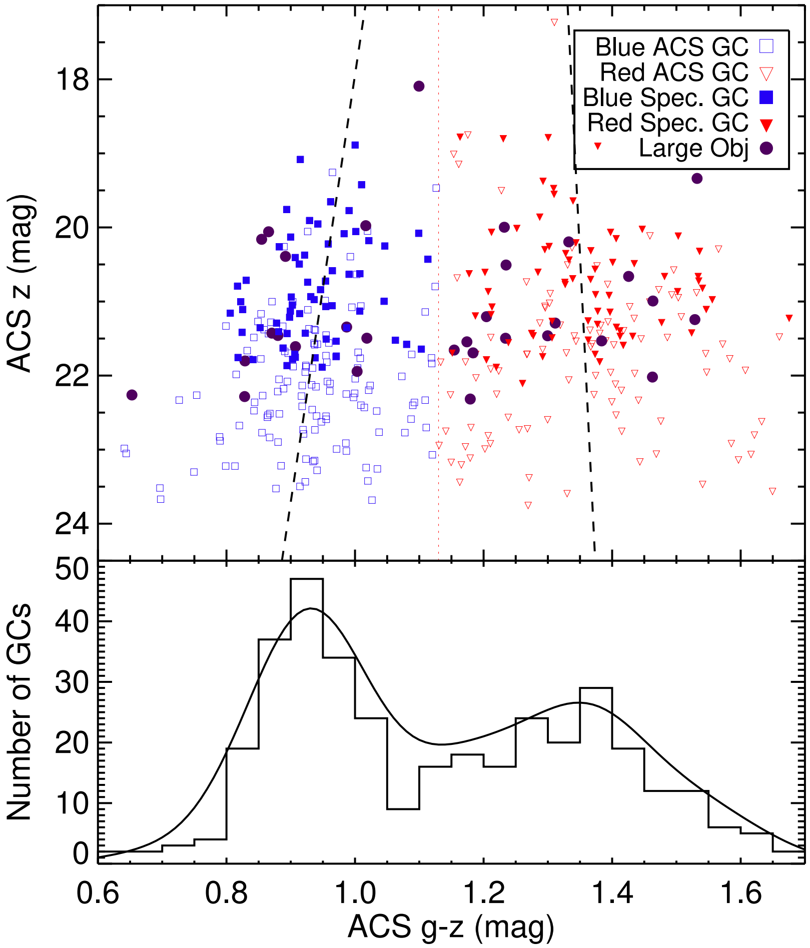

Figure 2.7: Top Panel: Observed CMD of GCs in our catalog, following application of our various quality cuts. Metal-poor and metal-rich subpopulations are plotted in blue and red respectively. Spectroscopically confirmed GCs from Arnold et al. (2011) are plotted as solid symbols, while those without spectroscopic confirmation are plotted as open symbols.. The well-studied bimodality of the GC system is clear in our data. The color dividing line is located at $g - z = 1.13$ and marked with a red dashed line. The "blue-tilt" mass-metallicity relation is clear in the blue subpopulation. There are also hints of an opposite trend in the very brightest metal-rich clusters, but it is of low significance. Bottom Panel: Color histogram of GC candidates, with Gaussian kernel density estimate overplotted. The Gaussian density plot and histogram are scaled to containe the same total number of GCs. The bimodality of the system is clearly visible.

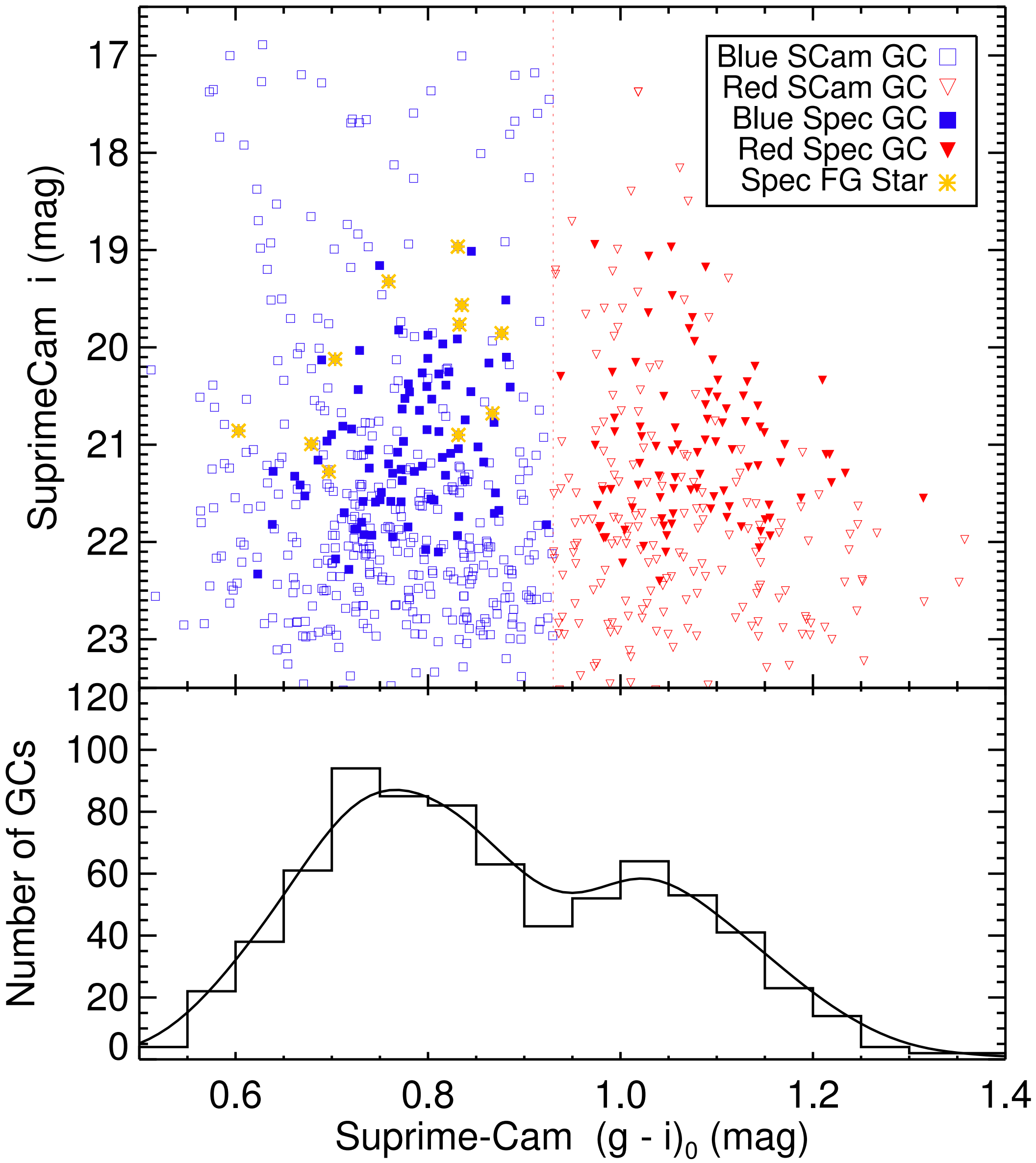

Figure 2.8: Top Panel: CMD of Suprime-Cam detected GCs. GCs with spectroscopic confirmation are plotted as sold symbols, while those without spectroscopic confirmation are plotted as open symbols. Bottom Panel: $(g-i)_0$ histogram for Suprime-Cam imaging, with Gaussian kernel density estimate overplotted. The division between blue and red subpopulations is located at $(g-i)_0 = 0.93$ and is marked with a dashed red line. The Gaussian density estimate is normalized so that the total number of GCs is the same as the histogram.

Modelling (Muratov & Gnedin, 2010), we find that a unimodal distribution is rejected at greater than 99.9% confidence. It has also been shown that the color bimodality of the system directly corresponds to a metallicity bimodality in the GC subpopulation, with the blue subpopulation being more metal-poor than the red subpopulation (Brodie et al., 2012). The clear division between the red and blue subpopulations implies that differences between the two subpopulations in other properties should be particularly obvious. Using a Gaussian kernel density estimate, we find that the subpopulations are separated at $g - z = 1.13$ (adopting a smoothing kernel of 0.07). We adopt this color as the dividing line between the two subpopulations, color the metal-poor subpopulation blue and the metal-rich subpopulation red, and retain this scheme in our subsequent figures. We also plot extended objects $R_{\mathrm{h}} > 8$ pc as purple points. These objects are not included in our fits nor our kernel density estimate.

Many of our candidate GCs have corresponding radial velocity measurements from Arnold et al. (2011). As mentioned in §2.2, we discard those candidates with measurements which exclude NGC 3115 membership. Those spectroscopically confirmed candidates with correct radial velocities are plotted with solid symbols, while those without spectroscopic confirmation are plotted as open symbols in Fig. 2.7.

To compare our measured colors with metallicities, we adopt the following conversions from Peng et al. (2006a):

$$[Fe/H] = -6.21 + (5.14 \pm 0.67) \times (g - z) \tag{2.4}$$

if $0.7 < (g-z) \leq 1.05$, and

$$[Fe/H] = -2.75 + (1.83 \pm 0.23) \times (g-z) \tag{2.5}$$

if $1.05 < (g-z) < 1.45$.

Using these conversions, the divide between metal-poor and metal-rich GCs is located at $[Fe/H] \sim -0.8$ dex.

For comparison, in Fig. 2.8, we plot the $(g-i)_0$ CMD from our photometrically-selected Suprime-Cam catalog. Again, bimodality is clear in the data; a Gaussian kernel density estimate places the dividing line between the red and blue subpopulations at $(g-i)_0 = 0.93$. As before, we plot spectroscopically confirmed candidates as solid symbols, while those without spectroscopic confirmation are plotted with open symbols. In addition, for comparison, we include spectroscopically confirmed foreground stars, which were not included in the Gaussian kernel estimate. A similar histogram is also displayed in the lower panel.

It is interesting to note the increased prevalence of blue GC candidates in the Suprime-Cam catalog, compared to the ACS CMD (see also Table 1). This is likely due to a combination of two effects. First, the spatial distribution of blue GC candidates around NGC 3115 is more extended than that of the red GC candidates. As the Suprime-Cam FOV is much larger than the ACS FOV, this extended population is preferentially sampled by the larger Suprime-Cam catalog. However, it is also apparent that most of the spectroscopically confirmed foreground stars are blue. There will certainly be more foreground contaminants in the purely photometrically selected GCs,

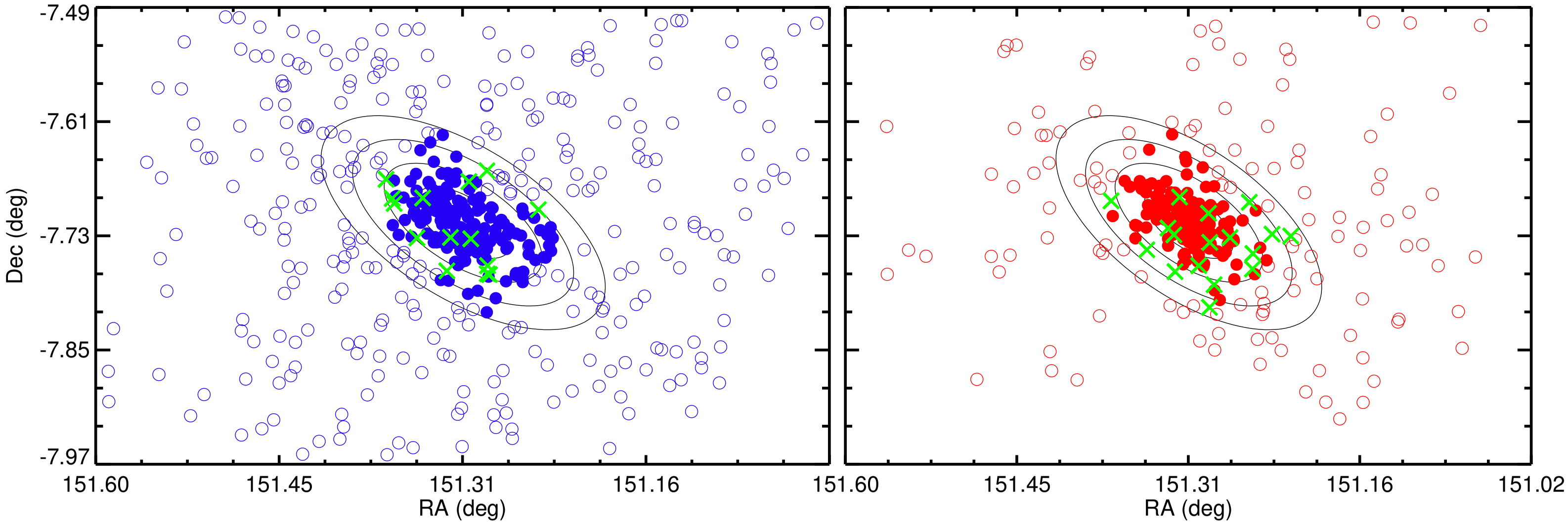

Figure 2.9: Spatial locations of blue and red GCs around NGC 3115. Filled circles are those GCs detected in the ACS imaging, while open circles are those only detected in the Suprime-Cam imaging. We also plot ellipses representing 1, 3, 5, 7, and 9 R_e (1 $R_\mathrm{e} \approx 2.6$ kpc) from NGC 3115. The blue GCs tend to be more spatially extended than the red GCs. Extended objects with $R_\mathrm{h} \geq 8.0$ pc are marked with green X's.

and this will increase the relative number of blue GCs. Disentangling these two effects is difficult without spectroscopic confirmation, and in reality both effects will contribute to the larger relative number of blue GC candidates in the Suprime-Cam photometric catalog.

In Fig. 2.9, we plot the locations of all the blue and red GC candidates in our sample. ACS detected GCs are plotted with solid circles, while those with open circles are only detected in the Suprime-Cam imaging. The blue GC subpopulation is clearly more spatially extended than the red subpopulation. We mark the locations of extended ($R_h > 8$ pc) clusters in our sample with X symbols.

2.3.2 The Blue Tilt

Blue tilts, wherein blue GCs tend to become increasingly red with increasing brightness, have been observed in many extragalactic GC systems (e.g., Strader et al. 2006; Harris et al. 2006; Mieske et al. 2006b). These gradients are typically taken as evidence of a mass-metallicity relationship among the clusters. This is likely due to self-enrichment; brighter, more massive clusters are able to retain more of their enriched material, producing redder (more metal-rich) photometric measurements. We find evidence for a blue-tilt in the GC system in ACS photometry. A least squares fit to the blue subpopulation gives a relation of

$$(g - z)_{\rm blue} = (-0.017 \pm 0.006) \times z + (1.31 \pm 0.14), \tag{2.6}$$

which we plot in Fig. 2.7. If we restrict our fit to only those GCs which are spectroscopically confirmed, we find a slope of -0.024 ± 0.012, indicating that even our most conservative sample still displays evidence for a blue-tilt.

The existence of corresponding red-tilts in extragalactic GC subpopulations is on somewhat shakier observational ground. In our sample, a linear fit to the red subpopulation gives

$$(g-z)_{\mathrm{red}} = (0.006 \pm 0.009) \times z + (1.23 \pm 0.20), \tag{2.7}$$

indicating that the red subpopulation may tilt in the opposite direction (brighter clusters are slightly bluer than dimmer clusters). However, the slope is not significant and is dependent on the degree of rejection of background galaxies, which almost always tend to be contaminants on the red end of the GC subpopulation. Fitting only the spectroscopically confirmed red clusters gives a slope of 0.012 ± 0.17, again not significantly constrained.

The strength of the blue tilt we measure for NGC 3115 is actually less than is typically seen for other galaxies (e.g. Strader et al. 2006; Usher et al. 2013). Typical measured slopes from similar ACS filter sets have found blue tilt slopes around -0.040 mag mag^{-1} for similar filters. Our measured value is roughly half of this. A plausible explanation for this smaller slope is the proximity of NGC 3115. While our data reach similar limiting apparent magnitudes as other extragalactic ACS GC studies, we are looking a magnitude further down the GCLF compared to other studies. If we convert the measured luminosity to a mass estimate, we are probing GCs of roughly half the mass in our ACS data.

Bailin & Harris (2009) proposed a quantitative self-enrichment model for GCs. The principle result was that GCs above the mass of $\sim 2 \times 10^6$ $M_\odot$(roughly $z = 19.2$ in our sample) will display a mass–metallicity correlation, while GCs less massive will not. In addition, a weak red tilt in the same direction as the blue tilt was also predicted. We attempted to measure the slope of the blue tilt for only the brightest clusters in our sample. While the slope became more negative as we restricted our sample to brighter and brighter GCs, we found that once we cut out clusters with magnitudes fainter than $z = 22$, the blue tilt detection becomes of marginal significance. For GCs brighter than $z = 21$, the detection is less than 1-σ. Thus while the magnitude of the blue tilt does appear to approach the slopes seen in previous studies for our brightest GCs, we cannot make this observation with any statistical significance.

Looking for a blue tilt in the photometrically selected Suprime-Cam sample instead gives a tilt in the opposite direction, with brighter candidates appearing bluer, in both color subpopulations. However, as mentioned in §2.3.1, we believe the purely photometric Suprime-Cam catalog contains significant contamination from foreground stars and does not constitute a sample of pure GCs. Given that the spectroscopic sample still displays a standard blue tilt, we consider this merely indicative of the degree of foreground contamination in the Arnold et al. (2011) sample.

2.3.3 Trends in Color with Radius

In Fig.2.10, we plot the observed color of the GCs in $(g - z)$ against their galactocentric elliptical radius R_g from the center of NGC 3115. For illustrative pur-

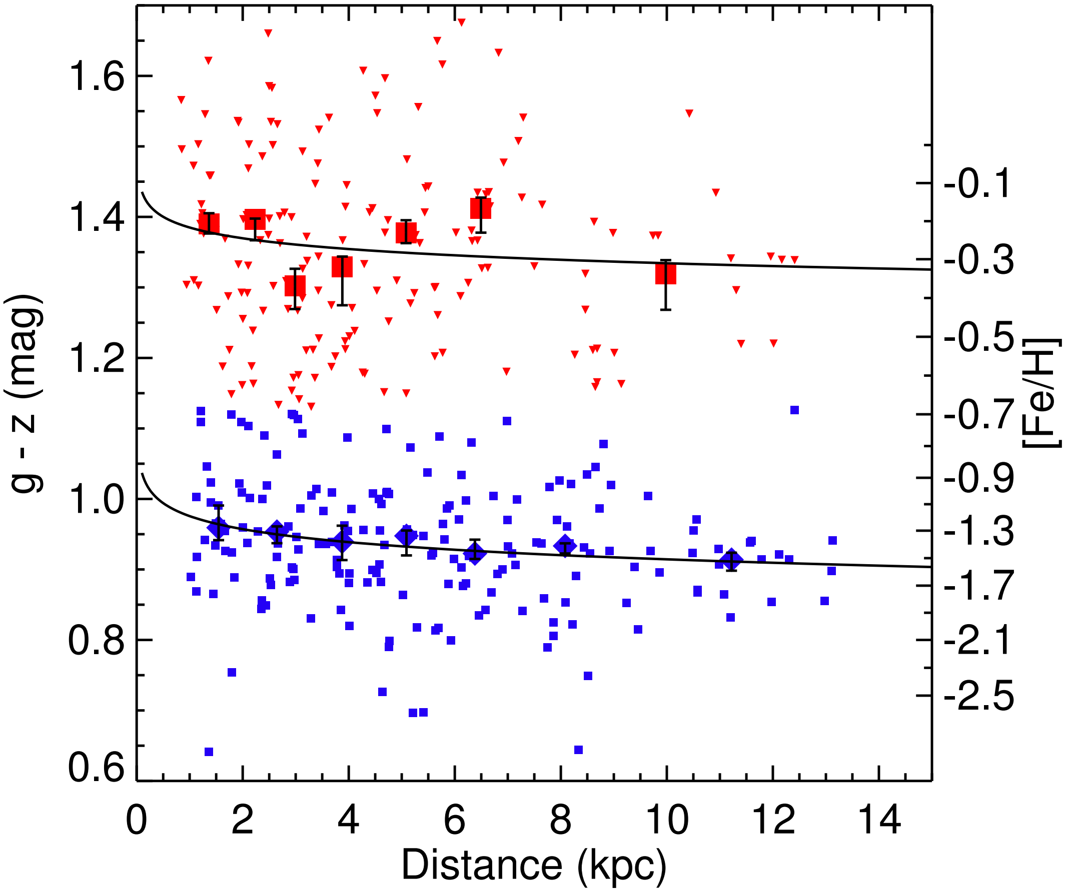

Figure 2.10: Plot of GC color vs. elliptical distance from NGC 3115 for our clusters. Clusters are colored according to their subpopulation. We also plot the median $g - z$ colors of both subpopulations for 7 equal number bins in each subpopulation. 68% uncertainties on the median colors from bootstrapping are also included. Both subpopulations display a color gradient, with clusters becoming bluer as they get farther away from NGC 3115. The blue clusters decrease uniformly, while the red clusters appear to display visible substructure in color as a function of distance. Least squares fits to both subpopulations are also plotted.

poses, we plot median colors for GCs in each subpopulation for 7 equal-numbered bins, binned as a function of distance. The red bins each contain 24 GCs, while the blue bins each contain 27. We also plot 68% uncertainties on these medians, estimated through bootstrapping. Both subpopulations appear to display gradients, with clusters becoming bluer farther out from the center of NGC 3115. To evaluate the color gradients in both subpopulations, we perform a least squares fit to the individual data points for the two subpopulations. We find the following relations:

$$(g - z)_{\mathrm{Red}} = (-0.05 \pm 0.04) \times \log R_{\mathrm{g}} + (1.38 \pm 0.02) \tag{2.8}$$

for the red subpopulation and

$$(g - z)_{\mathrm{Blue}} = (-0.06 \pm 0.02) \times \log R_{\mathrm{g}} + (0.97 \pm 0.02) \tag{2.9}$$

for the blue subpopulation. These relations are plotted in Fig 2.10.

We also compute simple linear gradients from least squares fitting, giving $(g - z)_{\mathrm{Red}} \propto (-0.004 \pm 0.003)R_{\mathrm{g}}$ and $(g - z)_{\mathrm{Blue}} \propto (-0.005 \pm 0.002)R_{\mathrm{g}}$. We convert our measured colors to metallicities using the Peng et al. (2006a) relations above and estimate metallicity gradients in [Fe/H] of -0.10 ± 0.07 dex dex^{-1} for the red subpopulation and -0.29 ± 0.11 dex dex^{-1} for the blue subpopulation, neglecting uncertainties on the conversion factors. The two gradients are clearly very comparable in color, while the [Fe/H] gradient is stronger for the blue subpopulation due to the relationship between color and metallicitiy for GCs. The decrease in color for the blue subpopulation is essentially monotonic, while the medians in the red subpopulation instead display some visible substructure, a trend seen in radial color studies in other GC systems (Strader et al., 2012). However, the uncertainties on the median quantities for the red subpopulation are large, and the change in color in the medians is comparable to these uncertainties.

It is interesting to compare our measured HST/ACS color profile to that found from Subaru photometry in Arnold et al. (2011), which extends roughly twice as far in radius from NGC 3115 but with reduced precision. We recover the jump in color in the red subpopulation located around $R_{\mathrm{g}} \sim 6$ kpc seen in Arnold et al. (2011), corroborating the visible features in the red color gradient we see in our data. Arnold et al. (2011) found gradients of -0.17 ± 0.04 dex dex^{-1} and -0.38 ± 0.06 dex dex^{-1} for the red and blue GCs, respectively. Thus, our color gradients agree to within the uncertainties on the quantities, although there is scatter. It is worth noting that the Arnold et al. (2011) values must also use an empirical correction from $(g-i)$ to $(g-z)$ to compare metallicities (equation A1 from Usher et al. 2012); the uncertainties on this filter conversion are also neglected in the Arnold et al. (2011) values. The photometric data from Arnold et al. (2011) extended roughly twice as far in radial distance from the center of NGC 3115 revealing, further structure in the red subpopulation including a large decrease in color around 15 kpc and a flattening of the color gradient farther out. It is likely that these two effects cancel out somewhat in the measured gradient from Arnold et al. (2011), leading to comparable values from both studies.

We also consider the Gaussian kernel density color distribution as a function

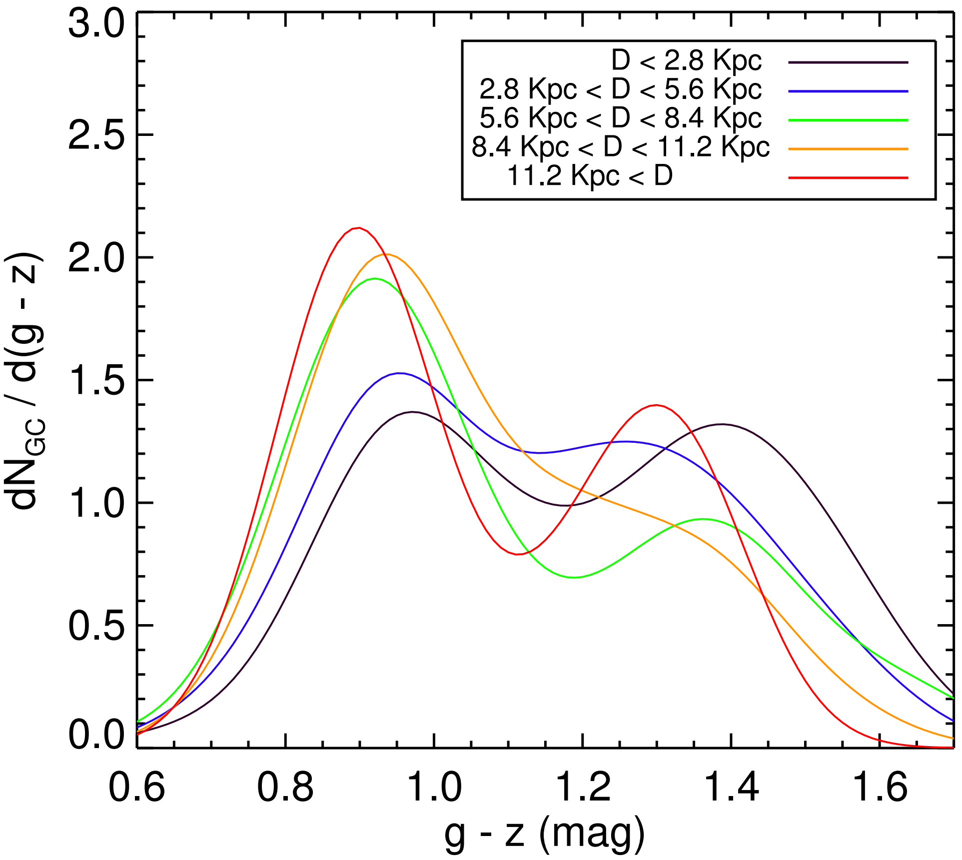

Figure 2.11: Gaussian kernel density distributions of color for the GC subpopulation in a series of 2.8 kpc projected galactocentric radius bins. The blue peak is fairly consistent in location, and decreases in color monotonically with the exception of the second farthest bin. In addition, the strength of the blue peak consistently increases with distance from NGC 3115. The red peak, on the other hand, displays possible color substructure. There is no consistent trend with galactocentric radius, and indeed the red peak disappears entirely in the second farthest radial bin.

of R_g. In Fig. 2.11 we plot the Gaussian kernel distribution evaluated at five 2.8 kpc distance bins. The blue peak is located fairly consistently and, with the exception of the second farthest bin, decreases in color monotonically. On the other hand, the red peak again displays visible color substructure. The peak moves around without a clear trend and indeed disappears completely in the second farthest bin, even though the overall subpopulation still displays a color gradient.

Generally speaking, declining galaxy metallicity gradients with a flattening at large galactocentric radii are a standard prediction of two-phase assembly scenarios (Naab et al., 2009; Bezanson et al., 2009; Hirschmann et al., 2013). An early monolithic collapse produces the inner gradient, while the outer flattening is produced by repeated accretion events. The existence of the outer flattening is unclear in our data, probably due to the limited radial coverage provided by the ACS mosaic. Smaller accreted satellites should be metal-poor in comparison to the central galaxy. Given the consistency of our measured profiles to those inferred in Arnold et al. (2011) from Suprime-Cam and spectroscopic data, we refer the reader to that paper for a more in-depth discussion of this point in the context of NGC 3115, including the incorporation of velocity information both in the GC population and integrated starlight.

2.3.4 Trends in Size

In Fig. 2.12, we plot the measured R_h as a function of projected galactocentric distance from the center of NGC 3115. Measurements of R_h tend to show a large variance. Many clusters of both subpopulations display R_h values significantly larger than those common for clusters, which are close to $R_h \sim 2-4$ pc. As we are chiefly interested in the trends of the most-likely GCs, we remove these outliers by only including GCs with $R_{\mathrm{h}} < 8$ pc in this subsection, as explained in §2.2.3. In general, inclusion of larger GCs does not affect the overall trend of R_{h} with distance, but the uncertainties on the medians and gradients increase.

It is well documented in the literature that R_{h} values tend to increase with galactocentric distance, and that the blue GCs tend to have larger sizes than red GCs, with differences typically on the order of ∼20% (Kundu & Whitmore, 1998; Larsen et al., 2001; Jordán et al., 2005). We find median sizes of $2.25^{+0.10}_{-0.04}$ pc for the blue subpopulation and $2.06^{+0.11}_{-0.14}$ pc for the red subpopulation. 68% confidence intervals are estimated through bootstrapping. These median values correspond to a fractional difference of ∼10%. This fraction is somewhat low compared to the above literature values, but the uncertainties on the medians and scatter of the measurements is large.

Trends in R_{h} with radius are typically parameterized in the form $R_{\mathrm{h}} = a(R/R_{\mathrm{e}})^{b}$. Performing a least squares fit to our data, we find the following relations:

$$R_{\mathrm{h,blue}} = (0.31 \pm 0.02)(R_{\mathrm{g}}/R_{\mathrm{e}})^{0.14\pm0.05} \text{ pc} \tag{2.10}$$

for the blue GCs and

$$R_{\mathrm{h,red}} = (0.30 \pm 0.02)(R_{\mathrm{g}}/R_{\mathrm{e}})^{0.08\pm0.07} \text{ pc} \tag{2.11}$$

for the red GCs. We plot these best fitting relations on Fig 2.12. In the literature, as with the median sizes of the respective subpopulations, differences are typically observed in the power-law slopes of the best-fitting $R_{\rm h}$ vs $R/R_{\rm e}$ relations, with blue GCs typically featuring smaller slopes than the red GCs. Our slopes are broadly consistent with those found in the literature (Spitler et al., 2006; Gómez & Woodley, 2007; Harris & Zaritsky, 2009; Harris et al., 2010; Strader et al., 2012), although literature studies have typically found the slopes of the red and blue subpopulations to be distinct. Instead, we find power-law slopes to be fairly consistent between the two subpopulations.

For completeness, we also performed a simple linear least squares fit to the data. We find best fit relations of the form

$$R_{\rm h,blue} = [(0.17 \pm 0.09) R_{\rm g}/R_{\rm e} + (2.0 \pm 0.2)]\ {\rm pc} \tag{2.12}$$

for the blue clusters and

$$R_{\rm h,bed} = [(0.11 \pm 0.07) R_{\rm g}/R_{\rm e} + (2.0 \pm 0.2)]\ {\rm pc} \tag{2.13}$$

for the red clusters. Thus, while the strengths of the gradients are roughly consistent, the significance of the red gradient is much lower than that of the blue.

We also plot the median values of each subpopulation in 4 radial bins of ~ 3 kpc. 68% uncertainties on the medians from bootstrapping are included on the median values. We bin in radius instead of number here because we are interested in comparing the properties of the two subpopulations at the same distances, as opposed to looking at internal gradients. For the blue subpopulation, the median $R_{\rm h}$ values increase monotonically with radius out to the final bin. Uncertainties on the values tend to be small, and the points are well clustered around the best-fitting relation. The red subpopulation, on the other hand, displays significant scatter around the best-fitting line, especially at large galactocentric distances, where there are very few clusters. It is questionable whether the red subpopulation displays any increase at all, given the few clusters located at large R_{g} and the large scatter of the subpopulation.

The small difference in median cluster size and the lack of a distinction in power-law slopes is somewhat interesting. The color-bimodality is especially pronounced in the GC system of NGC 3115, and it is well established that this bimodality also corresponds to a metallicity bimodality (Brodie et al., 2011). However, despite the distinct differences in color and metallicity of the subpopulations, they are not nearly as distinct in their sizes.

There is discussion in the literature about whether the observed size difference between red and blue clusters is due to an intrinsic, metallicity-dependent process (e.g., Jordán 2004a, or a projection effect due to the fact that red clusters tend to be more centrally concentrated (e.g., Larsen & Brodie 2003). The main prediction of the projection explanation is that the difference between the red and blue clusters will disappear at large radii, while the intrinsic explanation predicts that the separation will remain at all radii. While inferring broad trends in the data is questionable given the scatter, we do not see any evidence for a decreasing difference between red and blue R_{h} at larger R_{g}. This observation would seem to favor the intrinsic, metallicity-dependent explanation. However, this inference is tenuous, and the fact that the power-law slopes and median sizes of the two subpopulations are so similar is also peculiar in this context.

Observational support has been found for both the intrinsic explanation (Harris, 2009a; Paolillo et al., 2011; Blom et al., 2012b; Strader et al., 2012) and the projection hypothesis (Spitler et al., 2006). It is worth emphasizing that those studies that have found support for the intrinsic metallicity explanation have generally focused on giant elliptical galaxies. However, Spitler et al. (2006) examined M104, an edge-on SA galaxy in a group environment. Interestingly, M104 also displayed an unusually small difference (14%) in median values between the red and blue GC subpopulations, consistent with those we have measured for NGC 3115. The environmental and morphological conditions of M104 are quite similar to NGC 3115. Further investigation of GC $R_{\rm h}$ measurements across a wider range of morphological and environmental properties will serve to shed light on the full importance of cluster vs. group/field environments, morphology, and inclination in the size differences between the red and blue GC subpopulations. Given the similar trends in $R_{\rm h}$ with $R_{\rm g}$ and the consistency in the median size difference between this work and Spitler et al. (2006), we suppose that inclination and morphology in particular may play a role in the relative importance of projection effects compared to intrinsic size differences. In the end, there is only a limited amount we may infer about the NGC 3115 GC system other than that the two subpopulations are not very distinct in their sizes.

2.3.5 Ultra Compact Dwarf Candidates and other Extended Objects

There is significant discussion in the literature regarding the dividing line between the largest star clusters and the most compact galaxies. This division is typically explored in the parameter space of $R_{\rm h}$ and absolute magnitude. In the past, obser-

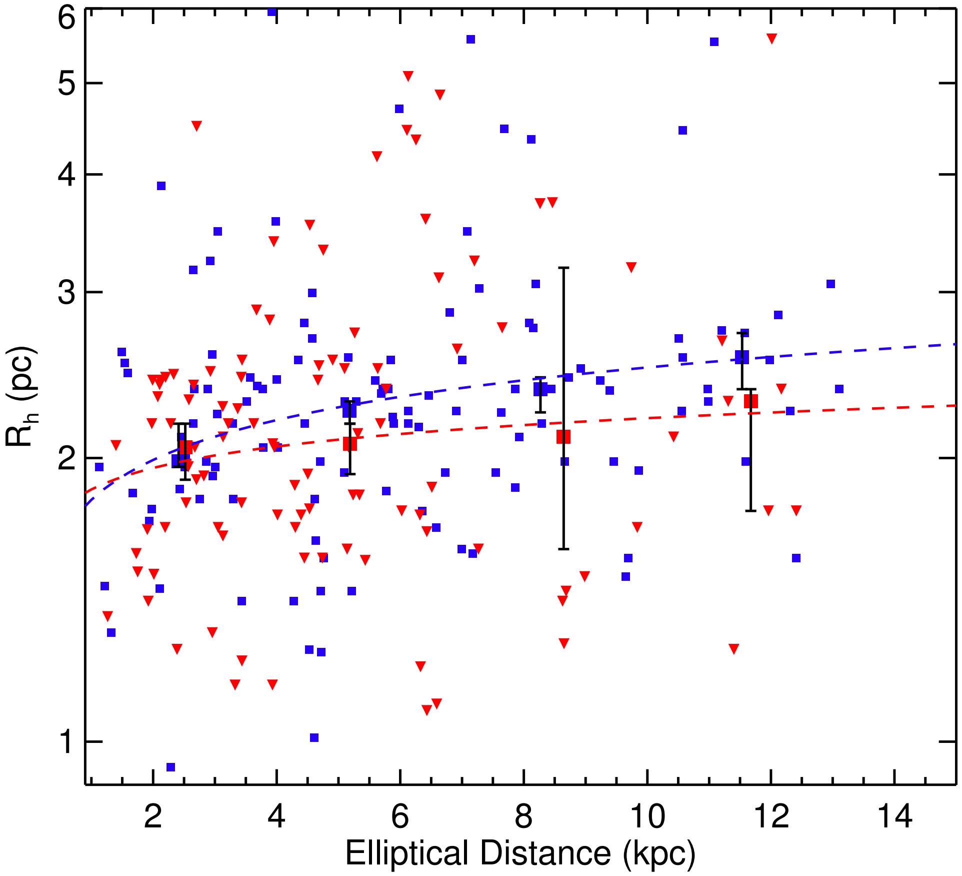

Figure 2.12: Plot of cluster half-light radius vs. projected galactocentric distance from NGC 3115. We also plot median half-light radii for equal number bins of clusters, measured separately for both subpopulations. 68% uncertainties on the medians from bootstrapping are also plotted. $R_{\rm h}$ measurements for both subpopulations of GCs become larger with increasing distance from NGC 3115. In general, the blue subpopulation displays slightly larger half-light radii than the red subpopulation.

vational searches of this parameter space have revealed ultra compact dwarfs (UCDs), which are brighter and more extended than typical GCs (Hilker et al., 1999; Drinkwater et al., 2000; Phillipps et al., 2001). They occupy a middle ground in size between GCs and dwarf elliptical galaxies. A traditional view of UCDs was that they represent the continuation of the size-luminosity trend to larger and brighter clusters, a view motivated by the fact that the first UCDs to be discovered were naturally the brightest. An apparent luminosity gap was also observed between UCDs and other extended objects, such as Local Group extended clusters (ECs) (e.g., Huxor et al., 2005), extragalactic "faint fuzzies" (FFs) (e.g., Brodie & Larsen, 2002), and "diffuse star clusters" (e.g., Peng et al., 2006b). No universal definition of a UCD exists, but a "traditional" definition of a UCD might be an object with luminosity $\sim 10^7\ L_\odot$ ($M_z \sim -13$) and $R_\mathrm{h} \sim 20$ pc, with significant scatter around these values.

However, as optical studies have continually probed lower luminosities, the boundaries of the UCD population have become somewhat ill-defined. Brodie et al. (2011) adopted provisional criteria of $M_V < -8.5$ and $R_\mathrm{h} > 10$ pc to account for the presence of new spectroscopically confirmed objects around M87 at lower luminosities. Forbes et al. (2013) noted a number of new spectroscopically confirmed objects which fully bridge the gap between the UCD and FF populations. In light of recent observational data, it is unclear that performing any luminosity cut on the extended object population is observationally motivated. There may still be interesting theoretical motivations, such as the $2 \times 10^6\ \mathrm{M}_\odot$ boundary for self enrichment estimated by Bailin & Harris (2009) or relaxation timescale arguments such as that presented in Misgeld &

Hilker (2011). However, for our brief consideration in this paper, we ultimately choose to employ no selection criteria aside from a size cut of $R_\mathrm{h} > 8$ pc. We wish to include all interesting extended objects, including traditional UCDs, FFs, and intermediate transition objects, in a catalog for potential future spectroscopic follow-up, and the proximity of NGC 3115 offers an ideal target for studying precisely these sorts of objects. Throughout this section we will frequently refer to all of these objects as "UCD candidates," despite the fact that many are not in traditional UCD parameter space and are instead more similar to FFs and other extended objects.

UCDs have primarily been studied in cluster environments, where targets tend to be more dense. Mieske et al. (2004) examined UCD-like objects in Fornax and found their formation was consistent both with a stripping scenario and a cluster merger scenario. Haşegan et al. (2005) and Price et al. (2009) studied UCD-like objects in Virgo and Coma, respectively, using *HST*/ACS imaging and found several strong candidates in each. Their results favored tidal stripping scenarios based on extrapolations of scaling relations. However, other studies have found cluster merger scenarios to be more plausible scenarios for UCD formation (e.g., Mieske et al. 2006a; Kissler-Patig et al. 2006). There is increasing evidence that multiple scenarios are necessary to fully explain the observed properties of UCDs across multiple environments (Taylor et al., 2010; Norris & Kannappan, 2011; Da Rocha et al., 2011; Penny et al., 2012).

It is unclear how environmental effects will affect the formation of UCD objects. If the stripping of galaxies is the primary mechanism, then naturally these objects will be more likely to form in denser environments. Only a few studies have investigated the properties of UCDs found in group/field environments (e.g., Evstigneeva et al. 2007; Hau et al. 2009; Norris & Kannappan 2011; Da Rocha et al. 2011, Norris et al. 2014 (MNRAS, Submitted)). Given the potential environmental dependence, the detection of candidates in non-cluster environments such as NGC 3115 is of value for future investigations of UCD formation.

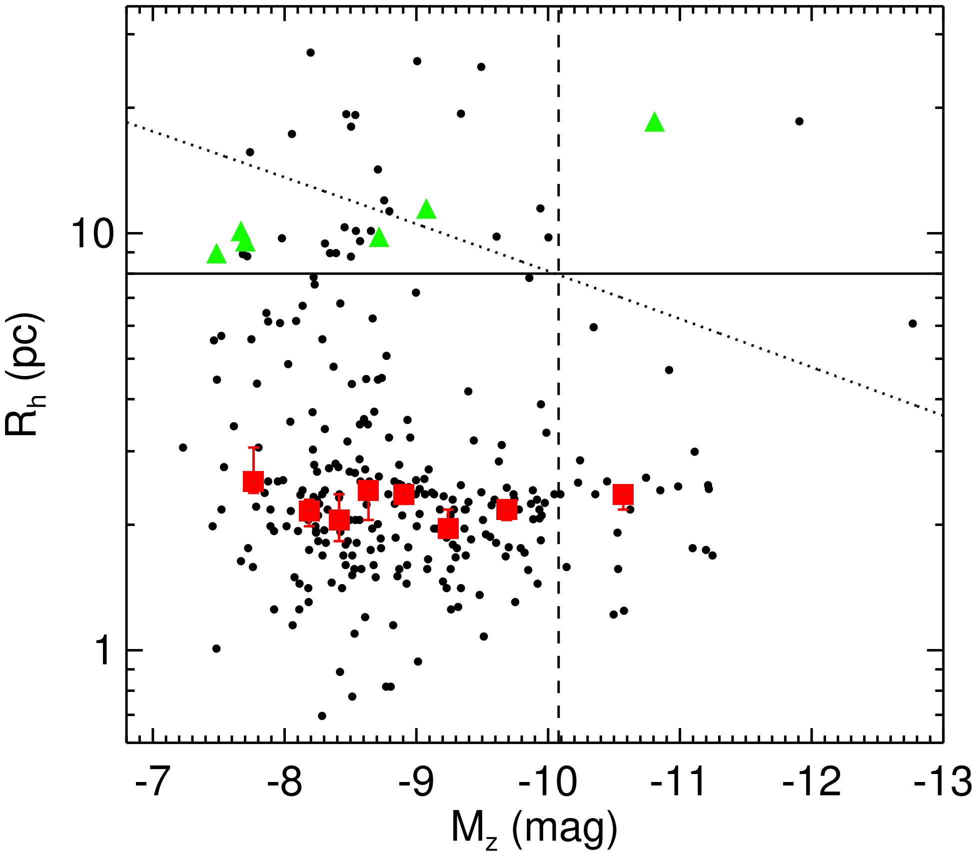

Figure 2.13: Plot of measured GC half-light radii against absolute z magnitude, M_z. We identify all clusters with $R_h > 8.0$ pc as potential UCD candidates. Six candidates have measured radial velocities from Arnold et al. (2011) that confirm NGC 3115 membership; we highlight these as green triangles. We recover a number of candidates that have luminosities consistent with faint GCs, but larger sizes. We also plot the median measured R_h values for 8 equal-number bins of clusters for only those clusters with $R_h < 8.0$ pc, with 68% uncertainties on these medians from bootstrapping included. The vertical line represents a 10^6 $M_\odot$cut, the horizontal line represents the adopted $R_h < 0.8$ pc size cut, and the diagonal line represents the dividing line for objects which will have undergone significant dynamical evolution within one Hubble time.

Table 2.2: UCD Candidates in ACS Data

ID	R.A. (J2000) (Deg.)	Dec. (J2000) (Deg.)	$M_{\rm g}$ (mag)	err (mag)	$M_{\rm z}$ (mag)	err (mag)	$R_{\rm h}$ (pc)	Vel.$^{\mathbf{A}}$ (km s^{-1})	X-ray?$^{\mathbf{B}}$ (Y/N)
UCD1	151.30216	-7.7355695	-10.748	0.002	-11.847	0.002	18.55	393	N
UCD2	151.22176	-7.7326969	-9.070	0.012	-10.602	0.008	80.16	-	N
UCD3	151.34482	-7.7344961	-8.947	0.011	-9.964	0.011	70.63	-	N
UCD4	151.31997	-7.7700997	-8.710	0.005	-9.943	0.004	9.77	-	N
UCD5	151.28906	-7.7722947	-9.016	0.004	-9.881	0.004	11.47	518	N
UCD6	151.28735	-7.773133	-8.925	0.011	-9.780	0.013	70.63	-	N
UCD7	151.37419	-7.6955633	-8.412	0.015	-9.745	0.012	73.62	-	N
UCD8	151.31825	-7.7340325	-8.657	0.005	-9.549	0.005	9.81	844	N
UCD9	151.29046	-7.7393686	-8.197	0.011	-9.432	0.012	25.05	-	N
UCD10	151.34388	-7.7470892	-7.853	0.017	-9.279	0.012	19.35	-	N
UCD11	151.27333	-7.7342231	-7.483	0.015	-8.947	0.011	25.86	-	N
UCD12	151.25691	-7.6970153	-7.531	0.009	-8.735	0.007	11.29	-	N
UCD13	151.31608	-7.6916319	-7.167	0.013	-8.696	0.011	11.99	-	N
UCD14	151.32590	-7.7242011	-7.337	0.014	-8.648	0.012	14.22	-	N
UCD15	151.28940	-7.6638911	-7.608	0.009	-8.595	0.008	10.13	878	N

A: Heliocentric velocity, if available, from the Pota et al. (2013b) catalog.

B: Whether or not the GC candidate hosts an X-ray source.

Table 2.3: UCD Candidates in ACS Data, continued

ID	R.A. (J2000) (Deg.)	Dec. (J2000) (Deg.)	M_g (mag)	err (mag)	M_z (mag)	err (mag)	R_h (pc)	Vel.[A] (km s^{-1})	X-ray?[B] (Y/N)
UCD16	151.36446	-7.6930417	-7.642	0.009	-8.513	0.009	9.57	661	N
UCD17	151.36931	-7.6728572	-7.601	0.010	-8.481	0.012	10.13	-	N
UCD18	151.25418	-7.7672714	-7.177	0.015	-8.477	0.012	19.21	-	N
UCD19	151.30366	-7.6752959	-7.426	0.012	-8.445	0.012	18.01	-	N
UCD20	151.32090	-7.7312989	-7.209	0.015	-8.444	0.014	8.79	-	Y
UCD21	151.25392	-7.7509972	-7.024	0.018	-8.408	0.014	19.3	-	N
UCD22	151.29983	-7.7638275	-7.221	0.011	-8.395	0.01	10.34	-	N
UCD23	151.34029	-7.6925642	-7.423	0.011	-8.330	0.013	8.96	579	N
UCD24	151.29070	-7.8077822	-7.130	0.014	-8.284	0.011	8.96	-	N
UCD25	151.29154	-7.7086903	-7.063	0.016	-8.247	0.015	9.45	-	N
UCD26	151.32115	-7.7692714	-7.309	0.018	-8.137	0.019	27.11	-	N
UCD27	151.36293	-7.6982394	-6.992	0.019	-7.996	0.017	17.30	-	N
UCD28	151.28682	-7.7838389	-6.457	0.020	-7.920	0.014	9.73	-	N
UCD29	151.24861	-7.704778	-7.025	0.015	-7.678	0.018	15.64	-	N
UCD30	151.28885	-7.7637978	-6.828	0.015	-7.656	0.019	8.80	-	N
UCD31	151.23764	-7.7306361	-6.444	0.018	-7.623	0.016	8.91	-	N

A: Heliocentric velocity, if available, from the Pota et al. (2013b) catalog.

B: Whether or not the GC candidate hosts an X-ray source.

As our ultimate goal in this section is inclusion of as many candidate UCDs as possible, we relax the size restrictions used in creating our catalog and no longer employ any maximum size cuts. We still include the depth cuts employed for our measured R_{h} sizes by only considering candidates with signal to noise greater than 50.

In Fig. 2.13, we plot the measured R_{h} against the absolute magnitude of clusters. Traditionally, UCDs are thought of as occupying the parameter space of bright clusters with $M_{\mathrm{z}} < -11$. However, as we are specifically interested in investigating faint candidates, we consider everything with measured $R_{\mathrm{h}} > 8$ pc a UCD candidate. We identify 31 such candidates, which we list in Table 3. Six of the brightest candidates have measured DEIMOS radial velocities from Arnold et al. (2011) consistent with NGC 3115 membership. We plot these with solid green triangles.

We include three potential definitions for what one might consider a UCD. The horizontal line is the size cut we adopt for our table of UCD candidates, $R_{\mathrm{h}} = 8$ pc. The vertical line is a luminosity cut which corresponds to a mass of $M = 10^6$ $\mathrm{M}_{\odot}$ ($\sim 7 \times 10^5$ $L_{\odot}$). Finally the diagonal line is the size–mass relation from Misgeld & Hilker (2011) (adapted from Dabringhausen et al. 2008) for an assumed relaxation timescale. Objects below the line will have been able to undergo significant dynamical evolution over a Hubble time, while those above would be expected to show a mass-size relation.

We identify a number of fainter UCD candidates, which would populate the parameter space occupied by the faint UCD sequence parallel to the GC population. However, it is unclear how distinct this population is from the normal GC sequence in our data. These candidates are also all towards the fainter end of the GC sequence, where background galaxy contamination will become most prevalent. Indeed, objects in this region of parameter space are in the regions where we would have expected clusters to undergo significant dynamical evolution, making it more likely that sources here are contaminants. The fact that many have red colors (see Fig. 2.7) reinforces this caveat. Further spectroscopic follow-up of UCD candidates will allow a more thorough investigation of this parameter space through rejection of background galaxy contamination.

In addition, we note that several of these objects have significant discrepancies between ground-based Suprime-Cam imaging and ACS photometry, as large as a couple magnitudes for a few objects. Such an offset is likely due to an object having a size-dependent correction applied which is either too large (i.e. the object is actually significantly smaller than what we measure using our King profile fit and therefore we overestimate the correction) or too small (the opposite case). For these large, extended objects, the S/N towards the edges of the profile is small, and so the uncertainties on measured sizes can be large. In addition, for any object which is in fact a background galaxy, the King profile is likely a poor parameterization of the light profile to begin with. For the reason of background contamination, we caution against inferring too much from non-spectroscopically confirmed candidates.

Six candidates, UCD1, UCD5, UCD 8, UCD15, UCD16, and UCD23, are spectroscopically confirmed to have NGC 3115 membership. While UCD1 occupies traditional UCD parameter space, the remainder extend to the fainter luminosities typically occupied by faint fuzzies. These additional confirmed candidates do support an interpretation that a similar population of extended clusters exists parallel to a traditional GC sequence, perhaps the result of a distinct formation mechanism. However, more spectroscopically confirmed clusters are necessary to evaluate the full extent of this population; some significant number of the unconfirmed candidates may still be contaminants.

In addition, object A1, not in the UCD catalog, is noteworthy for its density. Its size is large for, but not inconsistent with, a GC ($R_{\rm h}$ ~6 pc). However, it also features an extremely high luminosity, with $M_{\rm z} \sim -12.7$, corresponding to a mass of 1.18×10^7 $M_\odot$. This object is located very close to the center of NGC 3115, perhaps indicating some systematic effect from the galaxy light on the *ishape* measurement.

We also plot median $R_{\rm h}$ values for eight equal-numbered magnitude bins. We do not see a strong trend in $R_{\rm h}$ with absolute magnitude. Other studies have typically found correlations between $R_{\rm h}$ and absolute magnitude for the brightest clusters. We do find a monotonic increase in $R_{\rm h}$ with increasing luminosity for $M_{\rm z} < -9$. However, the median values below this point display significant scatter. The hints of a trend we see do match that found in other studies, wherein the $R_{\rm h}$ of a typical cluster appears to be larger both for the faintest and brightest candidates, and smallest for those of intermediate luminosity (Haşegan et al., 2005; Evstigneeva et al., 2008; Dabringhausen et al., 2008; Harris, 2009a; Harris et al., 2010; Misgeld & Hilker, 2011; Strader et al., 2012). However, the trend is very weak in our data.

2.4 X-ray/GC Matching

In this section, we discuss those GCs identified in §2.2.7 which are coincident with X-ray sources. We identify 45 X-ray sources within 3-σ X-ray PSF distances from our GC catalog. For those sources in the ACS FOV, we adopt the ACS $(g-z)$ color division between the red and blue subpopulations. Otherwise, we adopt the Supime-Cam photometry $(g-i)_0$ color division. We color-code and plot the two distributions in Fig 2.14. In general, the red X-ray GCs appear to be more centrally concentrated than the blue X-ray GCs, matching the trend in the population of GCs without X-ray sources.

Of the 45 sources, 29 are associated with red GCs, while 16 are associated with blue GCs. Given a total of 291 unique red and 490 unique blue GC candidates across both optical catalogs, we find a ∼10% chance that a red GC hosts an X-ray source and a ∼3% chance that a blue GC hosts an X-ray source. These fractions are broadly consistent with those reported in the literature (Jordán, 2004b; Fabbiano, 2006; Kim et al., 2006; Sivakoff et al., 2007) although they are certainly on the high side for both values (typically ∼5% for red GCs and ∼2% for blue GCs). If we match to only the more reliable ACS sources, the fraction of each increases to ∼14% for red GCs and to ∼ 7% for blue GCs, both extremely high for X-ray/GC coincidence. If we restrict our analysis to just those GCs which are ACS imaged and spectroscopically confirmed, rates increase further to ∼ 14% for both the red and blue subpopulations. Note, however, that the spectroscopically confirmed sample is naturally biased to the brightest clusters due to observational constraints. Brighter clusters are expected to be more likely to host LMXBs (Sivakoff et al., 2007). It is likely that these higher rates of X-ray/GC coincidence are due to the depth of the X-ray observations compared to similar studies, as well as the smaller distance of NGC 3115 compared to most other early-type galaxy GC studies.

In Fig. 2.14, we also note one particular feature in the blue matched GC subpopulation, a linear structure of X-ray associated GCs located at RA $\sim$ 151.31, Dec ~ -7.65. It is unclear exactly how to interpret this organized structure of X-ray GCs. They are all detected in the ACS mosaic, but apart from this they do not have any truly distinguishing features. They have typical sizes, colors, and luminosities typical of blue GCs. Three of the GCs in the line have measured radial velocities, all in the same direction as the rotation of NGC 3115's disk. The existence both of the plane of blue GCs and the overabundance of X-ray sources in the blue GCs may be linked, but given our current analysis, such an inference is speculative, with unclear implications.

We do not discuss further the properties of the X-ray hosting GCs beyond initial rates of incidence, nor the properties of the X-ray sources themselves. Analyses of these properties are presented in (Lin et al., 2015a,b)

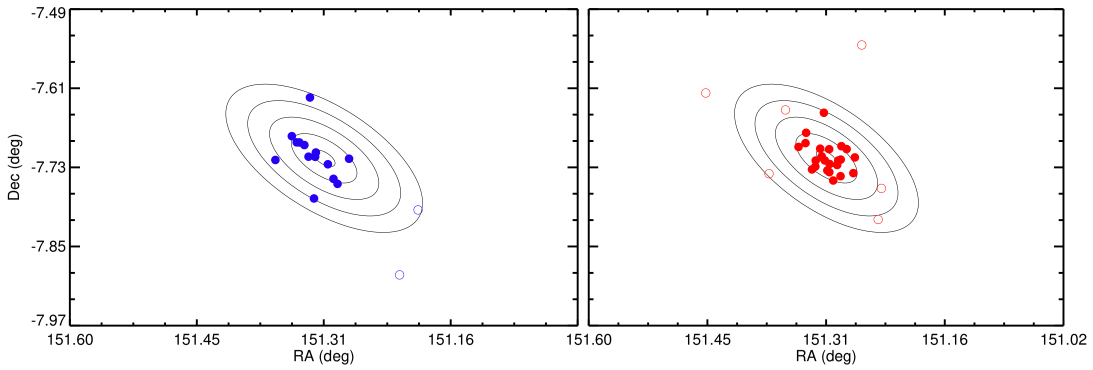

Figure 2.14: Spatial distribution of blue (left panel) and red (right panel) GCs with X-ray matches. Closed circles are detected in the ACS catalog, while open circles are only detected in the large FOV Suprime-Cam imaging. Contours of 1, 3, 5, 7, and 9 R_e are plotted for reference.

2.5 SUMMARY

We have performed photometry and size measurements for 360 GC candidates in *HST*/ACS imaging of NGC 3115. We have also presented Suprime-Cam photometry for 421 additional candidates. The bimodality of the system is very obvious in our data. There is evidence for a blue-tilt in the blue subpopulation, and we see weak hints of an opposing trend in the red GCs. Both subpopulations display a color gradient as a function of distance from the center of NGC 3115, and the magnitude of the gradient is similar to that found at larger radii in Arnold et al. (2011). The blue GCs display monotonic behavior, decreasing in color uniformly. However, the red GCs display visible color substructure in addition to the overall gradient. The size behavior of the two subpopulations is somewhat unusual. While the blue GCs are larger on average than the red GCs, the ratio of the average sizes is closer to unity than is typical for a GC system. We are unable to clearly confirm either a projection or an intrinsic explanation for the size distinction, but given the similarity of our result to that found in Spitler et al. (2006) for M104, we suppose that the morphology and inclination of the galaxy may have a significant effect on the measured relative sizes of the two subpopulations.

We identify 31 candidate UCD objects, including six with spectroscopic confirmation. Given their colors, it is possible that many candidates without measured velocities are in fact background contaminants. In addition, after matching our ACS sources with companion X-ray data, we find 29 X-ray sources associated with red GCs and 16 with blue GCs. The fraction of X-ray hosting GCs is larger for both subpopulations than is typical in the literature, especially for blue GCs, likely due to the increased depth of the X-ray data. We also observe an interesting linear spatial distribution in the blue X-ray hosting population. The implications of this distribution and its link to the overabundance of X-ray sources in blue GCs are unclear.

Chapter 3

A Bayesian Method For Simultaneous Globular Cluster Selection and Inference of Global Properties from Photometric Data

3.1 INTRODUCTION

When one is attempting to create a GC catalog from ground-based photometric data, one is typically interested in distinguishing GCs from two primary sources of contaminants: foreground stars located within the Milky Way, and distant galaxies in the background of the FOV.

When one has additional data besides simple ground-based photometry, these selections become much easier. The resolution of *HST* imaging is sufficient that, for galaxies within several tens of Mpc, GCs are marginally resolved and no longer point-like, allowing them to be clearly separated out from foreground star contamination. Background galaxies can often be selected-out based on morphological cuts or size-distinctions, although some ambiguity will exist about the dividing line between large GCs and small/distant galaxies. Spectroscopy also offers an outstanding means to select GCs. In most extragalactic contexts, a simple radial velocity cut cleanly separates GCs from foreground stars and background galaxies, allowing a pristine sample of GCs.

However, while both of these approaches offer significant improvements in GC selection over pure ground-based photometry, they are also limited in their own right. Spectroscopy of GCs is expensive, requiring significant time on 8m-class telescopes, and is still limited to probing the brightest GCs. *HST* data are also expensive to acquire, and the *HST* imagers have FOVs of order 100 times smaller than those of wide-field imagers on modern telescopes. If one is interested in inferring global properties about extragalactic GC systems, spectroscopy provides a small dataset baised towards the brightest clusters, and *HST* data provides a dataset baised towards the inner radii of galaxies. Neither of these are really suitable for purposes of cataloging and measuring GC systems at large R_e, leaving ground-based photometric data as the only effective means. In short, what wide-field imaging lacks in quality, it makes up for in quantity and feasibility of acquisition.

GCs are typically selected in ground-based imaging by first cutting extended sources, as GCs are almost completely point-like in such imaging (although note that such cuts may also exclude large, partially resolved star-clusters located these systems, e.g. Brodie et al. 2011; Jennings et al. 2015; Sandoval et al. 2015). Cuts are then made in color-color space. This may be done with methodology as simple as drawing a box around the location of the GC locus and selecting everything inside such a box, or may be done in a more sophisticated fashion by assigning GCs closer to the center of the locus a higher-probability of being a GC. Other cuts may perhaps be applied, such as in luminosity or projected distance away from the galaxy. While this methodology may be modified on a study-to-study basis, the basic concept of applying color-color cuts to select GCs is very standard across the field (e.g. Foster et al. 2011; Hargis & Rhode 2012; Blom et al. 2012b; Usher et al. 2012; Pota et al. 2013b; Kartha et al. 2014; Jennings et al. 2014; Kartha et al. 2016).

3.1.1 Motivation for a Probabilistic GC Model

This paper considers a Bayesian method of selecting GCs. Rather than relying on binary cuts in parameter space, we aim to construct a fully probabilistic model of the photometric and spatial properties of the GC and contaminant system. The advantages of such a system are two-fold: first, our selection of GCs is now probabilistic. By using our model, we are able to assign a probability to every source in an image as to whether it is part of a contaminant or science distribution. Having meaningful probabilities attached to sources allows any follow-up selection to be much more nuanced. Selection strategies can be optimized in a more nuanced way and can feature higher overall return rates.

Second, and perhaps more importantly, by writing down a model, we are able to fit the free parameters of this model to the data at hand. This allows for the GC selection to be naturally fit to each galaxy. In addition, the distributions of these free paramaters are also of great interest for understanding the overall GC system of a galaxy. Properties such as the number of GCs in a system, the fraction of red and blue GCs, and the locations of GCs in color and magnitude space cannot be fully evaluated without folding in selection errors. Old methods of accounting for these uncertainties rely on post-fitting corrections for contaminant level and incompleteness of data. A full probabilistic model of all sources in the system provides much more reliable inferences on the global properties for the system.

One of the chief advantages of constructing our GC selection problem in a Bayesian context is that we may begin with a simple model and add increasing complexity as is necessary. We do not make the claim that our model is a perfect description of the process that created the data. The actual processes that generate GC systems are obviously much more complex than can be described with a model as simple as this one. However, the model is a useful tool in which to gain insight into the problem, and areas where the model fails to perform satisfactorily offer roads to expand the model in future studies

3.1.2 Outline

In this paper, we introduce our fully probabilistic model for photometric GC systems. We first outline the basics of a Bayesian mixture model and then add in complexity to the model until it is a reasonable description of a real GC system. In §3.2, we first consider a simple mixture model as an instructive illustration of our basic methodology. In §3.3, we add complexity to this model to account for the specific difficulties of our problem. We apply our methodology to mock datasets in §3.4 to investigate any biases in our method, followed by an application to real photometry of the GC system around NGC 3115 in §3.5. Finally, we discuss future applications of our method in §3.6, as well as potential areas the model could be improved.

3.2 A SIMPLE MIXTURE MODEL

Mixture models, as their name implies, are probabilistic models in which the full data are assumed to have been drawn from a mixture of two or more other distributions. Mixture models are commonly used in statistical analysis to model situations with data drawn from multiple populations. In the context of GC selection, the two populations to be mixed are a model describing the distribution of the contaminant sources, and a model describing the distribution of the GCs. The combined likelihood of the two distributions can then be used to perform inference on the free parameters in the models of both distributions.

In §3.2, we consider a toy mixture model consisting of idealized data. We write down very simple distributions for both the GC and contaminant distributions so we can introduce the framework for our model. The discussion that follows draws heavily from Jordán et al. (2007a), Fraley & Raferty (2002), and Hogg et al. (2010).

3.2.1 Writing the Mixture Distribution

In general, we may treat a random variable $\mathbf{Y}$ as a linear combination of any number of other random variables,

$$\mathbf{Y_1} \sim d_1(\theta),\ ...,\ \mathbf{Y_i} \sim d_i(\theta), \mathbf{Y}(\theta) = f_1 d_1 + ... + f_i d_i, \tag{3.1}$$

where $d_i(\theta)$ is the (normalized) distribution function for the *ith* component, taking parameters θ and relative weight f_i. To make the function a valid probability distribution function (PDF), we must also require that the relative weights sum to one, i.e. $\sum_{i=1}^{I} f_i = 1$.

The likelihood for such a mixture model may be written as:

$$L(\mathbf{Y}|\theta) = \sum_{i=1}^{I} f_i d_i(\mathbf{Y}|\theta), \tag{3.2}$$

i.e. the likelihood of observing a specific data vector $\mathbf{Y}$ given parameters θ is equal to the sum of the individual likelihoods $d_i(\mathbf{Y}|\theta)$ multiplied by the individual weights f_i of each mixture.

We are interested in calculating the full likelihood for our entire dataset, which will consist of J data vectors, i.e. $\mathbf{Y} = \{\mathbf{y_1}, \mathbf{y_2}, ..., \mathbf{y_J}\}$

If we make the standard assumption that each data vector is independent and identically distributed (each data point is drawn from the full mixture distribution), the full likelihood will simply be the product of the individual likelihoods for each y_j:

$$L(\mathbf{Y}|\theta) = \prod_{j=1}^{J} \sum_{i=1}^{I} f_i d_i(\mathbf{Y_j}|\theta). \tag{3.3}$$

As is standard in probabilistic modeling, we will work with the log of the likelihood to change this product into a sum, giving

$$l(\mathbf{Y}|\theta) = \sum_{j=1}^{J} \log \big[\sum_{i=1}^{I} f_i d_i(\mathbf{Y_j}|\theta) \big]. \tag{3.4}$$

At this stage, we have the complete likelihood of observing data $\mathbf{Y}$ given parameters θ and mixture weights f_i. Note that, for convenience, we will sometimes parameter vector θ as including the weights f_i and sometimes with the weights written explicitly out of the parameter vector. There shouldn't be any locations in the paper where ambiguity in whether the weights are part of the parameter vector θ or outside of it affects the interpretation of the paper.

As an aside, mixture models such as these are frequently written using a hidden-variable formalization in which each data point has an un-observed parameter z_i corresponding to the mixture the parameter is drawn from. In expectation maximization (EM) strategies or in Gibbs sampling strategies, this z_i vector must be explicitly simulated. In the Gibbs sampling case in particular, the vector is marginalized over in the course of sampling as one constructs the posterior simulations for the parameters of interest. However, we employ the Affine Invariant sampler `emcee` to perform our simulations. The `emcee` sampler performs in a similar way to a Metropolis-Hastings algorithm in that it evaluates an entire vector of parameter proposals at once. Since we have an explicit formula for our posterior distribution up to a constant, we are free to draw samples from the distribution directly without employing our hidden variable formulation.

3.2.2 Specifying the Distributions

It is apparent that all complexity in how one models the full mixture depends on how one specifies the distribution functions used. In this section we consider simplistic distributions that still contain reasonable astronomical interpretations, assuming 3-filter g, r, i photometry.

As discussed above, after performing some basic point-like cuts on our photometry, we consider five total measurements for each source: two measured colors, a measured magnitude, and the spatial coordinates of the source. For purposes of our discussion in this paper, we consider a measured i band brightness, measured $g - i$ and $r - i$ color, and measured RA and DEC of the source. Note that any brightness and color combinations can be chosen without affecting the actual model, only the various parameters that will be inferred for the model.

Note that the specific bands used in the model aren't actually important, as long as one can write down a reasonable model for them. We will consider g, r, i as all of the SLUGGS Survey data consists of these three filters. For purposes of our discussion in this paper, we will speak explicitly of g, r, i magnitudes, but the methodology can be generalized to whatever filters are of interest, and indeed to any number of filters for which the data have detections.

As an aside on this last point, recent work has shown that incorporating u-band and z-band photometry can offer excellent leverage in selecting GC populations from contaminant sources (Muñoz et al., 2014). All of our methodology can easily be applied to whatever filter combinations are on-hand, provided reasonable contaminant distributions can be created. Future application of our work to galaxies with deep u and z band data will be an exciting tool to further investigate GC populations.

To introduce the simple mixture model, for the remainder of §3.2, we consider a simplified toy problem. We model only one single GC population (most GC populations are bimodal in color at some level). We also neglect any complexity in the distribution of contaminant sources; we simply make the poor assumption that the contaminant sources are uniformly distributed over the parameter spaces considered in the problem. Our GC distributions in color, magnitude, and spatial coordinates will be given simple probabilistic distributions. We will expand these simplistic distribution choices in §3.3. Finally, this toy model ignores incompleteness of the data, which we discuss how to incorporate into the model in §3.4.

This formulation requires us to define the allowable parameter spaces for all data involved in the problem. For purposes of this section, we simply define hard limits on the bounds of our data in RA/DEC space, color-color space, and magnitude space. We select approximately-realistic boundaries for our toy model to make the comparisons with the real problem easier. We define the magnitude boundaries to be between 18 and 25 in i-band magnitude, 0.0 to 1.0 in $r - i$ space, and 0.0 to 1.5 in $g - i$ space. We bound the RA/DEC with a circle of radius 0.3 degrees. As mentioned above, we simply consider the contaminants to be uniformly distributed over this space.

For our GCs, we will assume that they are distributed in color as a multivariate normal (MVN) distribution with mean vector μ and covariance matrix $\mathbf{\Sigma}$. We will parameterize the g-band distribution as a normal distribution with mean μ and variance σ^2. Finally, we will parameterize the spatial distribution of the sources as an exponential distribution, with free parameter R_e describing the effective radius of the system. We neglect any ellipticity of the spatial distribution in this model, although it is incorporated in the full model in §3.3.

The full log likelihood for this model looks like:

$$
\begin{aligned}
&l(\mathbf{Y}|\theta) && (3.5)\\
&= \sum_{j=1}^{J} \log \big[\sum_{i=1}^{I} f_i d_i(\mathbf{Y_j}|\theta) \big] && (3.6)\\
&= \sum_{j=1}^{J} \log \big[f \ \mathrm{MVN}(\mathbf{Y_j}|\mu, \Sigma) \ \mathrm{Exp}(\mathbf{Y_j}|R_e) \ \mathrm{N}(\mathbf{Y_j}|\mu, \sigma^2) && (3.7)\\
&\qquad + (1-f)C) \big]. && (3.8)
\end{aligned}
$$

C here represents the distribution of the contaminant sources. Since we have assumed the contaminants are uniformly distributed in all spaces, C is a constant. We may calculate C by requiring that it's distribution over all five measured dimensions integrates to one. In other words, C is equal to the area of our allowed RA and DEC space times the area of our allowed color distribution space times the area of our allowed magnitude space.

In general for a mixture model, care must be taken for that all distributions are normalized correctly to one. While this is true by definition for well-defined PDFs, our chosen GC spatial distribution is not a well-defined PDF; it instead has been truncated at some fixed radius chosen to match that of the contaminant distribution. We neglect this detail in our toy model and address it fully in §3.3.4, where we will introduce other distributions which are not normalized by definition.

3.2.3 The Bayesian Inference Problem

At this point, we have a functional form for the likelihood distribution of the data. However, writing a likelihood is only part of the problem of performing Bayesian inference.

Here we describe the general problem of Bayesian inference. We observe data $\mathbf{Y}$, which we believe to have been generated by some process. The process in question can be modeled with the likelihood function $L(\mathbf{Y}|\theta)$. In other words, given parameters θ, we can calculate the likelihood of the observed data being drawn from this model.

We are interested in inference on the posterior distributions of our parameters, θ. These posterior distributions encode all information and uncertainty on the GC distributions we are interested in measuring, conditional on the data we have observed, our prior knowledge of our parameters, and the model we have specified.

Bayes theorem provides the formula for the posterior distribution:

$$P(\theta|\mathbf{Y}) = \frac{L(\mathbf{Y})|\theta) \times P(\theta)}{P(\mathbf{Y})}. \tag{3.9}$$

$P(\mathbf{Y})$ is typically referred to as the evidence, and can be thought of as marginalizing over all possible values of the various parameters θ. As is standard in Bayesian inference, we note that the evidence has no dependence on the particular parameters of θ from the model and therefore has no information on the posterior distribution of θ. We are thus free to write Bayes theorem as a proportionality:

$$P(\theta|\mathbf{Y}) \propto L(\mathbf{Y})|\theta) \times P(\theta). \tag{3.10}$$

The prior distribution, $P(\theta)$, represents our information on the distributions of the parameters θ before we see any data. We consider our prior specifications in the next section.

3.2.4 Prior Specification

Specification of priors, as well as testing of prior sensitivity, is a vital step in Bayesian analysis. For purposes of this work, we choose to specify minimally-informative priors where possible. However, note that the need to specify a prior in Bayesian analysis ought to be seen as a strength of the method. Specifying a prior allows the researcher to incorporate information about where certain parameters ought to be concentrated, and also allows the researcher to specifically asses sensitivity of prior selection on final inference.

For the mean vector μ, we adopt a simple uniform prior, which is Jeffrey's prior for the mean of a multivariate normal. We adopt a $\mathrm{Symmetric} - \mathrm{Dirichlet}(1/2)$ distribution for the weights of the model, which is Jeffrey's prior for the multinomial distribution. For the scale parameter of the exponential distribution, we use a $1/\lambda$ prior, which again is Jeffrey's prior for the exponential. There is not necessarily an agreed-upon uninformative prior for the covariance matrix. We parameterize the prior with an inverse Wishart distribution with hyper parameters $\Psi = \begin{pmatrix} 0.03 & 0.00 \\ 0.00 & 0.03 \end{pmatrix}, \nu = 3$.

3.2.5 Summary of the Full Model

To summarize, our mixture model now consists of two distributions: a contaminant distribution defined to be uniform over specified ranges in color-color space, magnitude space, and spatial distribution over a specified circle. We also have a GC distribution consisting of a multivariate normal in color-color space, an exponential distribution in radius, and a normal distribution in i-band magnitude. This distribution features nine total free parameters: five parameters describe the location and covariance matrix of the multivariate normal, one describes the radial exponential distribution, two describe the scale and location of the i-band normal distribution, and one describes the relative strength of the two mixing distributions. The full model

3.2.6 Performing Inference on the Full Model

Once we have a full likelihood for the model, we are free to use standard Bayesian inference techniques to fit the model to our data. Markov Chain Monte Carlo (MCMC) sampling techniques are typically applied to these sorts of Bayesian inference problems, and we employ MCMC methods to sample our parameter posterior distributions. Many effective MCMC codes are available in the literature; we use `emcee`(Foreman-Mackey et al., 2013)[8] to perform our sampling. `emcee` is commonly

---

[8] https://github.com/dfm/emcee

used throughout the astrophysics literature, offers a fully-Python implementation that is easy to incorporate in the rest of our Python analysis code, and can be applied to any likelihood function that the user supplies.

`emcee` is an Affive-invariant ensemble sampler. Briefly, `emcee` works by initializing an ensemble of "walkers" to explore the parameter space. These walkers can be somewhat thought of as each executing a Metropolis-Hastings walk through parameter space, with some additional complexity.

In simple Metropolis algorithms, a new vector in parameter space is proposed, which is a random walk from the chain's current parameter location. The new location is accepted with probability unity if the likelihood at this new parameter location is higher than at the current one. If the likelihood is not higher, this new location is rejected with probability equal to the ratio of the likelihood at the new location and the ratio of the likelihood at the current location.

`emcee` is an extension of this simple algorithm. In each step of the chain, the algorithm randomly pairs off each walker with another. It then proposes a move in which it asks whether one of the walkers should move to the location of the other walker, with some additional jitter added. The use of walkers and the interpolative/extrapolative steps allows `emcee` to explore complicated posterior distributions more efficiently than with simple Metropolis algorithms.

3.2.7 Demonstration of the Model on Mock Data

As a demonstration of our methodology, we apply our toy model to some simple mock data. The mock data are drawn directly from the distributions that are being used in the model, so we would expect our model to fit these data well. However, it is both an important sanity check and a useful illustration of how the model works.

We create a mock data set consisting of 500 contaminant sources and 500 mock GCs. The contaminant sources are drawn from a uniform distribution in color with bounds $g - i \in [0.0, 1.5]$, $r - i \in [0.0, 1.0]$ and a uniform distribution in magnitude with $i \in [18, 26]$.

GCs are drawn from a MVN distribution in color-color space, with parameters

$$\mu = \begin{pmatrix} 0.75 \\ 0.5 \end{pmatrix}, \quad \mathbf{\Sigma} = \begin{pmatrix} 0.04 & 0.015 \\ 0.015 & 0.03 \end{pmatrix}. \tag{3.11}$$

In magnitude space, GCs are drawn from a normal distribution with $\mu = 22$, $\sigma = 1.5$. Finally, GCs were drawn from a 2D circular exponential distribution with scale radius $R_e = 0.3$.

Drawing GCs for the mock spatial distribution merits a bit more explanation, as definitions can differ and there is no simple `scipy.stats` distribution for a 2D exponential. We use the Python `astropy.modeling` package to parameterize and fit all our spatial distributions. The `modeling` package includes a `sersic2D` class that provides two-dimensional spatial distributions with arbitrary effective radius, position angle (PA), flattening parameter, and Sersic index. Fixing the Sersic index to $n = 1$ gives an exponential distirbution. In principle any of these parameters can be left free, and indeed in our full methodology, we fit for the PA and the flattening parameter. For this demonstration, we keep both parameters at zero, i.e. a symmetric circular exponential distribution.

The distributions from `astropy.modeling` are not, in general, normalized, and indeed the strength of the distribution is changed with the amplitude parameter, which we fix to one. To use the distribution as a probability distribution, we need to normalize the distribution so that it integrates to one over the parameter range of interest. We do this over a spatial grid with radius equal to the maximum radius of the contaminant distribution. Finally, to actually select points for this distribution, we use standard accept-reject methodology. We generate points from a uniform circle and accept or reject them with probability equal to the density of the exponential distribution at that particular point in space. This accept/reject methodology is then repeated until the number of desired sources are drawn. Such a method is not always efficient, but for generating mock distributions with less than many thousands of sources, this method runs very quickly.

We display a sample draw from these contamnant and GC distributions in Fig. 3.1.

After generating this sample draw of data, we are free to fit our model to these data and verify that the inferences returned are reasonable. As mentioned above, the toy model consists of nine free parameters: the two means of the color MVN, the three covariance terms if the MVN matrix, the mean of the luminosity distribution, the standard deviation of the luminosity distribution, the scale radius of the spatial distribution, and the fraction of GCs in the system.

We initialized 100 `emcee` walkers in small Gaussian balls around the specified

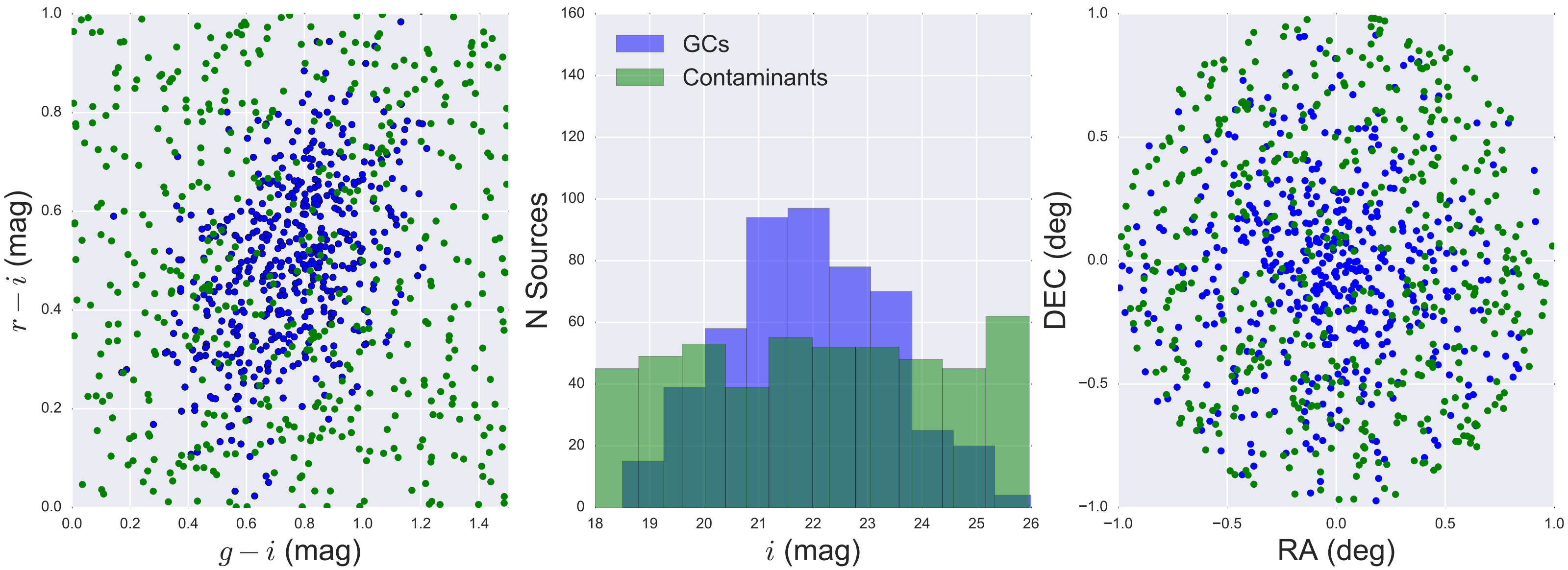

Figure 3.1: Mock data generated from the distributions in the toy model. Dataset consists of 500 contaminant sources uniformly drawn in color and i-magnitude space, and over a uniform circle in RA and Dec. GC data are drawn from a MVN in color space, a normal distribution in i magnitude, and a 2D exponential distribution in RA and Dec. Contaminants are plotted in green, while GCs are plotted in blue. The left plot is a color-color diagram, the middle is a luminosity histogram, and the right is a spatial distribution of sources.

values of our distributions and ran the full ensemble sampler for 2000 steps. Note that even if we hadn't started the walkers at the known values, they would have quickly walked into the typical probability set in only a few hundred steps for a distribution as simple as this one.

In Fig. 3.2, we plot the trace plots for 30 of our 100 walkers (walkers are omitted to make plots easier to see). It is clear that the chains are burnt in and are mixing well after just a couple hundred steps; indeed, 2000 steps is significant overkill for this particular model.

We also plot our full posterior distributions in standard corner-plot format in Fig. 3.3. In this plot, we only plot the second 1000 steps from our sampler to remove absolutely any burn in. We see that the posterior distributions appear very well-behaved, with all distributions approximately normally distributed. The "truth" parameters that we used for the distributions from which we drew data are plotted with blue lines. Note of course that any one particular draw of data can potentially be quite far away from the "truth" value for a particular parameter. For example, roughly one out of every two draws should contain a 2σ outlier from the truth, and a well-calibrated model should have some parameters for which the truth points are out in the wings of the marginal distributions.

3.2.8 Generating GC Probabilities

For analyzing general properties about a galaxy's GC system, one should use distributions which incorporate uncertainty in GC contamination and do analysis using the full posterior distributions for all model parameters. However, there are applications

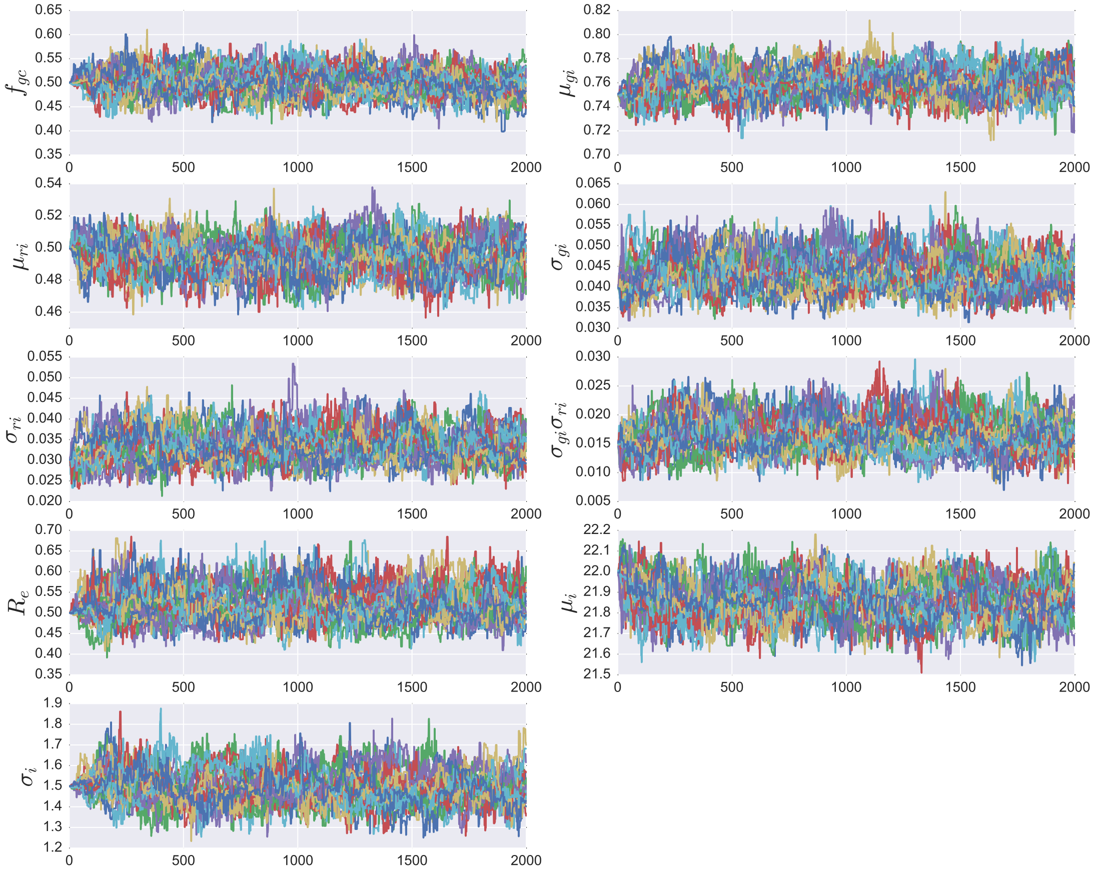

Figure 3.2: Trace plots for the nine free parameters in the model. Each plot features 30 of the 100 walkers. The full ensemble sampler was run for 2000 steps. It is clear that the chains burn in and walk around the typical set after a very short time.

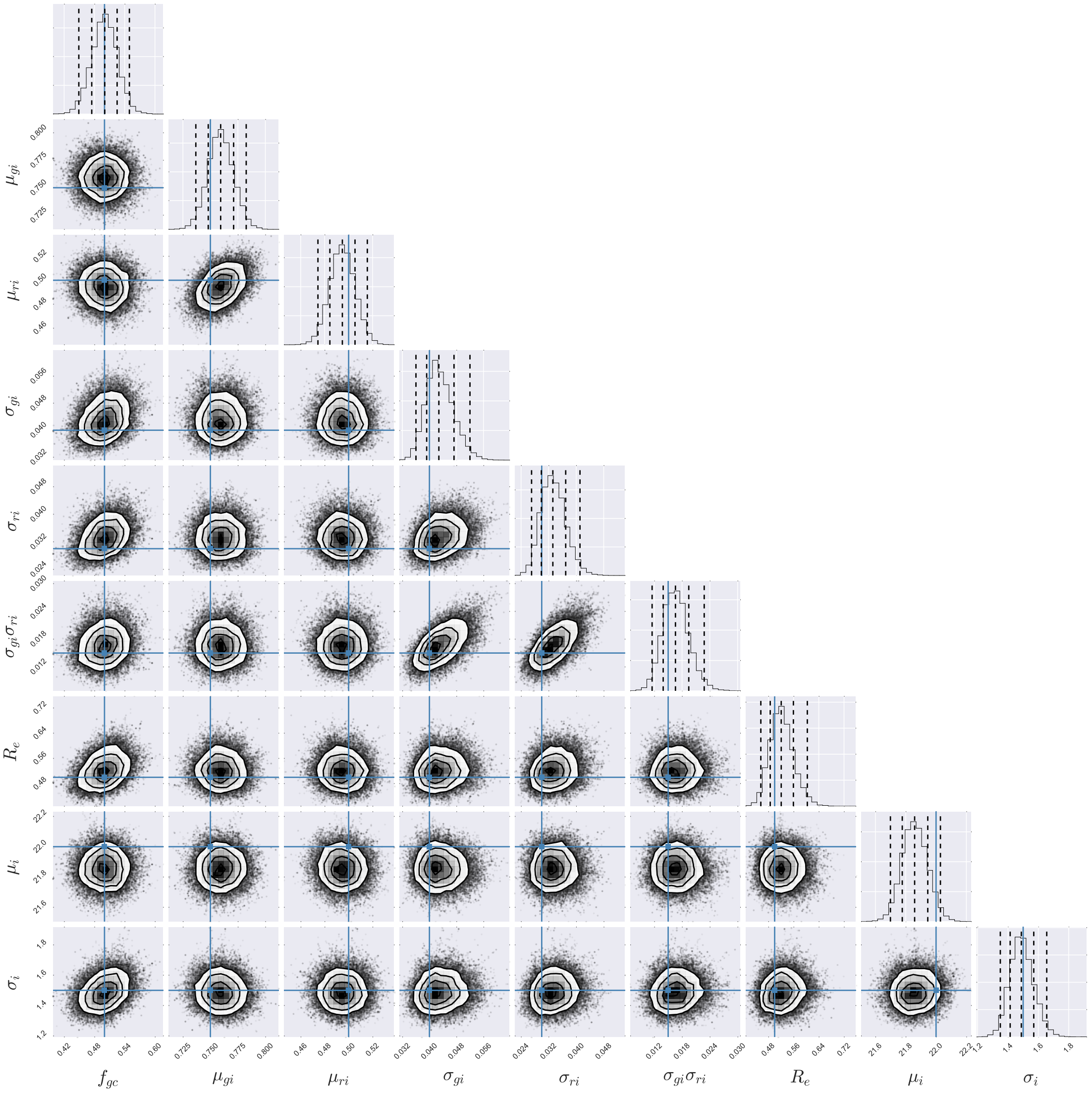

Figure 3.3: Corner plot showing 1000 steps of 100 walkers from our toy model. Solid lines through the plots indicate the ”truth” lines. All distributions are well behaved, and the marginals appear to all be approximately normal. 0.025, 0.16, 0.50, 0.84, and 0.975 quantiles are plotted over the marginal distributions. While no 2σ outliers appear to be present in for this particular dataset, note that roughly one out of every two datasets generated in this way should include one or more 2σ outliers.

for which having a probability for each source as to whether it is a GC or not can be useful, e.g. for optimizing selection of GC candidates for future spectroscopic follow-up. We term this probability P_{GC}.

Once one has posterior distributions, computing a point estimate for a source's P_{GC} value is trivial. It is simply equal to the likelihood that the source is a GC divided by the total likelihood of the source, i.e.

$$P_i(\mathrm{GC}|\mathbf{Y_i}, \theta) = \frac{L_{\mathrm{GC}}(\mathbf{Y_i}|\theta)}{L_{\mathrm{GC}}(\mathbf{Y_i}|\theta) \times L_{\mathrm{Cont}}(\mathbf{Y_i}|\theta)}, \tag{3.12}$$

where θ is taken to be the point estimate for each of our free parameters, i.e. the median of the posterior distribution of each free parameter. However, note that the value P_{GC} is itself a random variable; one may calculate a posterior distribution for P_{GC} for every source in the dataset. This can be done directly by simply calculating the right hand fraction for each step in the posterior distribution chain. In other words, the posterior distribution of every $P_{\mathrm{GC,i}}$ is completely defined once the posterior of θ is sampled. In general we default to simply providing a point-estimate of P_{GC} for each source in our dataset, as the utility of having the full posterior is not immediately obvious. However, they can be calculated trivially from the chains if needed.

In Fig. 3.4, we display the color-color and spatial distributions of the dataset generated in §3.2.8. However, we now color-code each point by the probability that the source is a GC given the posterior inferences sampled by the MCMC chain. Redder points are more likely to be contaminant sources, while bluer points are more likely to be GCs. Note that while the trends of the two distributions are clear, there is not a defined boundary between samples in any given space. Each source is assigned its own probability based on where it lies in the full multidimensional dataset. As the histogram no longer makes sense to include when considering probability P_{GC} as a continuous variable, we omitted the magnitude information in these plots.

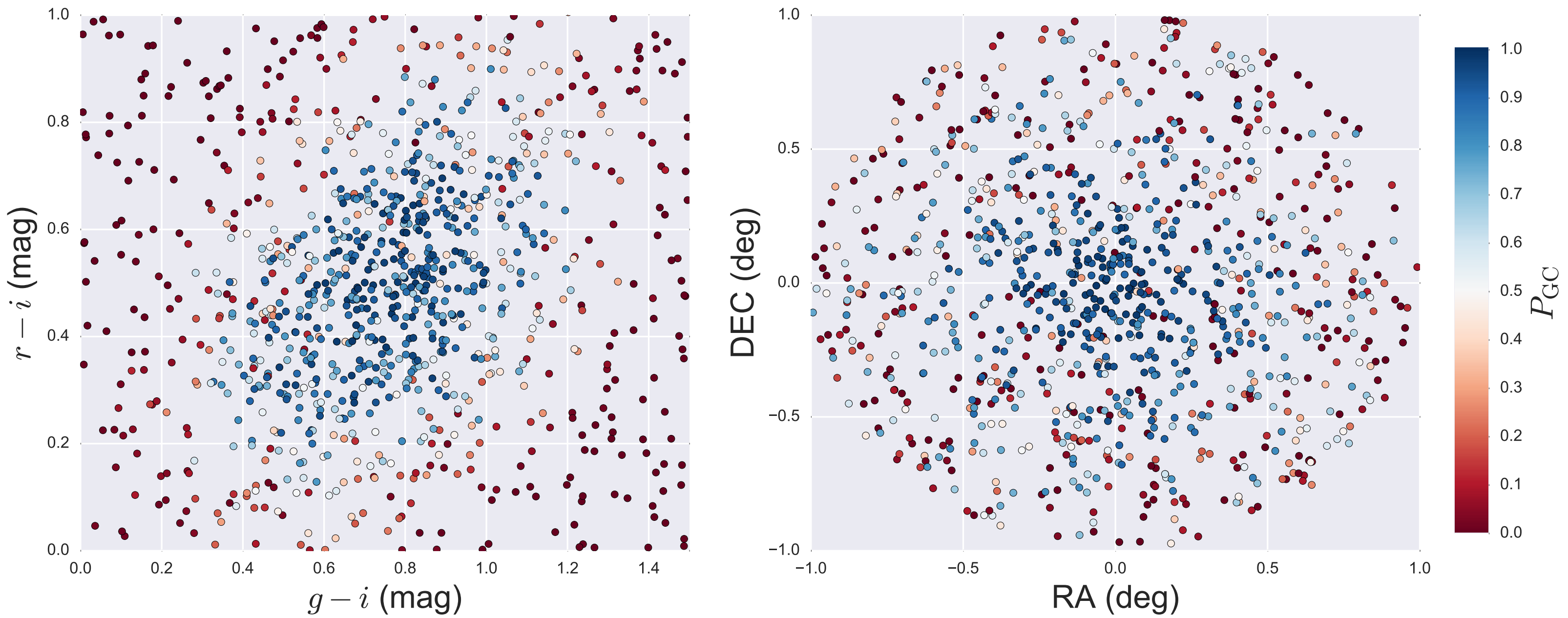

Figure 3.4: Color-color and spatial distributions of the mock dataset analyzed in §3.2.8. Points are now color coded with the probability that they are GCs; bluer points are more likely to be GCs, while redder points are more likely to be contaminants. Probabilities are calculated based on point estimates from the posterior distributions that were sampled in §3.2.8

3.3 A REALISTIC MODEL FOR GC SELECTION

The model considered in §3.2, while not entirely disconnected from real GC distributions, has some significant flaws. In this section, we improve the model and make it a more accurate description of a realistic GC dataset.

Perhaps most importantly, in the §3.2 toy model, we assumed contaminant sources were uniformly distributed over the allowable parameter ranges. In fact contaminants have significant structure in both color-color and luminosity space. Section §3.3.1 deals with creating a realistic distribution of contaminants in color-color space, and section §3.3.2 considers the same problem in luminosity space.

Finally, we also wish to expand our model to include more than one GC population. Most GC systems display significant evidence of bimodality. If this bimodality is apparent in the system, it must be included in the model in order to achieve a reasonable fit to the data. In addition, characterization of GC bimodality is a useful insight into the formation of the GC system. Section §3.3.3 explains including an additional GC population as an additional part of the mixture model.

Finally, in section §3.3.5, we apply this realistic model to an illustrative mock dataset and verify that we can still realistically recover GC system parameters given these more realistic models.

One additional complication which we neglect in this section is the issue of incompleteness in our dataset due to sources below our detection threshold. Due to the complexity of incompleteness, we discuss how we incorporate incompleteness in §3.4.

3.3.1 Modeling the Contaminant Population Color

In §3.2, we discussed the contaminant population as though it was uniformly distributed in spatial distribution, color, and luminosity. The spatial assumption is likely reasonable: on the sorts of sub-degree image scales we are dealing with, there is unlikely to be a significant gradient in the distribution of sources across the field of view. However, contaminant populations are most certainly not uniformly distributed in color. Instead, foreground star contaminants follow a stellar locus in color-color space, while background galaxies populate their own tracks. Significant work has been done on parametric modeling of the distribution of stars in all sorts of photometric bands. However, any parametric model naturally makes significant assumptions. Furthermore, the sorts of photometry performed by the study of interest will not perfectly mirror those methods adopted for our work.

Instead, we make use of NGVS control fields to model the distribution of contaminants in color-color space. As part of NGVS, four background fields were observed away from the actual Virgo cluster. As of submission of this work, three of these fields feature three-band g, r, i photometry, appropriately named NGVS_BG_1, 2, and 3. To build our contaminant catalogs, we analyzed these three fields in an identical manner to our science catalogs. We downloaded the full MEGAPIPE-stacked images (Gwyn, 2008) for each filter from the Canadian Astronomy Data Centre[9].

We then performed photometry on these fields and applied our standard quality and extended-object cuts, as described in Chapter 5. Since we are actually modeling

---

[9] http://www.cadc-ccda.hia-iha.nrc-cnrc.gc.ca/

our science distributions, we emphasize that the goal of these cuts is only to eliminate sources which are *clearly* not GCs because of their shapes and extended sizes. The entire point of modeling the distributions is to handle cases where the identity of the source is ambiguous. It is far more important that any photometry cuts be performed *consistently* across both science and background fields than it is for the cuts to achieve a precise elimination of contaminants.

After photometry is performed for each field, we combine all three fields into one large catalog to represent our contaminant distributions. Photometry across all three fields was remarkably consistent (see Fig. 3.5), indicating that all three fields can be combined into one single representative catalog of contamination.

We use the Python package `scikit-learn`'s implementation of kernel density estimation (KDE) to perform a 2D KDE on the $g - i$ and $r - i$ distributions. We plot a contour plot of the KDE in Fig. 3.6. The scikit-learn KDE module can be queried to return the log-density of a given sample of data points. We will denote this distribution as $d_{FG}(Y)$, indicating the probability of observing a data vector $\mathbf{Y}$ under the trained KDE model. The KDE model behaves just like any other probability distribution and represents the color distribution of the contaminant population in the mixture model.

KDEs have a single free parameter, the bandwidth, which represents the width of the kernel applied to each data point. We experimented with 5-fold cross-validation in `scikit-learn` to evaluate this parameter; however, the best-fit bandwidht from cross-validation, 0.02, was not smooth and appeared to contain some noise from the data. This added noise could occasionally throw off our Bayesian inference, as sometimes

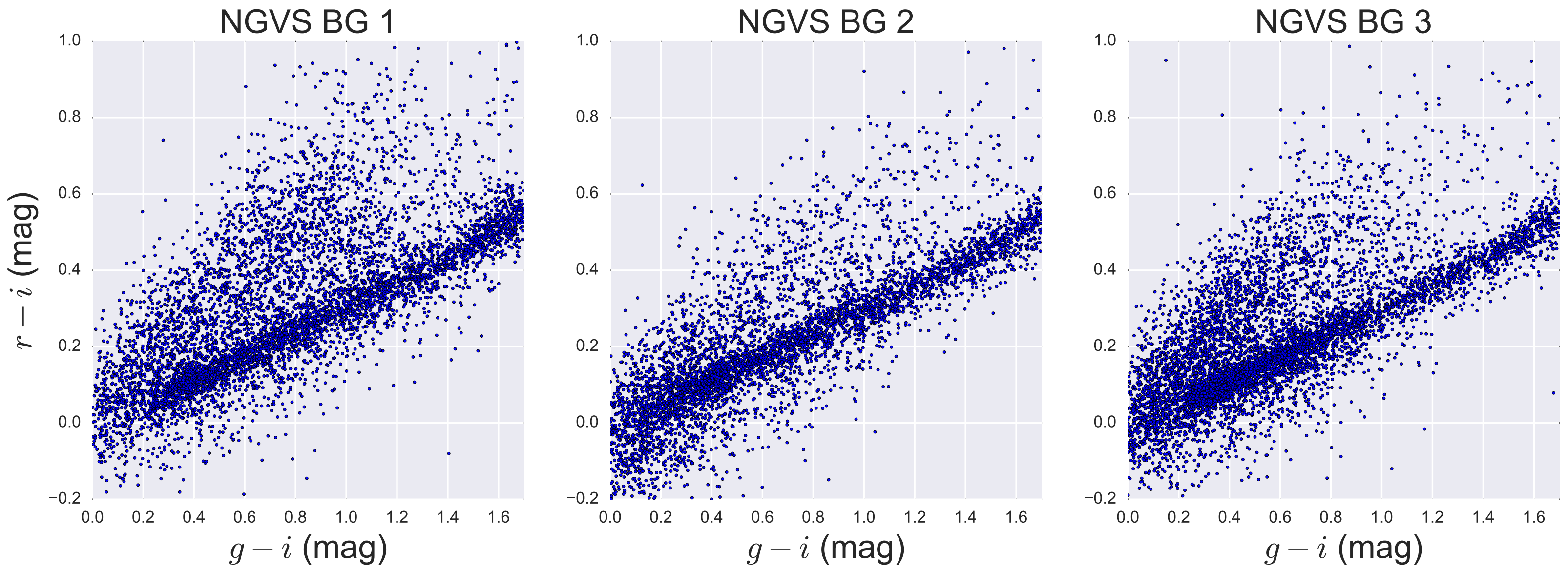

Figure 3.5: Color-color plots of the three NGVS contaminant fields. While we plot each field in an independent panel to make inspection easier, each field has remarkably similar photometry. The stellar loci of all fields overlap perfectly, indicating that the MEGAPIPE reduction pipeline has produced consistent reductions and zero-points. We combine all three fields together to create our final contaminant density estimate.

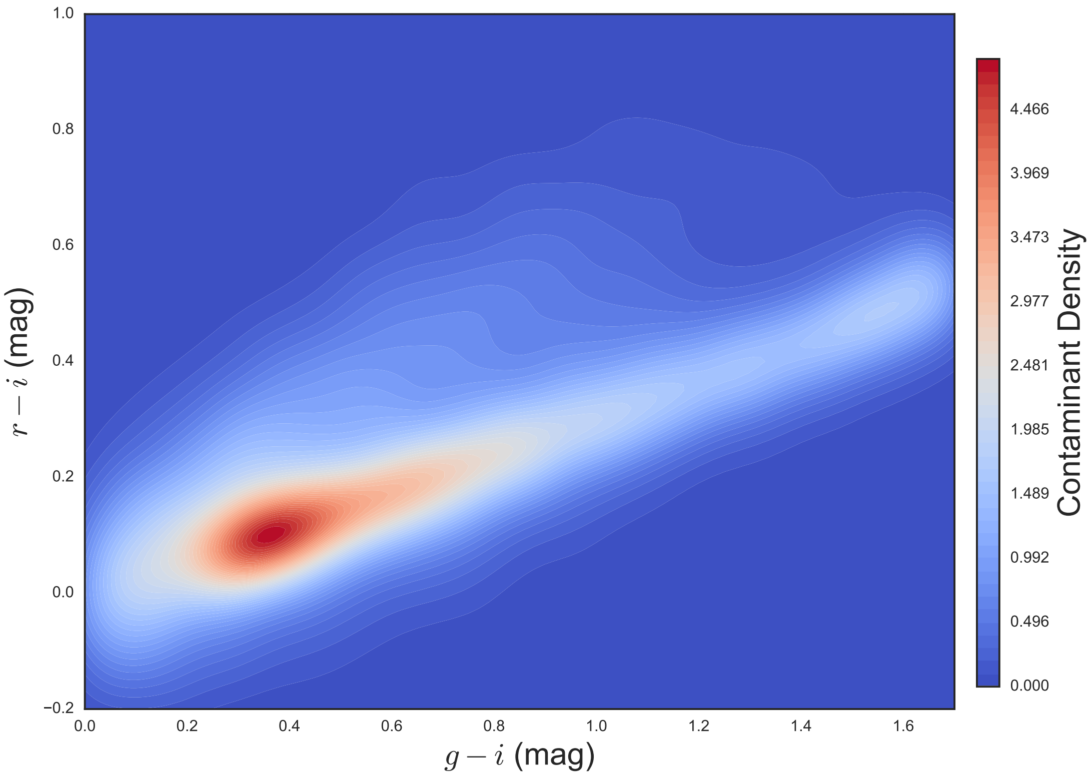

Figure 3.6: KDE of our contaminant population in $g-i$, $r-i$ space. The density estimate is created using `scikit-learn`'s KDE implementation with a bandwidth parameter of 0.05. The distribution is smooth while still retaining all information about the expected color distribution. We use this KDE as the contaminant distribution in all our inference.

the GC distribution "walked" in to one of these noisy, underpopulated regions. We found a bandwidth of 0.05 produced a reasonable and smooth contaminant distribution. Bandwidths greater than this began to wash out detail in the distribution.

An additional normalization must be applied to the KDE probability to account for the fact that we define color-color boundaries in our dataset. This is straightforward to calculate to arbitrary precision by simply calculating the KDE probabilities on a grid across the color-color space and summing them. We found that a grid resolution of ~ 0.02 mags in color normalized the contaminant KDE to a range of less than

0.1%, which was sufficient for our purposes.

The full model for the contaminant distribution, including the normalization therm, looks like

$$P_{\mathrm{FG}}(\mathbf{Y}) = \frac{d_{FG}(\mathbf{Y})}{C}, \tag{3.13}$$

$$C = \sum_{i=x_1}^{x_2} \sum_{j=y_1}^{y_2} d_{FG}(i,j)\Delta x \Delta y, \tag{3.14}$$

where $[x_1, x_2]$ and $[y_1, y_2]$ are the color limits over which the KDE is defined and Δx and Δy are small enough to achieve good approximation. This probability plugs directly in to our mixture model likelihood function, providing the distribution function for the contaminant distribution.

One important computational note is that this distribution in the context of the mixture model contains no free parameters. This means that the contaminant likelihood doesn't change as the MCMC runs, and therefore can be calculated at the beginning of the model. Querying the KDE probability takes a significant amount of time, and so if it was performed at every step in the chain, the time to run a chain of a given length would be drastically increased.

An implicit assumption of this method is that the color-color distribution of contaminant sources, i.e., Milky Way stars and background galaxies, is consistent across all our target galaxy fields. While this assumption is likely to be broadly reasonable, one important caveat will be if a science field overlaps with any halo substructure.

3.3.2 Modeling the Contaminant Distribution in Luminosity

In addition to creating a more realistic color-color contaminant distribution, we also wish to consider a more realistic distribution in luminosity. The constant luminosity model used in §3.2 is a very poor description of the luminosity of a random selection of astronomical sources. In fact, the luminosity of a random photometric sample increases significantly towards fainter magnitudes approaching the detection limit, then falls off sharply as sources become too faint to detect. Fig. 3.7 includes a histogram of point sources in the background field NGVS_BG_2, which is the deepest of the three NGVS background fields we use.

As a first step, we make a KDE of this *i*-band luminosity histogram. As usual, this KDE can be queried to return the likelihood given an *i*-band magnitude. This histogram also needs to be corrected for the incompleteness in the NGVS_BG_2 data. We quantify completeness in our standard manner as described in §3.4. We then create a completeness-corrected density estimate at each magnitude by dividing the KDE density by the probability of the source being observed at that point. This corrected distribution must be normalized so that it integrates to one over the range of the data under consideration. We display the steps in creating this distribution in Fig. 3.7, along with a comparison to the luminosity distribution of M87 (see Ch. 4).

3.3.3 Bimodality in GC Distributions

It is well established that most GC systems display some evidence of GC bimodality in their color and mellaticity distributions. Accounting for this bimodality

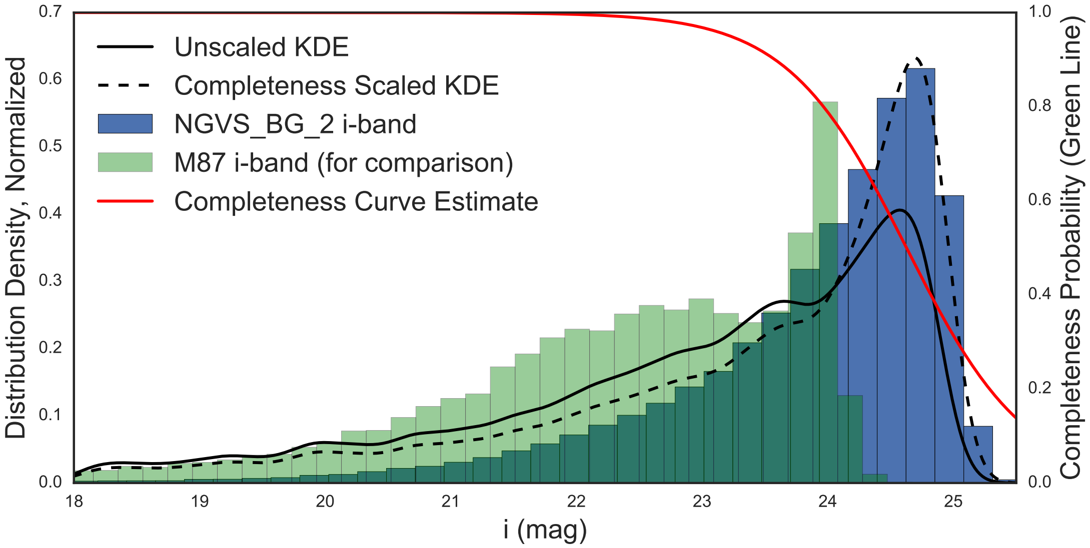

Figure 3.7: The blue histogram is the *i*-band luminosity histogram of sources in the contaminant field NGVS_BG_2. Green, we plot our recovered completeness function for this image. Note that the right y-axis applies to the completeness function. The solid black line represents a KDE of this luminosity histogram, while the dashed line is a scaled version of this KDE. This scaled version accounts for sources that are missed due to incompleteness. Finally, the green histogram is our measured *i*-band histogram from M87. The bump around $i \sim 23$ from M87's large GC population is clearly visible, and the data are clearly more shallow than in NGVS_BG_2.

is important for correctly modeling the GC systems, and measuring this bimodality also offers interesting scientific insights of its own.

Conceptually, color bimodality is easy to incorporate: we simply specify a second multivariate normal mixture component in our color distribution. Adding a second component means that the GC component of the likelihood now has additional free parameters, including a second mean vector and a second covariance matrix. In addition, we now have two mixture strength components, $f_{\mathrm{GC,blue}}$ and $f_{\mathrm{GC,red}}$.

One important complication introduced by a second mixture component is identifiability. Now that we have two mixture components with identical distributions, there is no intrinsic difference between the parameters for one distribution and the parameters for the other. If we were to run our sampler with no further information, the parameters for both distributions would switch places continuously in the course of sampling. To provide identifiability to the distributions, we adopt a simple prior of a specified value for the $g-i$ mean. In other words, the prior for the $g-i$ mean of the blue population is uniform from some low cut off value to a specified divider value, and the prior for the $g-i$ mean of the red population is uniform from that same specified divider value up to high cut-off. The $g-i$ divider value is difficult to know a-priori for a galaxy, so our usual procedure was to experiment for each galaxy to find a division that produced well-sampled chains. Strictly speaking, determining the $g-i$ cut-off in such a way is not in the true spirit of "prior" information. However, we consider the strongest prior information simply being the fact that we enforce a strict division between the two populations, i.e. a strong prior that there is both a red and a blue subpopulation.

While a prior requiring the mean of one distribution to be less than the mean of the other would not require experimentation for each galaxy, such a prior actually violates detailed balance and therefore the MCMC chains derived from such a prior would not be truly representative of the posteriors.

In the interest of simplicity, we ultimately decided not to extend the bimodal model to the spatial and luminosity distributions. In principle it is straightforward to write these distributions into the model; we simply allow for additional free parameters for both the red and blue GCs. If we were to do this, we would include total of five additional free parameters (luminosity mean, luminosity variance, scale radius, ellipticity, and position angle).

3.3.4 Bounding of the Mixture Distributions and Normalization

In order for the mixture distributions used in this model to provide valid inference, it is vital that they be normalized correctly. For distributions with common PDFs like exponentials and multivariate normals, such normalization is true by definition. However, in photometric analysis of GC datasets, we are usually dealing with a dataset that has been trimmed in some way, usually by applying some cut in color, luminosity, or radial space. Bounding one's dataset in such a way has important consequences when applying models to said dataset, and inferences drawn when such models are applied can be biased if these data selection rules are not taken in to account. The relative fractions of populations in mixture models are particularly prone to bias if normalization is not accounted for.

As discussed in §3.3.1, normalization of the contaminant color-color dataset can be accomplished numerically by summing the distribution over an appropriately-sized grid, and an identical procedure can be applied to the contaminant luminosity distribution in §3.3.2. While such grid approaches can be computationally intensive, they are completely tractable to evaluate to high precision as they must only be performed once, at the beginning of the MCMC chain.

Normalization of the GC luminosity distribution is also trivial: since the GC distribution is described by a normal distribution, the normalization term is simply equal to the value of the CDF at the faint luminosity cutoff minus the CDF of the bright luminosity cutoff. However, this normalization term depends on the free parameters $\mu_{\rm Lum}$ and $\sigma_{\rm Lum}$ and therefore must be recalculated for every step in the MCMC chain. Since the normal CDF is known as an easily evaluated distribution, this re-calculation adds negligible computation time.

A more complicated issue is normalization of the multivariate normal distribution. While one could calculate this normalization term with a grid approach, the GC color MVNs are dependent on both the means and covariance matrices and therefore normalization must be recalculated at each step in the chain. While there is no such documented routine in `scipy.stats`, a hidden implementation of Genz (1992)'s MVNDST routines exists in `scipy.stats`. These routines allow calculation of the CDF of a multivariate normal. In the course of this work, we wrote a wrapper module for these routines[10], allowing quick calculation of normalized truncated multivariate normal distributions within our MCMC chains.

Finally, the spatial distribution must also be normalized. Our standard pro-

---

[10] https://github.com/zachjennings/truncMVN

cedure for the spatial distribution of GCs is either to perform a radial cut or to take all sources on the image, which essentially amounts to a rectangular cut. Since we treat the contaminant distribution as being uniformly distributed spatially, the normalization of this distribution is simply equal to the inverse of the area of the region considered. However, the GC distribution is treated as having a 2D exponential radial distribution, which we model using the `astropy.modeling` Sersic implementation. Depending on our radial cut, it is straightforward to define grid either circularly or rectangularly distributed over the region of interest. We then evaluate the model at every point in this grid and sum to approximate the total probability contained within the bounds. Note that, while there are closed-form solutions for the normalization of a 1-D exponential distribution, even with ellipticity, we are unaware of any implementations that allow for the sorts of circular or rectangular bounding considered in this problem. As a result, we adopt a grid approach to normalize the spatial distributions.

Unlike the above normalization problems, this grid-based approach must be performed at every point in the MCMC chain since the GC spatial distribution contains free parameters that are being fit in the model. This normalization therefore adds significant computational overhead to the inference, with the amount of overhead essentially corresponding to the number of grid spaces where the model must be evaluated. We found adopting a grid of width 0.005 deg provided accuracy of the normalization constant to within 99.9% for an effective radius of 0.1 deg, which we deemed sufficient for our purposes (and significantly smaller than the general scatter in the posterior of the mixture fractions). 0.1 deg is typical of the sorts of effective radii seen in our GC analysis. The MCMC inference naturally proceeds slower with this grid-based approach, but at less than a factor of two increase.

3.3.5 Application of the Full Model to a Mock Dataset

In this section, we present an example of the full model applied to a mock dataset generated from the distributions outlined above. We consider a distribution of 1000 contaminants, 500 blue GCs, and 500 red GCs. The GC colors are drawn from red and blue multivariate normal distributions with parameters

$$\mu_{\text{Blue}} = \begin{pmatrix} 0.75 \\ 0.2 \end{pmatrix}, \quad \mathbf{\Sigma}_{\text{Blue}} = \begin{pmatrix} 0.01 & 0.003 \\ 0.003 & 0.005 \end{pmatrix} \tag{3.15}$$

for the blue GCs and

$$\mu_{\text{Red}} = \begin{pmatrix} 1.0 \\ 0.3 \end{pmatrix}, \quad \mathbf{\Sigma}_{\text{Red}} = \begin{pmatrix} 0.02 & 0.005 \\ 0.005 & 0.01 \end{pmatrix} \tag{3.16}$$

for the red GCs. GC spatial coordinates are drawn from an elliptical exponential distribution with $R_e = 0.5$ deg, $\epsilon = 0.5$, and $PA = \frac{\pi}{4}$. GC i-band magnitudes are drawn from a normal centered at $\mu_i = 22$ mag, $\sigma = 1.0$.

1000 contaminant colors are drawn by re-sampling from our contaminant KDE. Spatial coordinates for the contaminant distributions are drawn from a uniform circular distribution with radius 1.0 deg. Finally, contaminant i-band distributions are drawn from our completeness-corrected i-band KDE. This final sample must be drawn using accept/reject sampling method, since the corrected distribution is the ratio of two other

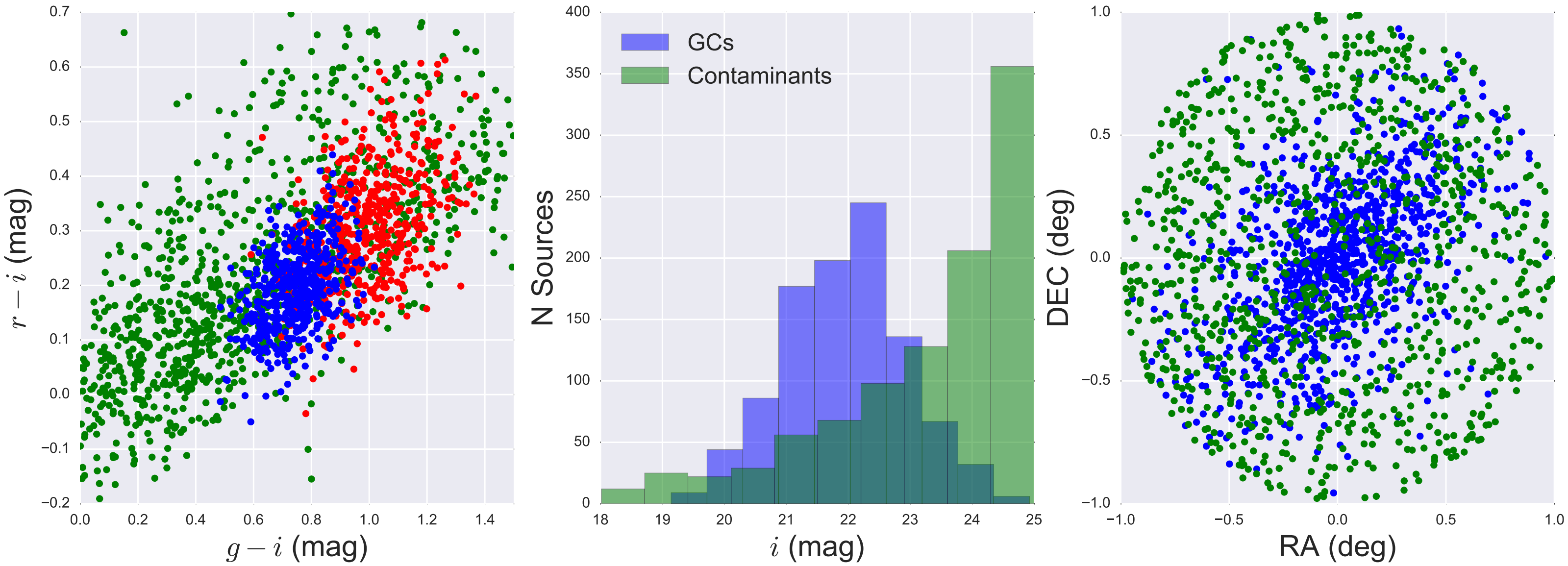

Figure 3.8: Mock data generated for our realistic model, as described in §3.3.5 of the text. The mock dataset consists of 500 Blue GCs, 500 Red GCs, and 1000 contaminant points. The left panel is a $g-i$, $r-i$ color-color diagram, the middle panel is a histogram of i-band magnitude, and the right panel is the spatial distribution in RA/DEC. We color-code the red and blue GCs separately in the color-color diagram and plot all GCs as blue in the middle and right panels. Contaminants are green in all plots.

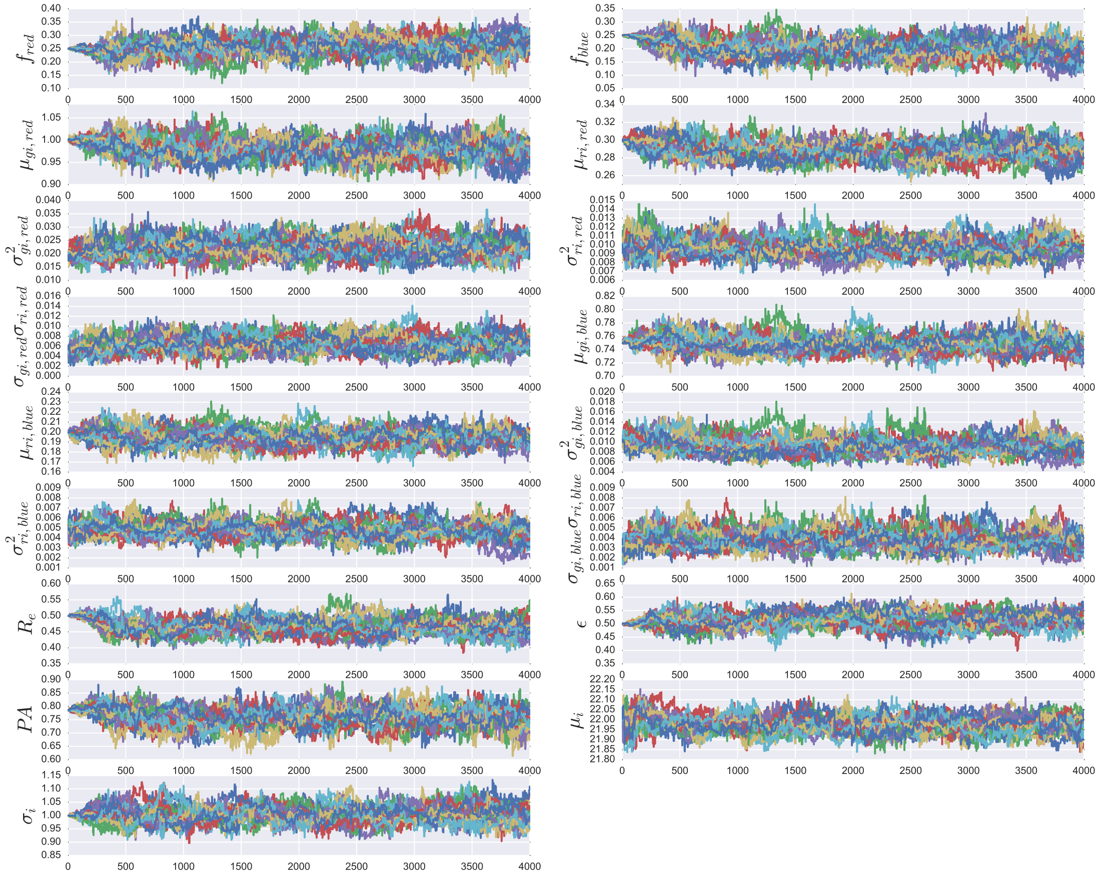

Figure 3.9: Traces of walkers for the sampler applied to the mock dataset shown in Fig. 3.8, plotted for each of the 17 free parameters in the model. We initialized 100 walkers and ran the sampler for 4000 steps. For clarity in the plot, we only plot 30 walkers from the ensemble. Walkers are clearly burnt-in after just a few hundred steps, and the chains appear well-mixed. For this simple mock dataset, the traces are not significantly influenced by the priors, aside from the boundary necessary for identifiability in the mixture model.

distributions at every point.

After our distributions are generated, we make the standard cuts we would apply when considering an extragalactic photometric dataset. We cut the colors to be within the ranges

$$0.0\ mag < (g - i) < 1.5\ mag \tag{3.17}$$

and

$$-0.2\ mag < (r - i) < 0.7\ mag. \tag{3.18}$$

Spatial coordinates are required to be within one degree of the center of our distribution, and the i-band magnitudes are restricted to the range

$$18\ mag < i < 25\ mag. \tag{3.19}$$

We plot the generated catalog in Fig. 3.8.

After generating the data, we sampled the posteriors using `emcee`. We ran the sampler for 4000 steps using 100 walkers. Traces from 30 of these walkers are plotted in Fig. 3.9. We discard the first 2000 samples from each walker as burn in and plot distribution plots for all 17 free parameters in Fig. 3.10. Finally, in Fig. 3.11, we plot the color-color and RA/DEC values of our sources. We color-code the points by the probability that they are a GC given our model inferences, just as was done in §3.2.8. Note that this plot could also be made for the probability that each source is a member of either the red GC population or the blue GC population, as these probabilities are also trivially available to be calculated in an identical manner.

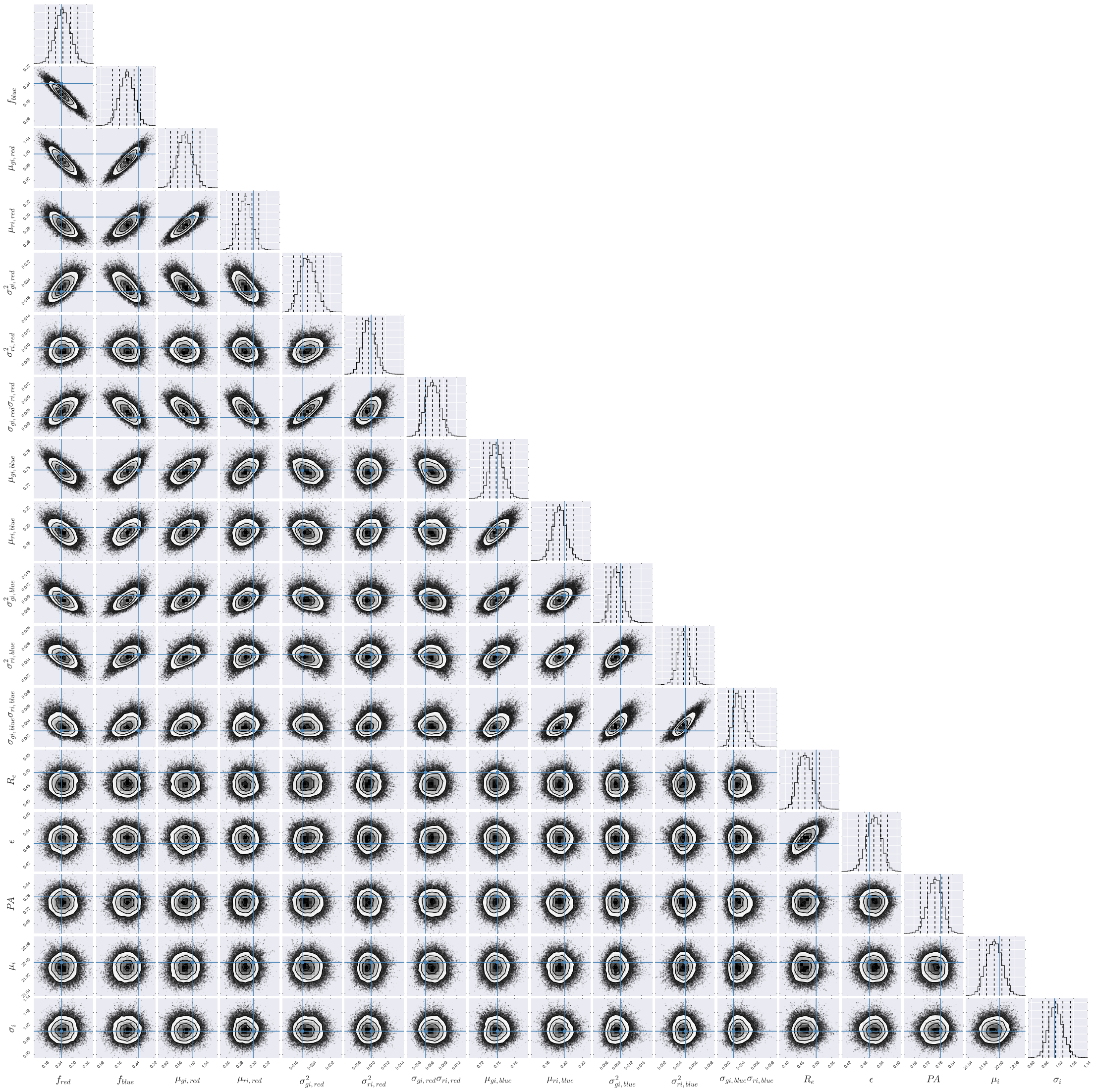

Figure 3.10: Corner plot for the ensemble show in Fig. 3.9. We discard the first 2000 steps of each walker as burn-in. While this is more than necessary, posterior distributions still each contain two million samples. The posterior distributions in general appear well-behaved, and match the truth values well. Outliers are within what would be expected for a calibrated model. Note that for data initialized in this way, there are significant covariances, such as between the $f_{\mathrm{GC,Blue}}$ and $f_{\mathrm{GC,Red}}$ parameters.

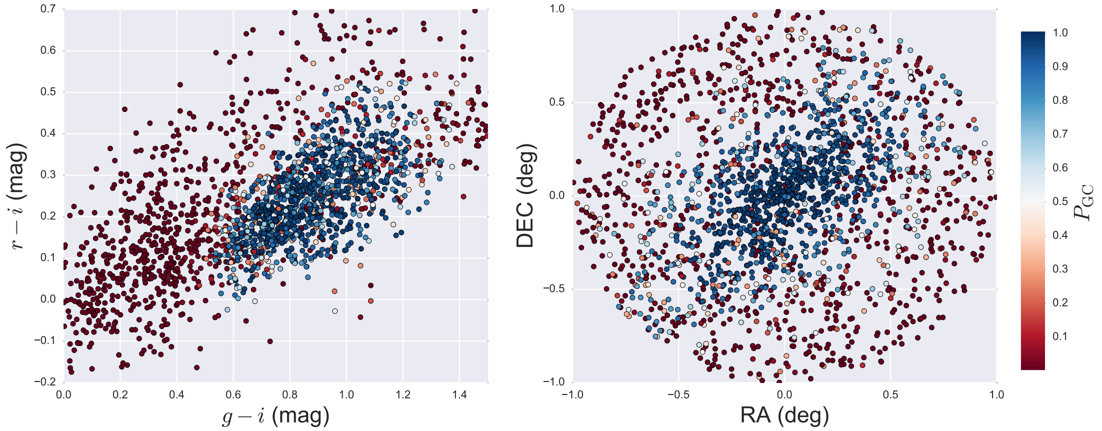

Figure 3.11: Color-color and spatial distributions of the mock dataset analyzed in §3.3.5. Points are now color coded with the probability that they are GCs; bluer points are more likely to be GCs, while redder points are more likely to be contaminants. Probabilities are calculated based on point estimates from the posterior distributions that were sampled in §3.2.8. While we consider the blue and red GCs to be the same class for this plot, probabilities may also be calculated based on source's membership probability to any of the three classes.

3.3.6 Discussion of the Posterior Distributions of the Mock Data

All plots indicate that our sampler is well-mixed and that our truth values are recovered well. As noted previously, al well-calibrated model ought not to recover perfectly true values for all its free parameters; indeed, with this many free parameters, it is very likely to see at least one ”two-sigma” outlier in a dataset realization such as this one.

There are many parameters that display significant covariances in the corner plots. For example, the $f_{\rm GC,Blue}$ and $f_{\rm GC,Red}$ parameters display a nearly diagonal corner plot. This indicates that the total number of GCs can be known to greater precision than total number of either population. In other words, uncertainty over which GC population a source belongs to is great than than uncertainty as to whether a source is a GC or a contaminant. Note that this isn't necessarily true for all GC populations; populations with either narrower distributions and/or more widely separated means would show easier separation between the two populations.

$g - i$ and $r - i$ mean for each population also show a large amount of covariance. This also makes logical sense: since the distributions from which the data were drawn were multivariate normals with covariance, there are preferred directions for the posterior distributions of the mean vectors. Covariances also exist among many of the parameters within the multivariate normal covariance matrix. Finally, interesting covariances exist between the $f_{\mathrm{GC,Blue}}$ and $f_{\mathrm{GC,Red}}$ parameters and the parameters of their distributions. These again make intuitive sense: in general, if there is probability among a scale parameter that leads to a wider distribution, it will also lead to an increase in the fractional weight attached to that distribution. The opposite is true for the fractional weight attached to the opposite distribution.

These covariances among the parameters indicate that there is a great deal more information encoded in a full GC distribution model than can be gleaned just from simple sample selection. Quantities such as the total number of GCs in a system can be known to greater precision than would be learned examining each GC distribution individually. Furthermore, this also reinforces the obvious notion that uncertainty in the parameters of GC distributions also contributes correlated uncertainty to the relative number of GCs in either population.

3.4 ACCOUNTING FOR INCOMPLETENESS

In astronomical surveys, we are naturally working with data that are incomplete at some level. Above some luminosity threshold, we expect to recover sources with near 100% efficiency, while below some threshold we expect one unable to detect sources, with some sigmoid-like functional form in the middle. Accounting for this in our Bayesian context can be accomplished by using a modified likelihood function.

3.4.1 Estimating Completeness Functions with Fake Star Tests

To estimate our completeness function, we employ fake star tests. Fake star tests are conceptually straightforward: into each image, we insert a series of stars of known magnitude using a model PSF. We then attempt to recover these stars, using the same photometric procedure applied to our science data. The rate at which stars are recovered as a function of magnitude through this procedure gives the incompleteness function of the data.

To quantify completeness, we used `scikit-learn`'s logistic regression classifier. Logistic regression is a form of generalized linear model, where a logistic function is used to link an underlying linear releationship to a binary outcome. As our training set to our logistic regression model, we take as our training set the recoveries and failures from our fake star tests, with the feature as the input magnitude of the source. We then train a one parameter model to get our optimal completeness curve. An advantage of logistic regression is that it is fundamentally probabilistic, so its outputs directly map to the probability that a source of a given magnitude is recovered. An example of a trained completeness curve can be seen in Fig. 3.7.

3.4.2 Single-Band Incompleteness

Much of the formalism below comes from Weisz et al. (2013), who considered the problem of incomplete data in the context of evaluating the mass function of resolved star clusters in the Panchromatic Hubble Andromeda Treasury *HST* dataset of M31 (Dalcanton et al., 2012). In this section, we adapt the formalism derived by Weisz et al. (2013) to our particular problem.

When we allow for the possibility of not observing the data, our likelihood becomes $P(Y|\theta, \mathrm{obs})$, i.e. the probability of observing data $\mathbf{Y}$ given both the current value of θ and the fact that the object was observed. Using Bayes theorem, we can write this probability as

$$P(\mathbf{Y}|\theta, \mathrm{obs}) = \frac{\mathrm{p}(\mathbf{Y}|\theta)\ \mathrm{p}(\mathrm{obs}|\mathbf{Y})}{\mathrm{p}(\mathrm{obs}|\theta)}. \tag{3.20}$$

$P(\mathbf{Y}|\theta)$ is the previous likelihood function before completeness of the data was considered. $P(\mathrm{obs}|Y)$ is our completeness function, the chance of actually observing a particular source given the measurements of our source. This function may, in principle, be evaluated to whatever precision we need through the use of fake star tests. We insert a number of sources into our image of known brightness, and attempt to recover them through an identical photometry procedure as that used to measure the data. We discuss our specific procedure for this work in §3.4.1.

$P(\mathrm{obs}|\theta)$ requires additional consideration. This is essentially a normalization term for the full likelihood. The fraction of data that we expect to have missed is itself dependent on the parameters of our model. This term can be calculated explicitly, given a parameter vector θ. The problem is most easily explained in a single band, for a single population of GCs; we will generalize to multi-band photometry with multiple populations in the next section.

We may write $P(\mathrm{obs}|\theta)$ asl

$$P(\mathrm{obs}|\theta) = \int_{-\infty}^{\infty} P(\mathrm{obs}|m)\ P(m|\theta)\ dm, \tag{3.21}$$

where m is the measured magnitude, $P(\mathrm{obs}|m)$ is the measured completeness at a given magnitude, and $P(m|\theta)$ is the likelihood of observing a magnitude for given luminosity parameter vector θ. In practice, we assume the completeness function $P(\mathrm{obs}|m)$ is approximately sigmoid-shaped, and therefore will be ≈1 for sources brighter than some magnitude m_1 and ≈0 for sources fainter than some magnitude m_2. This makes the integral

$$P(\mathrm{obs}|\theta) = \int_{m_0}^{m_1} P(m|\theta) dm)\ +\ \int_{m_1}^{m_2} P(\mathrm{obs}|m)\ P(m|\theta)\ dm, \tag{3.22}$$

where m_0 is the lowest magnitude of interest in the problem (i.e. where we integrate our luminosity PDFs down to).

We now substitute in our mixture-model likelihood function:

$$\begin{aligned} P(\mathrm{obs}|\theta) = f_{\mathrm{GC}} \int_{m_0}^{m_1} P_{\mathrm{GC}}(m|\theta)\ dm\ +\ (1 - f_{\mathrm{GC}}) \int_{m_0}^{m_1} P_{\mathrm{FG}}\ dm \\ +\ f_{\mathrm{GC}} \int_{m_1}^{m_2} P(\mathrm{obs}|m)\ P_{\mathrm{GC}}(m|\theta)\ dm\ +\ (1 - f_{\mathrm{GC}}) \int_{m_0}^{m_1} P_{\mathrm{FG}}\ P(\mathrm{obs}|m)\ dm. \end{aligned} \tag{3.23}$$

The first two integrals are simple to evaluate: since we assume a normally distributed luminosity function for the GCs, the first integral is just the CDF of a normal distribution with parameters θ evaluated at location m_1. The second integral is just $m_1 - m_2$, since we have assumed a constant distribution of contaminant sources.

The latter two terms require $P(\mathrm{obs}|m)$, which is not available in a functional form. Instead, we can attempt to approximate them using a simple summation:

$$f_{\mathrm{GC}} \int_{m_1}^{m_2} P(\mathrm{obs}|m)\ P_{\mathrm{GC}}(m|\theta)\ dm\ \approx\ f_{\mathrm{GC}} \sum_{i=1}^{I} P(\mathrm{obs}|m_i) P_{\mathrm{GC}}(m_i|\theta) \frac{m_2 - m_1}{I} \tag{3.24}$$

where we choose I to be large enough that we get a precise answer. An essentially identical functional form exists for the normalization of the contaminant distribution function.

Plugging these equations in to our full posterior, we get:

$$\begin{aligned}
P(\theta|\mathbf{Y},\mathrm{obs}) &\propto \frac{P(\mathbf{Y}|\theta)\ P(\mathrm{obs}|\mathbf{Y})P(\theta)}{P(\mathrm{obs}|\theta)} \\
&\propto P(\mathbf{Y}|\theta)\ P(\mathrm{obs}|\mathbf{Y})P(\theta)\ \times \\
&\Big[\Phi(m_2|\theta)\ +\ (m_1 - m_2)\ + \\
f_{\mathrm{GC}} \sum_{i=1}^{I} P(\mathrm{obs}|m_i) P_{\mathrm{GC}}(m_i|\theta)\big(\frac{m_2 - m_1}{I}\big)\ &+ \\
(1 - f_{\mathrm{GC}})\ \sum_{i=1}^{I} P(\mathrm{obs}|m_i) P_{\mathrm{CON}}(m_i)\big(\frac{m_2 - m_1}{I}\big)\Big]^{-1}&,
\end{aligned} \tag{3.25}$$

where $\Phi(m|\theta)$ is the CDF of a normal distribution with parameters θ.

We now have a formula for our posterior, incorporating incompleteness of the data. Given our likelihood function $P(\mathbf{Y}|\theta)$, our completeness function $P(\mathrm{jobs}|m)$, and our specified priors $P(\theta)$, we may use our standard MCMC algorithm to draw samples from our posterior. As before, note that formulas which don't depend on θ, i.e. $P_{\mathrm{CON}}(m_i)$ and $P(\mathrm{j},\mathrm{obs}|m)$, need not be evaluated in each step of the MCMC chain. They may be calculated before beginning the MCMC chain, making every step of the chain more efficient.

3.4.3 Correcting for Incompleteness in Mock Datasets

In this section, we demonstrate that our corrections for incompleteness accurately recover our input parameters. Furthermore, we illustrate the drastic effect that incompleteness that is not accounted for can have on inference.

In this section, we consider a mock dataset shown in Fig. 3.12. These data

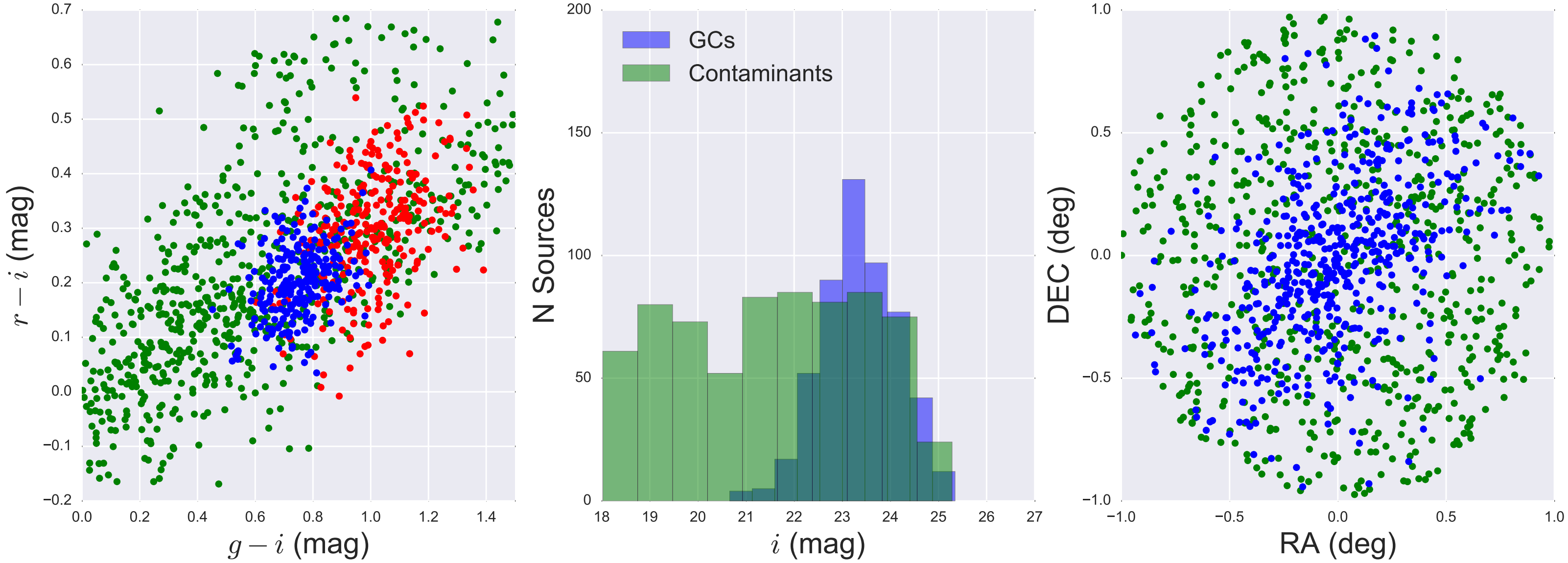

Figure 3.12: Incomplete data catalog considered in §3.4.3. The data are generated from identical distributions to those considered in §3.3.5, with the exception of the GC luminosity, which was generated from a normal with $\mu_i = 24$ mag. The data were then made incomplete following a completeness curve measured for i-band data in our M87 imaging.

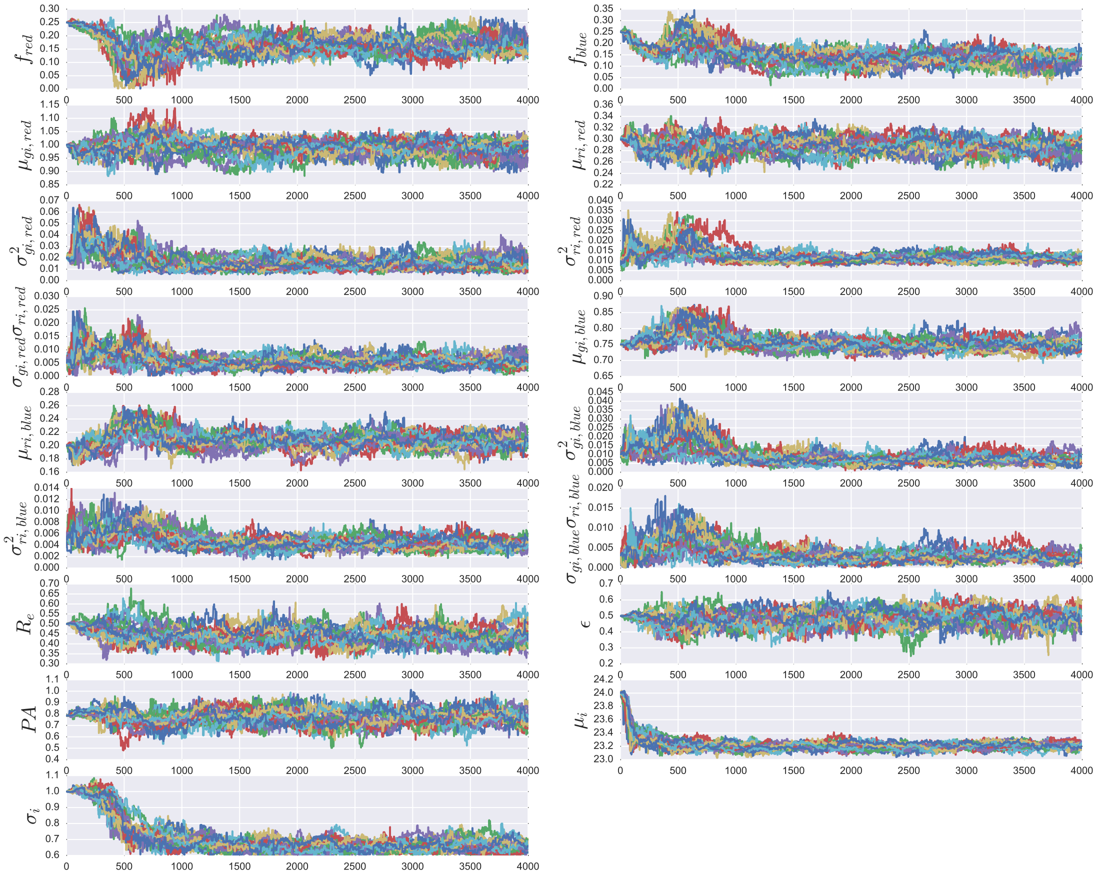

Figure 3.13: Trace plots for 4000 steps for inference applied to our incomplete dataset, ignoring corrections for incompleteness in our model. As we typically do, we only plot 30 walkers for illustrative purposes. While all walkers were initialized around the truth values for this dataset, for several parameters they quickly walked off these truths into different values. The difference is especially obvious for the μ_i, σ_i, f_{blue}, and f_{red} parameters. The walkers appear reasonably well-mixed around these parameter distributions, indicating that the differences are due to the fact that the model has been misspecified, rather than computational difficulties.

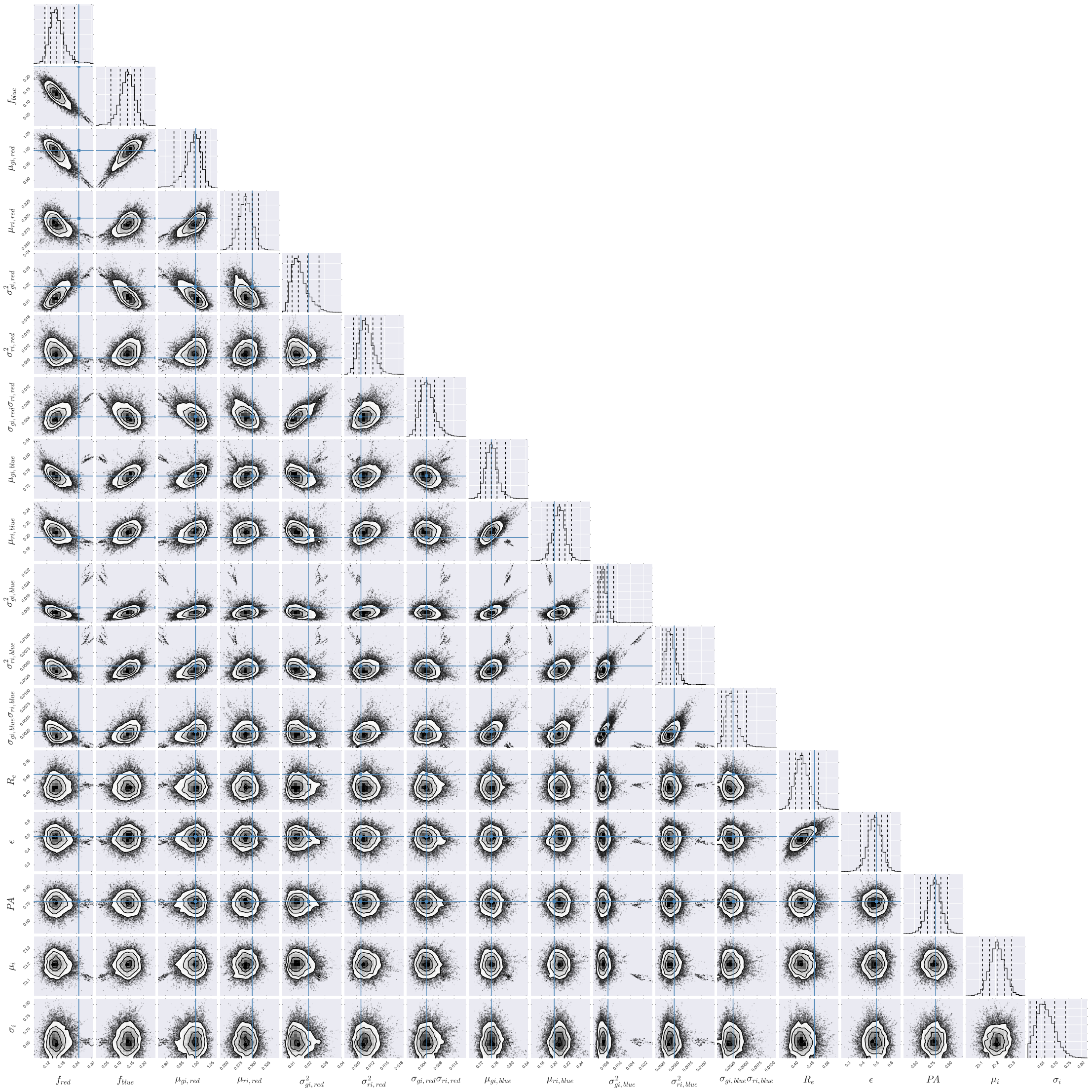

Figure 3.14: Corner plots for the traces in Fig. 3.13. We discard the first 2000 steps of each walker as burn in, leaving around 2 million total samples for each distribution. Truth values are plotted with blue lines; however, several parameters are so far away from their truth values that the blue lines are not visible.

originally consisted of 500 blue GCs, 500 red GCs, and 1000 contaminant sources. The sources were drawn from distributions identical to those considered in §3.3.5, except for the GC luminosity, which was drawn from a normal with $\mu_i = 24$ mag. We also limited our distributions to be brighter than $i = 25.5$, after which point our contaminant i-band magnitude distribution is no longer well-defined. The fainter mean was selected to make the effects of incompleteness more extreme, and would be a reasonable magnitude for the GC distributions from the most distant galaxies in our sample. After generation, the data were then made incomplete using M87's measured completeness function (see Ch. 4). We made the data incomplete by conducting 2000 Bernoulli trials in which the probability of success, p, was given by the value of the completeness function at the i-band magnitude of this source. For this particular dataset, 256 blue, 271 red, and 699 contaminant sources survived incompleteness.

After generating these data, we fit our full model to this distribution twice. For one inference, we ignored corrections for incompleteness in our model. For the second, we included these corrections. 100 walkers were initialized around the true values for each parameter, and the sampler was then run for 4000 steps in each case. For our corner and posterior distribution plots, we discarded the first 2000 steps of each walker as burn in.

In Fig. 3.13, we plot trace plots for our inference ignoring incompleteness of the data. Despite being initialized at true values, walkers quickly moved off of these to other parameter values that more correctly fit the incomplete data. The luminosity parameters μ_i and σ_i are both clearly off. However, other parameters such as the f_{blue}

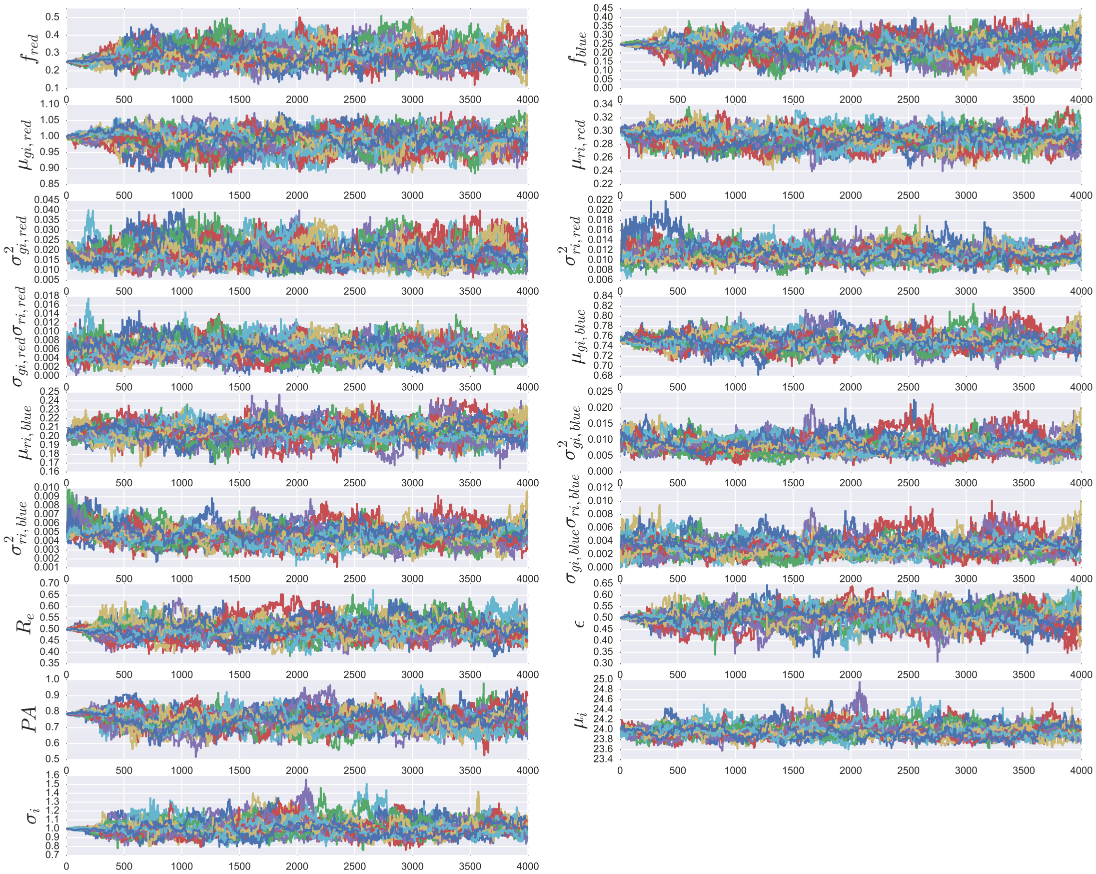

Figure 3.15: Trace plots for 4000 steps for inference applied to our incomplete dataset, ignoring corrections for incompleteness in our model. As we typically do, we only plot 30 walkers for illustrative purposes. While all walkers were initialized around the truth values for this dataset, for several parameters they quickly walked off these truths into different values. The difference is especially obvious for the μ_i, σ_i, f_{blue}, and f_{red} parameters. The walkers appear reasonably well-mixed around these parameter distributions, indicating that the differences are due to the fact that the model has been misspecified, rather than computational difficulties.

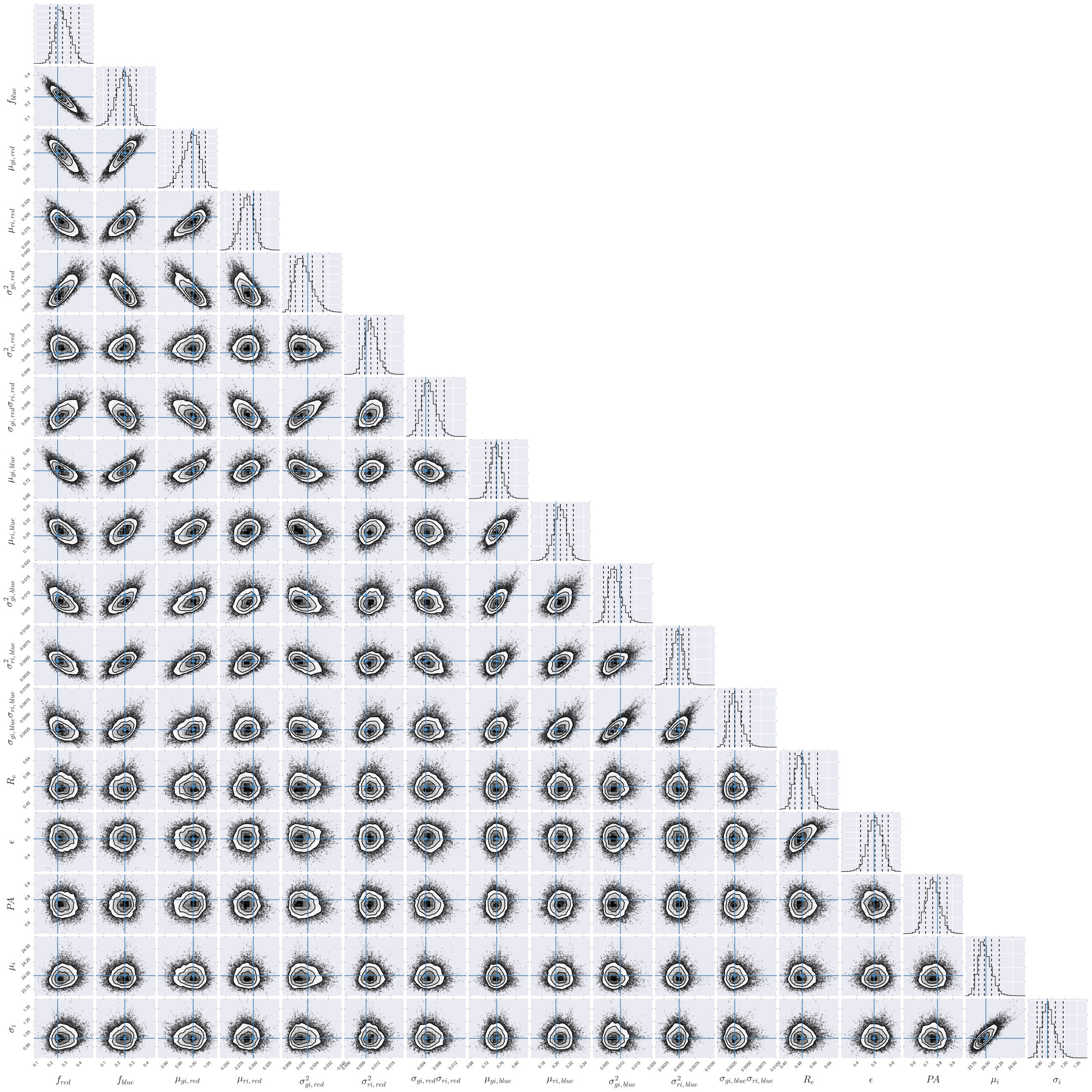

Figure 3.16: Corner plots for the traces in Fig. 3.15. We discard the first 2000 steps of each walker as burn in, leaving around 2 million total samples for each distribution. Truth values are plotted with blue lines. Posterior distributions are now all located near their truth values.

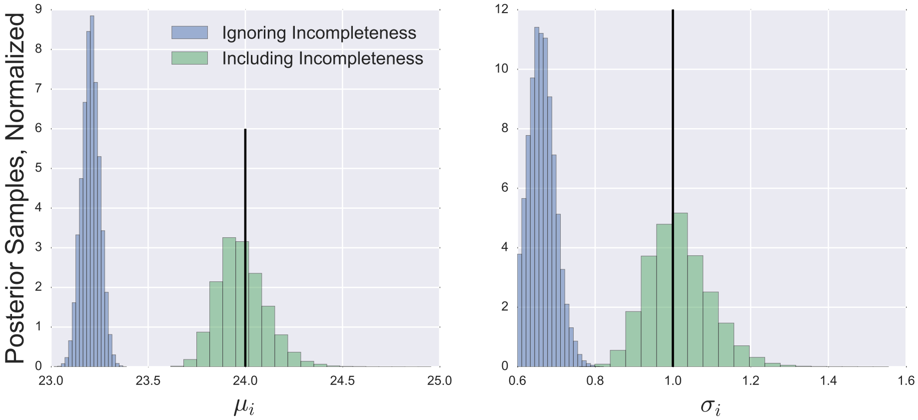

Figure 3.17: Histogram comparing inferred values for μ_i and σ_i for the mock dataset considered in §3.3.5. The blue histograms correspond to inferences when incompleteness is ignored, while the green histograms correspond to inferences for which the incompleteness is corrected for. Ignoring corrections for the incompleteness clearly leads to significant bias in the final results.

and f_{red} parameters also have clearly moved off from their true values. Inference about all parameters is affected by fitting what is ultimately an incorrect model. The point can be seen more clearly in the corner plots, which we show in Fig. 3.14. Truth values are plotted with blue lines; however, some parameters have walked so far off that they are no longer visible on the plot. The covariance matrix distributions are fairly consistent with truth values, and the means of both the color distributions also appear to recover values reasonable given the inputs.

Fig. 3.15 is the same as Fig. 3.13, but now for our model incorporating incompleteness. Walkers now appear to stay fairly close to their truth values, indicating that our incompleteness corrections perform inference on the missing data well. Fig. 3.16 is the corner plot for the traces show in Fig. 3.15. Values now correctly stay in their truth regions, and inferences on all parameters are reasonable.

Figure 3.18: Histogram comparing inferred values of f_{Red}, f_{Blue}, and N_{GC} for the mock dataset considered in §3.3.5. The blue histograms correspond to inferences when incompleteness is ignored, while the green histograms correspond to inferences for which the incompleteness is corrected for. Similar biases to the luminosity are observed here: when incompleteness is ignored, fewer GCs are found than are expected.

Figs. 3.17 and 3.18 display posterior histograms for the GC population fraction free parameters and the luminosity distribution free parameters, respectively. For these free parameters, when incompleteness is not considered, the inferred distributions are extremely far off. Clearly not accounting for incompleteness in the data when performing inference that depends on the luminosity will produce biased posterior distributions. While this behavior is trivially expected for the luminosity histogram (one will naturally infer biased values for a normal distribution if the distribution is severely truncated at one end), it is perhaps worth emphasizing that even estimates for the number of GCs in the system might be severely estimated if incompleteness is not considered in the selection and modeling of GC systems.

Note that the magnitude of this bias will, in general, be dependent on the values chosen to create our initial mock data catalog. We intentionally selected a value for the mean of the *i*-band magnitude distribution very close to the turnover magnitude for standard GC systems, making the bias very large in our mock dataset. Real-world galaxies may have more or less bias, depending on the depth of the data and the distance of the galaxy under consideration.

3.4.4 Interpretation of f_{Blue}, f_{Red}, and N_{GC} in the Context of Incompleteness

As is evident from the fits to mock data, the values for f_{Blue} and f_{Red} in the completeness-corrected inference don't correspond only to the data observed, but to the original distributions from which the data were drawn. There is subtlety here when applying these inferences in the context of what is observed in data.

Values inferred for f_{Blue} and f_{Red} correspond to distributions that have been completeness-corrected down to the limits of our incompleteness function. For most of our analysis, this corresponds to a fiducial limit of. 24.5, the limit down to which our foreground distributions are defined.

Converting from values of f_{GC}, f_{Blue}, and f_{Red} to actual values of N_{GC}, N_{Blue}, and N_{Red} requires extrapolating the total number of sources according to the incompleteness of the data. This value is essentially given by the $P(obs|\theta)$ term in Eqn. 20. This quantity must be calculated the same as any other random variable in the problem. We can use our chain for θ to calculate the normalization chain. We then divide the number of actual sources, N_{Obs}, by the chain of this normalization term to get a posterior distribution for the total number of sources, N_{Total}. To emphasize, since the total number of sources a quantity affected by incompleteness, and the degree of incompleteness is dependent in free parameters on the model, we must treat the N_{Total} number of sources in the system as another random variable, rather than a fixed quantity. After the PDF of the total number of sources has been determined, it is straightforward to get PDFs for $N_{\rm GC}$, $N_{\rm Blue}$, and $N_{\rm Red}$ by just multiplying the $N_{\rm Total}$ chain by the chains of $f_{\rm GC}$, $f_{\rm Blue}$, and $f_{\rm Red}$.

3.4.5 Extension to Multi-band Datasets

An important caveat to the above formulation is that it underestimates the true extent of sources lost to incompleteness due to the requirement that objects be detected in all three filters. Objects at the tail end of the luminosity distribution must pass completeness thresholds for detection in all three filters of our multi-band dataset.

Furthermore, there will be subtle effects on the color distribution due to this multi-band incompleteness. As an example, for two sources of equivalent i-band luminosity but different $g-i$ colors, the source that is redder (i.e. fainter g-band magnitude) will, in general, be more difficult to detect. As such, it should be weighted more in the model. Correcting for incompleteness on the color distributions must be done by marginalizing over completeness corrections for a given color.

One approach to this problem is to compute chance of incompleteness conditional on a specified color. In other words, we can calculate the chance of a source of a given color being undetected by fixing the color and integrating over our full range of magnitudes for our incompleteness functions for both bands, with the bands offset by the amount given by the color. This marginalized completeness can be calculated over the full 2D grid specified in our color-color region of interest.

The problem is fully tractable given specified boundaries of the color-color space, and an appropriate magnitude range in all three filters. However, this problem comes at the expense of significant computational overhead. Furthermore, we found inferences on mock data became more unstable when this grid approach was implemented. As above, for the GC distributions, the $P(\text{obs}|\theta)$ must be calculated at each step in the model over the entire color-color distribution, and we found that this normalization was dependent on the grid resolution, especially for very narrow covariance distributions. Grids that can produce sufficiently accurate normalizations for small distributions became intractably slow and large. Given these difficulties, we ultimately decided to neglect color-dependent incompleteness in our model. It is possible different ways of gridding, or perhaps some sort of adaptive grid model, could produce more stable fits. However, such investigation is beyond the scope of this work.

In practice, neglecting this incompleteness is not nearly as big a factor as it might appear initially. Throughout our model, we are always treating our GC distributions as excess density on top of our measured color-color distribution. We generate our contaminant KDE using an identical procedure to our GC photometry, and therefore any color-dependent incompleteness is also present in the contaminant distribution. Color-dependent incompleteness would only have a major effect on our inferences if the *relative* incompleteness of the different bands was significantly different from our science fields of interest.

3.5 DISCUSSION AND SUMMARY

In this section, we discuss our model and its application to fake data, and consider what we have learned about the modeling of GC systems. We also consider important assumptions made in the model and how restrictive these assumptions are to the modeling process. Finally, we examine ways in which the model could potentially be expanded in the future.

3.5.1 Noteworthy Assumptions Made in the Modeling Process

A beneficial side-effect of Bayesian modeling is that one must be quite specific about how one approaches their science task. Assumptions and approximations are explicitly shown in the modeling formalism. In our methodology, we have noted where we have made specific assumptions in the modeling. Here briefly summarize what we believe are the key assumptions in our model. We note these not to minimize their importance, but rather to note that our inferences (as in any study) are conditional on our modeling choices and assumptions made. We also wish to to highlight areas where our modeling procedure could be improved, as a guide for future work.

1.) **Assumption of constant contaminant spatial distributions.** In all our analysis, we treat the contaminant distributions as simply being uniformly distributed across the entire space under consideration in our model. In most cases, we believe this assumption to be well-justified. For foreground stars especially, we don't expect extremely strong over-densities of stars on scales as small as those in our image. There is definitely the potential for background galaxy clusters to have over-densities on the scales of our imaging; however, in general background galaxies will be fairly well-rejected during point source selection, and indeed the bulk of the background galaxy population will be around or below the completeness limit for most of our galaxies (e.g. Jordán et al. 2009). Nevertheless, there are situations where we know background galaxy clusters may exist; M87, for example, is known to have a background galaxy cluster (Huchra & Brodie, 1984).

Moreover, any such over-densities wouldn't bias our inference greatly, with the potential exception of the spatial parameters. It is certainly possible that a spatially correlated group of contaminant sources with colors and sizes comparable to GCs can lead to a more extended inferred R_e, or an inflated ellipticity/biased PA. However, it is questionable whether the magnitude of such an effect will be comparable to changes in detection threshold across the image due to the presence of bright stars, other galaxies, scattered light, and other miscellaneous artifacts. Overall, we believe our assumption uniform contaminant spatial density is unlikely to have a major effect on our inference.

2.) **Assumption of Identical Color and Luminosity Distributions Across Fields** Unlike our previous assumption, the assumption of identical color and luminosity distributions is almost wrong, with the potential to have a fairly significant effect on our final inference. As we noted above, the actual *level* of contamination is a free parameter in the model. However, if there are significant differences in the relative density of the contaminants in color-color space, our inference could be biased. For example, if a particular pointing had an overabundance of red stars with $g - i \sim 1.3$ relative to the number of to main sequence stars when compared to our contaminant populations, we would expect to infer an overabundance of red GCs instead (and a red GC distribution more expanded in color).

Perhaps giving more weight to this concern, the NGVS background fields are located near (and in some cases directly on) the Sagittarius stream (Lokhorst et al., 2016). The presence of this stream could both increase the relative amount of total contamination, as well as contribute a coherent stellar population to our contaminant fields. In general, most of the Sagittarius stellar population seems to not overlap significantly with GC parameter space in a color-color plot. Again, however, the concern is the relative number of stars with $g - i > 1.2$ compared with the main sequence population.

Training additional contaminant populations, perhaps at different galactic latitudes, would allow us to assess the effects of varying contaminant stellar populations on the inferences drawn from our modeling. However, at this point we would no longer be comparing like-to-like in terms of relative inference on the number of GCs. The relative effect of this trade-off could be assessed in future work.

3. **Assumptions of various levels of normality in GC distributions.** This assumption, while being quite restrictive, is perhaps less interesting. Indeed, the vast majority of GC studies will typically model GC distributions using normal models. We actually expand our models greatly by even allowing for multivariate normal distributions in color-color space, a step most GC studies don't take. Assumption of normality is, in general, a good default, as normal models tend to be well-behaved and make an assumption of maximum entropy (Hogg et al., 2010).

However, to assume normality is still to make a strong assumption about the strength of tails in the GC distributions, and a strong assumption about the symmetry of the two models under consideration. Furthermore, there is not necessarily a link between the parameters of normal models and direct physical interpretation. The actual physical processes that go in to creating GC systems are assured to be extremely complex. While there is no real statistical problem with assuming normality in the absence of a realistic alternative distribution, it is assuredly incorrect at some level.

3.5.2 Potential Expansion of the Model

In this section, we consider straightforward ways the model could be expanded to both better fit and to glean more information about GC systems.

1.) **Incorporation of bimodality in the GC system spatial distributions**. In general, it is fairly well-established that the blue GC population tends to be more spatially extended then the red GC population. The usual interpretation of this is that the red GC population tracks bulge light, while the blue GC population more tracks the galaxy halo. The blue GCs are typically more spherical as well, where the ellipticity can be reliably measured.

We neglected GC spatial bimodality in our model simply out of a desire for a simpler model. However, the mixture model is straightforward to expand. We simply move the spatial distribution to being within the same mixture as the color distribution, and expand the number of free parameters. As usual, we would wish to confirm that we can recover differences in the distributions that are similar to those observed in real data, and differences in the scale radii of the GC systems are often quite small (Strader et al., 2011).

2.) **Easing assumptions about normality**. Another potential avenue for expansion of the model is to move beyond the assumed normality of the dataset. This model expansion could be as simple as considering, for example, multivariate t distributions instead of multivariate normals. Furthermore, if a parametric model for GC distributions is proposed that maps a physically motivated quantity into photometric colors, it is straightforward to fit this more physical model instead and bypass the necessity of assuming a specific distribution in color.

An even more speculative avenue for expansion might be to eschew the necessity of specifying any parametric distribution at all. Non-parametric Bayesian methods could be applied to model the GC color distribution. These methods allow for the distribution chosen for the GCs to be arbitrarily complex in color-color space while still treating it probabilistically. A non-parametric Bayesian model would allow for the use of a fixed contaminant mixture model with an arbitrarily shaped GC distribution on top of it.

3.5.3 Summary of Results Inferred from Mock Dataset Analysis

Finally, in this section, we summarize some key takeaways from our analysis of mock datasets, as well as their implications for further studies of GC systems.

First, the first general takeaway is that mixture modeling can be effective at selecting GC systems and inferring the free parameters. Furthermore, the modeling can be performed with no assumptions about any sort of functional form for the contaminant populations and without assuming any specific location in GC space. Levels of contamination in GC systems may be directly modeled, and other methods of estimating contaminant level (such as fitting binned spatial distributions with contaminant offsets) can be avoided with direct modeling.

Second, there is often more information available in the inference than can be gleaned through simple box-cuts in various parameter spaces. For example, the large negative covariance between red and blue GCs indicates that the total number of GCs maybe known to a much greater precision than the fractional population of either. Similar covariances exist for many other parameters in the system.

Third, we noted that correct normalization of the GC PDFs is vital for correct inference on the parameters and relative strength of the GC and contaminant distributions. One must take into account that one is performing inference on distributions that are usually truncated to some fixed values; these normalization factors are, in many cases, non-negligible, and often will depend on the free parameters which are being fit in the model. Existing GC mixture modeling codes do not take this truncation into account.

Fourth, completeness ends up having a significant effect in various inferences in the problem. It is likely not surprising that completeness corrections will affect the inferred GC luminosity distributions, but they can also have a very large effect on the total number of GCs in the system. Performing accurate inference on the relative number of GCs to contaminants must take these corrections into account.

All these conclusions lend credence to adopting fully-probabilistic mixture-model approaches to GC system selection and inference. We have demonstrated that one can correctly recover GC systems and obtain good estimates for the posterior distributions of the parameters that went in to creating these distributions, all while correctly accounting for selection effects in the GC datasets.

Other ways of approaching the problem of GC system analysis all revolve around a series of sequential selection rules to obtain a sample for analysis before performing inference. Such approaches essentially never fully model the selection procedures that go into creating their catalogs, and therefore are not able to obtain calibrated probabilistic estimates for the free parameters in a GC system. Any approaches to doing so will involve approximations which at best will fail to correctly estimate uncertainties, and at worse will lead to significant bias. Probabilistic modeling instead offers estimates of these uncertainties that, while not devoid of assumptions, are at least explicit about these assumptions and will create well-calibrated estimates of the parameter distributions of interest.

Chapter 4

Bayesian Analysis of the GC Systems of SLUGGS Survey Galaxies

4.1 INTRODUCTION

The SLUGGS Survey is a combination photometric-spectroscopic survey of the globular cluster systems of 25 nearby early-type galaxies (Brodie et al., 2014). A key feature of the survey is the complimentary nature of wide-field photometry and multi-object spectroscopic follow-up. Data acquisition has been continuous since 2008, when the first wide-field images were taken using the SuprimeCam instrument on the Subaru telescope.

Many previous SLUGGS survey papers have published photometric analysis of a wide range of galaxies. However, the datasets published in previous works have not necessarily been undertaken with photometric methods and analysis techniques consistent across studies. Previous work has often featured methods tailored to specific galaxies of interest, and has stitched together data from a wide range of sources including wide-field imaging, available archival *HST* data, and potentially any spectroscopic follow-up.

In this study, we instead focus on a few specific goals:

First, we use consistent photometric methods across all galaxies in the sample. These consistent methods should reduce any galaxy-to-galaxy variation introduced by modifications to methods for particular galaxies or studies.

Second, we only consider wide-field imaging of our galaxies of interest. Many galaxies feature at least one pointing of *HST* imaging, with some featuring large *HST* mosaics (e.g. Usher et al. 2012; Blom et al. 2012b; Pota et al. 2013b; Jennings et al. 2014; Kartha et al. 2014). In addition, the SLUGGS galaxies now have several thousand spectroscopically confirmed GCs (Pota et al., 2013b; Forbes et al., 2017b). However, while these additional observations are powerful, they are fundamentally biased. *HST* data only probe the central parts of galaxies. Spectroscopic data are even more biased, since one can only get spectra of the brightest GCs in a system. Furthermore, in order to place spectroscopic candidates on a DEIMOS slit mask, one necessarily must already perform a photometric selection, introducing additional bias.

This leads into our third goal in this study: apply Bayesian mixture modeling to the photometry of these GC distributions and their contaminants. Approaching the problem from the perspective of modeling allows us to go beyond simple target selection and actually directly perform inference on the parameters of interest in our GC systems. Modeling these galaxies using heterogeneous datasets adds another layer of complexity, and makes the problem much less tractable. For this reason, we only consider homogeneous datasets consisting of wide-field, ground-based photometry. While modeling can in principle account for *HST* or spectroscopic data sets, incorporating such data into a Bayesian model requires a very thorough and quantitative understanding of the selection effects which go into creating these datasets.

Throughout this paper, we use Forbes et al. (2017a) for general information about our galaxies of interest. Unless otherwise noted, stellar mass measurements, effective radii, distances, and galaxy morphological classifications come from Table 1 of Forbes et al. (2017a). For convenience, we reproduce the table in Tables 4.1 and 4.2.

4.1.1 Data Acquisition and Selection

In this work, we consider wide-field photometry of several galaxies in the SLUGGS survey. Data for these galaxies comes from one of two instruments: the MEGACAM square-degree camera located on the Canada-France-Hawaii Telescope (CFHT), and the SuprimeCam wide-field camera on the Subaru telescope, with a 27x34 arcmin field of view. For all galaxies in our survey, we searched both the CFHT[11] and Subaru SMOKA archives[12] for deep imaging for our galaxies of interest. All MEGACAM imaging was downloaded as stacked MEGAPIPE images from the CFHT archives

---

[11] http://www.cadc-ccda.hia-iha.nrc-cnrc.gc.ca/en/megapipe/

[12] http://smoka.nao.ac.jp/

Table 4.1: SLUGGS galaxy sample and properties, reproduced entirely from Forbes et al. (2017a)

Galaxy [NGC] (1)	Type (2)	Core (3)	Dist. [Mpc] (4)	Age [Gyr] (5)	$m_{3.6}$ [mag] (6)	log M_* [$M_\odot$] (7)	R_e [arcsec] (8)	μ_e [mag/arcsec^2] (9)	n (10)
720	E5	1	26.9	7.8	6.92	11.27	29.1	17.54	3.8
821	E6	3	23.4	12.9	7.57	11.00	43.2	19.03	6.0
1023	S0	3	11.1	13.5	6.01	10.99	48.0	17.61	4.2
1400	E1/S0	1	26.8	13.8	7.44	11.08	25.6	17.87	5.0
1407	E0	1	26.8	12.0	6.16	11.60	93.4	19.19	4.9
2768	E6/S0	2	21.8	13.3	6.68	11.21	60.3	18.70	3.8
2974	E4/S0	3	20.9	11.8	7.47	10.93	30.2	17.99	4.3
3115	S0	3	9.4	9.0	5.58	10.93	36.5	16.75	4.7
3377	E5-6	3	10.9	11.3	7.09	10.50	45.4	18.81	5.9
3607†	S0	1	22.2	13.5	6.51	11.39	48.2	18.33	5.3
3608	E1-2	1	22.3	13.0	7.41	11.03	42.9	19.00	5.3
4111	S0	–	14.6	6.0	7.24	10.52	10.1	15.71	3.0
4278	E1-2	1	15.6	13.7	6.84	10.95	28.3	17.51	6.2
4365	E3	1	23.1	13.4	6.31	11.51	77.8	18.96	4.9
4374	E1	1	18.5	13.7	5.81	11.51	139.0	19.71	8.0

Notes: columns are (1) galaxy name, † = bonus galaxy, (2) Hubble type, (3) 1= core, 2 = intermediate, 3 = cusp central light profile, (4) distance from B14 (typical uncertainty is ±0.05 dex), (5) mean stellar age from McDermid et al. (2015), see text for exceptions), (6) 3.6 micron apparent magnitude in the Vega system (typical uncertainty is ±0.05), (7) stellar mass (typical uncertainty is ±0.1 dex), (8) effective radius (typical uncertainty is +0.18 and –0.13 dex), (9) μ_e (typical uncertainty is +0.52 and –1.11 mag.), (10) Sersic n (typical uncertainty is +0.13 and –0.11 dex). Spitzer 3.6μm imaging is not available for NGC 4474: M_* and R_e are from 2MASS 2.2μm imaging. This table is reproduced in its entirety from Forbes et al. (2017a), for convenient reference. Unless otherwise noted, we take all galaxy values for stellar mass, effective radius, morphology, and distance from this table.

Table 4.2: SLUGGS galaxy sample and properties, reproduced entirely from Forbes et al. (2017a), continued.

Galaxy [NGC] (1)	Type (2)	Core (3)	Dist. [Mpc] (4)	Age [Gyr] (5)	$m_{3.6}$ [mag] (6)	log M_* [$M_\odot$] (7)	R_e [arcsec] (8)	μ_e [mag/arcsec^2] (9)	n (10)
4374	E1	1	18.5	13.7	5.81	11.51	139.0	19.71	8.0
4459	S0	3	16.0	11.9	6.76	10.98	48.3	18.52	5.4
4473	E5	1	15.2	13.0	6.74	10.96	30.2	17.67	5.0
4474	S0	3	15.5	11.1	–	10.23	17.0	–	–
4486	E0/cD	1	16.7	12.7	5.30	11.62	86.6	18.24	5.1
4494	E1-2	3	16.6	11.0	6.68	11.02	52.5	18.53	4.5
4526	S0	–	16.4	13.6	6.17	11.26	32.4	17.05	3.6
4564	E6	3	15.9	13.3	7.78	10.58	14.8	16.93	3.2
4594†	Sa	1	9.5	12.5	4.56	11.41	72.0	17.06	3.2
4649	E2/S0	1	16.5	13.2	5.33	11.60	79.2	18.06	4.6
4697	E6	3	12.5	13.4	5.85	11.15	95.8	19.08	5.3
5846	E0-1/S0	1	24.2	12.7	6.50	11.46	89.8	19.38	5.2
5866†	S0	–	14.9	5.9	6.50	10.83	23.4	16.59	2.8
7457	S0	3	12.9	6.1	7.94	10.13	34.1	18.67	2.6

Notes: columns are (1) galaxy name, † = bonus galaxy, (2) Hubble type, (3) 1= core, 2 = intermediate, 3 = cusp central light profile, (4) distance from B14 (typical uncertainty is ±0.05 dex), (5) mean stellar age from McDermid et al. (2015), see text for exceptions), (6) 3.6 micron apparent magnitude in the Vega system (typical uncertainty is ±0.05), (7) stellar mass (typical uncertainty is ±0.1 dex), (8) effective radius (typical uncertainty is +0.18 and –0.13 dex), (9) μ_e (typical uncertainty is +0.52 and –1.11 mag.), (10) Sersic n (typical uncertainty is +0.13 and –0.11 dex). Spitzer 3.6μm imaging is not available for NGC 4474: M_* and R_e are from 2MASS 2.2μm imaging. This table is reproduced in its entirety from Forbes et al. (2017a), for convenient reference. Unless otherwise noted, we take all galaxy values for stellar mass, effective radius, morphology, and distance from this table.

(Gwyn, 2008), while all Subaru imaging was reduced using standard methods (see the next section for details).

Generally speaking, for most of the SLUGGS galaxies located in the Virgo cluster, the deepest imaging was from the NGVS Survey (Ferrarese et al., 2012), while most other galaxies had imaging taken directly by the SLUGGS survey over the years. This was mostly intentional, as doubling up on galaxies with imaging from different telescopes isn't explicitly useful if there is no reason to do so. However, there are situations in which galaxies were imaged with multiple telescopes. In these situations, we take the deepest data acquired for those galaxies.

We list the pointings analyzed in this work in Table 4.3.

4.1.2 Subaru/SuprimeCam Reduction

We performed reduction using modified versions of the standard SDFRED pipelines[13]. SuprimeCam underwent a CCD upgrade in mid 2008, offering a large improvement in quantum efficiency over the previous chips. Pre- and post-upgrade data require different versions of the pipeline.

In general, we use the usual tasks from the SDFRED reduction process. However, the default astrometry solutions from the SuprimeCam imaging are frequently poor. Instead, we use our own custom process to calibrate the astrometry of our images, which we describe in 4.1.3. Final image stacking was performed using the Montage software package [14].

---

[13] https://www.naoj.org/Observing/Instruments/SCam/sdfred/sdfred2.html.en

[14] http://montage.ipac.caltech.edu/

Table 4.3: Imaging Analyzed in Chapter 4

Galaxy (NGC)	Filter	Target Name (if ambiguous)	Obs. date	Telescope	Exp. time (s)
1400/1407	g		2006 Sep. 22	Subaru	14640
	r		2006 Sep. 22		6240
	i		2006 Sep. 22		5600
2768	g		2011 Jan. 03	Subaru	4320
	r		2011 Jan. 04		1860
	i		2011 Jan. 04		1296
3115	g		2008 Apr. 02	Subaru	200
	r		2008 Apr. 02		75
	i		2008 Apr. 02		75
3607/3608	g		2011 Jan. 04	Subaru	1200
	r		2011 Jan. 04		1560
	i		2011 Jan. 04		1200
4111	g		2010 Apr. 12	Subaru	994
	r		2010 Apr. 12		295
	i		2009 Apr. 21		425
4278	g		2009 Mar. 27	CFHT	588
	r		2011 Jan. 04	Subaru	450
	i		2009 Mar. 27	CFHT	476
4365	g	NGVS-2-5	2009 Mar. 23	CFHT	3170
	r	NGVS-2-5	2009 Feb. 22		2061
	i	NGVS-2-5	2009 Feb. 22		2055
4486	g	G003.187.706+12.391	2004 Mar. 21	CFHT	3840
	r	G003.187.706+12.391	2004 Mar. 21		3300
	i	G003.187.706+12.391	2004 Mar. 19		3300
4459	g	NGVS-1+2	2009 June 26	CFHT	3170
	r	NGVS-1+2	2009 June 26		4374
	i	NGVS-1+2	2009 June 26		2055
4494	g		2010 Apr. 12	Subaru	1014
	r		2010 Apr. 12		355
	i		2010 Apr. 12		540
4697	g		2010 Apr. 12	Subaru	300
	r		2010 Apr. 12		300
	i		2010 Apr. 12		300

4.1.3 Bayesian Astrometric Calculation

If our pointings overlap with the SDSS field of view, then we cross-reference with SDSS stars for astrometric calibration. Otherwise we cross-reference with the USNO-B catalog. We first define a rough astrometric solution by hand for each exposure's full mosaic. We match six sources across the full mosaic and calculate rough offsets. After a rough solution has been defined, we create a fine calibration on a chip-by-chip basis. Using SExtractor, we create a quick photometric catalog for each chip and cross-reference this catalog with the reference catalogs. We then use a Bayesian procedure to sample posterior distributions for the astrometric parameters of our images. Point estimates derived from the medians of these posterior distributions then represent the astrometric solution of our images.

For the Bayesian problem, we are interested in defining five free parameters: X and Y offsets (the CRPIX WCS parameters), a rotation angle for the chip, and delta parameters defining the arcseconds per pixel (the CDELT WCS parameters). We neglect the final WCS parameter as we found we could easily attain sufficient astrometry for image stacking without it.

To map from these free parameters into actual data, we use the `astropy` WCS package. We plug the free parameters into a new astrometric solution. We then pass the image coordinates of the sources on our chip through the solution to get new WCS values. Finally, we calculate the difference between the WCS source location given by the parameter values and the referenced source location from the catalog. We assume this differences are normally distributed with a mean of zero. This normal distribution thus serves as our likelihood function, linking the unknown WCS parameters of the image to the measured data on the chip.

There is motivation to consider the ΔX and ΔY distributions jointly as a multivariate normal, with a mean vector of zero and a covariance matrix describing the approximate scatter of the relation. However, we found we attained excellent astrometric solutions by considering the ΔX and ΔY distributions as independent normals, which we ultimately used as our final model for simplicity.

One final complication regards the treatment of outliers in our distribution. The model we have laid out is essentially a squared-error loss function, wherein we penalize errors in source astrometry according to the square of the difference. However, such methods are prone to outliers. Instead, we write down the likelihood as a mixture model consisting of a narrow distribution and a wide outlier distribution. The outlier distribution allows for sources which are not well-matched between the photometry and the data to be naturally down-weighted in the fit.

To summarize, we use the following likelihood distribution for our data:

$$L(\Delta X, \Delta Y|\theta) = \tag{4.1}$$

$$f(N(\Delta X|\mu = 0, \sigma = 4) \times N(\Delta Y|\mu = 0, \sigma = 4) \tag{4.2}$$

$$+(f-1)(N(\Delta X|\mu = 0, \sigma = 10) \times N(\Delta Y|\mu = 0, \sigma = 10). \tag{4.3}$$

As with our photometric modeling, we use `emcee` to sample from our posterior distributions to determine our astrometric solutions. Our general procedure was to run our sampler for 600 steps with 100 walkers, then discard the first 400 steps for each walker as burn-in. We found that running the samplers in this manner was more than sufficient to produce accurate astrometric solutions for stacking our images.

4.2 FULL PHOTOMETRIC CATALOG PROCEDURES

One of the primary goals in this work is to perform consistent reduction and photometric procedures across all our scientific fields. In this section, we detail those procedures.

4.2.1 Galaxy Subtraction

Our goal in this work is the analysis of a galaxy's GC system. As such, we didn't attempt to perform reliable modeling of the galaxy light using tools like `galfit` (Peng et al., 2002). However, GCs are frequently located within the galaxy light. In ground-based imaging especially, this light can cover up a significant fraction of the GC population. As a result, at least some rudimentary galaxy subtraction is necessary to sample from the full GC population. We elected to use the simple iterative fitting procedures from `iraf.ellipse` to subtract of the galaxy light.

We used the `pyraf` version of `ellipse` to perform galaxy subtraction. Masking of bright sources is important to not throw off the fitting procedure. All obvious bright sources (usually bright foreground stars and dwarf/background galaxies) are masked out by hand in `ds9`, and these regions are then converted to a pixel mask using standard `iraf` tasks.

In general, `ellipse` fitting is fairly robust to choice of initial conditions, as long as they are reasonable. We estimate starting coordinates, ellipticity, and position angle just by eye on the image; all these quantities are then re-fit as ellipse runs. The maximum semi-major axis to be fit for is important; we estimate this value by identifying the approximate point at which the galaxy light reaches sky background, and check in the residuals that the fit is not being thrown off. We then make the maximum semi-major axis lager if the fits have not reached sky background levels, or make it smaller if the ellipse twists heavily or eats significantly into sky background levels. We set 20 pixels as the minimum fitting level; fits usually fail at semi-major axes below 50 pixels, but there are generally hardly any GCs located that close to the galaxy center, and they wouldn't be suitable to measure reliable photometry regardless.

We emphasize that these methods are not well-suited for actual analysis of the galaxy light, if that was our science goal. In order to perform actual analysis of the galaxy light, one should write down a model for the light and then use sampling methods to evaluate the posterior distributions of the parameters of this model; indeed, approaching modeling tasks in such a way is central to this work's approach to GC analysis. Our fitting methods fail at small radii, and don't provide properly-calibrated uncertainties at any semi-major axis radius. However, our only goal in galaxy subtraction is to remove most of the galaxy light to enable us to perform reliable photometry of the hidden sources, and these methods are sufficient for that.

4.2.2 Photometric Details

We make use of SExtractor (Bertin & Arnouts, 1996) to perform photometry. SExtractor offers a wide range of options for photometry, background estimation, and other parameters. Since accurate color measurements are very important for our work, we use simple aperture photometry for measurements, which we describe in more detail in the aperture correction section.

In general, our astronomical images are not completely flat. For one, reduction of SuprimeCam imaging is not perfect, and the degree to which this is true depends on the observing conditions. There are also varying degrees of background light throughout our images, caused by both residual galaxy light and other bright sources in our imaging. SExtractor creates an estimate of the background in the image using a sophisticated smoothing algorithm. We found that setting the background estimate size to 64 pixels achieved a smoothly varying background without subtracting off light actually from our point sources of interest. We used this background size, along with a filter width of 3, throughout our photometric procedure.

4.2.3 Aperture Correction

We use standard curve-of-growth measurements to calibrate aperture corrections. In general, for aperture photometry, one wants to measure photometry from within a small radius to maximize S/N, and then correct this value to a larger aperture to account for the light missed in the wings of the PSF. To calibrate these aperture corrections, we select the brightest, non-saturated stars in our imaging.

We perform an initial SExtractor run using a wide range of pixel diameters for apertures. First, we We make measurements at a wide range of pixels, typically 4, 5, 6, 8, 10, 12, 15, 25, 40, 50, 60, 70, 80, 90, and 100 pixels (although the precise values may be modified slightly). Using a plot of aperture difference vs. apparent magnitude, we identify bright, point-like, unsaturated objects. We make simple cuts in FWHM and magnitude to select suitable stars. We then make plot of SExtractor's magnitude error vs. pixel diameter to select our optimal S/N pixel. In almost all our images, this optimal aperture is either at 8 or 10 pixels, which typically corresponds to 2x the FWHM of our imaging, depending on seeing. Note that the Megacam and SuprimeCam imaging have slightly different pixel scales ($0.2^{\acute{\prime}}$ pix^{-}1 vs. $0.187^{\acute{\prime}}$ pix^{-}1). Since the aperture corrections are always measured on an image-by-image basis, the actual precise spatial scales of the measurement apertures are not hugely important. All photometry is self-consistent on its own image.

Since crowding is not an issue for our GC data, aperture photometry is an appropriate choice of method. PSF photometry would essentially accomplish the same task as the aperture correction step while incorporating additional complexity through the step of PSF fitting. We favor aperture photometry for consistency and simplicity, although in practice for this task we would expect both photometric methods to perform well.

4.2.4 Calibrating Zero-Points

Data from the MegaPipe data stacking pipeline comes pre-calibrated to a zero-point of 30 mags for all filters. Our SuprimeCam images are not calibrated, and while in photometric conditions zero-points won't be significantly different from image to image, they still need to be calibrated to achieve reasonable photometry.

We make use of the recent Pan-STARRS survey data to calibrate our zero-points (Chambers et al., 2016). Pan-STARRS is a survey conducted from a dedicated telescope at Haleakala on Maui in Hawaii, and therefore has nearly identical sky coverage to the Subaru and CFHT telescopes on Mauna Kea. The survey uses the standard SDSS u, g, r, i, z filters for its photometry and therefore overlaps completely with our imaging data. All of the SLUGGS survey galaxies feature PanSTARRS observations, and there is significant overlap between between the magnitude coverage ranges of our non-saturated Suburu/CFHT bright sources and well-measured Pan-STARRS sources, making the Pan-STARRS dataset ideal for calibration of our images.

Our procedure for calibration is straightforward. We query the PanSTARRS database on MAST for all sources within the field of view of our pointing on the galaxy. We require that the PanSTARRS source be detected in all three g, r, i filters. We then make cuts to select only point-like, bright stars for comparison. As suggested on the Pan-STARRS webpage, we make a cut for point sources by comparing the difference of their provided PSF magnitudes and their Kron magnitudes. Since the Kron magnitudes correspond to a specific aperture, for a point-like object, the Kron magnitudes are slightly fainter than PSF magnitudes. However, for extended sources have larger Kron apertures and therefore are brighter than in their PSF magnitudes. We also impose a brightness cut to only select well-measured sources; we found cutting at g and r at 21 mags and i at 20.5 mags to be effective cuts. We also found cutting at a aperture difference value of exactly 0.0 did an excellent job selecting out point-like sources.

In Fig. 4.1, we plot an illustration of these cuts applied to Pan-STARRS data around NGC 3115. Sources plotted in green passed these cuts in all three Pan-STARRS filters. We consider these stars appropriate to match to our SuprimeCam photometry.

We apply identical cuts to our SuprimeCam photometry that we did to calculate our aperture corrections. Finally, we match our cut SuprimeCam Photometry with our cut Pan-STARRS photometry and calculate the median offset to determine our zero-points. Typically there are around 25 matched sources across the images, and a scatter of ~ 0.05 mag is typical for the differences.

For consistency, we also re-calibrate zero-points for the downloaded MegaPipe data using the identical procedure to the above. In general, we find excellent agreement between the MegaPipe calibrations and our re-calibrated zero-points. Offsets are rarely larger than 0.02 mags, with scatter generally similar to the SuprimeCam photometry at ~ 0.05 mags. The consistency of our zero-point and the MegaPipe zero-point indicates that our aperture corrections and zero-points are well-calibrated and our photometric procedures are effective.

4.2.5 Final Catalog Matching and Completeness Corrections

Once zero-points are calibrated and aperture corrections are applied, assembling the final catalog is trivial. We cross-reference all three catalogs and require that sources be located within $0.5''$ of each other to be considered a match. A source is only included in the final catalog if it is detected in all three filters; given that all our modeling methodology is contingent on using all three filters, this requirement is necessary. We also apply foreground extinction corrections from Schlafly & Finkbeiner (2011), assuming a uniform foreground extinction across the entire field. While there may be slight variations in foreground extinction across the field, the variations are small compared to other uncertainties in the problem. We also require that the source

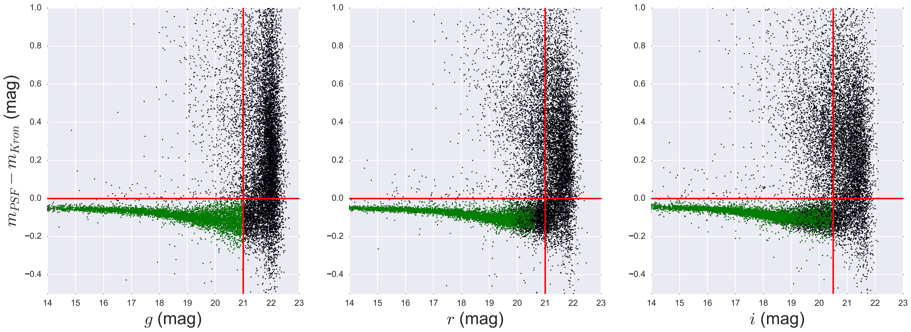

Figure 4.1: Pan-STARRS point-source selection. The horizontal axis is the Pan-STARRS PSF magnitudes, while the vertical axis is the difference between the PSF magnitude and the Kron magnitude. Since the Kron magnitude is measured over a fixed aperture, a point source's Kron magnitude will be slightly fainter than its PSF magnitude. However, the opposite is true for extended sources, which will have expanded profiles not captured by the PSF. We found a difference cut of 0.0 achieved good separation between point and extended sources. We also institute a lower magnitude cutoff at the specified values, where measurements become noisy and clean point-source selection becomes difficult.

have no SExtractor flags, indicating that it has well-measured photometry.

After assembling final catalogs, we calculate completeness curves for the i-band imaging of each pointing, as described in 3. These completeness curves allow us to correct for data below detection thresholds in our datasets. In general the i-band data tend to be the shallowest in our catalogs, and therefore it makes the most since to perform completeness corrections on the i-band.

4.2.6 Point-source Selection

To achieve point-source selection, we use plots of FWHM vs magnitude. We identify the filter that has the best seeing, as that filter should be the one that offers the most discrimination between point-sources and extended sources. Once this filter is identified, we make a simple box cut in this parameter space. We place an upper limit on this box to remove obvious saturated stars, although most of these are already flagged by SExtractor anyway. The point-source locus is usually obvious in these plots.

Note that this simple box selection offers a prime area where one can improve selection through modeling methods. As we emphasize many times, our modeling methodology is designed to offer improvements on simple color-color and luminosity cuts, and yet we still employ a similar cut to identify point-sources. At the faint end especially, there can be significant ambiguity as to whether a source is point-like or extended.

4.2.7 Ad-hoc Cuts

For all galaxies, we considered only sources within 0.25 degrees of the galaxy in question. This 0.25 degree limit was motivated by the width of our Subaru/SuprimeCam imaging; while the SuprimeCam imager is only 27 arcmin wide, our galaxies are observed in a dither pattern which can increase this effective area. We found 0.25 degrees generally included all our sources.

4.2.8 Bayesian GC Procedures

As much as possible, we attempted to set default procedures for our galaxies which would allow our Bayesian inference to be performed in a consistent manner. In practice, many galaxies required some special procedures to be adopted, which we note below in 4.3. However, in all cases, the procedures below were tried before any modifications were performed.

We typically began by attempting to assume very uninformative priors. However, we often found that we were forced to modify these somewhat in order to achieve reasonable fits.

To start, we usually just ran a sampler with values initialized at reasonable values for all parameters. After this initial run, we would see which regions of parameter space the walkers would like to inhabit, and if any seemed to be dependent on priors. After this, we would usually change our starting values so that our walkers were close to their typical sets, and modify priors to try to assess prior sensitivity. In general, the choice of starting value was fairly irrelevant, as long as our starting values were in allowed regions of prior space. We found running our sampler for 2000 steps with 100 walkers produced well-sampled posteriors in the majority of cases.

The priors we most frequently were forced to modify were the μ_{gi} red limit. and the $g - i$ division prior. We modified the $g - i$ division prior when either the blue or red μ_{gi} walkers began running up against the middle, but we were in almost all cases able to find a value for which both distributions would stay on their sides of the dividing line.

The μ_{gi} limit was more difficult to deal with. We sometimes found that the red distribution wished to have μ_{gi} parameter greater than 1.4, which would be nearly unheard of for the red GC distribution in a galaxy. In addition, in these cases, the red GC distribution would simply expand in $g - i$ space until the spread of the distribution basically covered the entire available parameter space. In these situations the blue GC distribution sometimes became a highly dense probability distribution located with in an expanded probability distribution intended to represent the ”red” GCs. In these situations, we simply chose to impose strict priors on the red distribution, where we restricted the prior to be within a physically motivated range of values for this distribution. One galaxy, NGC 3115, produced excellent fits once this informative prior was imposed, and we have confidence that our inference is performing well despite the informative prior.

To keep our models simple, we didn't include information about the ellipticity of GC systems, instead preferring to treat our galaxies as circular symmetric. However, one exception to this is NGC 2768; we found that including this elliptical information was critical to achieve good fits to the galaxy; without the free parameters for ellipticity, fits to the GC system were poor and didn't recover the GC distributions correctly.

Two other galaxies, NGC 4111 and 4459, simply had too few GCs to obtain any reasonable inference. For this galaxy, we ultimately disregarded spatial and luminosity information and fixed the GC color distributions to be identical to NGC 3115. As a result, the fits to this galaxy only include two free parameters, the relative strengths of both the red and blue populations.

4.3 RESULTS BY GALAXY

The SLUGGS Survey constitutes a photometric sample of 25 galaxy in a wide array of environments and observing conditions. In this section, we present our analysis on a galaxy-by-galaxy basis.

For each galaxy, we produce some representative plots to illustrate both our the catalog of sources around the galaxy, and our inference on these sources. The figures show the same data for each galaxy. In the top panel, we plot a color-color diagram of sources in our color range of interest. Points are color-coded by the probability that the source is a GC. The bottom left panel displays an *i*-band histogram of all modeled sources, while the line line displays our inferred GC *i*-band magnitude distribution. The bottom right panel displays the spatial distribution of all modeled sources, again color-coded by the probability that they are GCs. The color bar displays the color mapping for these probabilities. Finally, the histograms along both the top and side of the color-color plot represent the color distributions of all sources with $P_{GC} > 0.5$. While naturally such a binary cut ignores all complexity in the distributions, it can be useful to compare our inferred color distributions with other studies.

We also include a table for each galaxy with representative summary statistics from the modeling. We include percentiles for each parameter which correspond to 95% and 68% credible probability regions, as well as the median 50% of each parameter. For information about the fits may be found in the appendix, where we provide both full trace plots and full corner plots for all parameters.

Galaxies are listed in order of NGC number, with the exception of NGC 1407/NGC 1400 and NGC 3607/3608, which are both companion galaxies.

4.3.1 NGC 1407

NGC 1407, an E0 galaxy, is roughly the second most massive galaxy in our sample after NGC 4486. Its stellar mass is $10^{11.6}$ $M_{\odot}$, comparable with the galaxy NGC 4649 (Forbes et al., 2017a). It is also one of the most distant in our sample. NGC 1400 is a nearby, less massive companion galaxy located roughly ~ 100 kpc to the south west.

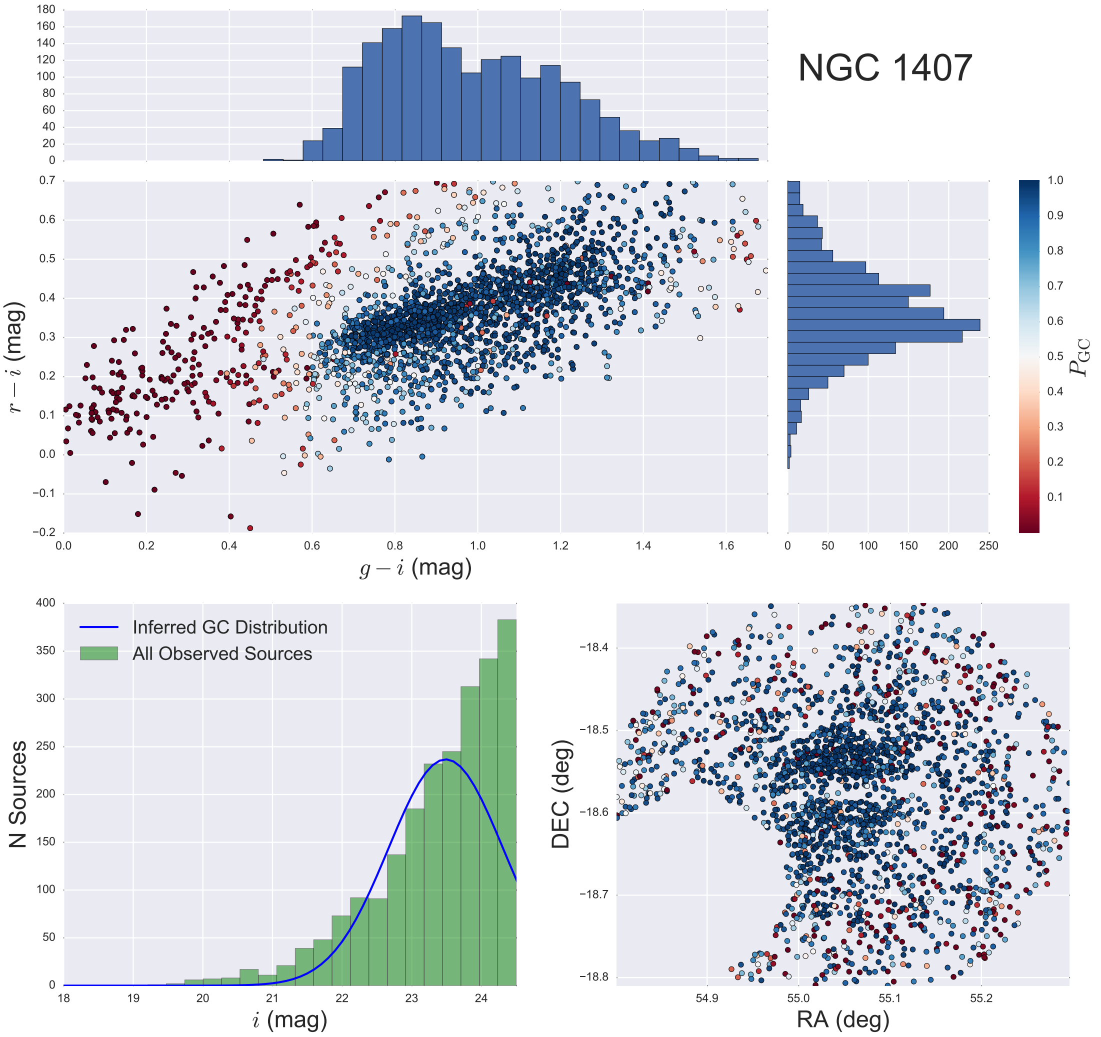

Figure 4.2: Inferences from modelling

Table 4.4: NGC 1407 Parameters

Modelled Parameters

Parameter	2.5%	16.0%	50.0%	84.0%	97.5%
f_{red}	0.216	0.229	0.243	0.258	0.272
f_{blue}	0.104	0.114	0.126	0.138	0.15
$\mu_{gi,red}$	0.792	0.801	0.81	0.82	0.829
$\mu_{ri,red}$	0.28	0.281	0.283	0.287	0.292
$\sigma^2_{gi,red}$	0.021	0.023	0.025	0.027	0.029
$\sigma^2_{ri,red}$	0.009	0.009	0.01	0.011	0.012
$\sigma_{gi,red}\sigma_{ri,red}$	0.008	0.009	0.01	0.011	0.012
$\mu_{gi,blue}$	0.543	0.55	0.556	0.564	0.571
$\mu_{ri,blue}$	0.228	0.231	0.233	0.236	0.239
$\sigma^2_{gi,blue}$	0.004	0.005	0.006	0.007	0.008
$\sigma^2_{ri,blue}$	0.001	0.001	0.001	0.002	0.002
$\sigma_{gi,blue}\sigma_{ri,blue}$	0.001	0.001	0.002	0.002	0.002
R_e	0.091	0.095	0.098	0.102	0.106
μ_i	23.29	23.332	23.379	23.427	23.476
σ_i	0.867	0.898	0.934	0.97	1.011

Derived Quantities

Quantity	2.5%	16.0%	50.0%	84.0%	97.5%
$N_{Sources}$	2554.6	2565.3	2576.5	2589.5	2602.8
N_{GCs}	882.8	917.5	952.2	990.2	1027.0
N_{RedGCs}	553.6	590.1	627.2	665.5	704.3
$N_{BlueGCs}$	266.9	293.9	325.2	356.0	388.4
N_{GCs} (Extrapolated)	1139.7	1206.1	1273.7	1353.4	1433.2
N_{RedGCs} (Extrapolated)	722.6	779.7	839.4	904.5	971.1
$N_{BlueGCs}$ (Extrapolated)	351.8	391.0	435.5	480.8	531.4
f_{red}/f_{blue}	1.49	1.69	1.93	2.21	2.54

We consider NGC 1400 separately in §4.3.2.

Our data for NGC 1407 are among the deepest in our sample. As a result, NGC 1407 is one of the only galaxies for which our contaminant luminosity distribution is actually fainter than our science luminosity distributuon. As a result, we are forced to trim off all sources below $i = 25$ mag, as we don't have information from about what the contaminant distribution ought to look like in our sample.

In Fig. 4.2, we plot the results of our inference on our galaxy. We found NGC 1407 was well-fit by a bimodal population, as has been noted in previous studies (Pota et al., 2013b, 2015). We also provide our inferred values for the model parameters of the GC distribution in Table 4.4.

4.3.2 NGC 1400

NGC 1400 is a smaller E1/S0 galaxy located nearby to the much larger NGC 1407. As mentioned above, to analyze the system, we only examined sources within 0.11 deg (~ 6.5 arcmin, or ~ 50 kpc). This has the advantage of allowing us to include spatial information for this galaxy; furthermore, while the radial restriction means we are not investigating the full extent of the system, it has the advantage of creating a catalog which will likely have a small amount of contamination. We display the results of the fit to this galaxy in Fig 4.3.2, and provide the inferred model parameters in Table 4.5.

We note that the NGC 1407/1400 system could benefit from adding additional radial profile information. A natural solution is to expand the mixture model and allow for both galaxies to have their own radial distribution parameters. However, such an expansion is beyond the scope of this work.

4.3.3 NGC 2768

NGC 2768 is a medium-sized E6/S0 galaxy, and is fairly distant at ∼21 Mpc. Pota et al. (2013b) analyzed SuprimeCam photometry from the galaxy and identified an apparent color bimodality. However, it is clear that the color bimodality essentially disappears when examining just spectroscopically confirmed sources. Kartha et al. (2014) performed an updated analysis of the same data and reached similar conclusions, although the spectroscopically confirmed sample seems to suggest a much flatter distribution.

We were initially unable to derive good fits for NGC 2768, with bimodality not fitting without very strong priors. However, we were able to get better fits to the data when we allowed for ellipticity in the spatial distribution of GCs. When this was including in the fitting, we now recovered very reasonable inference for all values, including a fairly clear bimodal distribution. NGC 2768 suggests that when GC distributions are highly elliptical, including this ellipticity in the fitting can be important for correctly identifying the distributions, especially when galaxies are distant and GC signal is not as strong. Given the clear improvement from allowing for elliptical fitting, we chose to include it in the final results for this galaxy, something we didn't include for the others. We provide the results of this fit in Fig. 4.3.3, as well as the inferred model parameters in Table 4.6.

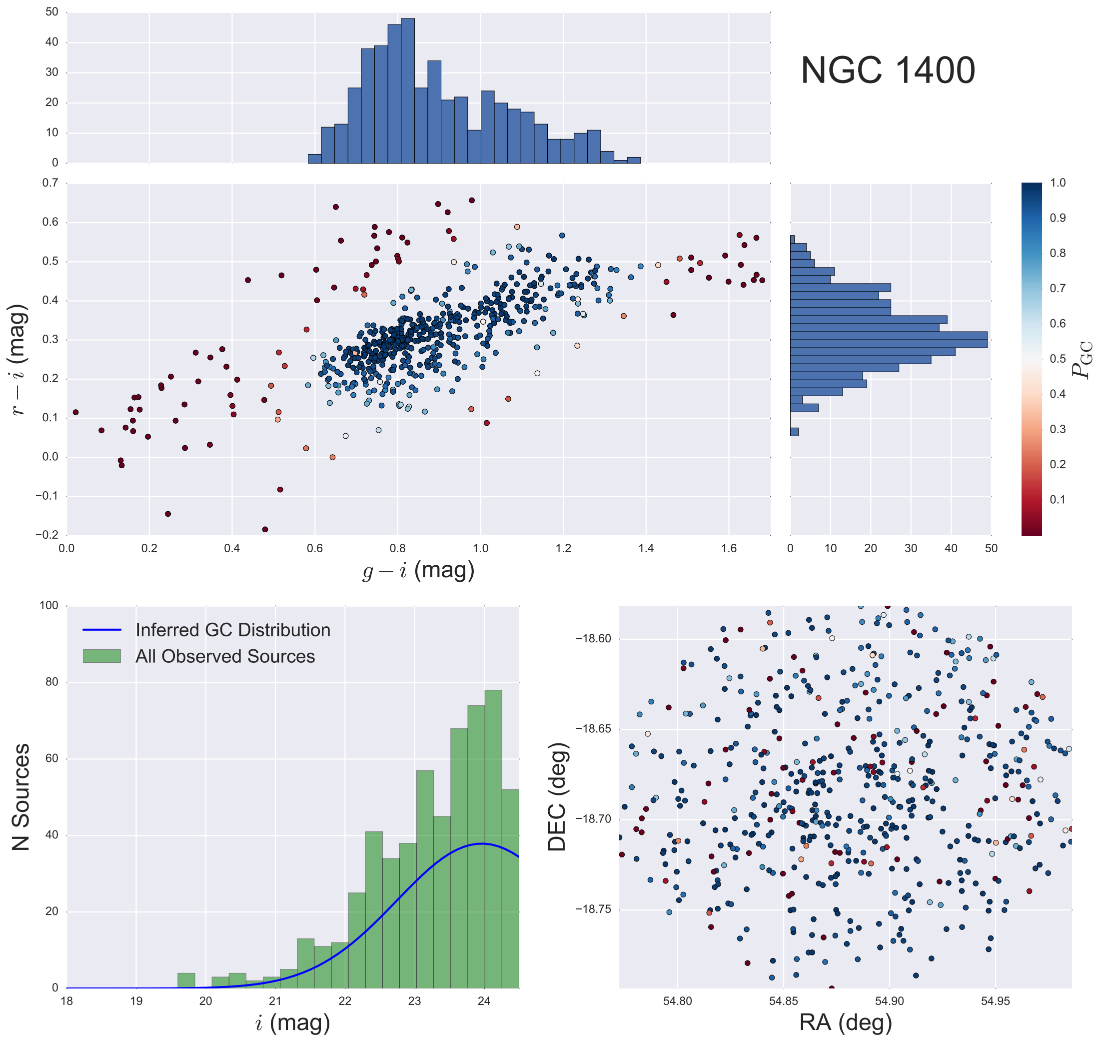

Figure 4.3: Same as for Fig. 4.2, but for NGC 1400. The NGC 1400 catalog is restricted to sources within 0.11 degrees of the galaxy to minimize contamination from NGC 1407.

Table 4.5: NGC 1400 Parameters

Modelled Parameters

Parameter	2.5%	16.0%	50.0%	84.0%	97.5%
f_{red}	0.354	0.475	0.529	0.575	0.617
f_{blue}	0.195	0.232	0.271	0.322	0.439
$\mu_{gi,red}$	0.933	0.949	0.967	0.988	1.049
$\mu_{ri,red}$	0.319	0.327	0.334	0.343	0.377
$\sigma^2_{gi,red}$	0.02	0.026	0.029	0.033	0.036
$\sigma^2_{ri,red}$	0.006	0.009	0.01	0.011	0.012
$\sigma_{gi,red}\sigma_{ri,red}$	0.007	0.011	0.013	0.014	0.016
$\mu_{gi,blue}$	0.754	0.762	0.77	0.779	0.791
$\mu_{ri,blue}$	0.274	0.282	0.288	0.293	0.299
$\sigma^2_{gi,blue}$	0.003	0.004	0.005	0.006	0.007
$\sigma^2_{ri,blue}$	0.001	0.001	0.002	0.002	0.004
$\sigma_{gi,blue}\sigma_{ri,blue}$	0.001	0.002	0.002	0.003	0.003
R_e	0.087	0.096	0.107	0.121	0.137
μ_i	23.65	23.787	23.959	24.183	24.486
σ_i	1.047	1.123	1.216	1.329	1.468

Derived Quantities

Quantity	2.5%	16.0%	50.0%	84.0%	97.5%
$N_{Sources}$	670.5	674.1	677.8	681.6	685.2
N_{GCs}	510.9	526.3	543.3	559.5	574.7
N_{RedGCs}	237.7	321.2	358.1	390.4	419.8
$N_{BlueGCs}$	132.5	156.9	184.0	218.1	297.9
N_{GCs} (Extrapolated)	841.8	931.5	1058.7	1236.1	1508.6
N_{RedGCs} (Extrapolated)	441.4	584.3	697.0	838.6	1025.4
$N_{BlueGCs}$ (Extrapolated)	245.1	296.4	363.3	456.6	612.6
f_{red}/f_{blue}	0.79	1.49	1.95	2.47	3.1

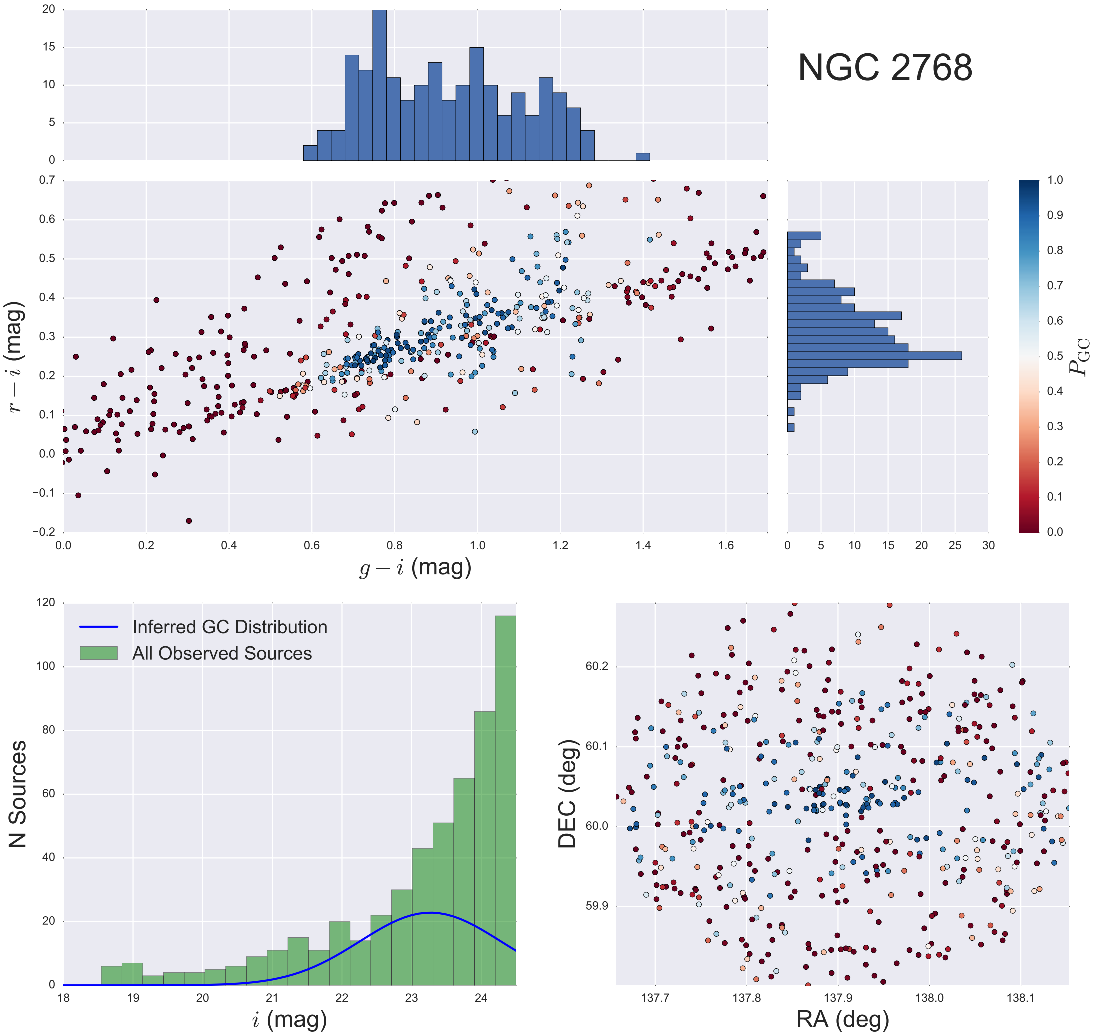

Figure 4.4: Same as for Fig. 4.2, but for NGC 2768.

Table 4.6: NGC 2768 Parameters

Modelled Parameters

Parameter	2.5%	16.0%	50.0%	84.0%	97.5%
f_{red}	0.145	0.178	0.217	0.259	0.301
f_{blue}	0.106	0.132	0.162	0.195	0.228
$\mu_{gi,red}$	1.006	1.028	1.06	1.092	1.127
$\mu_{ri,red}$	0.335	0.35	0.367	0.388	0.416
$\sigma^2_{gi,red}$	0.012	0.017	0.023	0.032	0.041
$\sigma^2_{ri,red}$	0.006	0.008	0.011	0.017	0.023
$\sigma_{gi,red}\sigma_{ri,red}$	0.003	0.005	0.008	0.013	0.017
$\mu_{gi,blue}$	0.729	0.747	0.768	0.789	0.812
$\mu_{ri,blue}$	0.241	0.249	0.259	0.268	0.277
$\sigma^2_{gi,blue}$	0.004	0.006	0.009	0.014	0.019
$\sigma^2_{ri,blue}$	0.001	0.001	0.002	0.003	0.004
$\sigma_{gi,blue}\sigma_{ri,blue}$	0.001	0.002	0.004	0.005	0.007
R_e	0.179	0.213	0.264	0.345	0.478
ϵ	0.472	0.559	0.643	0.719	0.785
PA	-0.14	-0.053	0.027	0.108	0.188
μ_i	23.029	23.144	23.259	23.385	23.502
σ_i	0.869	0.936	1.012	1.089	1.176

Derived Quantities

Quantity	2.5%	16.0%	50.0%	84.0%	97.5%
$N_{Sources}$	592.1	597.8	605.1	613.5	624.2
N_{GCs}	178.7	203.6	230.6	259.4	290.4
N_{RedGCs}	86.2	106.8	131.3	157.6	185.4
$N_{BlueGCs}$	63.9	79.5	98.0	118.9	140.1
N_{GCs} (Extrapolated)	220.0	257.5	300.8	349.8	410.1
N_{RedGCs} (Extrapolated)	107.3	135.9	171.3	211.9	260.4
$N_{BlueGCs}$ (Extrapolated)	80.6	102.6	127.8	157.4	193.6
f_{red}/f_{blue}	0.74	0.97	1.34	1.83	2.45

4.3.4 NGC 3115

NGC 3115 is a nearby, fairly isolated S0 galaxy. At sim10 Mpc away, it is the closest galaxy in the SLUGGS survey. Because of its proximity, NGC 3115 is a frequent target for studies of GC systems, and a variety of useful datasets exist. Extensive spectroscopic datasets (Arnold et al., 2011) and an HST/ACS mosaic exist of this galaxy (Ch. 1). As noted in Ch. 1, bimodality is clear in box-selection ground-based imaging, size-selected ACS imaging, and even in spectroscopic estimates for GC metallicity (Brodie et al., 2012).

We found we were able to obtain reasonable fits for bimodality; however, we were forced to include a fairly restrictive prior on the mean distribution of the red GC distribution. We found that when the high end of the red GC population was left unbounded, it tended to run off to very high values, well beyond what would be expected in a typical GC system. We imposed a prior that the red mean must be less than 1.1. While this was certainly informative (the traces indicate that the walkers do touch this edge), we still see a reasonably-peaked PDF for the this mean vector. In addition, the rest of the parameters appear to be reasonably well-sampled.

We plot our inferences for NGC 3115 in Fig. 4.3.4. With the informative prior, we recover the bimodal GC distribution for this galaxy extremely well. Both distributions appear well-behaved, with a slightly more extended red GC distribution, as is typical for most systems. We also provide our inferred values for the distribution parameters in Table 4.7.

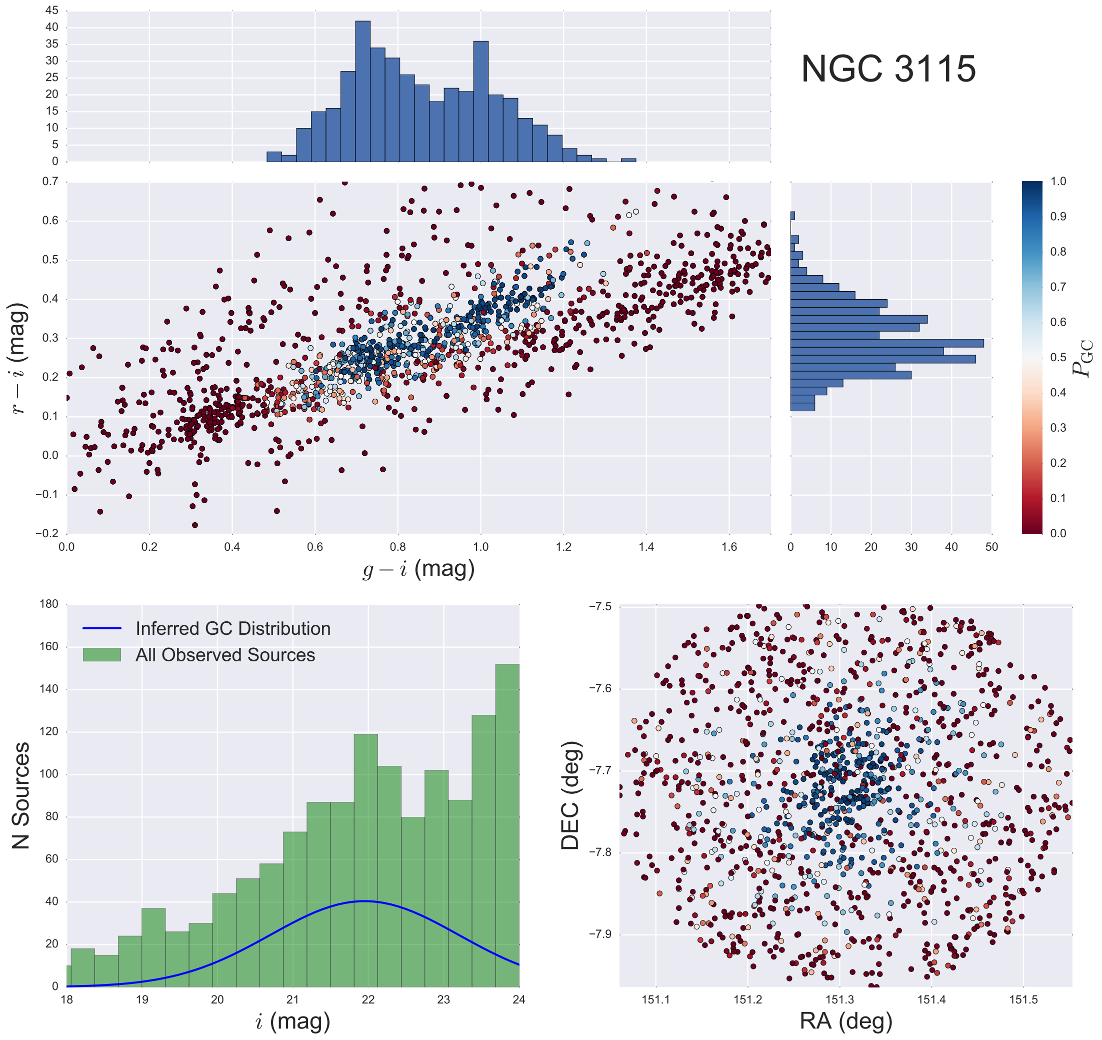

Figure 4.5: Same as for Fig. 4.2, but for NGC 3115.

Table 4.7: NGC 3115 Parameters

Modelled Parameters

Parameter	2.5%	16.0%	50.0%	84.0%	97.5%
f_{red}	0.092	0.111	0.131	0.154	0.186
f_{blue}	0.104	0.13	0.153	0.176	0.202
$\mu_{gi,red}$	0.956	0.986	1.011	1.032	1.046
$\mu_{ri,red}$	0.329	0.343	0.355	0.367	0.377
$\sigma^2_{gi,red}$	0.008	0.01	0.013	0.017	0.025
$\sigma^2_{ri,red}$	0.004	0.005	0.006	0.007	0.008
$\sigma_{gi,red}\sigma_{ri,red}$	0.004	0.006	0.007	0.009	0.012
$\mu_{gi,blue}$	0.691	0.707	0.723	0.739	0.758
$\mu_{ri,blue}$	0.232	0.239	0.246	0.253	0.26
$\sigma^2_{gi,blue}$	0.006	0.007	0.01	0.013	0.019
$\sigma^2_{ri,blue}$	0.003	0.003	0.004	0.004	0.005
$\sigma_{gi,blue}\sigma_{ri,blue}$	0.003	0.004	0.004	0.006	0.008
R_e	0.071	0.075	0.08	0.085	0.091
μ_i	21.725	21.829	21.944	22.071	22.219
σ_i	1.079	1.155	1.243	1.34	1.446

Derived Quantities

Quantity	2.5%	16.0%	50.0%	84.0%	97.5%
$N_{Sources}$	1618.6	1620.4	1623.6	1626.5	1629.8
N_{GCs}	413.7	419.7	404.9	401.4	391.2
$N_{Red\ GCs}$	169.8	176.2	193.0	195.1	190.3
$N_{Blue\ GCs}$	243.9	243.5	211.9	206.3	200.9
N_{GCs} (Extrapolated)	428.3	436.8	423.1	421.6	414.0
$N_{Red\ GCs}$ (Extrapolated)	175.8	183.4	201.7	204.9	201.4
$N_{Blue\ GCs}$ (Extrapolated)	252.5	253.4	221.4	216.7	212.6
f_{red}/f_{blue}	0.7	0.72	0.91	0.95	0.95

4.3.5 NGC 3607/3608

As with NGC 1407 and 1400 above, NGC 3608 and 3607 are companion galaxies. NGC 3608 is officially a galaxy in the SLUGGS survey, as it was chosen for its location in galaxy parameter space. However, 3607 is actually the larger of the two galaxies. Kartha et al. (2016) examined the photometric properties of both GC systems. They discovered significant bimodality in both systems under GMM, once various cuts were performed. Kartha et al. (2016) used the relative light profiles of both galaxies to separate out GCs belonging to either system in order to assign catalogs to the two galaxies. After doing this, they were able to analyze the two GC profiles separately and found clear bimodal results for both. In general, analysis of either GC system is difficult simply because the two galaxies are located so close to each other.

We found that the NGC 3607/3608 system posed a fair amount of difficulty in attempting to get reasonable inference with our standard fitting procedure. To begin performed galaxy subtraction on both galaxies independently, then performed our photometry on the galaxies to create one full catalog. While 3608 is the official SLUGGS galaxy, our imaging is actually centered on NGC 3607, which is in fact the larger of the two galaxies. The galaxies are also extremely close together, seperated by only ~ 5.5 arcmin. The close proximity of the two systems means that the GC distributions of the two galaxies certainly overlap and, depending on their relative projection, likely are interacting.

For 1407/1400, we simply cut sources within a certain distance from NGC 1400, which we justified by the fact that NGC 1407 is significantly larger than NGC 1400.

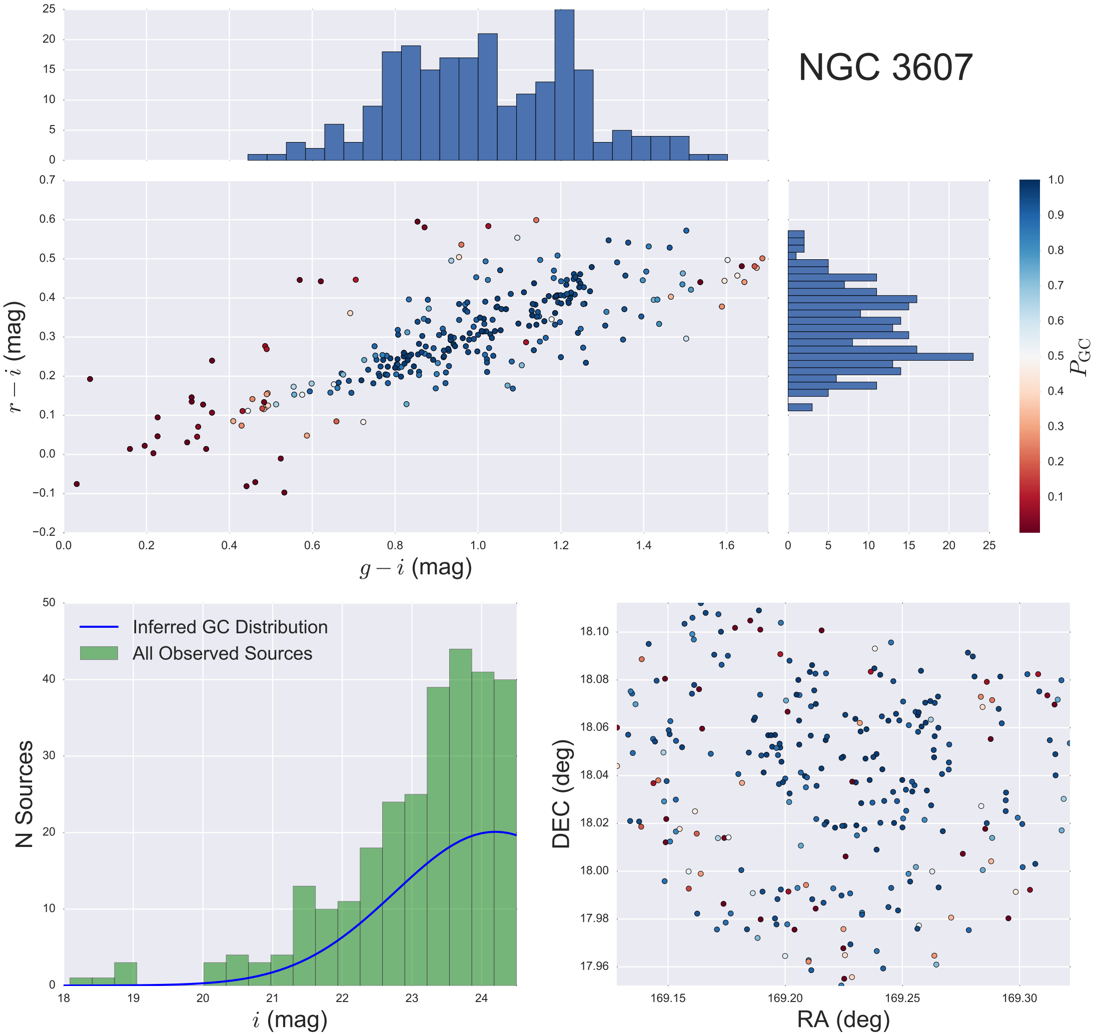

Figure 4.6: Same as for Fig. 4.2, but for NGC 3607.

Table 4.8: NGC 3607 Parameters

Modelled Parameters

Parameter	2.5%	16.0%	50.0%	84.0%	97.5%
f_{red}	0.314	0.409	0.497	0.564	0.622
f_{blue}	0.144	0.198	0.266	0.35	0.436
$\mu_{gi,red}$	1.042	1.073	1.104	1.134	1.166
$\mu_{ri,red}$	0.326	0.34	0.354	0.367	0.381
$\sigma^2_{gi,red}$	0.028	0.034	0.043	0.053	0.068
$\sigma^2_{ri,red}$	0.007	0.008	0.009	0.011	0.014
$\sigma_{gi,red}\sigma_{ri,red}$	0.007	0.009	0.013	0.016	0.021
$\mu_{gi,blue}$	0.758	0.805	0.85	0.919	0.971
$\mu_{ri,blue}$	0.217	0.233	0.251	0.283	0.304
$\sigma^2_{gi,blue}$	0.009	0.017	0.031	0.045	0.061
$\sigma^2_{ri,blue}$	0.001	0.002	0.005	0.008	0.01
$\sigma_{gi,blue}\sigma_{ri,blue}$	0.003	0.006	0.012	0.018	0.023
R_e	0.062	0.07	0.081	0.095	0.113
μ_i	23.626	23.854	24.219	24.663	24.941
σ_i	1.124	1.262	1.445	1.639	1.785

Derived Quantities

Quantity	2.5%	16.0%	50.0%	84.0%	97.5%
$N_{Sources}$	325.4	327.9	330.6	333.5	336.1
N_{GCs}	220.0	236.5	252.2	266.6	279.9
N_{RedGCs}	103.7	135.1	164.0	187.2	206.4
$N_{BlueGCs}$	47.3	65.5	88.0	115.9	143.8
N_{GCs} (Extrapolated)	378.6	449.2	575.9	750.6	903.2
N_{RedGCs} (Extrapolated)	192.6	272.6	369.5	502.1	623.8
$N_{BlueGCs}$ (Extrapolated)	96.2	138.9	203.4	286.5	377.1
f_{red}/f_{blue}	0.76	1.18	1.88	2.78	4.16

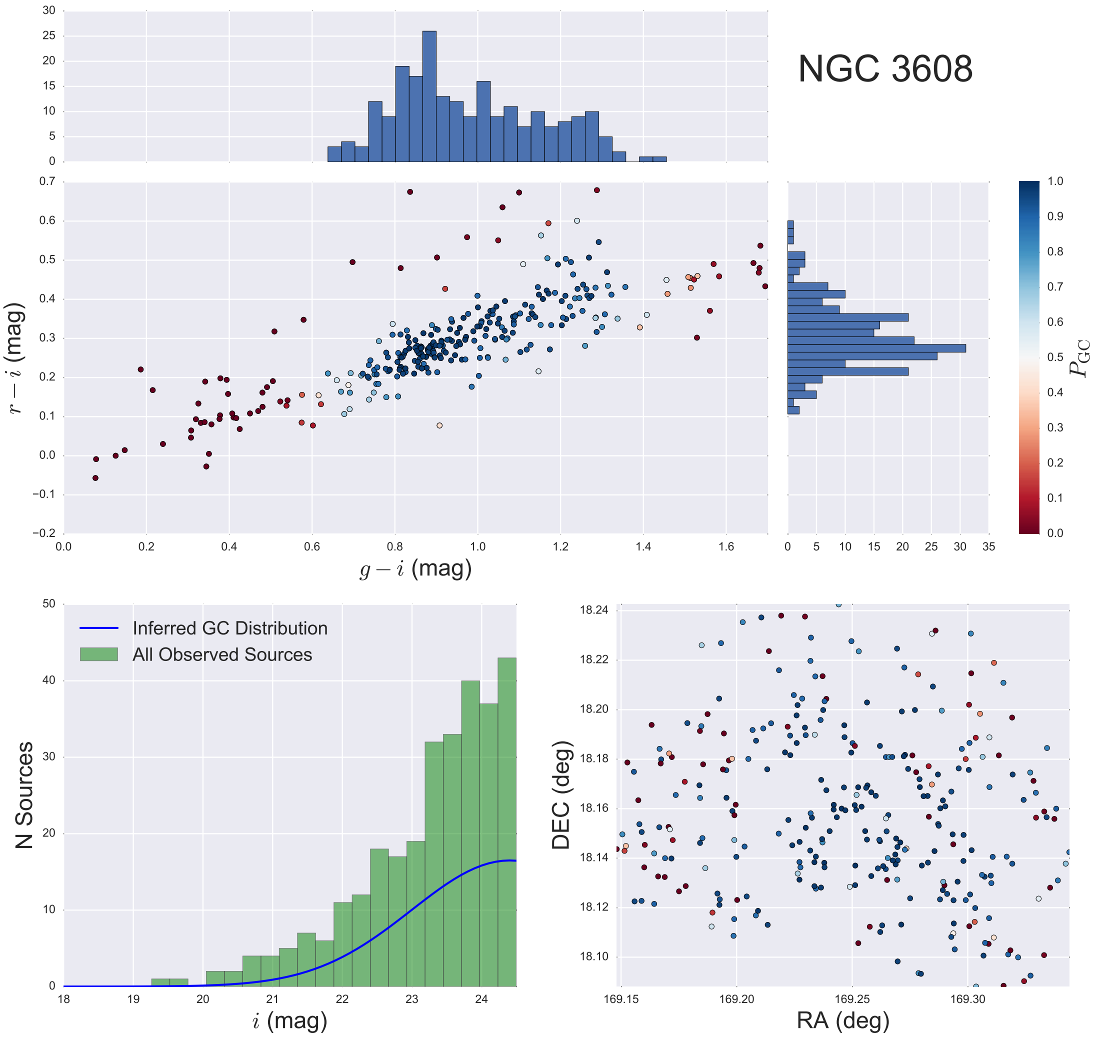

Figure 4.7: Same as for Fig. 4.2, but for NGC 3608.

Table 4.9: NGC 3608 Parameters

Modelled Parameters

Parameter	2.5%	16.0%	50.0%	84.0%	97.5%
f_{red}	0.161	0.212	0.28	0.384	0.481
f_{blue}	0.259	0.353	0.445	0.511	0.566
$\mu_{gi,red}$	1.038	1.094	1.151	1.184	1.197
$\mu_{ri,red}$	0.319	0.339	0.363	0.382	0.401
$\sigma^2_{gi,red}$	0.008	0.011	0.022	0.044	0.067
$\sigma^2_{ri,red}$	0.005	0.006	0.008	0.01	0.013
$\sigma_{gi,red}\sigma_{ri,red}$	0.002	0.005	0.008	0.014	0.022
$\mu_{gi,blue}$	0.847	0.862	0.879	0.896	0.917
$\mu_{ri,blue}$	0.253	0.261	0.269	0.276	0.286
$\sigma^2_{gi,blue}$	0.005	0.008	0.011	0.015	0.021
$\sigma^2_{ri,blue}$	0.002	0.002	0.003	0.004	0.005
$\sigma_{gi,blue}\sigma_{ri,blue}$	0.002	0.003	0.005	0.007	0.009
R_e	0.052	0.057	0.064	0.072	0.083
μ_i	23.795	24.024	24.34	24.693	24.929
σ_i	1.122	1.239	1.376	1.528	1.661

Derived Quantities

Quantity	2.5%	16.0%	50.0%	84.0%	97.5%
$N_{Sources}$	339.2	341.8	344.5	347.2	349.8
N_{GCs}	223.9	237.4	251.2	264.7	278.4
N_{RedGCs}	55.1	72.9	96.3	132.5	165.7
$N_{BlueGCs}$	89.1	121.2	153.1	176.2	195.8
N_{GCs} (Extrapolated)	418.2	495.9	626.1	791.7	936.1
N_{RedGCs} (Extrapolated)	116.9	168.9	245.1	349.3	479.7
$N_{BlueGCs}$ (Extrapolated)	197.7	277.4	372.9	490.4	612.8
f_{red}/f_{blue}	0.29	0.42	0.62	1.08	1.79

However, NGC 3607 is in fact the larger galaxy, although the two are of comparable masses. For our analysis of these two galaxies, we first attemted to use a simple distance cut: any sources closer to NGC 3608 are assumed to correspond to its GC distribution, and sources closer to NGC 3607 are assigned to that model instead.

Dividing the GCs is this manner is logical, but it does present difficulties with normalizing the spatial distributions. Both the GC and contaminant distributions must now be normalized over an irregular polygon in this space. Furthermore, logical priors for the GC spatial distribution are more difficult to determine with this irregular truncation of the distribution. As a result of these difficulties, we experimented with turning off any spatial information about the galaxies. We simply used the above distance cut to divide the source distributions of the two systems.

We ultimately encountered a lot of difficulty obtaining fits in this manner. Without spatial information for these galaxies, distributions tended to simply walk in to parameter space. We typically inferred GC distributions which were far too wide in $g-i$ space for both reds and blues, and with a $\mu_{gi,red}$ value which would walk until the prior limit at the far red end. The fits were recovering GC distributions without clear bimodality, and for which sources far too red were likely to be GCs.

We had considerably more success by drastically restricting the spatial regions over which we were performing our fitting. We restricted our catalogs for each galaxy to just the 0.1 degrees immediately surrounding the galaxy. Making a range this restrictive only includes a couple hundred total sources in our fitted sample; however, the vast majority of these sources would be expected to be GCs. In addition, restricting the catalogs in this way still allowed us to use the spatial information to fit these galaxies. We display the results of this fit to the GC system of NGC 3607 in Fig. 4.3.5 and NGC 3608 in Fig. 4.3.5, with tables of the inferred parameters in Table 4.8 and Table 4.9 respectively.

4.3.6 NGC 4111

NGC 4111 is a small S0 galaxy, located roughly 10 Mpc away. It is among the least massive galaxies in our sample, and as such we expect it to have a very small GC population. Furthermore, analysis of this galaxy is complicated by the presence of a bright foreground star just to the north east of the galaxy. NGC 4111 is also known for its association with a prominent stellar stream.

In general, we found that there were simply far too few sources to get any sort of reasonable fits out from this galaxy. Walkers for all sorts of different free parameters were unable to converge, and routinely ran up against specified prior ranges. We adopted the strategy of not fitting any spatial or luminosity information, and setting the color distribution parameters to be fixed to those we inferred for NGC 3115. NGC 3115 was selected due to its similar morphology and clear bimodality, and while it is more massive than NGC 4111, almost all galaxies in our sample are.

After fixing these two parameters, the only free parameters in the sample are the $\mathrm{f}_{\mathrm{red}}$and $\mathrm{f}_{\mathrm{blue}}$parameters which control the strength of the two mixing distributions. Both parameters mixed well for a model this simple. We display the resulting inference in Fig. 4.3.6, and give our inferred values for the free parameters in Table 4.10.

While we were unable to get reasonable fits for the NGC 4111 distribution,

Table 4.10: NGC 4111 Parameters

Modelled Parameters					
Parameter	2.5%	16.0%	50.0%	84.0%	97.5%
f_{Red}	0.066	0.085	0.104	0.125	0.145
f_{Blue}	0.018	0.033	0.049	0.065	0.083

this galaxy does represent an example of using our fitting methodology purely for GC selection. In this sense, fixing the values of the color distributions is akin to setting hard boundaries in color-color space and performing simple box selection. We still get probabilities for every source in the image being a GC, but conditional on the fixed values. In addition, while we chose to just neglect spatial and luminosity information, we could have fixed these values too if we had reasonable guess for what these distributions looked like. This would have folded additional information into the system.

NGC 4111 is thus an example of how our methodology will still be comparable to simple box selection, even in situations where we can't fit our full model. In addition, the parameters controlling the number of GCs in the system may still be fit for, but the posterior distributions will be conditional on the other fixed parameters.

4.3.7 NGC 4278

NGC 4278 is a medium-sized E1-2, also in the Virgo cluster. Usher et al. (2013) examined Subaru/SuprimeCam data of this galaxy, combined with *HST*/ACS data, and identified clean color bimodality with classic results for the differences in the reds and blues. Usher et al. (2013)'s dataset covered different filters than our data; however, the overall color distribution (see Fig. 4.9) looks very similar, with a potentially depressed

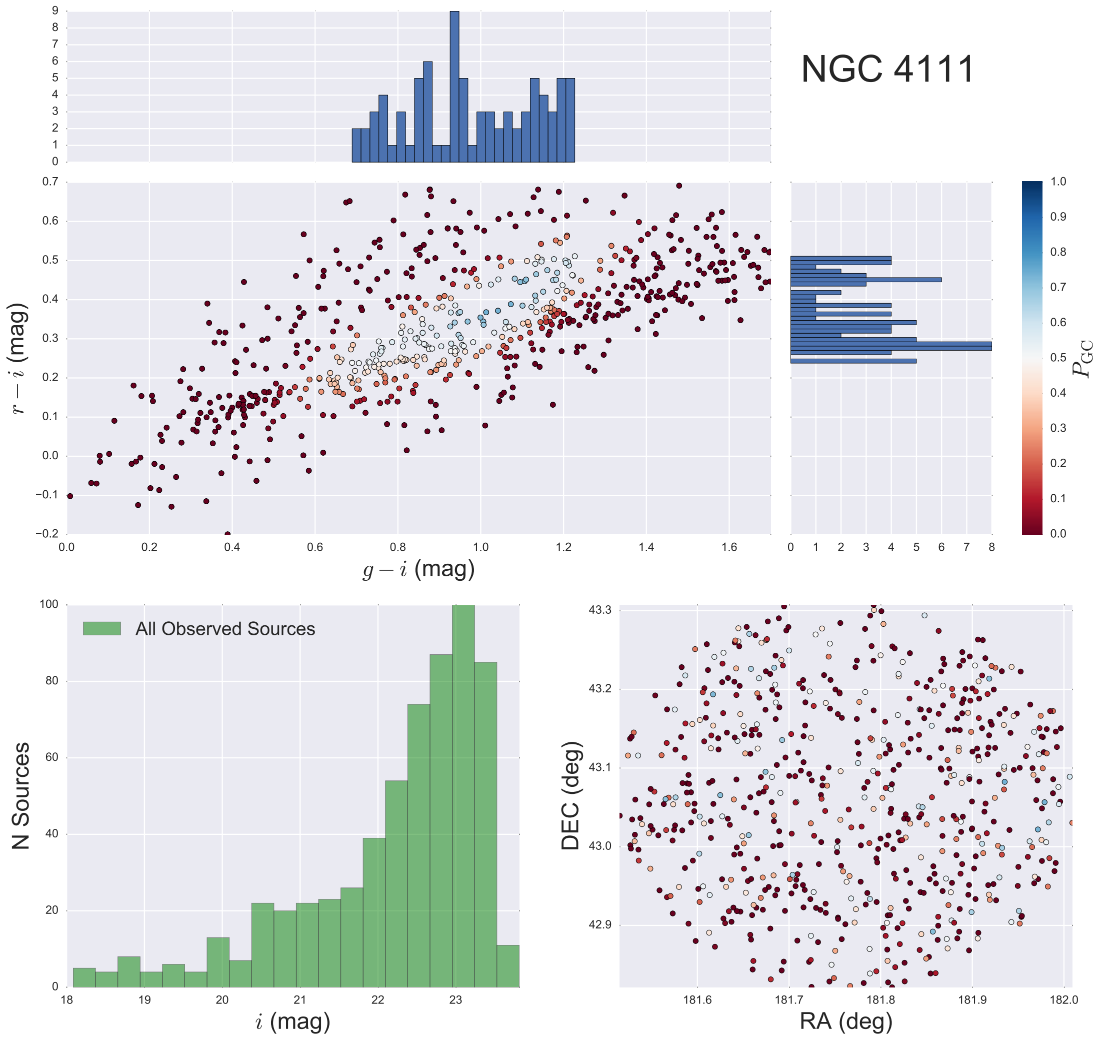

Figure 4.8: Same as for Fig. 4.2, but for NGC 4111. Note that spatial and luminosity information was not fit for NGC 4111, and color distributions were fixed to match those of NGC 3115. The only free parameters in the inference are the $\mathrm{f}_{\mathrm{red}}$and $\mathrm{f}_{\mathrm{blue}}$mixture distribution strengths. Because there is no *i*-band fit, we don't display any fit in the bottom left panel.

red stellar population.

We found we were able to get reasonable fits for NGC 4278 using our methodology, with the caveat that bimodality, while not a poor fit, seemed to be driven entirely by prior choice. We found that both distributions seemed to want to lie on top of one another, with a narrow, well-peaked blue distribution surrounded by a higher variance "red" distribution at nearly the same mean. Results for the other quantities in the model, and indeed the individual GCs selected by the model, are essentially unchanged whether a bimodal or unimodal fit is used. This finding is consistent with the appearance of the marginalized color distribution both in Fig. 4.9 and in Usher et al. (2013). While the model clearly seems to be poorly fit by a unimodal normal distribution, the second peak isn't obvious in the histogram. We ultimately adopt the unimodal model for simplicity; however, if we wished to apply stronger prior information (for example, the peaks from the ACS data or from spectroscopic data), we could include the second distribution and constrain its relative strength. We display the resulting fits to the GC population in Fig. 4.9, and provide our inference on the free parameters of the galaxy in Table 4.11.

4.3.8 NGC 4365

NGC 4365 is one of the most massive galaxies in the SLUGGS survey. It is a fairly distant galaxy that has been studied previously in the literature. Blom et al. (2012b) examined the galaxy in wide-field imaging, and found evidence for a potential third population among the GC system. Blom et al. (2012a) followed up on this finding with expanded velocity information for spectroscopically confirmed GCs, and found

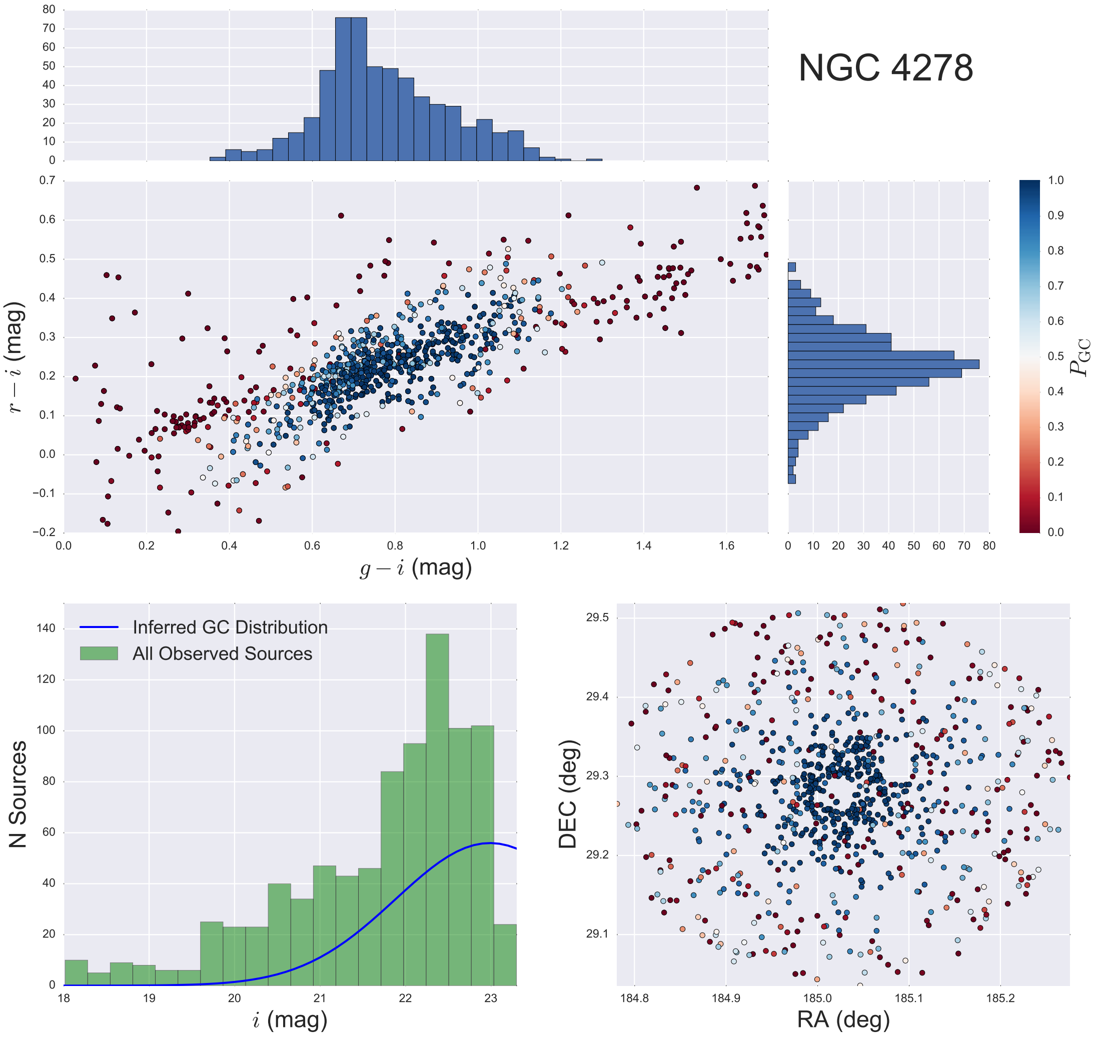

Figure 4.9: Same as for Fig. 4.2, but for NGC 4278.

Table 4.11: NGC 4278 Parameters

Modelled Parameters

Parameter	2.5%	16.0%	50.0%	84.0%	97.5%
f_{gc}	0.583	0.61	0.638	0.666	0.692
μ_{gi}	0.761	0.768	0.776	0.784	0.791
μ_{ri}	0.217	0.221	0.225	0.23	0.234
σ_{gi}^2	0.023	0.024	0.026	0.028	0.031
σ_{ri}^2	0.007	0.008	0.008	0.009	0.01
$\sigma_{gi}\sigma_{ri}$	0.01	0.011	0.012	0.013	0.014
R_e	0.082	0.086	0.09	0.095	0.099
μ_i	22.727	22.843	22.99	23.169	23.399
σ_i	0.965	1.029	1.105	1.193	1.295

Derived Quantities

Quantity	2.5%	16.0%	50.0%	84.0%	97.5%
$N_{Sources}$	1997.0	2103.7	2245.1	2429.9	2683.8
N_{GCs}	1189.8	1296.3	1430.9	1602.0	1819.7
$N_{GCs,extrapolated}$	1325.51	1497.67	1744.94	2103.12	2659.23

distinct kinematic behavior for the multiple subpopulations.

We had difficulty getting a successful two-population fit without informative priors. Fits to two populations were well-behaved, but the red GC distributions tended to have inferred values for $\mu_{gi,red}$ and $\mu_{ri,red}$ which were quite high. Fits to the blue population expanded to fill the middle ground, leading to large σ^2_{blue} terms in the covariance matrix. As a result of this, the value for $\mathrm{f_{blue}}$grew to encompass most of the GC population, also leading to very small values for f_{red}/f_{blue}. However, this is fairly artificial, as really the blue population in our fits is simply expanding to fill much of the region that one would typically think of as red GCs. If the underlying GC population is indeed trimodal (or at least if a bimodal normal is a very poor model), behavior such as this is what we expect to see. It would be interesting to expand the GC color distribution model of this galaxy to investigate if a third population would be well-fit, especially given previous studies of this galaxy. Even if the third population isn't necessarily physically meaningful, the inclusion of distributions with additional free parameters might mean the color distribution fits the data better. This also invites the exploration of non-normal color distributions, which might similarly replicate the improvement in fit from including a third population.

We experimented with restricting the values for $\mu_{ri,red}$ to be below 0.4, as an informative prior. However, this still resulted in essentially identical values for the $\mathrm{f_{red}}$and $\mathrm{f_{blue}}$parameters, indicating that the blue population does indeed "want" to be this large. Our difficulties fitting this galaxy may be more due to the poor match of bimodal multivariate normals to the GC color-color distribution, especially given previous results on the NGC 4365 color distribution. We display the results of this restrictive prior fit in Fig. 4.3.8, and give our inference on the model parameters in Table 4.12.

4.3.9 NGC 4486

NGC 4486 is the brightest cluster galaxy in Virgo, and as such has an extremely large GC population. It is also the most massive galaxy in the SLUGGS sample. We found our model fit very well the observed source distributions with no modification. Outside of fixing a precise value for the $g - i$ division parameter, no real fine-tuning was needed. NGC 4486 has long been a target of GC surveys due to its large GC system, and extensive photometric and kinematic studies of the galaxies are in the literature (Harris, 2009b; Strader et al., 2011; Agnello et al., 2014). Most studies confirm typical trends of GC bimodality, with the usual dichotomy between reds and blues.

Given the number of sources in the NGC 4486 system, we would expect to see our parameters be very well-constrained, and indeed that is what we find. Our posterior distributions are among the narrowest we have encountered in our inferences, indicating that we have a high degree of confidence in the values inferred for this system. We display the results of our fits to the GC system in Fig. 4.3.9, and the inferred values for the posterior distributions in Table 4.13.

It is worth noting that NGC 4486 represents what is probably the ideal case for our model, given how it is formulated. Since our contaminant fields are all taken from NGVS, in the proximity of the Virgo cluster, we expect these fields to be very well-matched to the contaminant population around NGC 4486. The data are also all

Table 4.12: NGC 4365 Parameters

Modelled Parameters

Parameter	2.5%	16.0%	50.0%	84.0%	97.5%
f_{red}	0.027	0.048	0.073	0.095	0.125
f_{blue}	0.385	0.424	0.454	0.484	0.512
$\mu_{gi,red}$	0.912	0.93	0.941	0.953	0.965
$\mu_{ri,red}$	0.371	0.387	0.406	0.439	0.478
$\sigma^2_{gi,red}$	0.002	0.003	0.004	0.005	0.008
$\sigma^2_{ri,red}$	0.002	0.004	0.006	0.007	0.009
$\sigma_{gi,red}\sigma_{ri,red}$	0.0	0.001	0.002	0.003	0.005
$\mu_{gi,blue}$	0.715	0.731	0.743	0.757	0.771
$\mu_{ri,blue}$	0.256	0.263	0.269	0.275	0.281
$\sigma^2_{gi,blue}$	0.021	0.024	0.027	0.03	0.033
$\sigma^2_{ri,blue}$	0.005	0.006	0.006	0.007	0.007
$\sigma_{gi,blue}\sigma_{ri,blue}$	0.008	0.009	0.01	0.011	0.013
R_e	0.105	0.11	0.116	0.123	0.129
μ_i	22.407	22.446	22.485	22.527	22.571
σ_i	0.776	0.809	0.845	0.885	0.926

Derived Quantities

Quantity	2.5%	16.0%	50.0%	84.0%	97.5%
$N_{Sources}$	1521.6	1522.9	1524.4	1525.9	1527.6
N_{GCs}	742.7	771.4	802.9	833.3	862.0
N_{RedGCs}	41.6	73.2	111.3	145.0	190.2
$N_{BlueGCs}$	588.1	646.1	692.6	737.7	779.7
N_{GCs} (Extrapolated)	767.0	799.3	833.5	867.9	901.3
N_{RedGCs} (Extrapolated)	43.2	75.9	115.7	150.9	197.5
$N_{BlueGCs}$ (Extrapolated)	609.2	670.5	719.3	767.2	813.3
f_{red}/f_{blue}	0.05	0.1	0.16	0.22	0.32

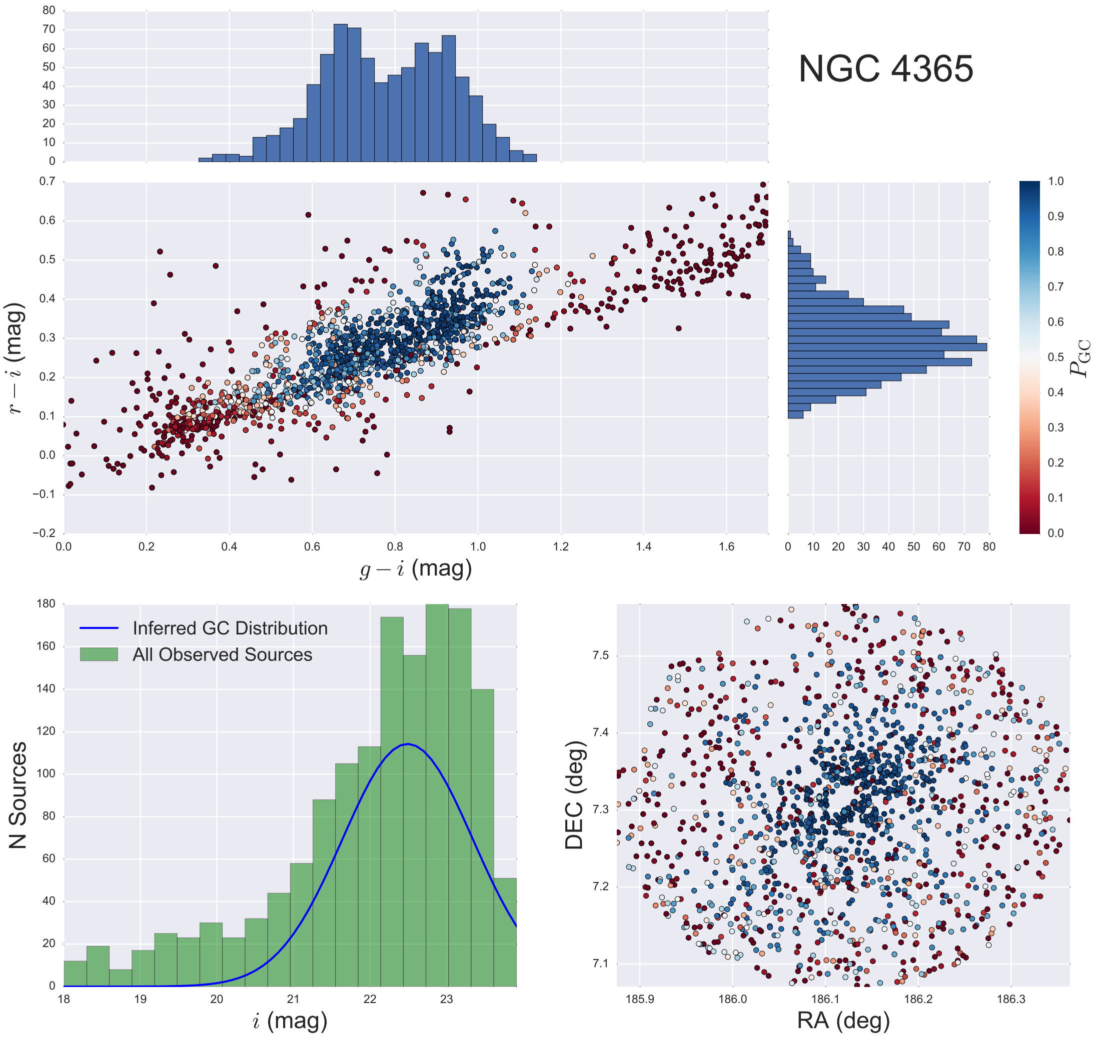

Figure 4.10: Same as for Fig. 4.2, but for NGC 4365.

MEGACAM data, and are of comparable depth, which is important given how our luminosity distribution was trained.

Our chief takeaway from our application to NGC 4486 is that our model performs extremely well in situations that are ideal for it.

4.3.10 NGC 4459

NGC 4459 is another Virgo cluster galaxy, with a fairly average mass for our survey at $\sim 10^{1}1\mathrm{M}_{\odot}$. The galaxy is located in close proximity to two other SLUGGS galaxies, NGC 4473 and 4474. The difficulties here are similar to other systems, like NGC 1400/1407 and NGC 3607/3608, where we expect the GC systems to potentially overlap with each other. We apply our standard methods of making radial cuts, wherein we only include sources within 0.25 degrees, and remove any sources that are closer to either NGC 4473 or NGC 4474 than NGC 4459. Unfortunately, these cuts prevent us from applying our usual spatial modeling procedures, so as with NGC 4111, we disregard spatial information for our fits in NGC 4459.

Despite the intermediate mass of the galaxy, we were unable to get well-behaved fits for this galaxy. Walkers were poorly mixed and influenced heavily by prior information. Given this, we ultimately adopted a procedure similar to NGC 4111, where we took fixed color distributions from NGC 3115. NGC 3115 has very similar mass and morphology to NGC 4459, so it is likely a reasonable choice for this galaxy, although the environment is different (cluster vs. field). After these quantities are fixed, the only free parameters in the model are $\mathrm{f}_{\mathrm{red}}$and $\mathrm{f}_{\mathrm{blue}}$. We show the fitting results for this galaxy in Fig. 4.12 and include the inferred values for the parameters in Table 4.14.

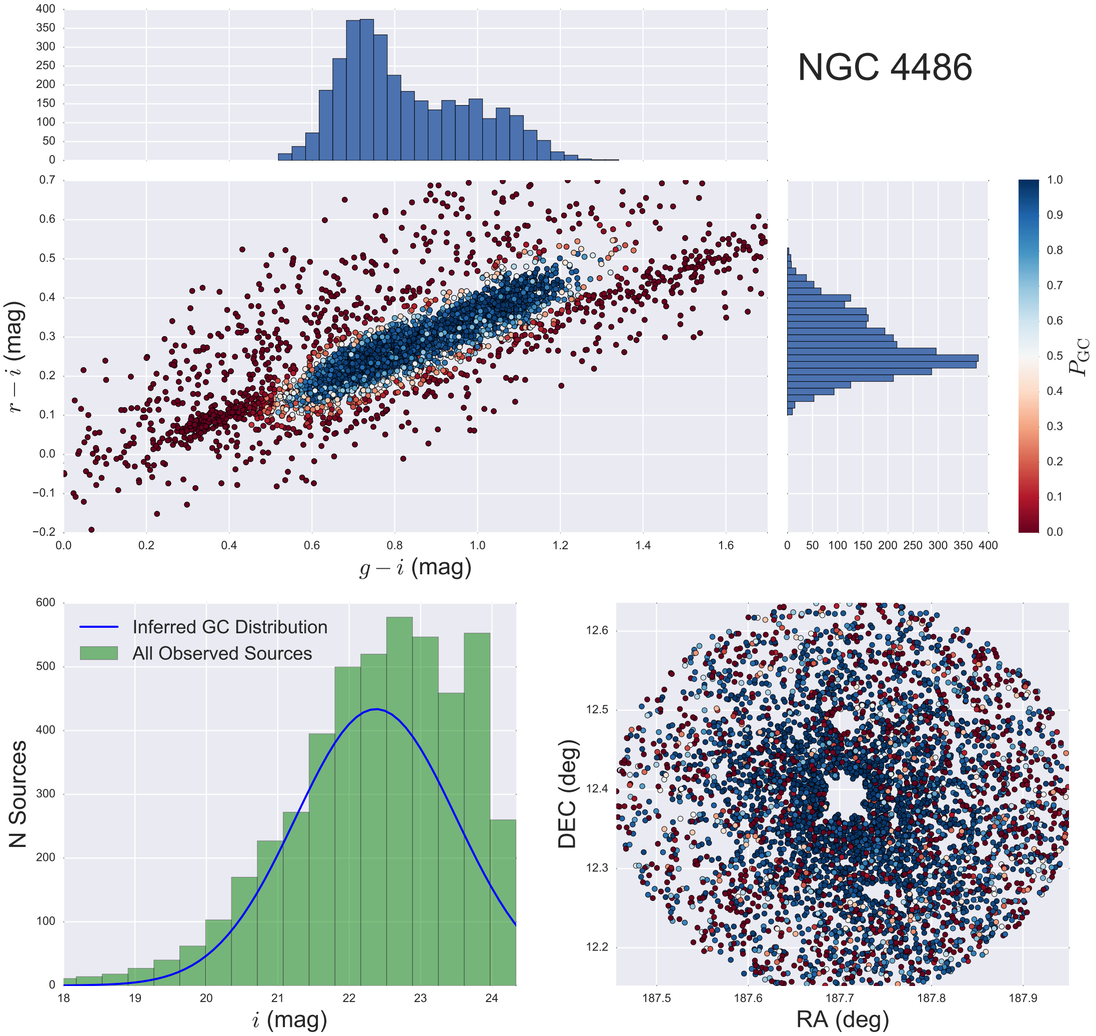

Figure 4.11: Same as for Fig. 4.2, but for NGC 4486.

Table 4.13: NGC 4486 Parameters

Modelled Parameters

Parameter	2.5%	16.0%	50.0%	84.0%	97.5%
f_{red}	0.237	0.251	0.267	0.286	0.314
f_{blue}	0.327	0.354	0.373	0.39	0.405
$\mu_{gi,red}$	0.949	0.967	0.979	0.988	0.997
$\mu_{ri,red}$	0.327	0.336	0.341	0.346	0.351
$\sigma^2_{gi,red}$	0.011	0.012	0.013	0.015	0.018
$\sigma^2_{ri,red}$	0.003	0.004	0.004	0.005	0.005
$\sigma_{gi,red}\sigma_{ri,red}$	0.005	0.006	0.006	0.007	0.009
$\mu_{gi,blue}$	0.714	0.717	0.721	0.724	0.727
$\mu_{ri,blue}$	0.228	0.23	0.231	0.233	0.234
$\sigma^2_{gi,blue}$	0.004	0.005	0.005	0.006	0.006
$\sigma^2_{ri,blue}$	0.002	0.002	0.002	0.002	0.002
$\sigma_{gi,blue}\sigma_{ri,blue}$	0.002	0.002	0.002	0.003	0.003
R_e	0.143	0.147	0.15	0.154	0.159
μ_i	22.321	22.347	22.374	22.401	22.429
σ_i	1.085	1.104	1.125	1.146	1.167

Derived Quantities

Quantity	2.5%	16.0%	50.0%	84.0%	97.5%
$N_{Sources}$	5779.6	5799.8	5820.6	5841.9	5863.4
N_{GCs}	3623.7	3675.5	3730.2	3783.0	3836.2
$N_{Red\ GCs}$	1380.9	1463.1	1555.1	1666.0	1827.6
$N_{Blue\ GCs}$	1906.4	2062.5	2171.3	2267.6	2356.2
N_{GCs} (Extrapolated)	3883.2	3952.5	4028.5	4105.4	4184.0
$N_{Red\ GCs}$ (Extrapolated)	1487.6	1578.5	1679.9	1801.8	1980.7
$N_{Blue\ GCs}$ (Extrapolated)	2061.1	2224.8	2344.6	2452.7	2556.5
f_{red}/f_{blue}	0.59	0.65	0.72	0.8	0.96

Table 4.14: NGC 4459 Parameters

Modelled Parameters

Parameter	2.5%	16.0%	50.0%	84.0%	97.5%
f_{Red}	0.013	0.031	0.048	0.067	0.086
f_{Blue}	0.101	0.122	0.145	0.169	0.193

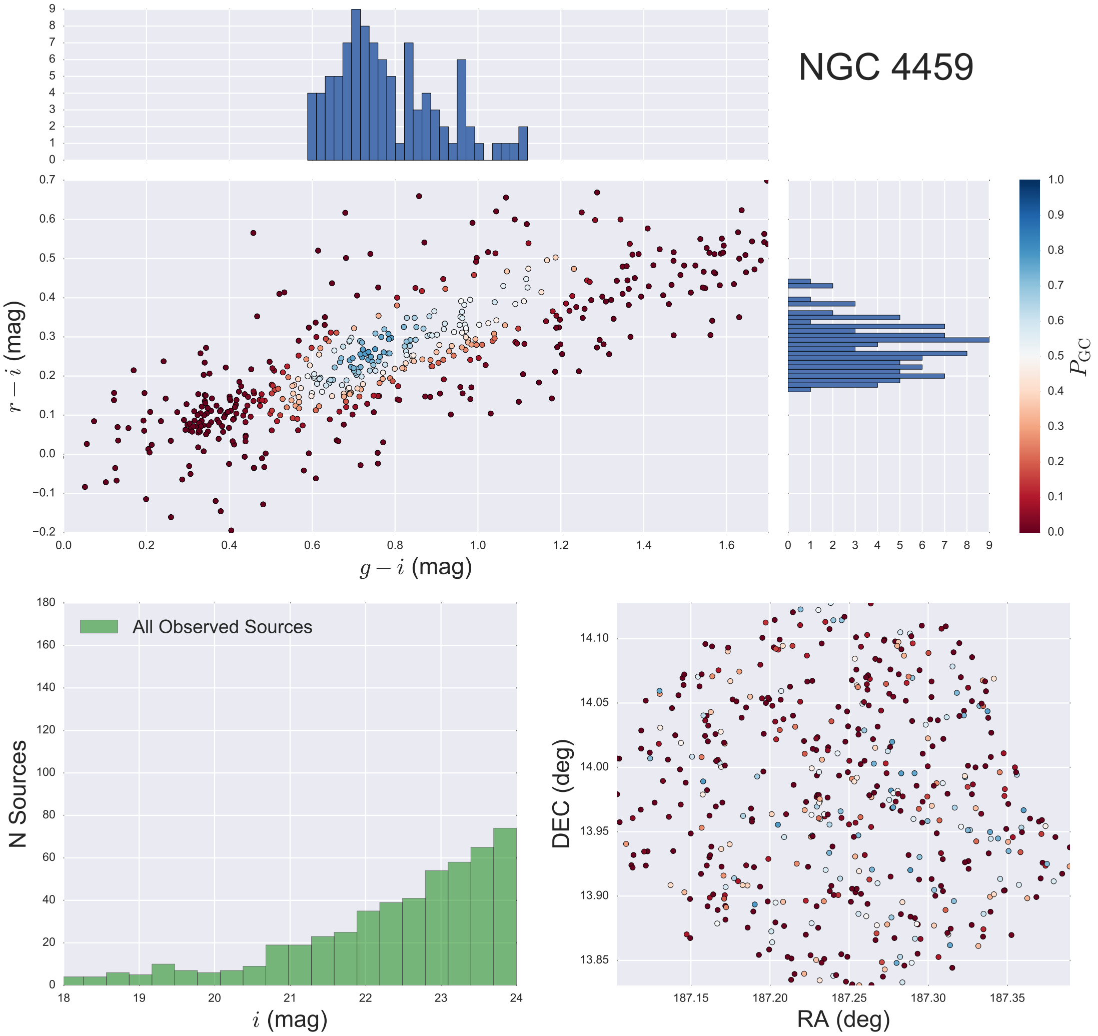

Figure 4.12: Same as for Fig. 4.2, but for NGC 4459. Note that spatial and luminosity information was not fit for NGC 4111, and color distributions were fixed to match those of NGC 3115. The only free parameters in the inference are the $f_{\rm red}$and $f_{\rm blue}$mixture distribution strengths. Because there is no i-band fit, we don't display any fit in the bottom left panel.

4.3.11 NGC 4494

NGC 4494 is a medium-sized E1/2 galaxy, also located in the Virgo cluster. (Foster et al., 2011) presented a combined photometric and spectroscopic analysis of the NGC 4494 GC system, finding typical GC system properties. Bimodality was statistically favored, and kinematical evidence for a third GC population was found.

We display the results of our fits to NGC 4494 in Fig. 4.3.11, and the inferred values for our model parameters in Table 4.15. Fits to the red population of NGC 4494 are complicated by the fact that the distributions for the red population wish to expand to be quite large, beyond where we would typically expect GCs to be found. We experimented with more informative priors, but the red GC distribution would still expand to fill much of this space. Given the possibility of a more complex, non-bimodal GC color distribution, it is possible the model is not well suited to fit NGC 4494. It is also possible that underlying differences between the

4.3.12 NGC 4697

NGC 4697 is a mid-sized, fairly nearby E6 galaxy. While the field was very well populated with sources, the actual number of GCs is expected to be smaller given the size of the galaxy. We found a typical bimodal population fit the NGC 4697 system well, with two distinct, well-separated populations. We show our fits to the system in Fig. 4.3.12. NGC 4697 is a good indication that our method is capable of recovering good GC populations even when the field has a good population of contaminants, as long as the populations are well-described by the model. We also give the inferred values

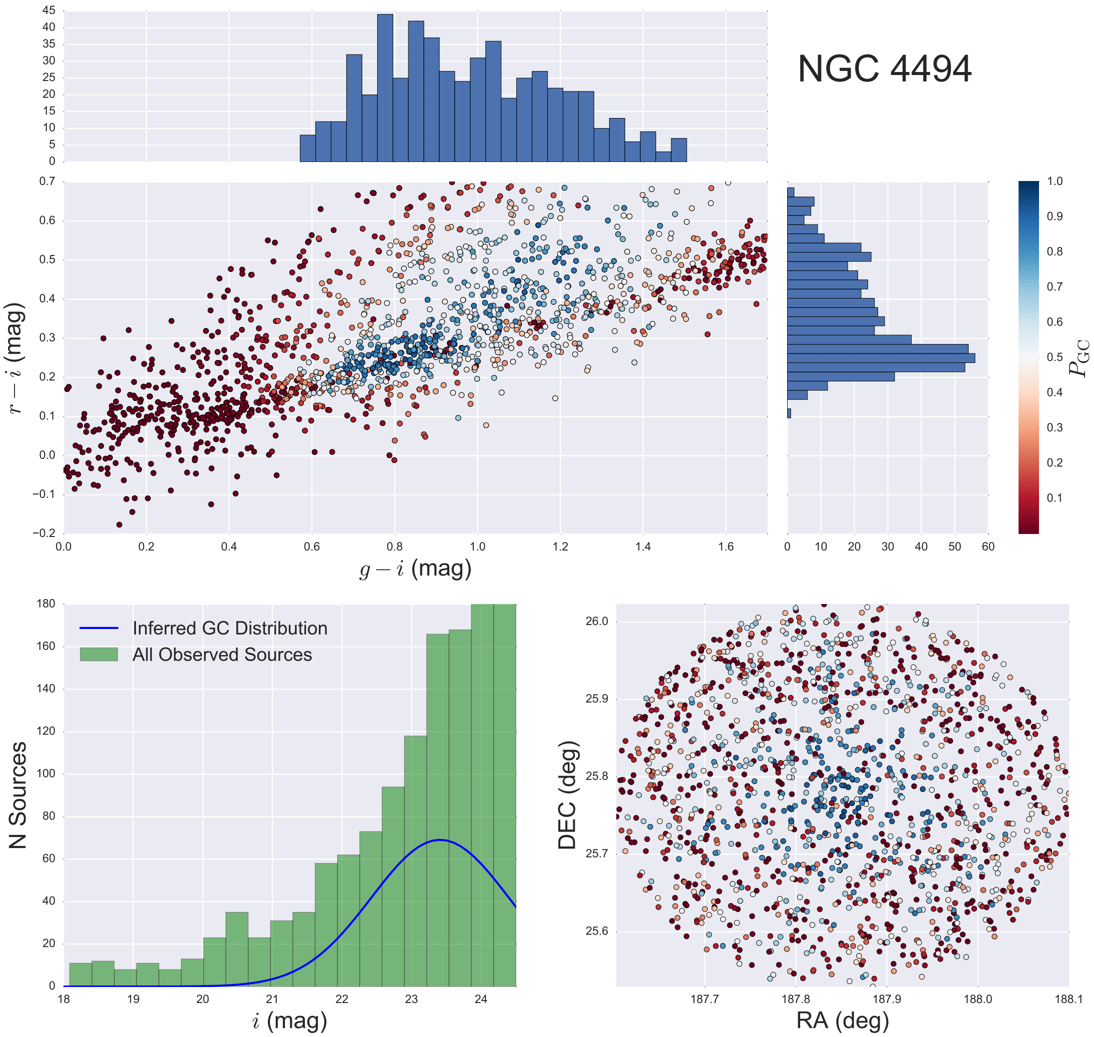

Figure 4.13: Same as for Fig. 4.2, but for NGC 4494.

Table 4.15: NGC 4494 Parameters

Modelled Parameters

Parameter	2.5%	16.0%	50.0%	84.0%	97.5%
f_{red}	0.185	0.219	0.25	0.282	0.313
f_{blue}	0.097	0.11	0.125	0.141	0.157
$\mu_{gi,red}$	1.028	1.049	1.073	1.097	1.121
$\mu_{ri,red}$	0.388	0.394	0.398	0.399	0.4
$\sigma^2_{gi,red}$	0.037	0.046	0.055	0.065	0.076
$\sigma^2_{ri,red}$	0.012	0.014	0.016	0.018	0.021
$\sigma_{gi,red}\sigma_{ri,red}$	0.007	0.01	0.013	0.016	0.02
$\mu_{gi,blue}$	0.745	0.761	0.777	0.793	0.808
$\mu_{ri,blue}$	0.229	0.235	0.24	0.246	0.252
$\sigma^2_{gi,blue}$	0.009	0.011	0.014	0.017	0.022
$\sigma^2_{ri,blue}$	0.001	0.002	0.002	0.002	0.003
$\sigma_{gi,blue}\sigma_{ri,blue}$	0.002	0.003	0.004	0.005	0.006
R_e	0.169	0.192	0.219	0.254	0.296
μ_i	23.252	23.328	23.409	23.487	23.567
σ_i	0.872	0.925	0.986	1.054	1.125

Derived Quantities

Quantity	2.5%	16.0%	50.0%	84.0%	97.5%
$N_{Sources}$	1641.5	1656.3	1672.2	1690.1	1709.9
N_{GCs}	512.1	572.9	628.7	685.2	744.3
N_{RedGCs}	305.3	362.5	419.1	475.2	531.4
$N_{BlueGCs}$	161.4	183.7	209.0	236.7	264.0
N_{GCs} (Extrapolated)	668.4	768.6	866.8	973.1	1090.3
N_{RedGCs} (Extrapolated)	401.2	488.1	578.1	670.6	774.1
$N_{BlueGCs}$ (Extrapolated)	217.2	250.1	288.2	329.8	373.0
f_{red}/f_{blue}	1.3	1.62	2.01	2.44	2.92

for our model parameters in Table 4.16.

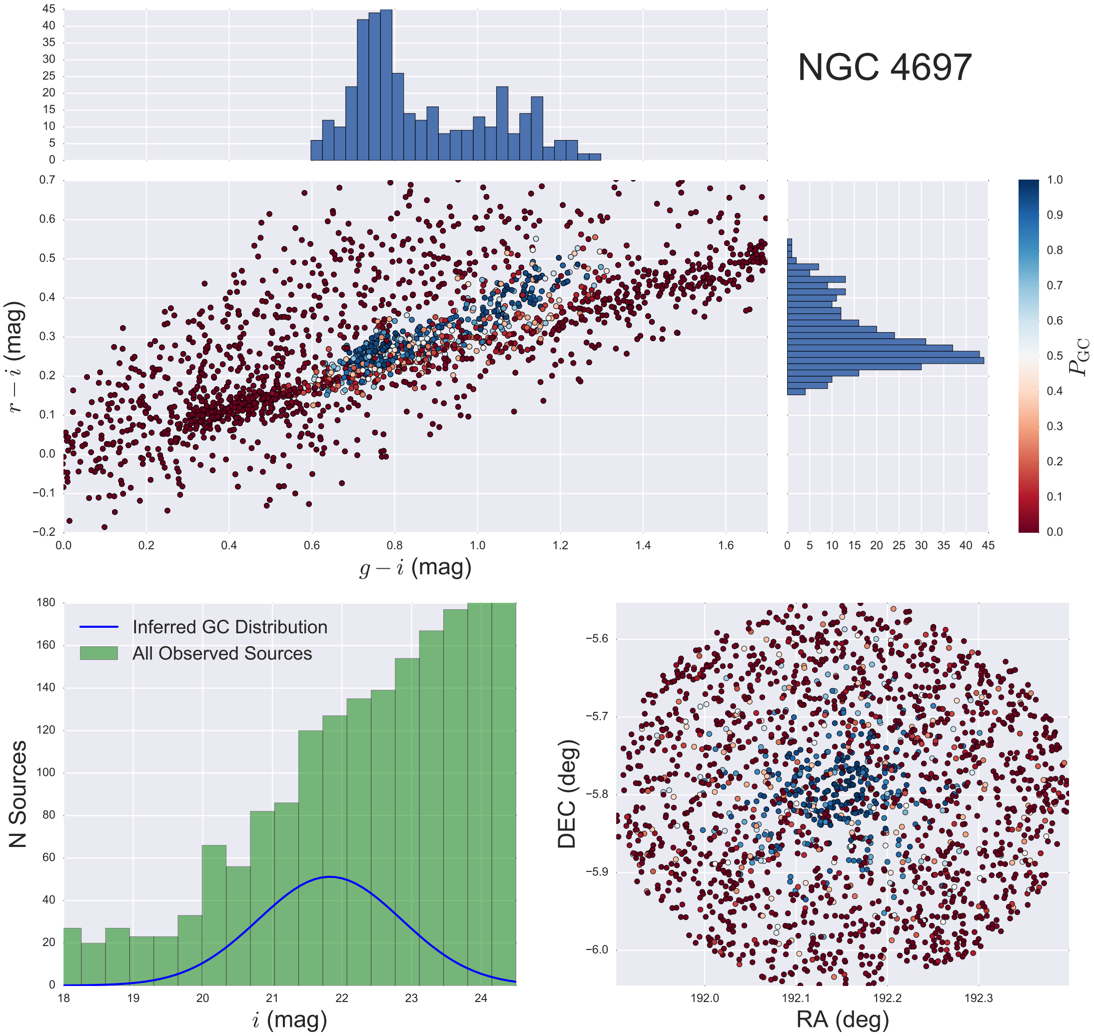

Figure 4.14: Same as for Fig. 4.2, but for NGC 4697.

Table 4.16: NGC 4697 Parameters

Modelled Parameters

Parameter	2.5%	16.0%	50.0%	84.0%	97.5%
f_{red}	0.045	0.053	0.061	0.069	0.08
f_{blue}	0.086	0.097	0.108	0.119	0.131
$\mu_{gi,red}$	1.026	1.054	1.076	1.094	1.11
$\mu_{ri,red}$	0.358	0.371	0.383	0.393	0.403
$\sigma^2_{gi,red}$	0.006	0.008	0.01	0.013	0.017
$\sigma^2_{ri,red}$	0.003	0.004	0.005	0.006	0.007
$\sigma_{gi,red}\sigma_{ri,red}$	0.002	0.003	0.005	0.006	0.009
$\mu_{gi,blue}$	0.744	0.752	0.761	0.769	0.777
$\mu_{ri,blue}$	0.244	0.247	0.251	0.254	0.258
$\sigma^2_{gi,blue}$	0.003	0.005	0.006	0.008	0.01
$\sigma^2_{ri,blue}$	0.001	0.001	0.002	0.002	0.002
$\sigma_{gi,blue}\sigma_{ri,blue}$	0.001	0.002	0.002	0.003	0.004
R_e	0.071	0.076	0.081	0.087	0.093
μ_i	21.68	21.751	21.826	21.909	21.994
σ_i	0.911	0.968	1.03	1.1	1.177

Derived Quantities

Quantity	2.5%	16.0%	50.0%	84.0%	97.5%
$N_{Sources}$	2446.2	2450.4	2455.0	2459.8	2464.0
N_{GCs}	358.9	385.7	415.1	443.0	474.1
N_{RedGCs}	111.3	128.9	149.0	170.4	196.1
$N_{BlueGCs}$	211.1	238.5	264.6	292.7	320.4
N_{GCs} (Extrapolated)	363.5	391.9	422.8	453.4	487.6
N_{RedGCs} (Extrapolated)	112.8	131.1	151.9	174.0	200.9
$N_{BlueGCs}$ (Extrapolated)	214.0	242.5	269.8	298.8	328.1
f_{red}/f_{blue}	0.38	0.46	0.56	0.68	0.85

4.4 SUMMARY AND DISCUSSION

We reduced Subaru SuprimeCam wide field imaging for a subset of 13 SLUGGS galaxies, supplemented with additional CFHT MegaCam imaging. We then created full photometric catalogs using aperture photometry through SExtractor. After combining the catalogs, we have full three-filter photometric data for thousands of sources in each mosaic. We performed point-source cuts, then measured completeness curves for all data and applied our Bayesian fitting methodology from Chapter 3 to the photometric catalogs for these systems.

We in general had mixed-success applying the Bayesian fitting methodology to the GC systems of galaxies. While we were ultimately able to obtain fits to all galaxies using the model, it frequently had to be modified slightly to obtain reasonable fits for the GC system, often by fixing certain parameters or including stronger priors. Ultimately, we were able to obtain reasonable bimodal fits for NGC 1400, 1407, 2768, 3607, 3608, 3115, 4486, 4494, and 4697. NGC 3115 and 4494 both required strong priors to obtain these fits, and even then the fits to NGC 4494 were not perfect; when covariance matrices were left free, we found that some very red sources were still considered likely GCs due to the width of the red GC distributions. However, despite these difficulties, the resulting fits appeared well mixed, and the inferences (especially for which sources are likely to be GCs) appear to be strong. Difficulties may arise when directly interpreting the inferred values for the GC color distributions especially.

NGC 4365 suffered from the opposite problem to NGC 4494; the blue GC distribution tended to become very wide, and even though the red GC distribution was positioned in a reasonable location, the large values for the spread of the blue population meant that the ratio of f_{red} to f_{blue} was unusually small. NGC 4365 has been noted in the past for its strange color distribution (Blom et al., 2012b), with previous suggestions of trimodality in the GC system. While our model, as currently specified, cannot test whether a trimodal fit is a good one for this system, the difficulties of the bimodal multivariate normal distribution in fitting the system indicates that expanding the model is a reasonable step. Trimodality could be an avenue to pursue here, although other model-expansion methods might also work.

NGC 4278 has been previously claimed to have a strong detection of bimodality (Usher et al., 2012; Pota et al., 2013b). However, we found that we were unable to get reasonable fits with a bimodal model. Specifying informative priors simply meant that the posterior distributions for the means of the red distribution ran right up to the edge of the allowed space, and the width of the red distribution would then expand to compensate. We ultimately elected to simply use a unimodal distribution to fit this galaxy, for which we achieved reasonable fits. While a bimodal model might still ultimately be a reasonable description of the GC system, our current methodology couldn't achieve strong fits for it.

Finally, NGC 4111 and 4459 both suffer from having extremely small GC populations. We attempted to leave various parameters free, but fits were never satisfactory for either galaxy, with distributions often expanding to fill all available parameter space. We ultimately decided, for these galaxies, to neglect spatial and luminosity information and fixed the color distributions to those values from NGC 3115. This essentially is placing extremely strong prior information on the distributions of these galaxies, and any inferences gleaned from these galaxies must incorporate that information. In addition, by neglecting luminosity information, we are unable to correct for the incompleteness in these galaxies in our current formulation of the fitting model, which requires parameterization of the GC luminosity distribution. While the distribution could in principle be fixed to a certain value and then corrected for incompleteness, the values to fix the distribution to are distance dependent, and it is unclear that our uncertainties on the completeness correction would be meaningful anyway in that case.

Overall, the fitting methodology produced at least some information about all 13 galaxies analyzed. We felt the full model performed well in nine of the 13 cases, and in the remaining ones, the inference is still meaningful, but must be viewed with larger caveats. The ability of the model to infer values for the GC distributions of these galaxies, while simultaneously incorporating contamination and incompleteness of the data, offers a powerful tool for GC photometry analysis. Application of the model to more galaxies will allow for better galaxy-to-galaxy comparisons in the context of other galaxy properties, allowing a better understanding of the link between GC system evolution and galaxy assembly.

Chapter 5

NGC 3628-UCD1: A possible ω Cen Analog Embedded in a Stellar Stream

5.1 INTRODUCTION

Since the discovery of ultra-compact dwarfs (UCDs) a decade and a half ago (Hilker et al., 1999; Drinkwater et al., 2000), there has been considerable discussion in the literature regarding their origin. The conversation can be distilled down to a simple question: are UCDs the largest star clusters, or the smallest galaxies?

The earliest UCDs discovered have $R_h \sim 20$ pc and luminosities $> 10^7$ $L_\odot$. These objects represent a middle-ground between globular clusters (GCs), with R_h of ~ 3 pc and luminosities of $\sim 10^6$ $L_\odot$, and dwarf galaxies, with $R_h > 100$ pc. Expanded observational studies have found that UCDs occupy a sequence with similar luminosity to GCs, but larger R_h (Brodie et al., 2011; Misgeld & Hilker, 2011; Norris et al., 2014). We adopt the definition of UCDs from Brodie et al. (2011): UCDs are objects with R_h ranging from ∼10 to 100 pc, and luminosities $M_i < -8.5$ mag (or $L_i > 10^5 L_\odot$).

The simplistic galaxy vs. cluster distinction breaks down further. UCDs could include objects resulting from mergers of globular clusters (e.g. Fellhauer & Kroupa 2002; Kissler-Patig et al. 2006), or objects formed primordially in intense star formation episodes (Murray, 2009). Characterizing the UCD population would have implications for cluster formation physics. In the galaxy scenario, these objects could form primordially in association with distinct dark-matter halos, or they could be the remnant nuclei of larger galaxies which have undergone tidal stripping during accretion onto larger galaxy halos (e.g. Bekki et al. 2001; Pfeffer & Baumgardt 2013). Understanding the origins of the UCD population has important implications for understanding sub-halos in a ΛCDM context.

The most massive Milky Way (MW) GC, ω Cen, is an outlier among the MW population and may be an example of a sripped dwarf-galaxy nucleus. The cluster has a large velocity dispersion (e.g. Anderson & van der Marel 2010), rapid rotation leading to flattening (e.g. Merritt et al. 1997), unusual abundance patterns revealing multiple populations (e.g. King et al. 2012), and odd orbital properties (e.g. Dinescu et al. 1999). However, definite confirmation of this formation scenario has remained elusive.

In this work, we identify and describe a star cluster, which we call NGC 3628-UCD1 (hereafter UCD1), embedded in a stellar stream around the nearby spiral galaxy

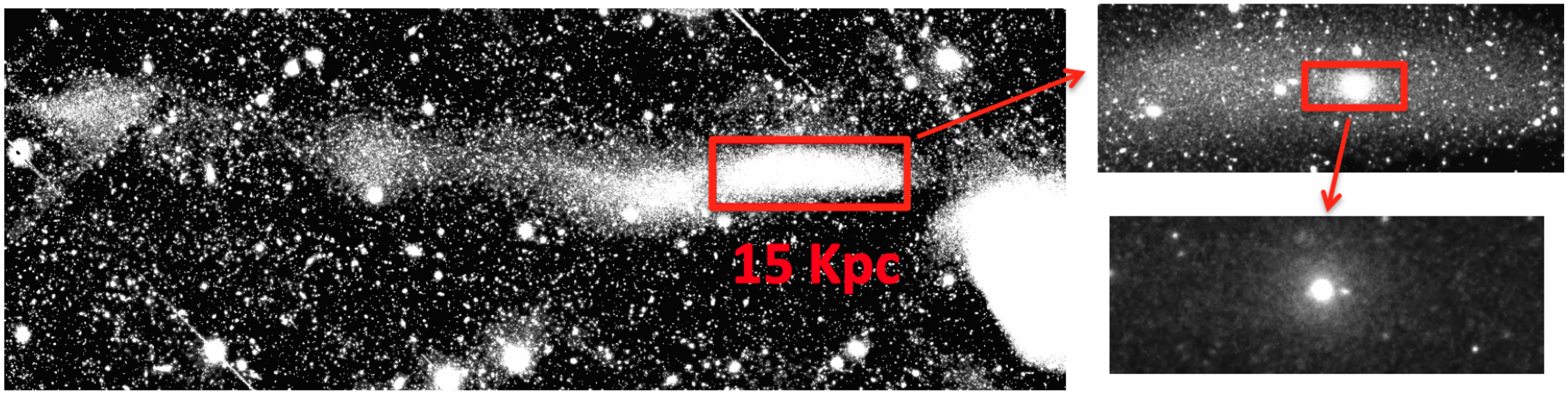

Figure 5.1: Smoothed image of stellar stream next to NGC 3628 from our i-band Subaru/SuprimeCam imaging. The left-most edge of NGC 3628 is visible at the far right of the image. We highlight the location of UCD1 in zoom-in panels. North is up and east is left. The limiting surface brightness in the large image is roughly $\mu_i \sim 28.5$ mag arcsecond^{-2}. The stretch is modified in each image. Angular sizes are approximately 26x10 arcmin, 4.5x1.5 arcmin, and 0.9x0.4 arcmin from largest to smallest scale.

NGC 3628. NGC 3628 is an Sb galaxy with $M_V = -21.37$. It is located in the Leo Triplet, a loose group with two other large companions, NGC 3623 and NGC 3627. An obvious stellar stream extends ∼140 kpc away from the galaxy, shown in Fig. 1. UCD1 is located within the plume nearest to NGC 3628. As shown in §5.2, UCD1's size and luminosity are very similar to those of ω Cen.

The stream itself has been studied extensively since its first characterization (Zwicky, 1956; Kormendy & Bahcall, 1974). The stream contains significant neutral hydrogen (Rots, 1978; Haynes et al., 1979). Chromey et al. (1998) identified two blue clumps along the stream and estimated young ages for both.

There are several known examples in the literature of UCDs connected with tidal stripping events. Norris & Kannappan (2011) identified a young UCD around NGC 4546 and argued, based on the properties of the galaxy, that it is a result of stripping. Foster et al. (2014) identified an object likely to be the nucleus of the dwarf galaxy forming the "umbrella stream" around NGC 4651. Mihos et al. (2015) identify a nucleus of an ultra diffuse galaxy in Virgo, which they argue is in the process of tidal threshing.

Using Subaru/Suprime-Cam imaging, we measure photometry and size of both UCD1 and the full stellar stream. We propose that UCD1 is an example of a UCD in formation through tidal stripping. By measuring the UCD and inferring the properties of the potential progenitor galaxy, we are able to draw an evolutionary line in size/luminosity parameter space between the original parent galaxy and the stripped cluster. In §5.2, we explain our imaging analysis and results, and in §5.3, we do the same for our spectroscopy. We discuss our results in §5.4.

NGC 3627 has a Cepheid distance measurement of 10.6 Mpc (Kanbur et al., 2003). We adopt this value for NGC 3628 and include an approximate distance uncertainty of ±1 Mpc on distance-dependent properties, given the potential offset of NGC 3628 from NGC 3627.

5.2 Imaging

5.2.1 Data Reduction

We imaged NGC 3628 in r-band for 425s on 2009 April 20th with the Suprime-Cam instrument on the Subaru Telescope. UCD1, a marginally-resolved source in the center of plume just east of NGC 3628, was first noticed in this pointing. We subsequently acquired imaging centered on UCD1 in the i-band on 2014 March 3 (425s exposure time) and in the g-band on 2014 December 19 (1225s exposure time). Seeing was $\sim 0.80''$, $\sim 0.70''$, and $\sim 0.75''$ in g, r, i respectively. We employed a modified version of the SDFRED-2 pipeline[15] to reduce our Suprime-Cam data. AB Zeropoints were calculated by comparing photometry for bright, unsaturated stars in both the SDSS catalog and the Suprime-Cam imaging. We used the Schlafly & Finkbeiner (2011) values from NED to correct for Galactic extinction.

---

[15] http://subarutelescope.org/Observing/Instruments/SCam/sdfred/sdfred2.html.en

UCD1 Properties

Parameter	Value	Uncertainty
R.A. (J2000, from SDSS)	170.25493	-
Dec (J2000, from SDSS)	13.60813	-
Suprime-Cam Photometry		
g	19.98 mag	0.05 mag
r	19.57 mag	0.04 mag
i	19.29 mag	0.04 mag
$(g-r)$	0.41 mag	0.05 mag
$(g-i)$	0.69 mag	0.05 mag
R_h, r-band	10 pc	3 pc
Ellipticity	0.9	-
Luminosity	$L_i = 1.4 \times 10^6$ $L_\odot$	$\pm 0.2 \times 10^6$ $L_\odot$
ESI Spectroscopy		
Vel.	815 km s^{-1}	4 km s^{-1}
Vel. Dispersion	$\lesssim$ 23 km s^{-1}	-
Age	6.6 Gyr	$^{+1.9}_{-1.5}$ Gyr
[Z/H]	-0.75	0.12
[α/Fe]	-0.10	0.08
MODS Spectroscopy		
Age	6.6 Gyr	$^{+1.4}_{-1.2}$ Gyr
[Z/H]	-0.77	0.16
[α/Fe]	-0.08	0.15

Surface Photometry

Filter	Apparent Mag	Luminosity
Full Stream		
g	14.15 mag	$(2.7 \pm 0.5) \times 10^8$ $L_\odot$
i	13.14 mag	$(4.1 \pm 0.8) \times 10^8$ $L_\odot$
$(g-i)$	1.01 mag	-
Plume Containing UCD1		
g	15.34 mag	$(9.^{+1.8}_{-1.7}) \times 10^7$ $L_\odot$
i	14.19 mag	$(1.6 \pm 0.3) \times 10^8$ $L_\odot$
$(g-i)$	1.15 mag	-

5.2.2 Photometry and Size of UCD1

We performed aperture photometry of UCD1 using an aperture roughly twice the size of the FWHM for each image, chosen to maximize the S/N. Aperture corrections were measured using several bright, unsaturated stars in the field. Uncertainties in aperture corrections were 0.04 mag in g and 0.03 mag in r and i. Choice of sky subtraction annulus introduced systematic uncertainties of 0.03 in all filters, with no effect on color. Our photometry is listed in Table 1. At our assumed distance, the luminosity of UCD1 is $\mathrm{L_i} = (1.4 \pm 0.2) \times 10^6\ \mathrm{L_\odot}$ with the uncertainty dominated by the distance. The color measured for UCD1 is dependent on the aperture selected. When an aperture equal to the FWHM is used, the color is $g - i = 0.86$, which is comparable to $g - i = 0.91$ inferred from the stellar populations in the ESI spectrum (see §5.3). Note that the seeing FWHM in our imaging is roughly comparable to the width of the ESI slit used. Using the max S/N aperture results in bluer colors ($g - i = 0.69$). This effect may be due to contamination by the stream, or could be caused by some gradient intrinsic to UCD1. Robust determination of UCD1's color will require more sophisticated stream/source decomposition. Given the varying quality of our ground-based images, our current dataset is not well-suited to this task.

UCD1 is marginally resolved in our imaging; we used *ishape* (Larsen, 1999) to measure $\mathrm{R_h}$, exploring Sersic and King profile fits. *ishape* convolves a model light profile with an empirical PSF and fits it to the source. We measured the PSF from bright, unsaturated stars in the FOV. Both Sersic and King profiles feature a parameter to describe the shape of the profile. When left completely free, the resulting fits featured unphysical values for shape parameters. However, we found that varying these parameters over a reasonable range changed $\mathrm{R_h}$ at roughly the 20% level.

Across all filters, a model+PSF was always a better fit than the PSF-only model. As the r-band imaging features the best seeing, we adopt our r-band fits for UCD1's fiducial $\mathrm{R_h}$. In general, fits to the i-band data tended to be ∼10% smaller, while fits in g-band data tended to be ∼10% larger than r-band measured $\mathrm{R_h}$.

We find a size of 7.5 pc for a $c = 15$ a King profile and 12.5 pc for an $n = 4$ Sersic profile The differences in residuals are not large between the two assumed models. We ultimately choose to adopt the average of the two values and note a ±2 pc systematic uncertainty on this measurement depending on the choice of profile. We also note the 10% uncertainty from our assumed distance, as well as ∼20% scatter for choices of concentration parameter. Our final r-band $\mathrm{R_h}$ estimate for UCD1 is thus 10 ± 3 pc.

5.2.3 Surface Photometry of NGC 3628 Stream

One possible explanation for the stellar stream is the accretion of a dwarf galaxy. If this scenario is true, then the total luminosity of the NGC 3628 stream offers a useful constraint on the luminosity of this accreted dwarf.

The Suprime-Cam reduction pipeline subtracts a constant sky brightness off the image. We use SExtractor to model any remaining varying background, adopting a mesh size of 512 pixels. This size was chosen to be significantly larger than the stream. We inspected the background maps to verify the stream was not being included. Bright objects were masked in the imaging. We then use *adaptsmooth* (Zibetti, 2009; Zibetti et al., 2009) to perform adaptive smoothing to a uniform signal to noise ratio (S/N) on the background-subtracted images. We select a S/N threshold of five (limiting surface brightness of $\mu_i \sim 28.5$ mag arcsecond^{-2}).

We performed aperture photometry of the stream in this smoothed image using a custom aperture (the same for all filters) and the *polyphot* task in IRAF, with pixels below the S/N threshold excluded from the measurement. The resulting measurements are listed in Table 2.

We measure a total apparent i-band magnitude of 13.14. Statistical uncertainties are small (a few thousandths of a magnitude), but doubling or halving the required signal-to-noise modifies the final answer by around 0.1 mag. We adopt ±0.1 mag as a rough estimate of the systematic uncertainty in the measurement, which is smaller than the distance uncertainty (±0.2 mag). The total luminosity of the stream is $\mathrm{L}_i \simeq (4.1 \pm 0.8) \times 10^8$ $\mathrm{L}_\odot$. We emphasize that this estimate could miss additional starlight below our detection threshold or behind NGC 3628, or could include contamination from faint contaminant point sources, and therefore should be regarded with caution when interpreted directly as the accreted galaxy luminosity. We measure $g - i = 1.01$ for the color of the full stream.

The plume which contains UCD1 has $i = 14.19$ and $g = 15.34$, giving $(g-i) = 1.15$. The approximate area used for the aperture photometry is marked in Fig. 1. Using the galaxy stellar population models of Into & Portinari (2013), the corresponding i-band stellar mass-to-light ratio ($\mathrm{M/L}_*$) is 2.5–2.9. This color may be more representative of the stellar population of the progenitor dwarf galaxy, as the full-stream measurement can be more sensitive to contaminants and choice of aperture. Both the plume and full stream color and luminosity measurements fall on the red side of galactic scaling relations from Janz & Lisker (2009), but they still are broadly within the scatter.

5.3 SPECTROSCOPY OF UCD1

A 3600s KECK/ESI spectrum of NGC3628 UCD1 was acquired on 2014 March 20th with the $0.75''$ longslit, with a S/N of $\sim$23 Å^{-1}. We subsequently acquired a 2400s LBT/MODS spectrum on 2015 June 6th with the $0.80''$ longslit, with a S/N of $\sim$15 Å^{-1}. We follow the same procedure as Janz et al. (2015) to measure stellar populations. Briefly, we measure all Lick indices. These are then compared to the single stellar population models of Thomas et al. (2011), which give the best age, metallicity and alpha element abundance via a χ^2 minimization process. Poorly fitting lines are excluded from the analysis in an iterative way. The final fit and residuals to both the observed spectra are shown in Fig. 5.2.

For the ESI spectrum, we find an old age of $6.6^{+1.9}_{-1.5}$ Gyr and a metal-poor population of $[Z/H] = -0.75 \pm 0.12$, and alpha-element abundance of $[\alpha/Fe] = -0.10 \pm 0.08$. The MODS spectrum gives consistent results, with an age of , $6.6^{+1.4}_{-1.2}$ Gyr, $[Z/H] = -0.77 \pm 0.16$ and $[\alpha/Fe] = -0.08 \pm 0.15$. Using the relation $[Fe/H] = [Z/H] - 0.94 \times [\alpha/Fe]$ (Thomas et al., 2003), we find $[Fe/H] = -0.84$ for the ESI data.

As the ESI spectrum has higher resolution, we use it to measure kinematics (MODS is limited to $\sigma \sim$55 km s^{-1}). We measure a heliocentric velocity of 815±4 km s^{-1}. While we find a best-fit velocity dispersion of 10.5 km s^{-1}, this measurement is significantly below the resolution of the ESI spectrograph (σ =23 km s^{-1}). Velocity

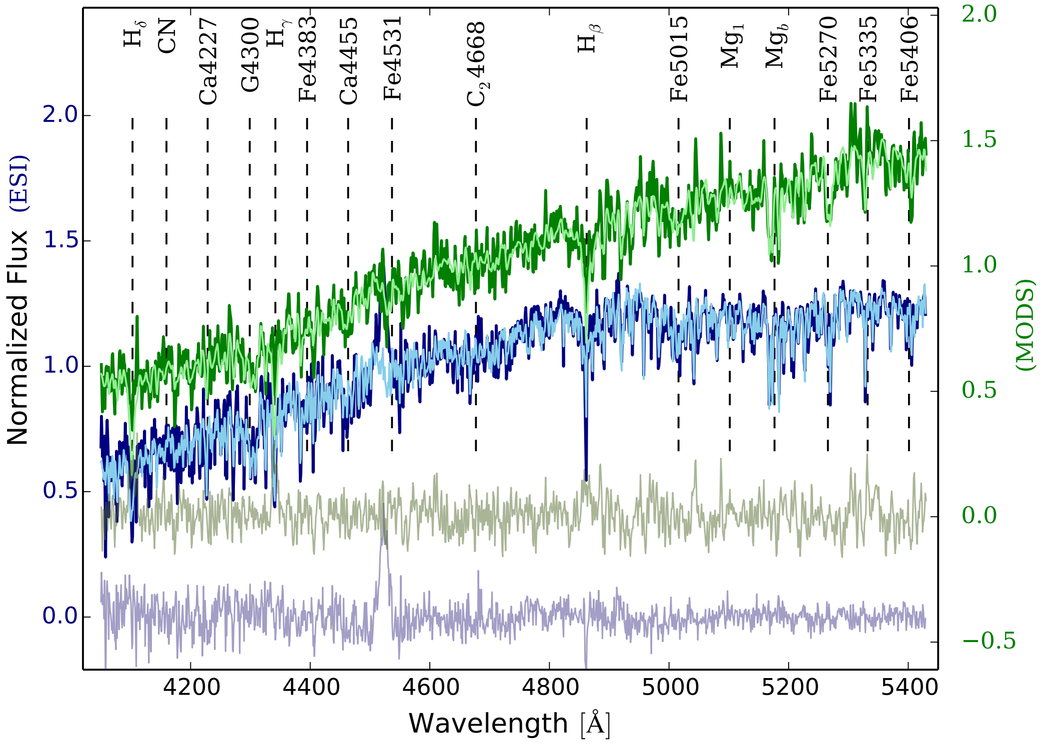

Figure 5.2: Keck/ESI and LBT/MODS spectra of UCD1. ESI data are shown in dark blue, while MODS data are shown in dark green. Light blue and light green represent model fits to both spectra. Residuals are shown at the bottom. The MODS scale is offset from the ESI scale.

dispersions so low include unquantified systematics, and it is unclear if meaningful constraint can be obtained that low (see also Geha et al. 2002; Janz et al. 2015). As a result, we adopt σ =23 km s^{-1} as the upper limit for the velocity dispersion.

We may make an estimate of the dynamical mass of UCD1 using the expression $M_{\mathrm{dyn}} = CG^{-1}\sigma^2 R$, where R is taken to be the half-light radius and C is the viral coefficient. We follow Forbes et al. (2014) and adopt a value of 6.5, although values between 4 to 7.5 are reasonable. Given this expression and using our measured size of 10 pc, we estimate M_{dyn} to be less than $\sim 8 \times 10^6$ $M_{\odot}$.

There is a significant offset of ~75 km s^{-1} between the measured heliocentric velocity of UCD1 and the heliocentric velocity measured from the HI gas in the stream. Nikiel-Wroczyński et al. (2014) found a gas velocity of ~890 km s^{-1} in the vicinity of UCD1. While this could indicate that UCD1 is not associated with the stream, we find this unlikely. UCD1 appears directly at the center of the brightest plume in the stream, and displays a blotchy morphology similar to that in the stream itself. UCD1 is the brightest point in the stream, with the surface brightness of the stream falling off slowly in all directions away from UCD1. It is unclear that we would expect the velocity of the HI gas to follow that of the stream; the gas obeys different physics than the stars in the stream (e.g. ram pressure stripping), and so it would not be surprising to see a velocity offset between the two. UCD1 is blue-shifted by ~30 km s^{-1} compared to NGC 3628, while the gas is red-shifted by ~45 km s^{-1}.

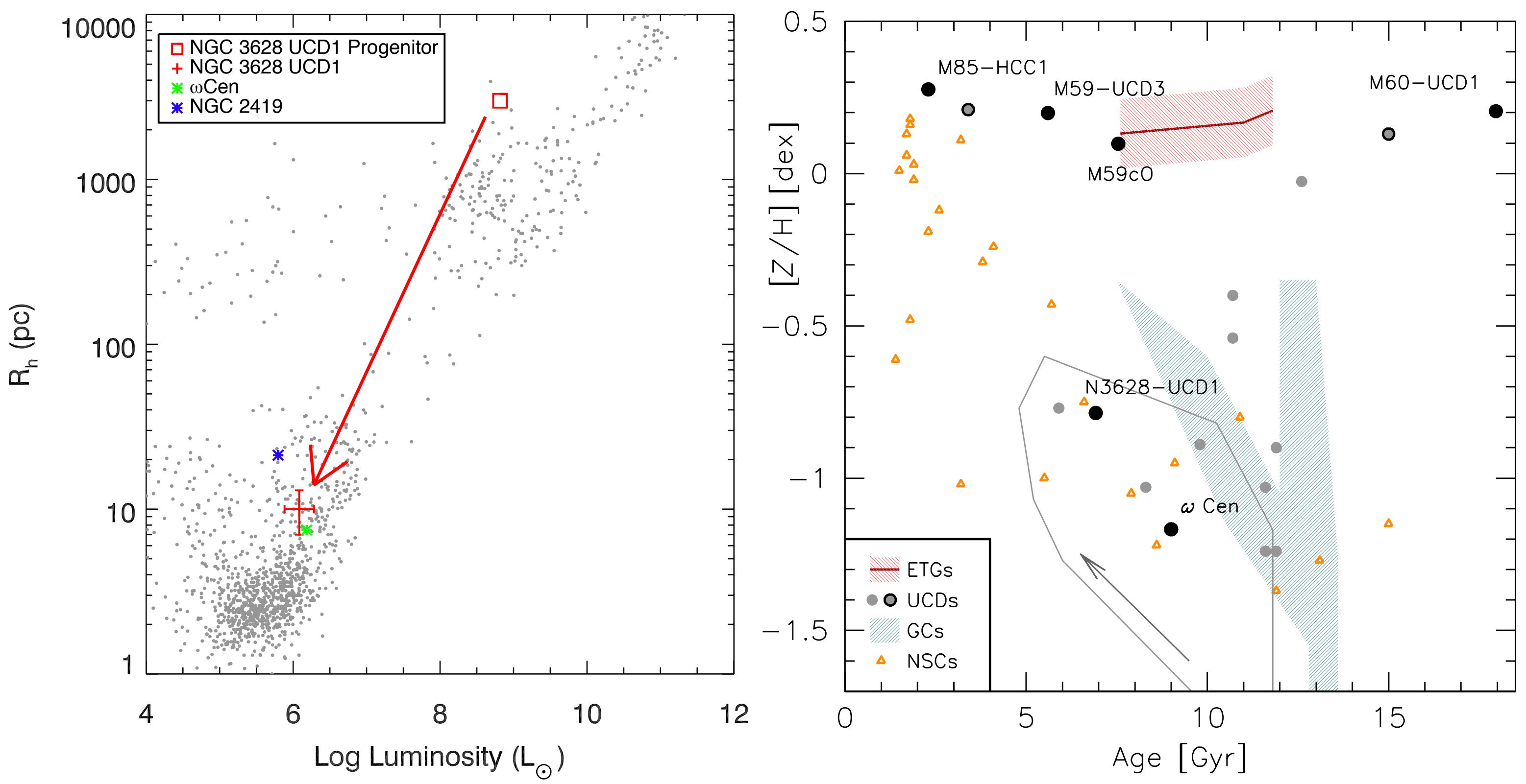

Figure 5.3: Left panel: Plot of R_h (pc) vs. V-band luminosity ($L_\odot$) for a collection of distance-confirmed dispersion supported stellar systems. Data are from a compilation begun in Brodie et al. (2011), updated in Brodie et al. (2014). The location of UCD1 is marked. We also mark the location of the MW GCs ω Cen and NGC 2419 for comparison. We mark the location where the UCD1 progenitor galaxy may have originated based on the stellar stream (note that the box size of this point is arbitrary and not indicative of uncertainty). Right panel: plot of age (Gyr) vs. [Z/H], modified from Sandoval et al. (2015). The grey outline corresponds the approximate ranges in both quantities among stars within ω Cen, and the arrow indicates the expected direction of evolution (Villanova et al., 2014). UCD1 and ω Cen are compared to centers of ETGs (red shaded region), MW GCs (green shaded region), confirmed UCDs (grey points), and NSCs (orange triangles). See Pritzl et al. (2005); Brodie et al. (2011); Dotter et al. (2011); Conroy et al. (2014). Clusters with likely tidal-stripping origins are also plotted (see Sandoval et al. 2015.

5.4 DISCUSSION AND SUMMARY

5.4.1 The Origin of the Tidal Stream

In the literature, this stellar stream has often been considered the result of an interaction between NGC 3628 and another galaxy in the group, typically NGC 3627. However, the properties of UCD1 give us cause to consider a potential dwarf galaxy minor-merger scenario as the source of the stream.

Rots (1978) carried out a restricted 3-body simulation of a tidal interaction between NGC 3627 and NGC 3628. The simulation did a reasonable job of reproducing some features but also had some discrepancies with observations, such as a smaller velocity difference between the two large galaxies than was actually observed (a full list of issues is enumerated in Haynes et al. 1979). This early simulation also did not take into account other bodies in the system, an important caveat given that the galaxies share a group environment with NGC 3623 to the south east.

Now that we have identified and characterized UCD1, a successful simulation must be able to explain the presence of a $\sim 10^6$ $M_\odot$ compact star cluster with a $\sim$6 Gyr, metal-poor stellar population. It is not immediately obvious how such an object could result simply from the interaction of NGC 3627 and NGC 3628, as we would expect objects resulting from such an interaction to be younger, metal-rich, and less compact. It is important to note that, in this work, we are not making any direct comment on the tidal interaction. We have not yet conducted dynamical modeling of our own, and so we are not in a firm position to endorse a minor-merger picture for this tidal interaction over the NGC 3628/NGC 3627 interaction model currently in the literature. The study of this system would benefit greatly from more sophisticated dynamical modeling, exploring the possibility of minor mergers and including the dynamical effects of all three group galaxies. For the moment, we consider the nature of the merger an open question.

5.4.2 UCD1 compared to other UCDs

It is informative to consider the properties of UCD1 in the context of other UCDs. In the left panel of Fig. 3, we plot the measured half-light radius in pc against the absolute V-band magnitude for a large collection of distance-confirmed dispersion-supported stellar systems across a wide range of sizes and luminosities (Brodie et al., 2014).

In the right panel of Fig. 3, we plot the age and metallicity of various star clusters including confirmed UCDs, MW GCs, nuclear star clusters (NSCs), and early-type galaxy (ETG) centers. We also hightlight an assortment of metal-rich UCDs with a likely tidal stripping origin (e.g. M60-UCD1, see Sandoval et al. 2015).

ω Cen represents an interesting analogue to UCD1 in these parameters. Its size and luminosity are very similar to UCD1 and both are low metallicity compared to other clusters with a likely tidal origin. The Harris 1996 (2010 edition) catalog lists values of $\sigma = 16.8$ km s^{-1} (e.g. McLaughlin & van der Marel 2005), $M_V = -10.26$, and $\mathrm{R_h}$= 7.5 pc (e.g. van den Bergh et al. 1991), all comparable to UCD1 within the uncertainties (note that we only estimate an upper limit for σ for UCD1). ω Cen is even more metal-poor than UCD1, [Fe/H] = -1.53 (e.g. Johnson et al. 2009) vs. -0.84, and, generally speaking, is alpha-enhanced (e.g. Johnson & Pilachowski 2010). Such differences are not unexpected, since UCD1 is only currently being stripped. Given that ω Cen was likely accreted several Gyr ago, UCD1 is naturally expected to have a more extended SF history, enhancing its metallicity and potentially erasing any alpha-enhancement. In this context, objects like UCD1 may be reasonable modern-day examples of accretion events which, Gyr ago, would have resulted in ω Cen-like star clusters. These clusters offer interesting contrasts in size, luminosity, and metallicity compared to more metal-rich, tidally stripped UCDs.

5.4.3 Properties of a Potential Dwarf Galaxy Progenitor

In this section, we consider the implications if UCD1 did indeed result from a minor merger. Using the stellar stream luminosity to estimate the stellar mass in the stream is straightforward. As discussed in §5.2.3, for a stream of this color, a $M/L_* \sim 2.7$ is reasonable. Given the measured luminosity of $(4.1 \pm 0.8) \times 10^8$ L$_\odot$, we estimate a stellar mass of $\sim 1.1 \times 10^9$ M$_\odot$. We take this value as a rough estimate of the stellar mass of a potential accreted dwarf galaxy, also noting neglected systematics from the mass-to-light estimate. This mass is comparable to the spheroid mass estimated in Norris & Kannappan (2011) for the progenitor of the confirmed stripped nucleus NGC 4546 UCD1 ($3.4^{+1.2}_{-1.5} \times 10^9$ M$_\odot$). Following the specific frequencies of Peng et al. (2008), such an accretion event would have contributed ~9 GCs to the halo of NGC 3628, which could possibly be found as a discrete GC population in phase space.

To estimate a width for the stream, we use a region to the east of UCD1 ~100 arcseconds wide and sum up the light horizontally along the direction of the stream,. We identify the peak of the light distribution as the stream center, and mark the outer end of the stream as the point where the light profile approximately flattens. Finally, we define the distance from the center that contains half the total integrated light of the region as the half-light width of the stream. We find a value of $\sim 60''$, or ~3000 pc. We then adopt this half-light width as a proxy for the R_h of the accreted parent galaxy. In Fig. 3, we plot the estimated location of this dwarf galaxy in the same parameter space. We emphasize that the connection between stream-width and progenitor size is unclear, and will at the very least depend on viewing angles and orbital phase.

If a minor-merger picture is correct, it is natural to compare UCD1 to nuclear star clusters (NSCs). NSCs typically have effective radii of a few to tens of parsecs, and luminosities from a few times 10^5 $L_\odot$ to $\sim 10^8$ $L_\odot$ (Georgiev & Böker, 2014). Early-type galaxies in particular may have more compact NSCs; Côté et al. (2006) found a median R_h of 4.2 pc for prominent NSCs in early-type galaxies. The precise effects of the stripping process on NSC R_h are complicated and depend on a wide range of orbital parameters and initial conditions, but for most scenarios, we wouldn't expect drastic changes in cluster R_h (Pfeffer & Baumgardt, 2013). Bianchini et al. (2015) found that, as galaxies are stripped, central clusters expand to reach the sizes they would have in isolation, i.e. similar to GC/UCD-sized objects. A late-type nucleated galaxy could be a possible source, though presumably the bulge would need to be red enough to explain the colors seen in UCD1's plume.

For UCD1, if the properties remain roughly comparable, then the stripping process has, at the order of magnitude level, resulted in a decrease of roughly 100 in size and 1000 in luminosity. Similar factors of stripping have been seen in simulations of dwarf-elliptical galaxies (Pfeffer & Baumgardt, 2013), although the precise amounts of mass loss depend on the orbital parameters. In any case, we find the properties of UCD1 consistent with the cluster being the final result of a minor merger, offering support that some portion of the large star cluster population may be created through the tidal stripping of dwarf galaxies.

Chapter 6

Summary and Future Direction

6.0.1 Summary

We have presented a wide array of studies of extragalactic GC systems in various contexts. First, in Ch. 2, we analyzed the NGC 3115 GC system using high-quality *HST*/ACS imaging, supplemented with Subaru/SuprimeCam photometry of the galaxy. NGC 3115 is a well-studied bimodal galaxy, and the bimodality has been spectroscopically confirmed to arise from an underlying non-unimodal metallicity distribution (Brodie et al., 2011). Since GCs are partially-resolved in *HST*/ACS imaging, they are able to be selected with a higher degree of confidence than is possible in ground-based imaging, and we are able to analyze GCs to much greater depth than is possible with spectroscopically. We find a monotonically decreasing radial gradient in the blue GC system color, but a much more chaotic behavior in the red GC system. The red GC system also decreases in relative fraction as a function of radius when compared to the blue GCs, as is often found in extragalactic GC studies. The red GC behavior radial behavior matches radially with some of the behavior also noted by Arnold et al. (2011) in the kinematic profile of the red GC system, possibly indicating a shift in accretion around NGC 3115. Finally, we identify a number of extended clusters. While most of these are likely contaminant background galaxies, some of these objects will be UCD or "faint-fuzzy" type star clusters. Indeed, three have spectroscopically-confirmed velocities.

In Ch. 3, we introduced a method for improving some of the difficulties with GC analysis in ground-based data, chiefly the issue of contamination from foreground and background sources. We created a Bayesian formalism in which we treat the distribution of photometric sources in color, luminosity, and position as a mixture model including a fixed contaminant distribution and parameterized distributions for the GCs. The free parameters of these distributions are then inferred using standard MCMC techniques. We also demonstrated how incompleteness in the data can be incorporated in the model by modifying some of the formalism of Weisz et al. (2013). Finally, we verified the inference from this model on mock datasets drawn from realistic models of GC distributions. We discover that certain parameters, such as $\mathrm{f_{red}}$ and $\mathrm{f_{blue}}$, have significant covariance, depending on the other parameters in the distributions. This covariance means that quantities like N_{GC} maybe known to greater precision than the number of GCs of small distributions, and values like the relative ratio of red GCs to blue GCs can only be known to limited precision. Finally, we identify a number of areas where the model can be expanded to produce better inference for GC systems.

In Ch. 4, we perform photometry on a subset of SLUGGS survey galaxies in wide-field imaging data from both Subaru/SuprimeCam data and CFHT/MegaCam data. The SuprimeCam data are reduced by us, while the MegaCam data are downloaded from the MegaPipe stacked archives. We perform standard aperture photometry using SExtractor, and create point-source catalogs of sources around our selected galaxies. After full catalogs are created, we apply the Bayesian fitting methodology in Ch. 3 to these galaxies. We find most galaxies give reasonable fits when the Bayesian mixture model is applied. Bimodality is recovered in most cases, although there are some, such as NGC 3115, in which we need to specify informative priors to recover such bimodality. We commonly find that the ratio of red to blue GCs is a very uncertain quantity due to the covariance of the two parameters, while the N_{GC} quantity can be known to a high degree of precision, at least with respect to statistical uncertainties. Galaxies with very sparse GC systems were often poorly-fit by the model, likely simply due to having such a low GC "signal" compared to contamination. Systems such as NGC 4111 and 4459 are limited in what can be inferred about the systems with no prior information. We elected to fix most of the parameters in the model for these systems and simply leave the $\mathrm{f}_{\mathrm{red}}$ and $\mathrm{f}_{\mathrm{blue}}$ parameters free, allowing inference on the relative number of red and blue GCs as well as the total number of GCs in the system.

Finally, in Ch. 5, we have identified the object NGC 3628 UCD1, an object slightly larger than a typical GC. Using Subaru/SuprimeCam imaging, we analyze NGC 3628 UCD1 and find the object to be partially-resolved, allowing us to infer a physical size for the object of ~10 pc. More importantly, we identified that NGC 3628 UCD1 is embedded in a stellar stream, indicating that the object is in the process of being accreted onto NGC 3628. The overlapping discovery of UCD1 with the stellar stream confirms that at least some UCD-like objects will be placed in to the halos of galaxies through accretion events. We also identify a number of interesting parallels between NGC 3628 UCD1 and ωCen, the MW's largest GC. ωCen has long been considered an outlier among the MW GC population due to its size and bizarre chemical enrichment and other strange properties (e.g. King et al. 2012). Keck/ESI spectroscopy of UCD1 confirms that it is located in the NGC 3628 system, and reveals that it also displays some of the same strange enrichment patters among certain elements. Finally, we are able to infer rough information about the stellar system by measuring the luminosity of the stellar stream. We are able to extrapolate that the galaxy in which UCD1 was originally embedded in was a small dwarf galaxy, and that its luminosity will be reduced by a factor of ~100 when UCD1 is ultimately stripped to just its cluster.

6.0.2 Future Directions

The most important future direction is to complete Bayesian inference for the remaining SLUGGS galaxies. After the full set of SLUGGS galaxies has been analyzed in a consistent way, there are interesting lines of inquiry regarding trends in GC system properties vs. galaxy properties. For example, the relative fractions of reds and blues and the total number of GCs as a function of galaxy stellar mass, halo mass, and supermassive black hole mass are all correlations that have been noted in the literature, and investigating such correlations with the inference presented here will be powerful. Previously, these quantities as measured on the GC systems didn't always feature well-calibrated uncertainties, which were often estimated in ad-hoc ways. Our

Bayesian methodology of inference for these quantities means that, at least statistically, our uncertainties are well-calibrated. Better understanding of systematic uncertainties still remains to be precisely quantified.

Another possibility to investigate is the use of μ_i of the GC system as a distance indicator. Since the peak luminosity of a GC system is thought to generally remain fixed from galaxy to galaxy, the GC luminosity function is often used as a distance indicator for nearby galaxies (e.g. Villegas et al. 2010). The uncertainties on μ_i provided by our inference mean that our ground-based imaging could be used to help constrain distances to the galaxies we investigate. However, it is debatable whether such an approach will be competitive with current *HST* photometric approaches, which have the dual advantage of probing much deeper data and having a less-contaminated dataset. While GCLF measurements from ground-based imaging might not ultimately be as well-suited as space-based imaging, the methodology laid out in Ch. 3 might still be applied in other contexts.

Finally, a useful future direction will be in expansion of the models considered here. One of the biggest advantages of considering the problem of GC system inference in a Bayesian context is that we are free to expand our model in any way we are able to parameterize. One expansion of immediate interest is extending GC bimodality into spatial distributions, as it is already well-established that there are different degrees of spatial concentration between red and blue GCs. Further expansion might allow for third populations in the GC color distribution, or perhaps other non-normal distributions entirely. Ultimately, we would like to move past the specification of arbitrary distributions towards more physically motivated models, which actually link the processes of GC system formation and assembly to observables. If such models may be written down in a probabilistic manner, they can be folded in to the analysis performed here in a straightforward manner, and therefore direct inference on the physical parameters of interest can be performed. Such an approach will allow theory and observation to be directly linked together, leveraging all the observed data to directly inform our knowledge of GC assembly in a probabilistic way. Ultimately, the methods discussed here are simply a first step, and we should always seek to find areas where our proposed model performs poorly and be open to updating our inference to reflect both better data and superior approaches to the problem.

Appendix A

Full Bayesian Fits for Each Galaxy

In this Appendix, we include traces and corner plots for all free parameters for all SLUGGS galaxies analyzed in Ch. 4. Refer to §4.3 for discussion of the results for each galaxy.

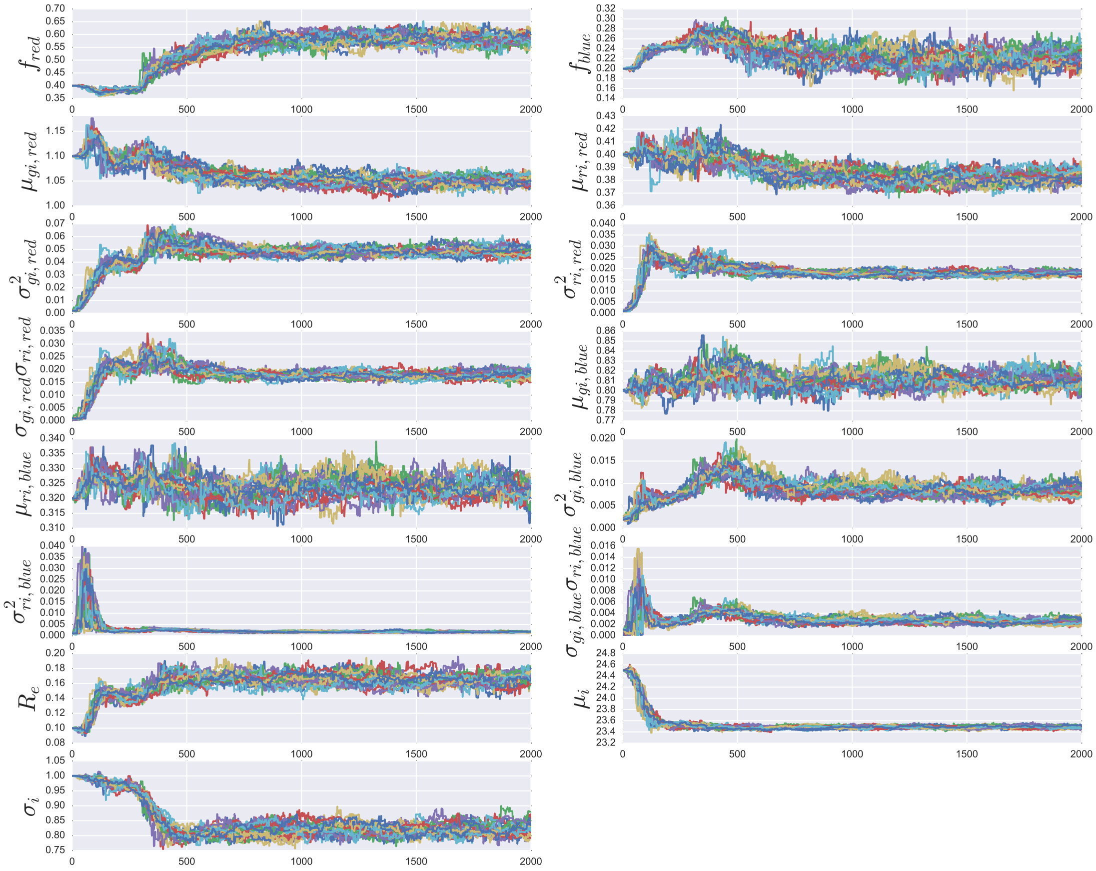

Figure A.1: Full trace plots for all free parameters in NGC 1407

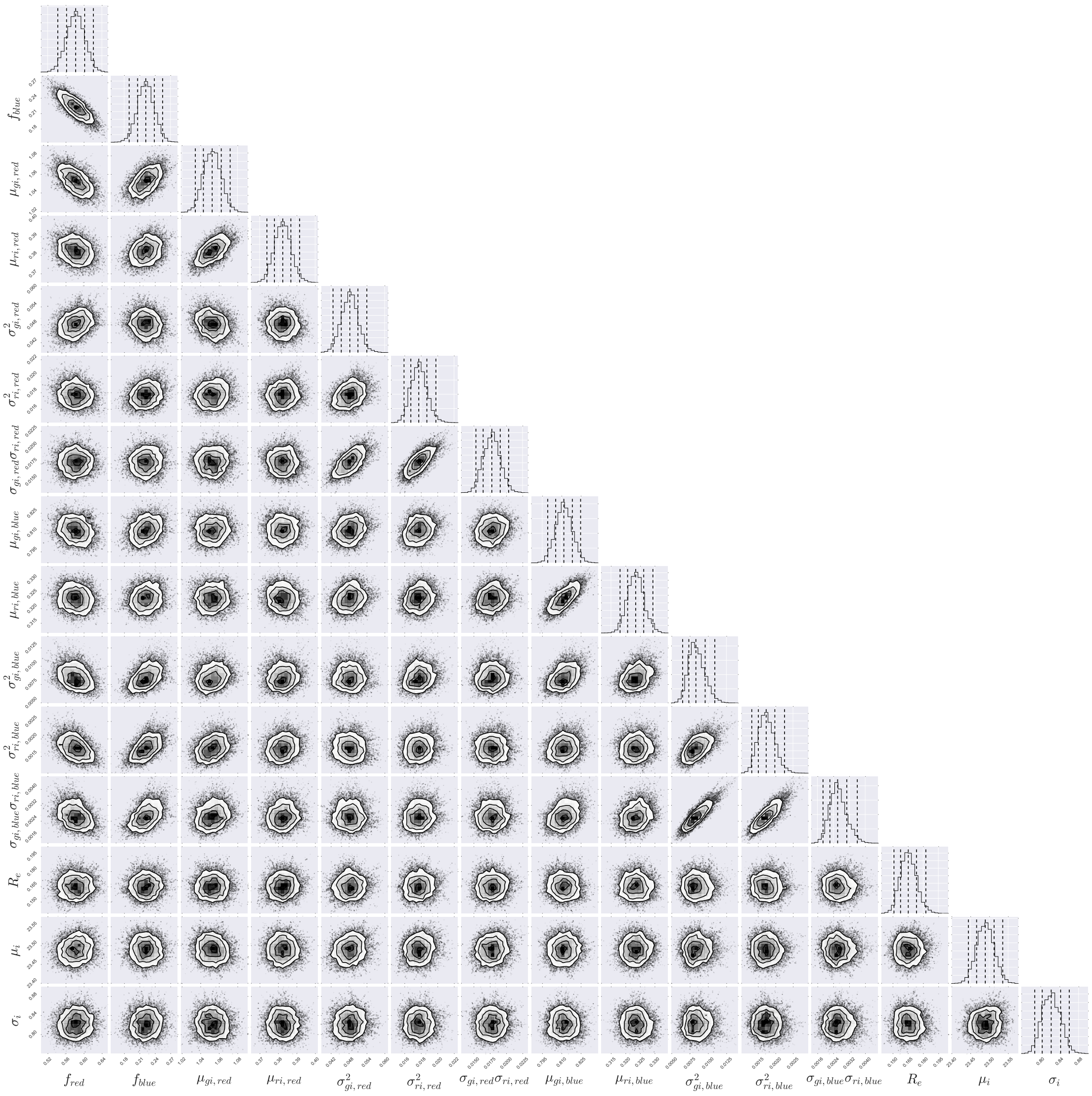

Figure A.2: Full corner plots for all free parameters in NGC 1407

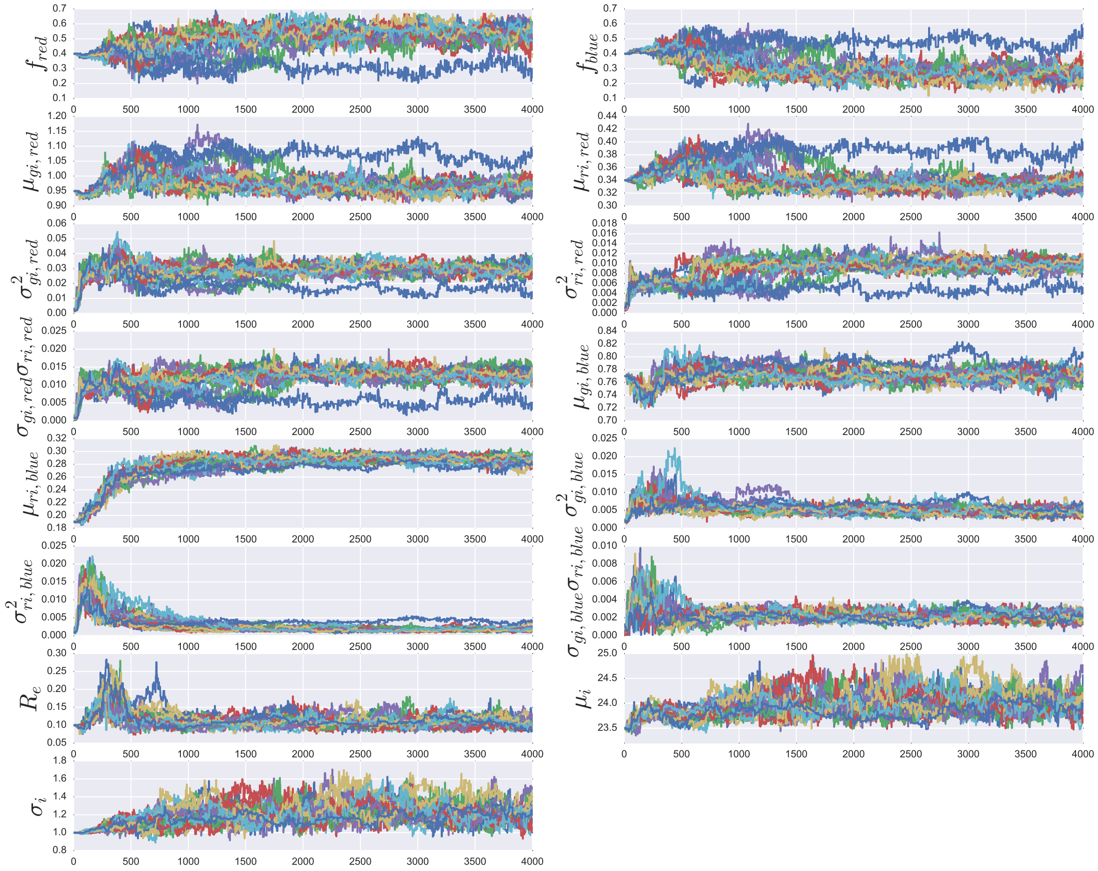

Figure A.3: Full trace plots for all free parameters in NGC 1400

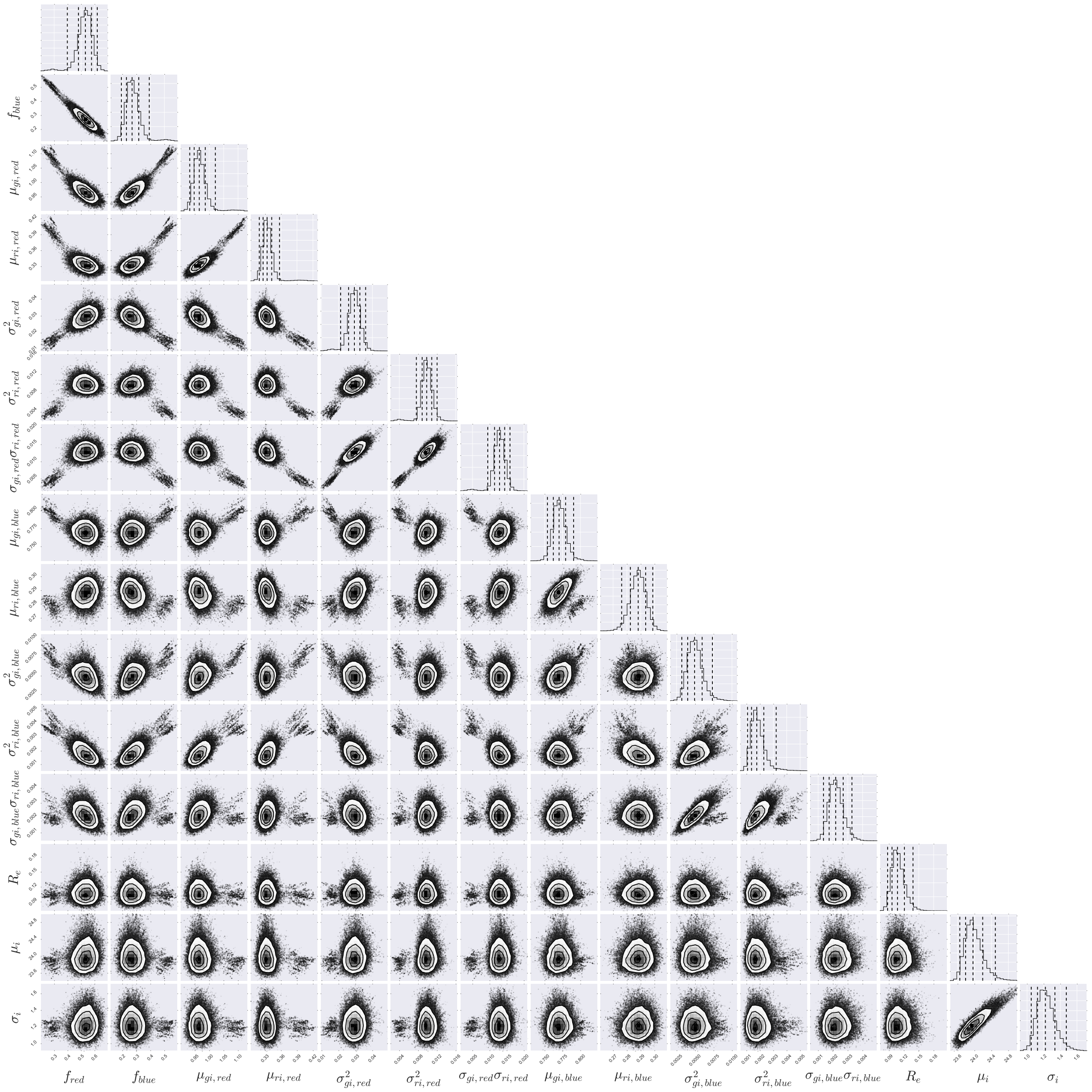

Figure A.4: Full corner plots for all free parameters in NGC 1400

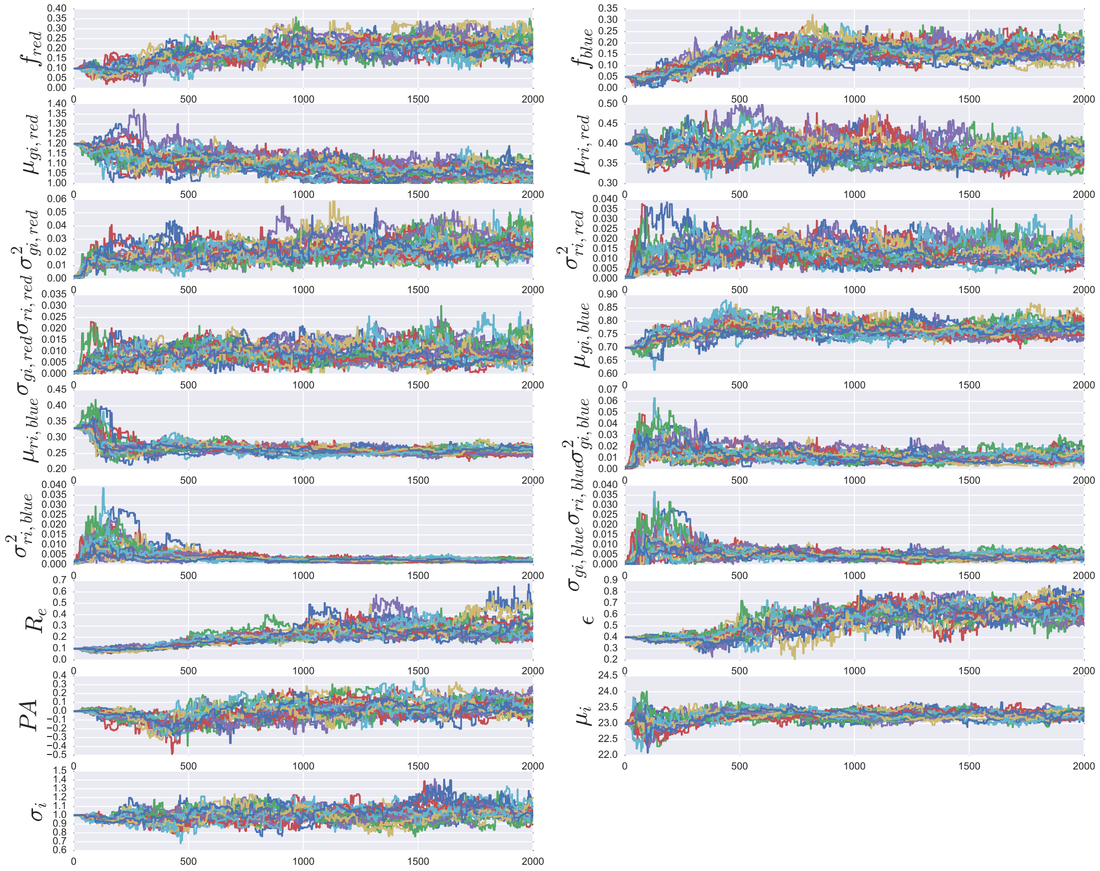

Figure A.5: Full trace plots for all free parameters in NGC 2768

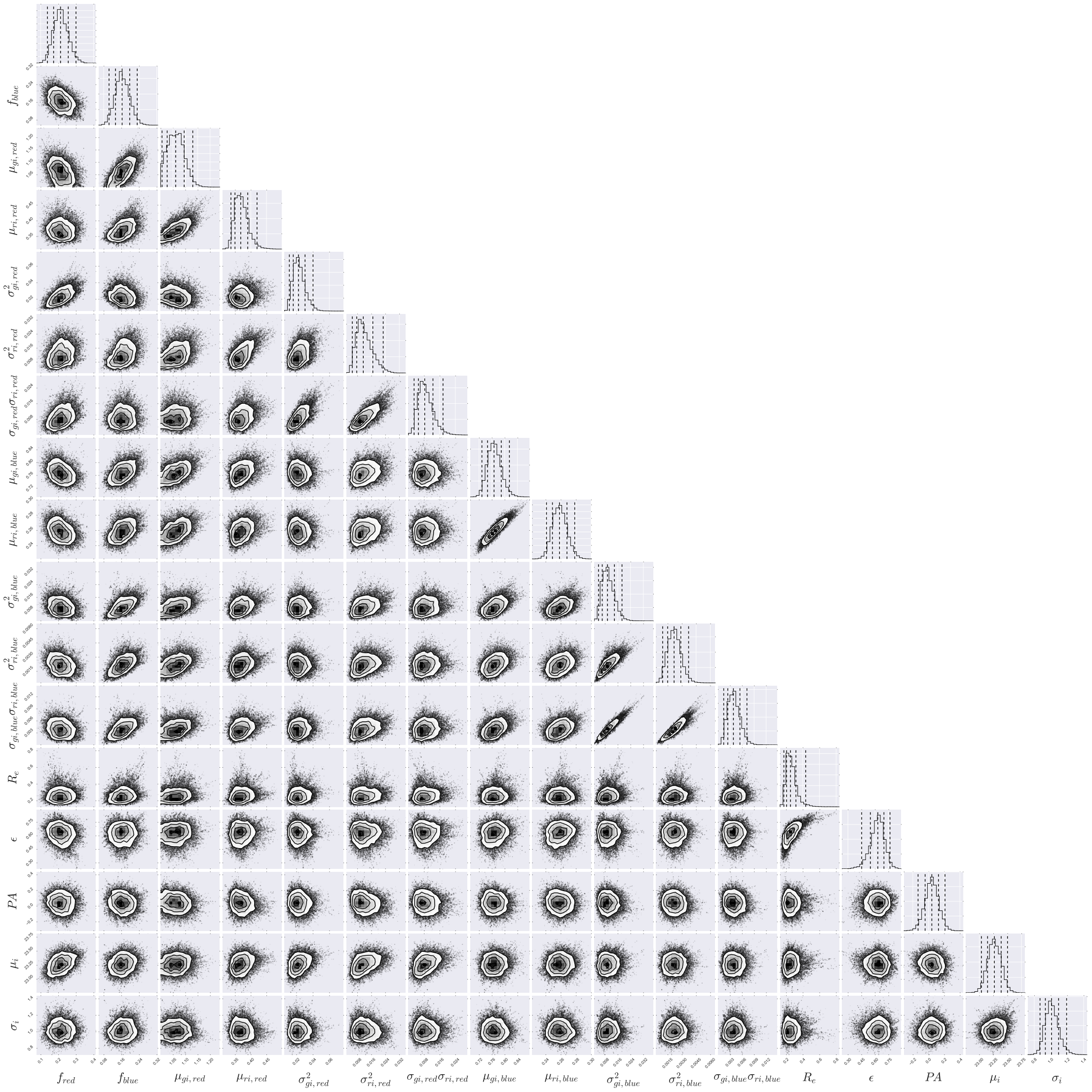

Figure A.6: Full corner plots for all free parameters in NGC 2768

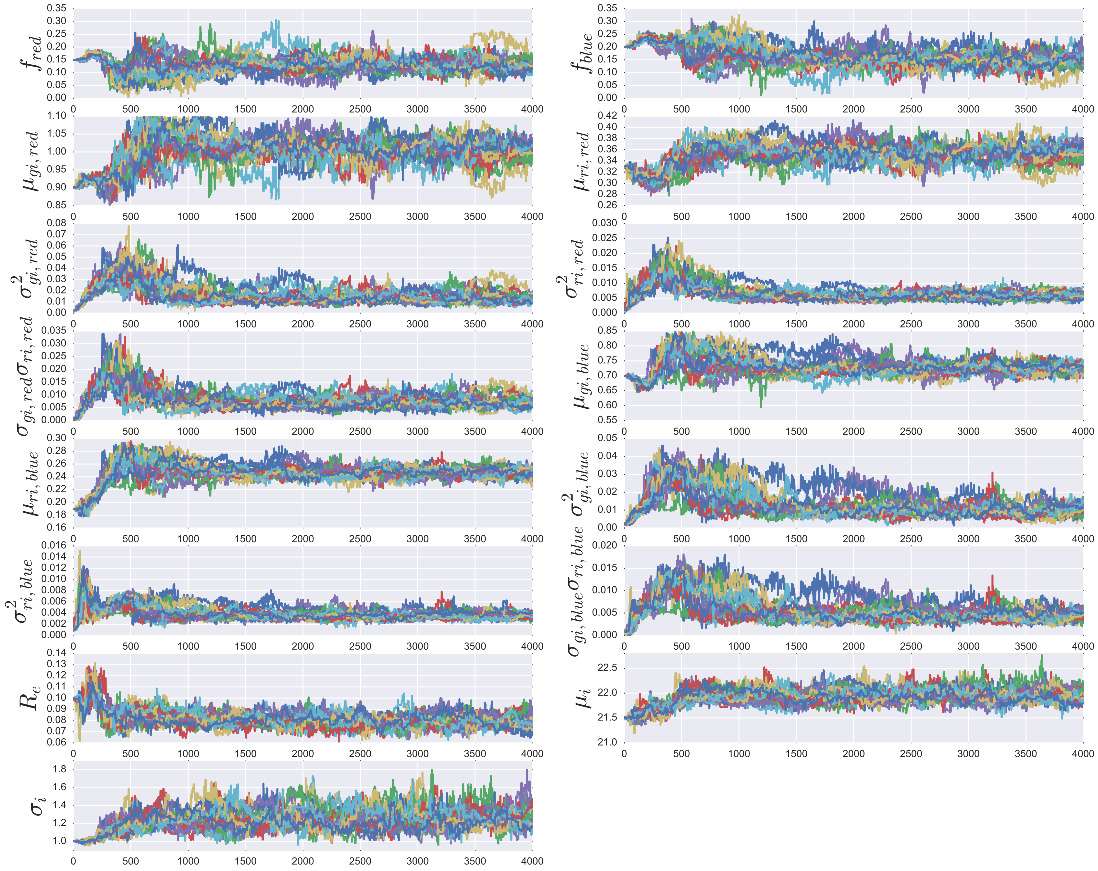

Figure A.7: Full trace plots for all free parameters in NGC 3115

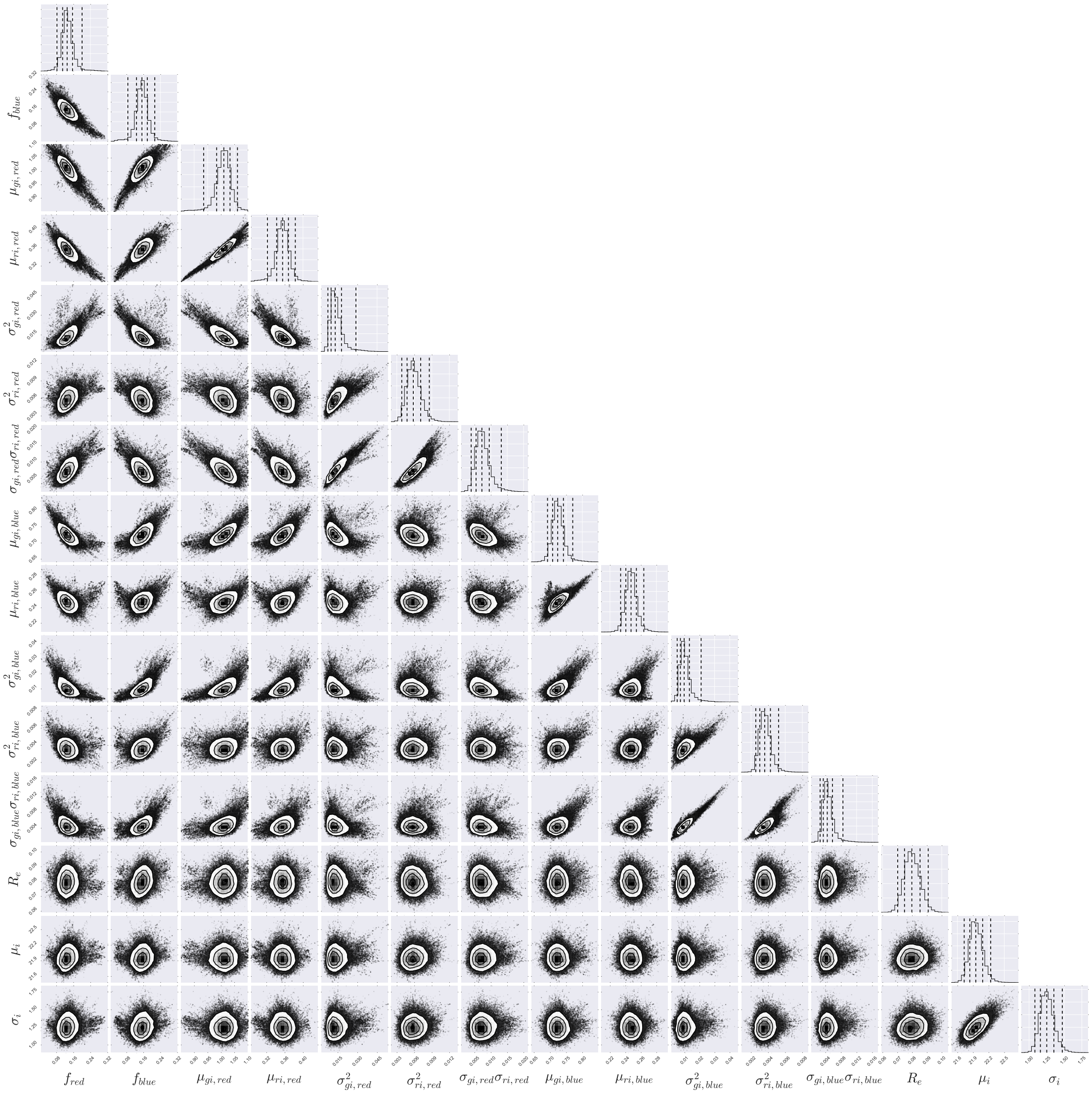

Figure A.8: Full corner plots for all free parameters in NGC 3115

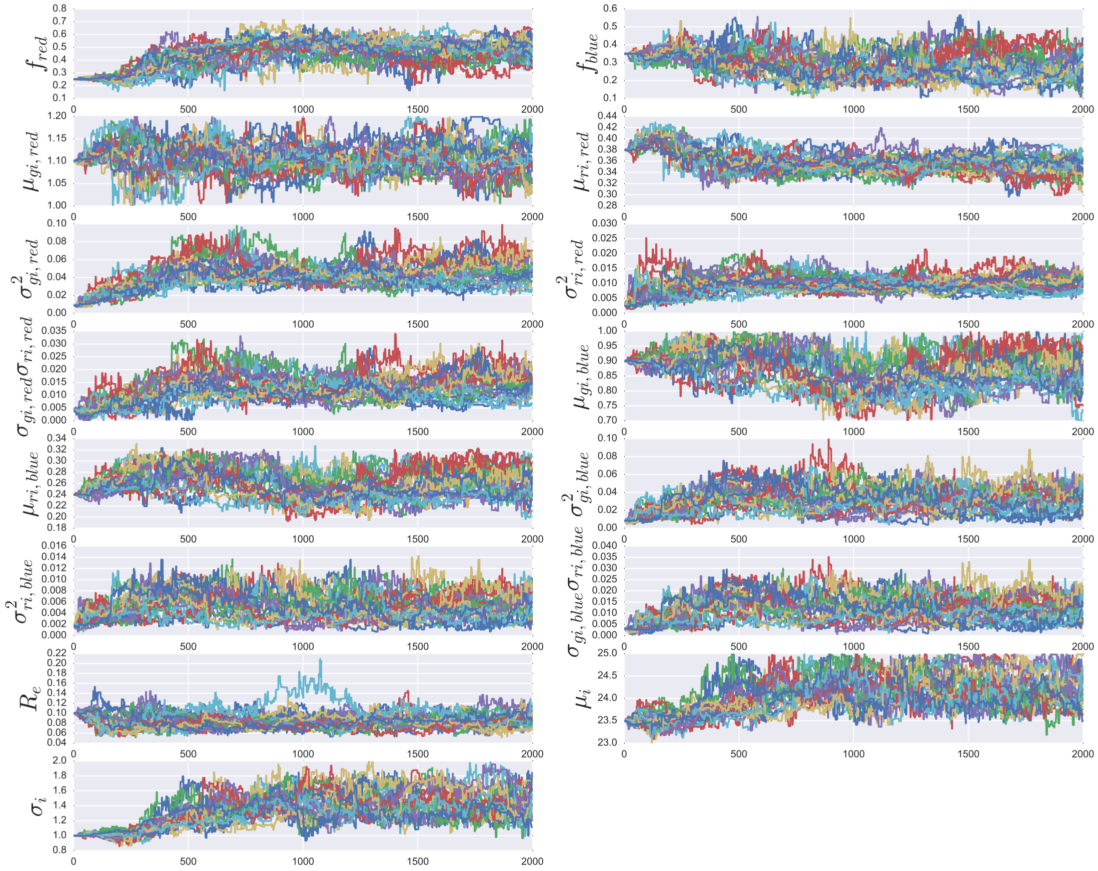

Figure A.9: Full trace plots for all free parameters in NGC 3607

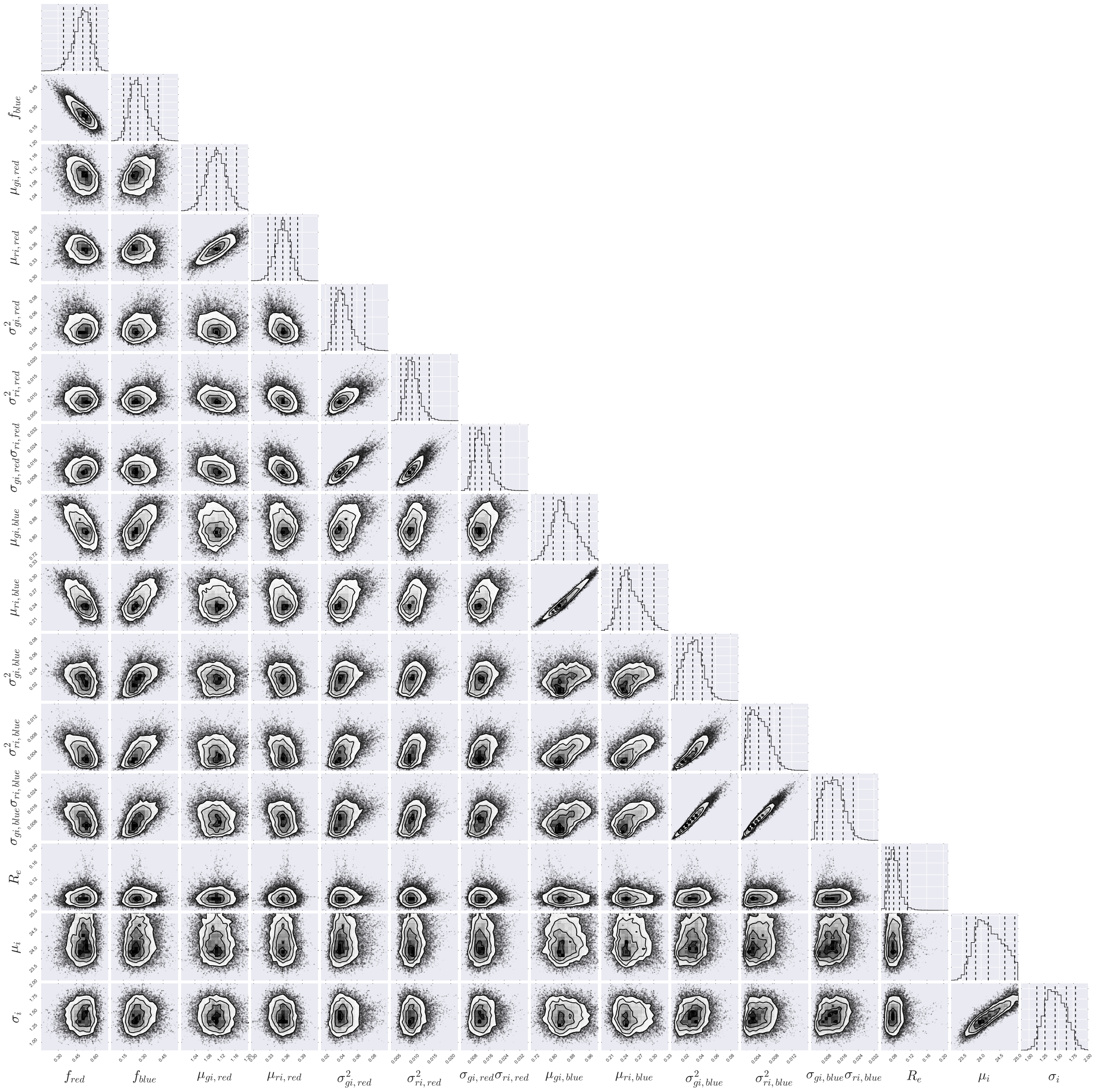

Figure A.10: Full corner plots for all free parameters in NGC 3607

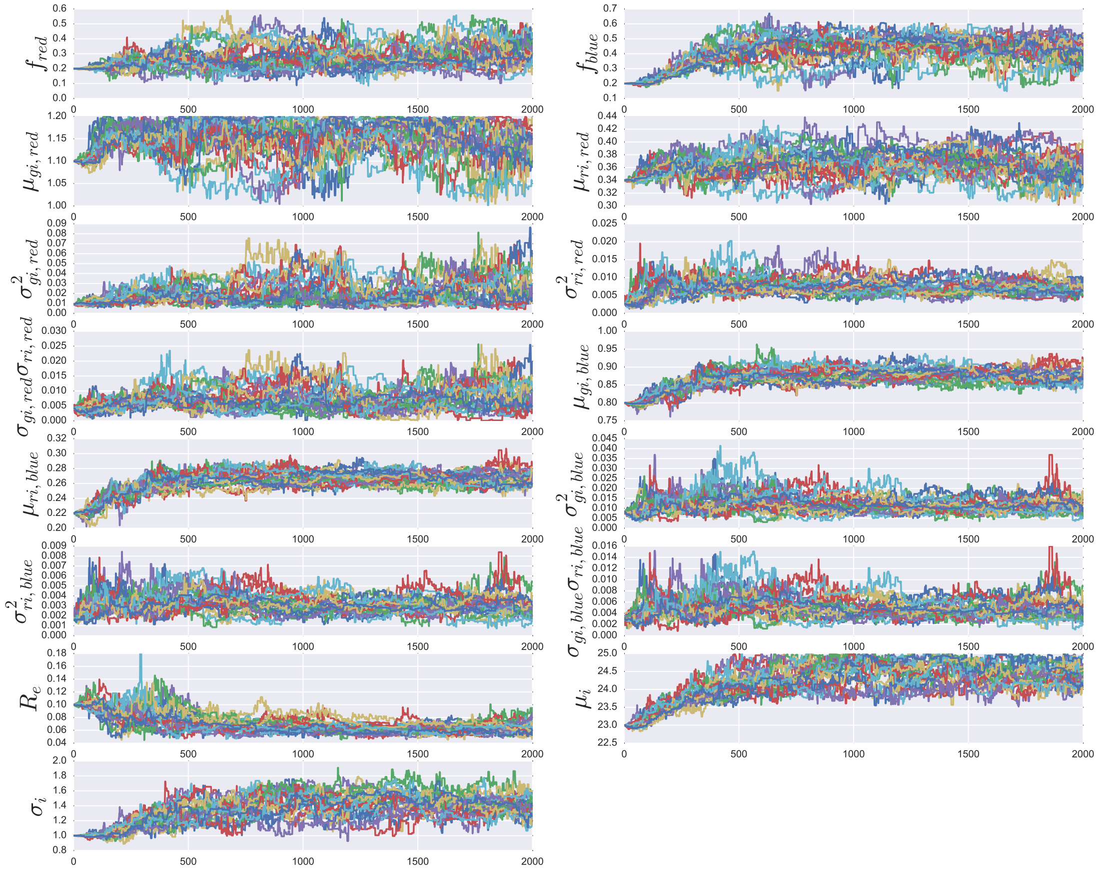

Figure A.11: Full trace plots for all free parameters in NGC 3608

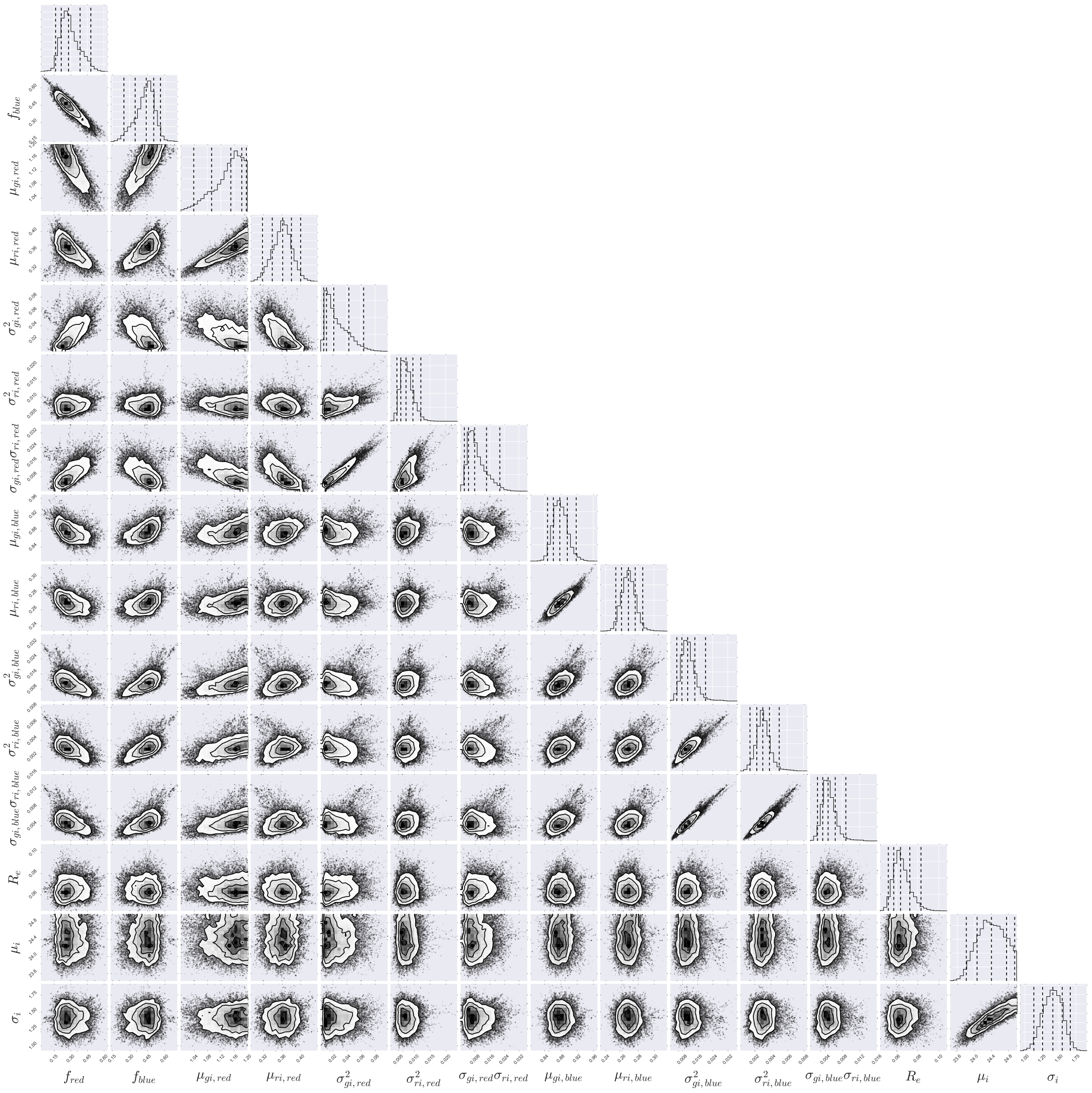

Figure A.12: Full corner plots for all free parameters in NGC 3608

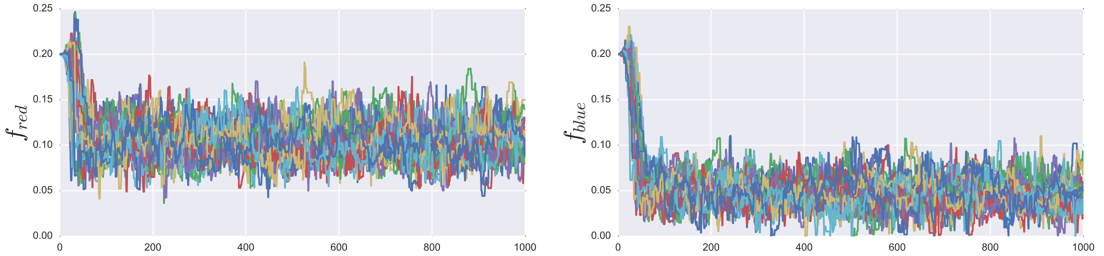

Figure A.13: Full trace plots for all free parameters in NGC 4111

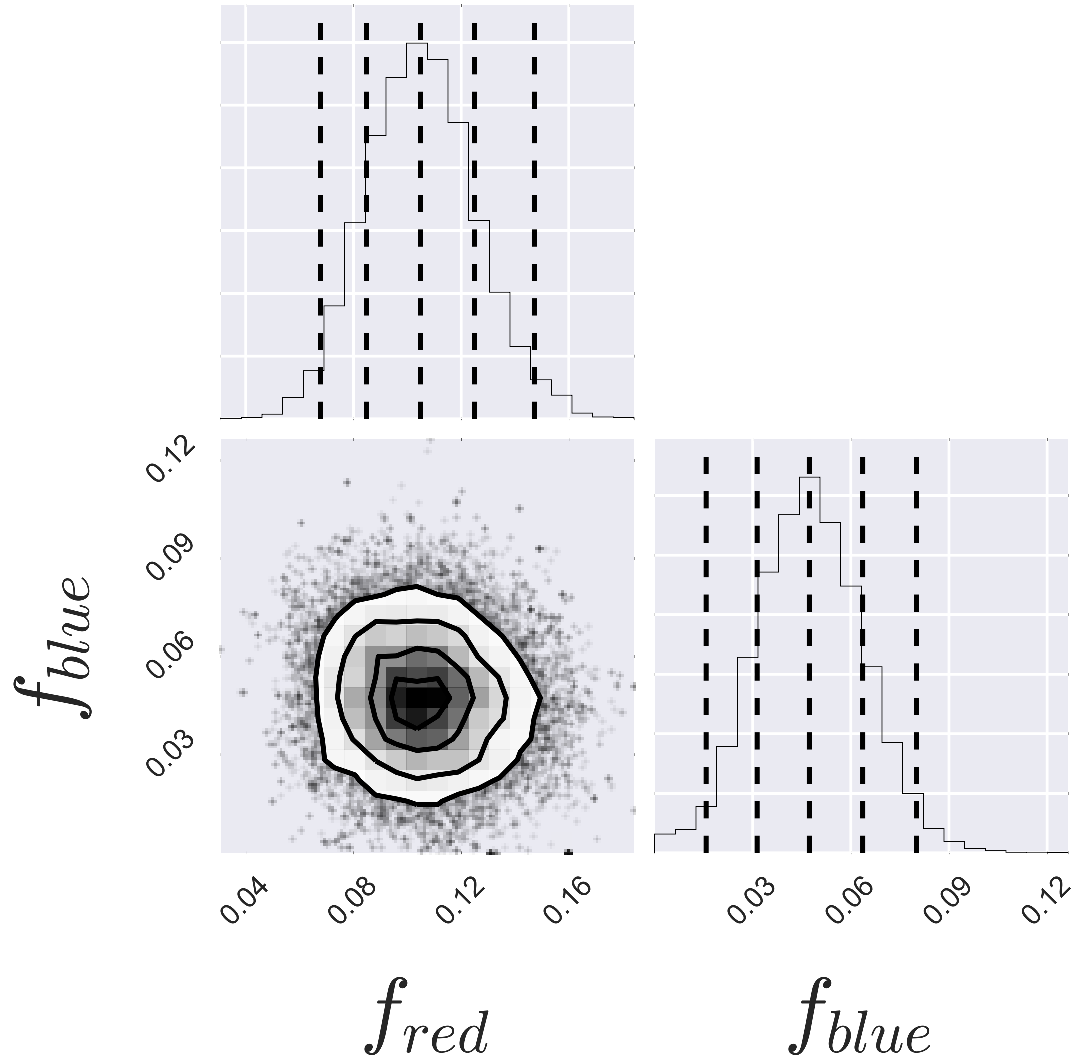

Figure A.14: Full corner plots for all free parameters in NGC 4111

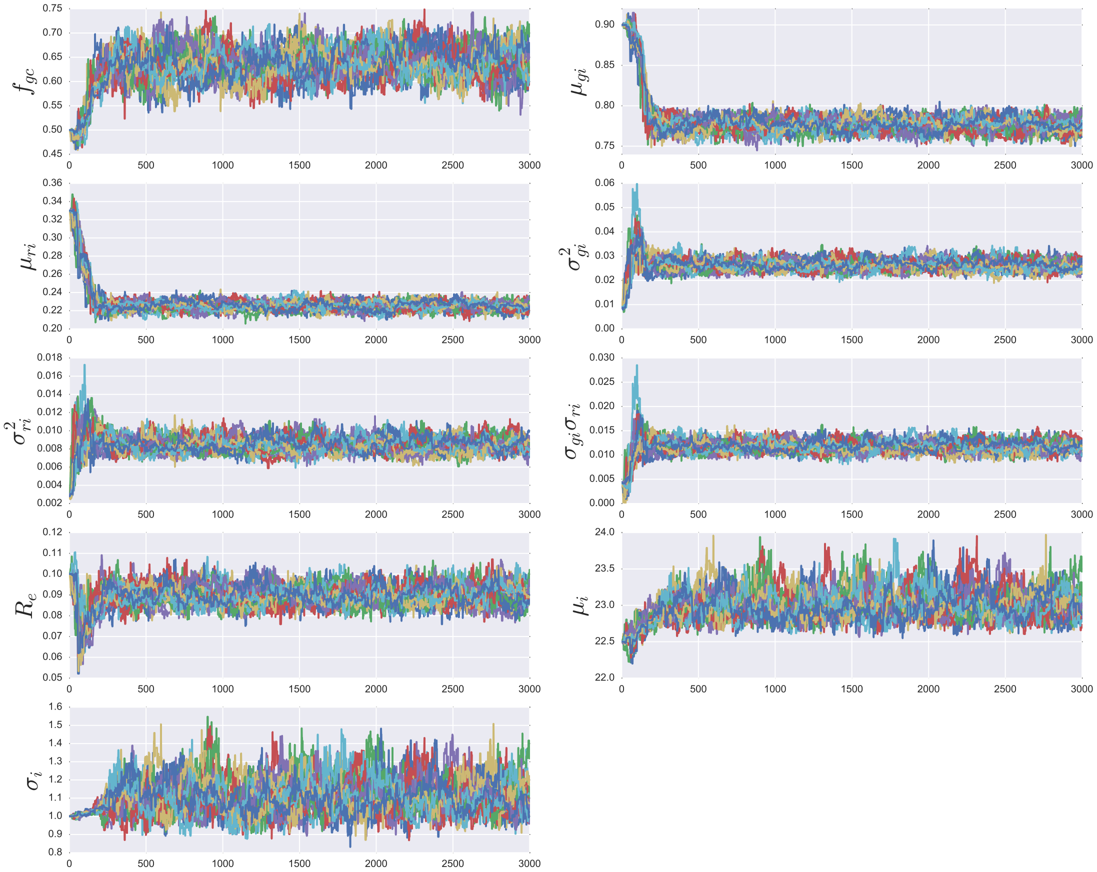

Figure A.15: Full trace plots for all free parameters in NGC 4278

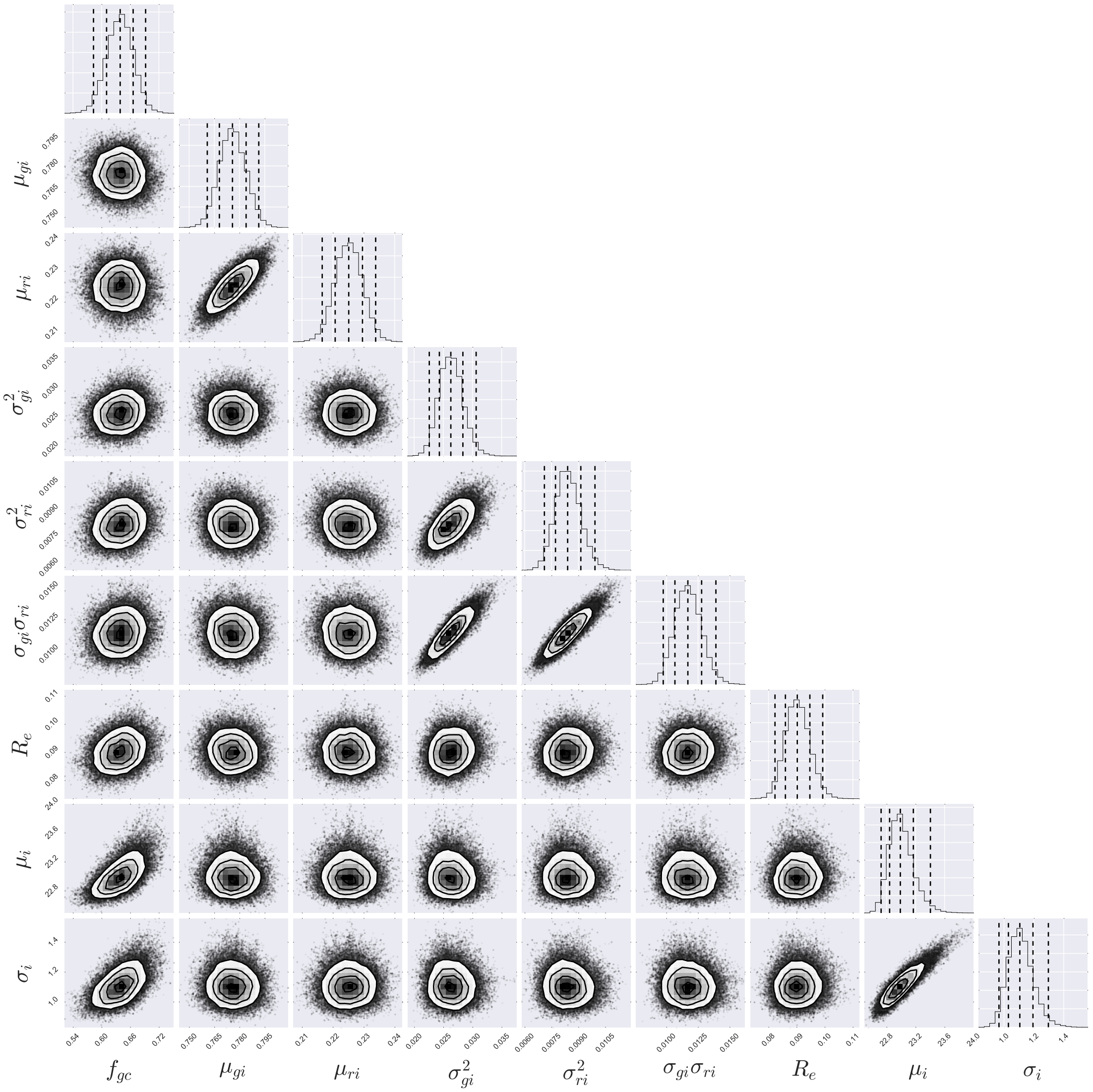

Figure A.16: Full corner plots for all free parameters in NGC 4278

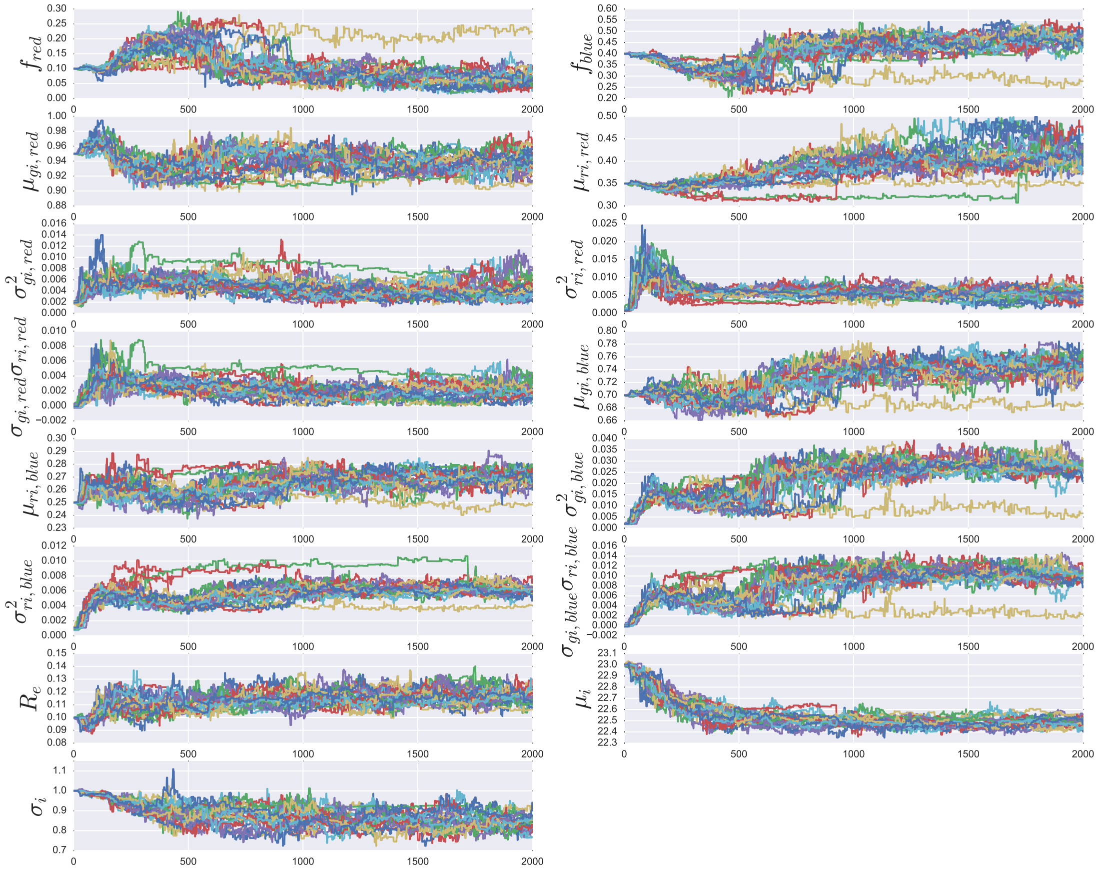

Figure A.17: Full trace plots for all free parameters in NGC 4365

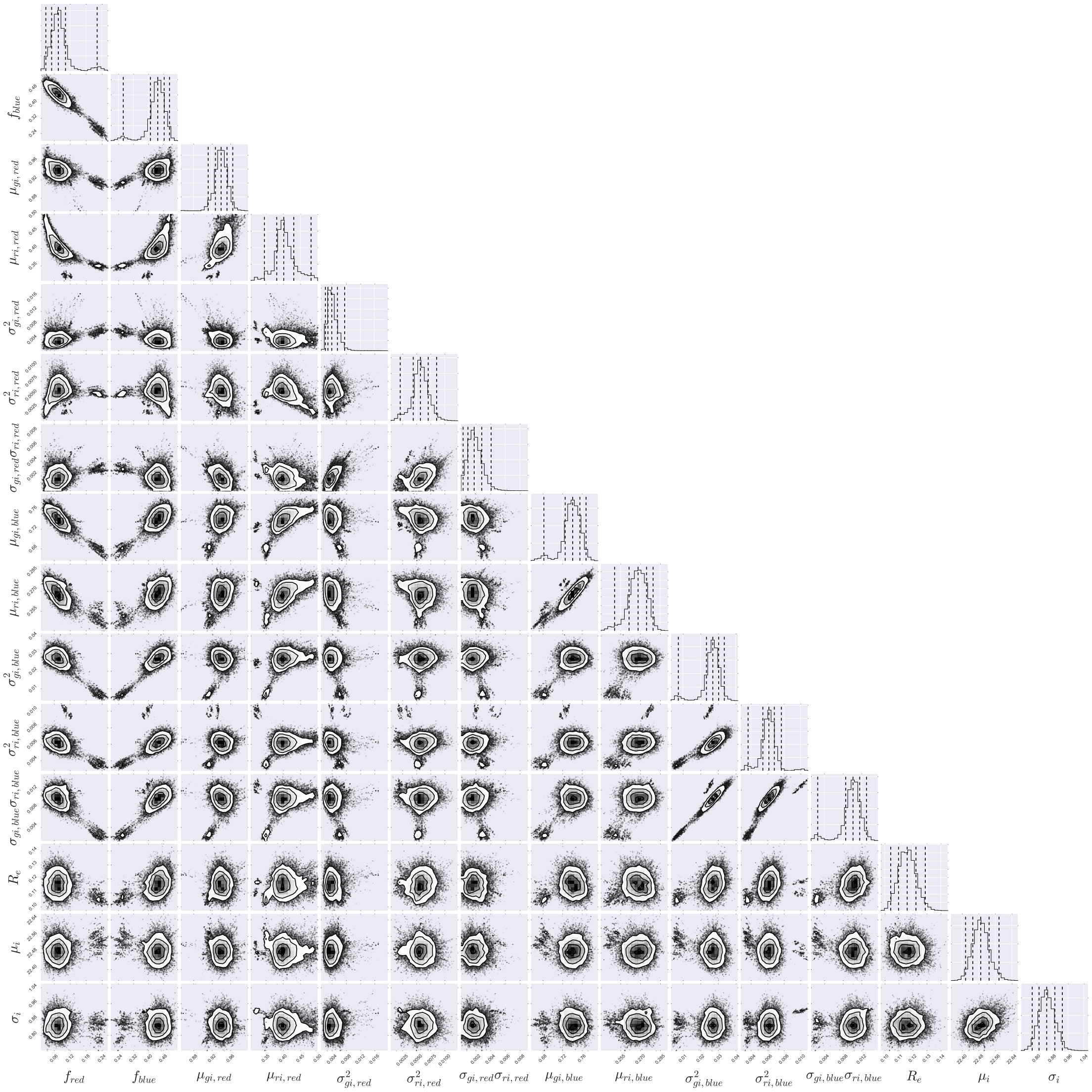

Figure A.18: Full corner plots for all free parameters in NGC 4365

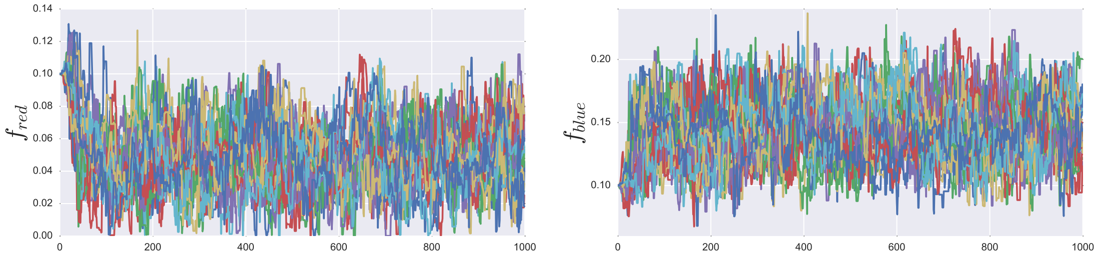

Figure A.19: Full trace plots for all free parameters in NGC 4459

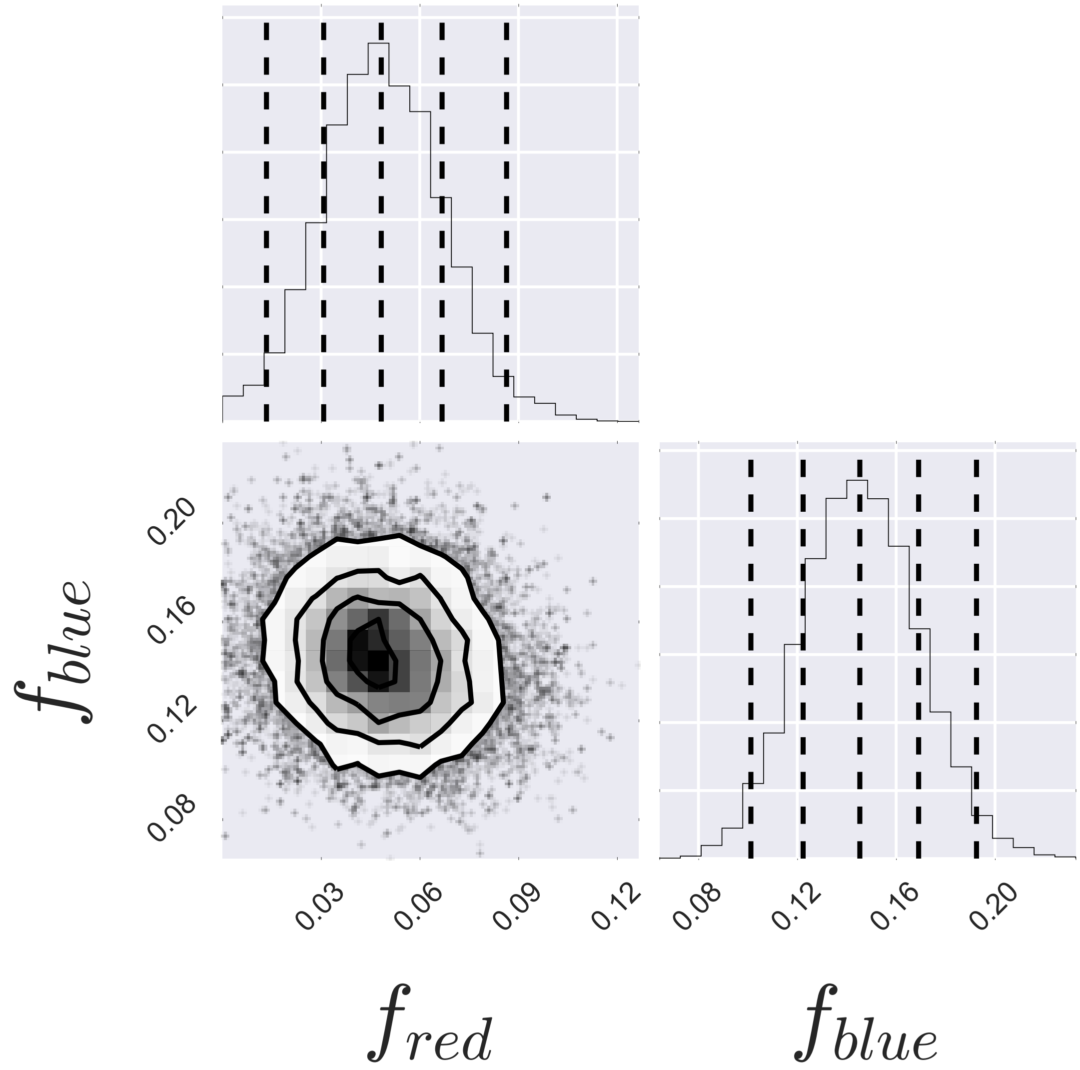

Figure A.20: Full corner plots for all free parameters in NGC 4459

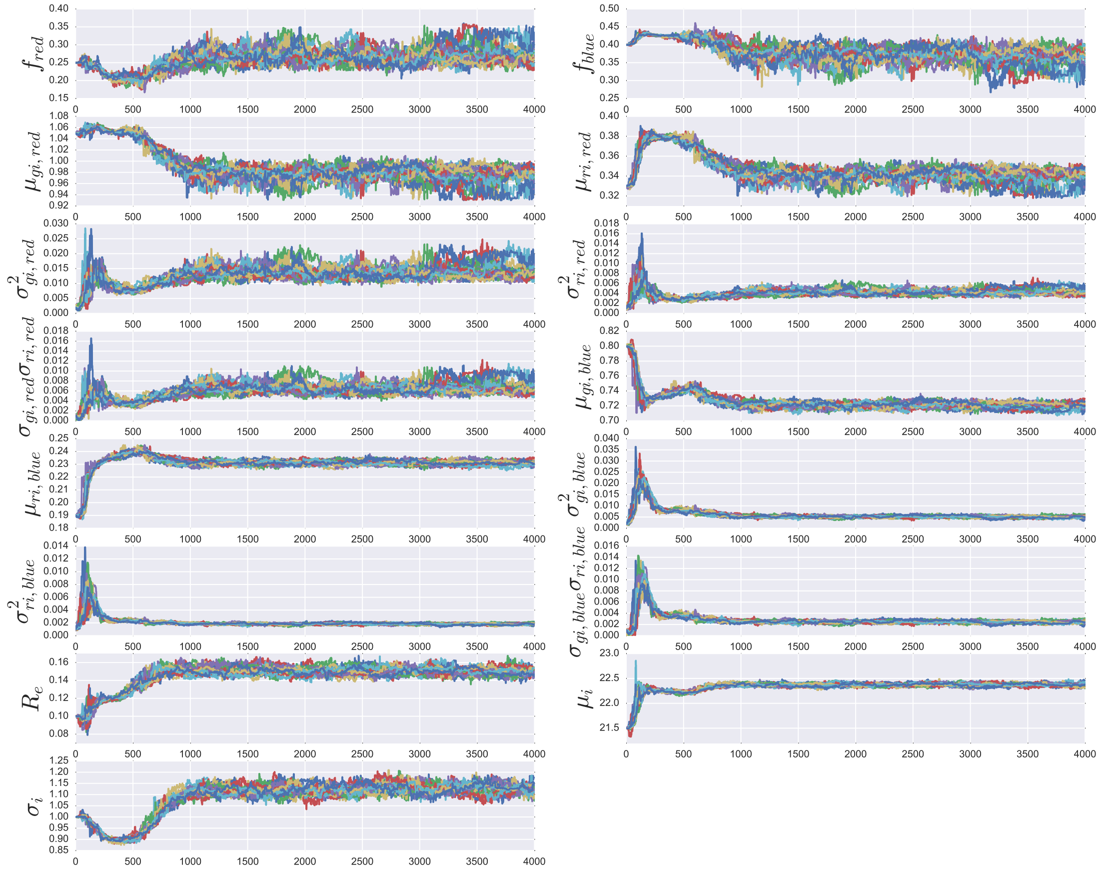

Figure A.21: Full trace plots for all free parameters in NGC 4486

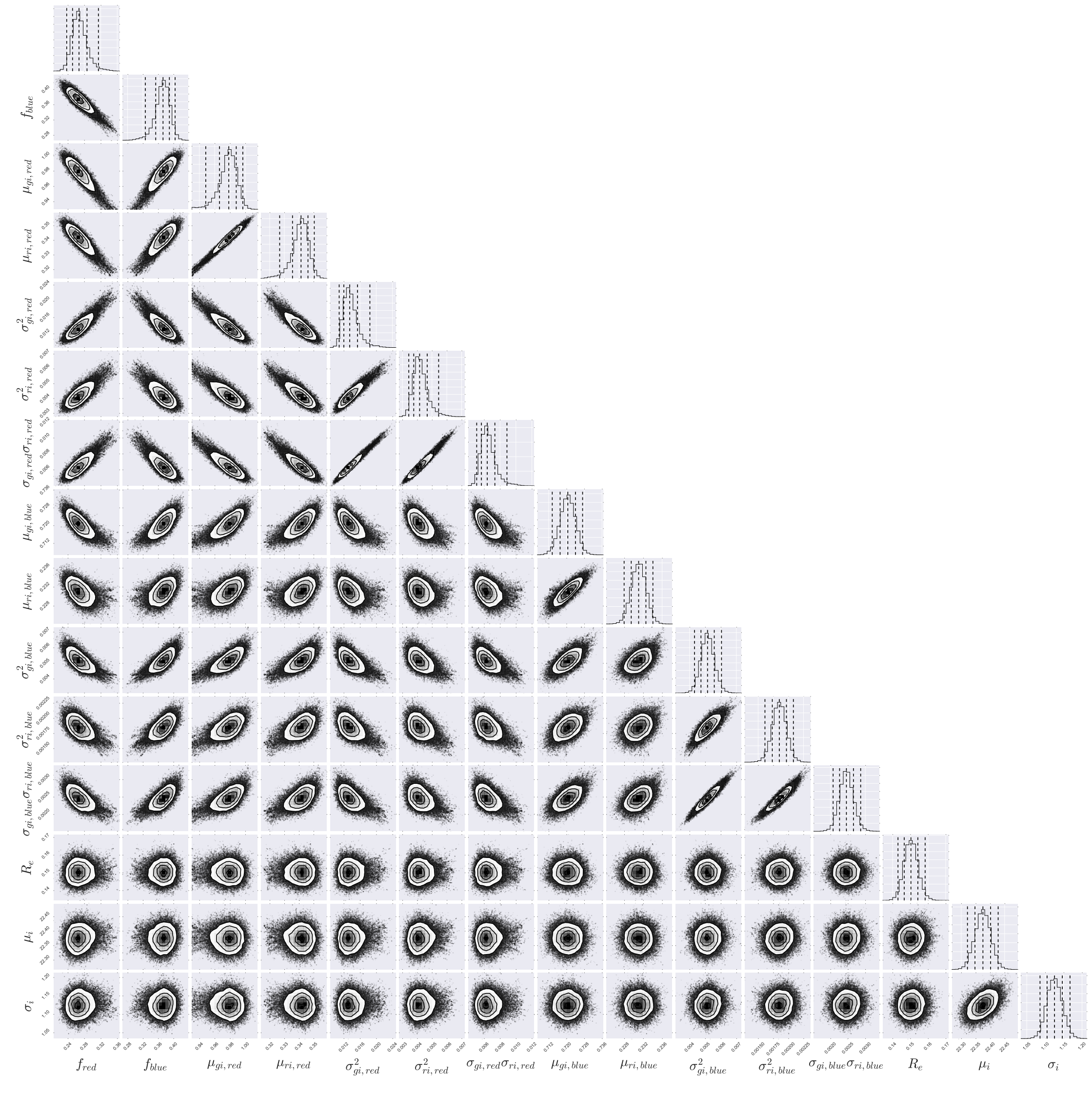

Figure A.22: Full corner plots for all free parameters in NGC 4486

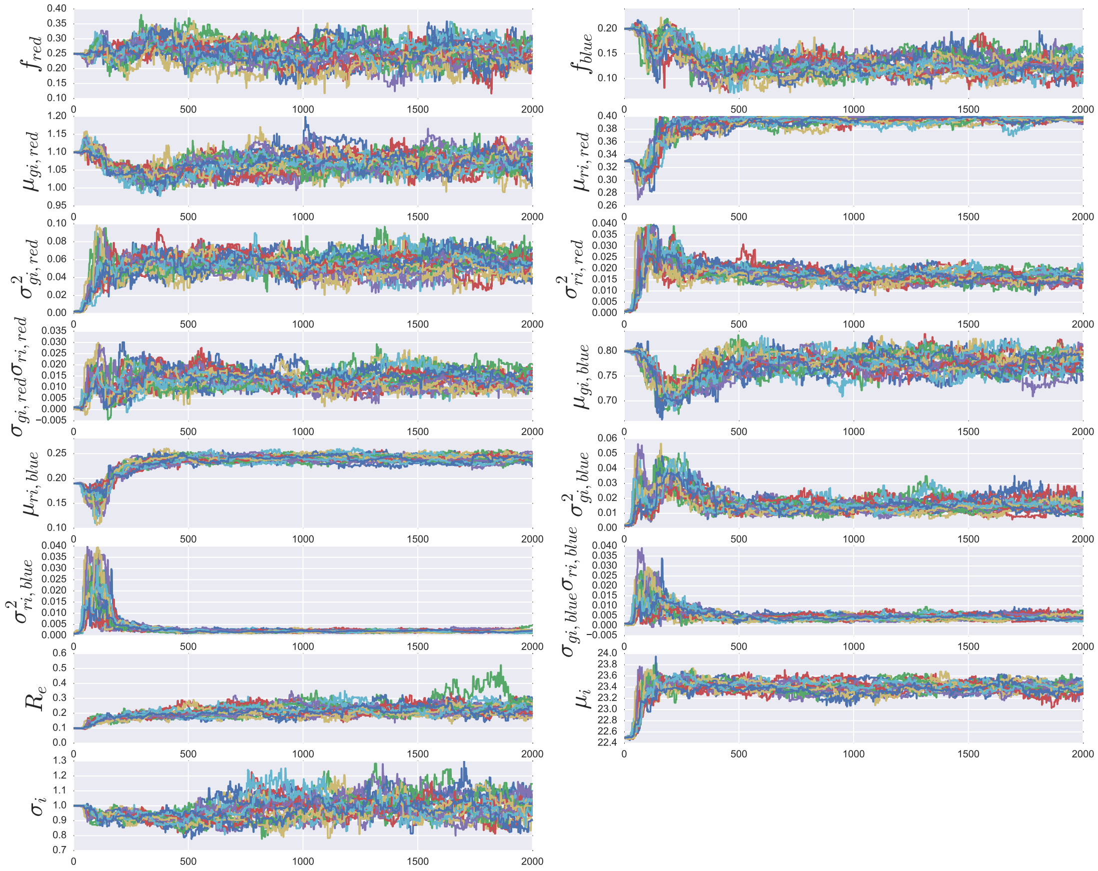

Figure A.23: Full trace plots for all free parameters in NGC 4494

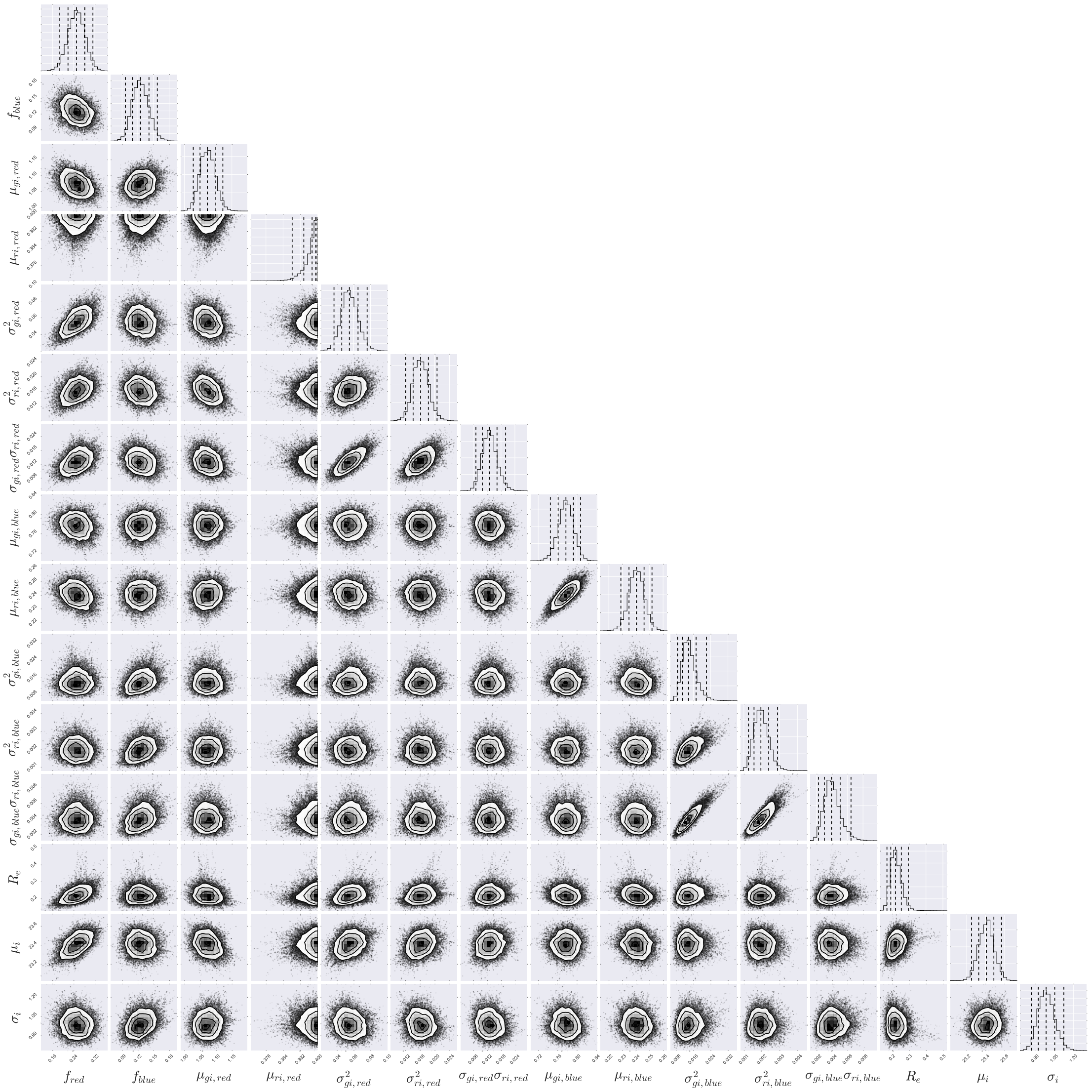

Figure A.24: Full corner plots for all free parameters in NGC 4494

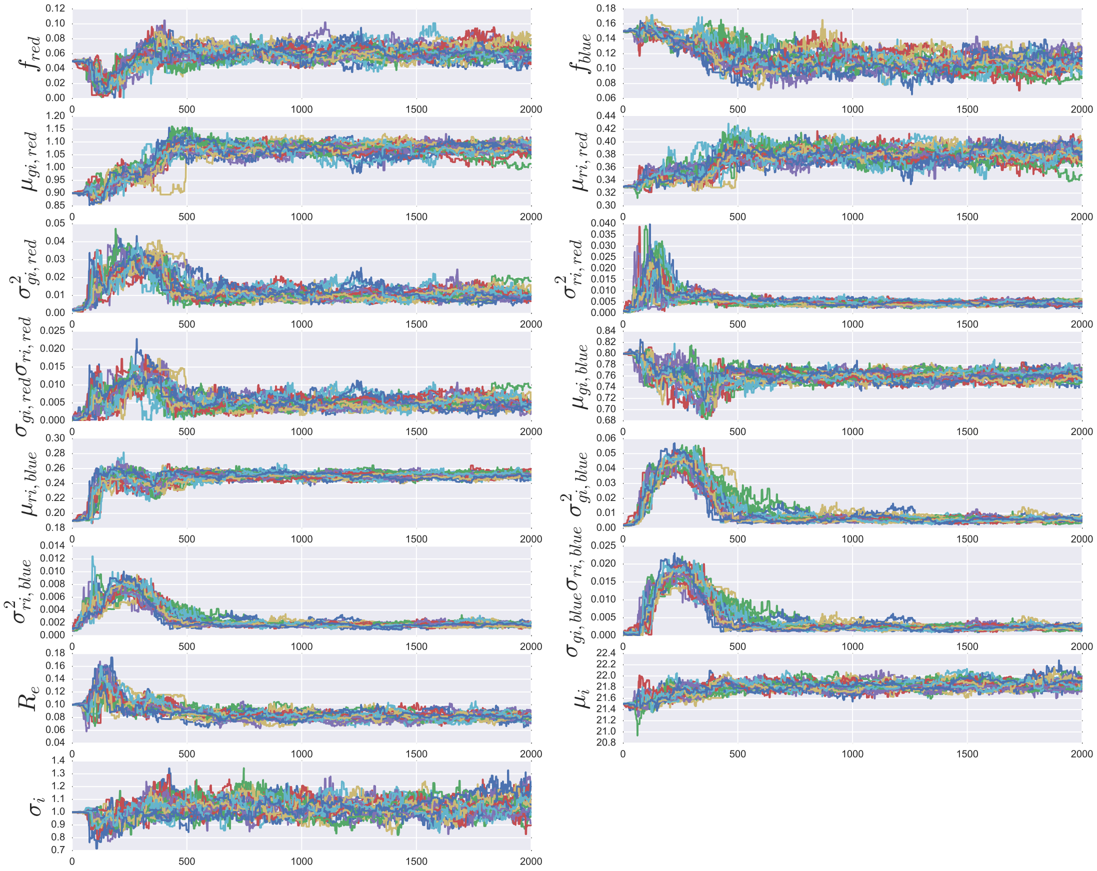

Figure A.25: Full trace plots for all free parameters in NGC 4697

Figure A.26: Full corner plots for all free parameters in NGC 4697

Bibliography

Agnello, A., Evans, N. W., Romanowsky, A. J., & Brodie, J. P. 2014, MNRAS, 442, 3299

Ahn, C. P., Seth, A. C., den Brok, M., et al. 2017, ApJ, 839, 72

Alves-Brito, A., Hau, G. K. T., Forbes, D. A., et al. 2011, MNRAS, 417, 1823

Anderson, J., & van der Marel, R. P. 2010, ApJ, 710, 1032

Arnold, J. A., Romanowsky, A. J., Brodie, J. P., et al. 2011, ApJ, 736, L26

Ashman, K. M., Bird, C. M., & Zepf, S. E. 1994, AJ, 108, 2348

Bailin, J., & Harris, W. E. 2009, ApJ, 695, 1082

Beasley, M. A., Bridges, T., Peng, E., et al. 2008, MNRAS, 386, 1443

Bekki, K., Couch, W. J., & Drinkwater, M. J. 2001, ApJ, 552, L105

Bertin, E., & Arnouts, S. 1996, A&AS, 117, 393

Bezanson, R., van Dokkum, P. G., Tal, T., et al. 2009, ApJ, 697, 1290

Bianchini, P., Renaud, F., Gieles, M., & Varri, A. L. 2015, MNRAS, 447, L40

Blom, C., Forbes, D. A., Brodie, J. P., et al. 2012a, MNRAS, 426, 1959

Blom, C., Spitler, L. R., & Forbes, D. A. 2012b, MNRAS, 420, 37

Brodie, J. P., & Larsen, S. S. 2002, AJ, 124, 1410

Brodie, J. P., Romanowsky, A. J., Strader, J., & Forbes, D. A. 2011, AJ, 142, 199

Brodie, J. P., & Strader, J. 2006, ARA&A, 44, 193

Brodie, J. P., Usher, C., Conroy, C., et al. 2012, ApJ, 759, L33

Brodie, J. P., Romanowsky, A. J., Strader, J., et al. 2014, ApJ, 796, 52

Burkert, A., & Tremaine, S. 2010, ApJ, 720, 516

Cantiello, M., Blakeslee, J. P., & Raimondo, G. 2007, ApJ, 668, 209

Capaccioli, M., Held, E. V., & Nieto, J.-L. 1987, AJ, 94, 1519

Chambers, K. C., Magnier, E. A., Metcalfe, N., et al. 2016, ArXiv e-prints, arXiv:1612.05560

Chromey, F. R., Elmegreen, D. M., Mandell, A., & McDermott, J. 1998, AJ, 115, 2331

Conroy, C., Graves, G. J., & van Dokkum, P. G. 2014, ApJ, 780, 33

Côté, P., Piatek, S., Ferrarese, L., et al. 2006, ApJS, 165, 57

Da Rocha, C., Mieske, S., Georgiev, I. Y., et al. 2011, A&A, 525, A86

Dabringhausen, J., Hilker, M., & Kroupa, P. 2008, MNRAS, 386, 864

Dalcanton, J. J., Williams, B. F., Lang, D., et al. 2012, ApJS, 200, 18

Dinescu, D. I., Girard, T. M., & van Altena, W. F. 1999, AJ, 117, 1792

Dotter, A., Sarajedini, A., & Anderson, J. 2011, ApJ, 738, 74

Drinkwater, M. J., Jones, J. B., Gregg, M. D., & Phillipps, S. 2000, PASA, 17, 227

Elson, R. A. W. 1997, MNRAS, 286, 771

Evstigneeva, E. A., Drinkwater, M. J., Jurek, R., et al. 2007, MNRAS, 378, 1036

Evstigneeva, E. A., Drinkwater, M. J., Peng, C. Y., et al. 2008, AJ, 136, 461

Fabbiano, G. 2006, ARA&A, 44, 323

Fellhauer, M., & Kroupa, P. 2002, MNRAS, 330, 642

Ferrarese, L., Côté, P., Cuillandre, J.-C., et al. 2012, ApJS, 200, 4

Forbes, D. A., Norris, M. A., Strader, J., et al. 2014, MNRAS, 444, 2993

Forbes, D. A., Pota, V., Usher, C., et al. 2013, MNRAS, 435, L6

Forbes, D. A., Sánchez-Blázquez, P., Phan, A. T. T., et al. 2006, MNRAS, 366, 1230

Forbes, D. A., Sinpetru, L., Savorgnan, G., et al. 2017a, MNRAS, 464, 4611

Forbes, D. A., Spitler, L. R., Harris, W. E., et al. 2010, MNRAS, 403, 429

Forbes, D. A., Spitler, L. R., Strader, J., et al. 2011, MNRAS, 413, 2943

Forbes, D. A., Alabi, A., Brodie, J. P., et al. 2017b, AJ, 153, 114

Foreman-Mackey, D., Hogg, D. W., Lang, D., & Goodman, J. 2013, PASP, 125, 306

Foster, C., Spitler, L. R., Romanowsky, A. J., et al. 2011, MNRAS, 415, 3393

Foster, C., Lux, H., Romanowsky, A. J., et al. 2014, MNRAS, 442, 3544

Fraley, C., & Raferty, A. 2002, Journal of the American Statistical Association, 97, 611

Gebhardt, K., & Kissler-Patig, M. 1999, AJ, 118, 1526

Geha, M., Guhathakurta, P., & van der Marel, R. P. 2002, AJ, 124, 3073

Gelman, A., Carlin, J., Stern, H., et al. 2013, Bayesian Data Analysis, Third Edition, Chapman and Hall/CRC Texts in Statistical Science

Genz, A. 1992, Journal of Computational and Graphical Statistics, 1, 141

Georgiev, I. Y., & Böker, T. 2014, MNRAS, 441, 3570

Gómez, M., & Woodley, K. A. 2007, ApJ, 670, L105

Gwyn, S. D. J. 2008, PASP, 120, 212

Haşegan, M., Jordán, A., Côté, P., et al. 2005, ApJ, 627, 203

Hargis, J. R., & Rhode, K. L. 2012, AJ, 144, 164

Harris, G. L. H., Poole, G. B., & Harris, W. E. 2014, MNRAS, 438, 2117

Harris, J., & Zaritsky, D. 2009, AJ, 138, 1243

Harris, W. E. 1996, AJ, 112, 1487

—. 2009a, ApJ, 699, 254

—. 2009b, ApJ, 703, 939

Harris, W. E., Ciccone, S. M., Eadie, G. M., et al. 2017, ApJ, 835, 101

Harris, W. E., Spitler, L. R., Forbes, D. A., & Bailin, J. 2010, MNRAS, 401, 1965

Harris, W. E., Whitmore, B. C., Karakla, D., et al. 2006, ApJ, 636, 90

Hartigan, J. A., & Hartigan, P. M. 1985, Ann. Statist., 13, 70

Hau, G. K. T., Spitler, L. R., Forbes, D. A., et al. 2009, MNRAS, 394, L97

Haynes, M. P., Giovanelli, R., & Roberts, M. S. 1979, ApJ, 229, 83

Hilker, M., Infante, L., Vieira, G., Kissler-Patig, M., & Richtler, T. 1999, A&AS, 134, 75

Hirschmann, M., Naab, T., Davé, R., et al. 2013, MNRAS, 436, 2929

Hogg, D. W., Bovy, J., & Lang, D. 2010, ArXiv e-prints, arXiv:1008.4686

Huchra, J., & Brodie, J. 1984, ApJ, 280, 547

Huxor, A. P., Tanvir, N. R., Irwin, M. J., et al. 2005, MNRAS, 360, 1007

Into, T., & Portinari, L. 2013, MNRAS, 430, 2715

Janz, J., Forbes, D. A., Norris, M. A., et al. 2015, MNRAS, 449, 1716

Janz, J., & Lisker, T. 2009, ApJ, 696, L102

Janz, J., Norris, M. A., Forbes, D. A., et al. 2016, MNRAS, 456, 617

Jennings, Z. G., Strader, J., Romanowsky, A. J., et al. 2014, AJ, 148, 32

Jennings, Z. G., Romanowsky, A. J., Brodie, J. P., et al. 2015, ApJ, 812, L10

Johnson, C. I., & Pilachowski, C. A. 2010, ApJ, 722, 1373

Johnson, C. I., Pilachowski, C. A., Michael Rich, R., & Fulbright, J. P. 2009, ApJ, 698, 2048

Jordán, A. 2004a, ApJ, 613, L117

—. 2004b, ApJ, 613, L117

Jordán, A., Côté, P., Blakeslee, J. P., et al. 2005, ApJ, 634, 1002

Jordán, A., Blakeslee, J. P., Côté, P., et al. 2007a, ApJS, 169, 213

Jordán, A., McLaughlin, D. E., Côté, P., et al. 2007b, ApJS, 171, 101

Jordán, A., Peng, E. W., Blakeslee, J. P., et al. 2009, ApJS, 180, 54

Kanbur, S. M., Ngeow, C., Nikolaev, S., Tanvir, N. R., & Hendry, M. A. 2003, A&A, 411, 361

Kartha, S. S., Forbes, D. A., Spitler, L. R., et al. 2014, MNRAS, 437, 273

Kartha, S. S., Forbes, D. A., Alabi, A. B., et al. 2016, MNRAS, 458, 105

Kim, E., Kim, D.-W., Fabbiano, G., et al. 2006, ApJ, 647, 276

King, I. R., Bedin, L. R., Cassisi, S., et al. 2012, AJ, 144, 5

Kissler-Patig, M., Jordán, A., & Bastian, N. 2006, A&A, 448, 1031

Kormendy, J., & Bahcall, J. N. 1974, AJ, 79, 671

Kundu, A., Maccarone, T. J., & Zepf, S. E. 2007, ApJ, 662, 525

Kundu, A., & Whitmore, B. C. 1998, AJ, 116, 2841

Kuntschner, H., Ziegler, B. L., Sharples, R. M., Worthey, G., & Fricke, K. J. 2002, A&A, 395, 761

Larsen, S. S. 1999, A&AS, 139, 393

Larsen, S. S., & Brodie, J. P. 2003, ApJ, 593, 340

Larsen, S. S., Forbes, D. A., & Brodie, J. P. 2001, MNRAS, 327, 1116

Lin, D., Irwin, J. A., Wong, K.-W., et al. 2015a, ApJ, 808, 19

—. 2015b, ApJ, 808, 20

Lokhorst, D., Starkenburg, E., McConnachie, A. W., et al. 2016, ApJ, 819, 124

McLaughlin, D. E., & van der Marel, R. P. 2005, ApJS, 161, 304

Mei, S., Blakeslee, J. P., Côté, P., et al. 2007, ApJ, 655, 144

Merritt, D., Meylan, G., & Mayor, M. 1997, AJ, 114, 1074

Mieske, S., Hilker, M., & Infante, L. 2004, A&A, 418, 445

Mieske, S., Hilker, M., Infante, L., & Jordán, A. 2006a, AJ, 131, 2442

Mieske, S., Jordán, A., Côté, P., et al. 2006b, ApJ, 653, 193

Mihos, J. C., Durrell, P. R., Ferrarese, L., et al. 2015, ApJ, 809, L21

Misgeld, I., & Hilker, M. 2011, MNRAS, 414, 3699

Miyazaki, S., Komiyama, Y., Sekiguchi, M., et al. 2002, PASJ, 54, 833

Muñoz, R. P., Puzia, T. H., Lançon, A., et al. 2014, ApJS, 210, 4

Muratov, A. L., & Gnedin, O. Y. 2010, ApJ, 718, 1266

Murray, N. 2009, ApJ, 691, 946

Naab, T., Johansson, P. H., & Ostriker, J. P. 2009, ApJ, 699, L178

Nantais, J. B., Huchra, J. P., Zezas, A., Gazeas, K., & Strader, J. 2011, AJ, 142, 183

Nikiel-Wroczyński, B., Soida, M., Bomans, D. J., & Urbanik, M. 2014, ApJ, 786, 144

Norris, M. A., & Kannappan, S. J. 2011, MNRAS, 414, 739

Norris, M. A., Sharples, R. M., & Kuntschner, H. 2006, MNRAS, 367, 815

Norris, M. A., Kannappan, S. J., Forbes, D. A., et al. 2014, MNRAS, 443, 1151

Ostrov, P., Geisler, D., & Forte, J. C. 1993, AJ, 105, 1762

Paolillo, M., Puzia, T. H., Goudfrooij, P., et al. 2011, ApJ, 736, 90

Peng, E. W., Ford, H. C., Freeman, K. C., & White, R. L. 2002, AJ, 124, 3144

Peng, E. W., Jordán, A., Côté, P., et al. 2006a, ApJ, 639, 95

Peng, E. W., Côté, P., Jordán, A., et al. 2006b, ApJ, 639, 838

Peng, E. W., Jordán, A., Côté, P., et al. 2008, ApJ, 681, 197

Penny, S. J., Forbes, D. A., & Conselice, C. J. 2012, MNRAS, 422, 885

Pfeffer, J., & Baumgardt, H. 2013, MNRAS, 433, 1997

Phillipps, S., Drinkwater, M. J., Gregg, M. D., & Jones, J. B. 2001, ApJ, 560, 201

Pota, V., Graham, A. W., Forbes, D. A., et al. 2013a, MNRAS, 433, 235

Pota, V., Forbes, D. A., Romanowsky, A. J., et al. 2013b, MNRAS, 428, 389

Pota, V., Romanowsky, A. J., Brodie, J. P., et al. 2015, MNRAS, 450, 3345

Price, J., Phillipps, S., Huxor, A., et al. 2009, MNRAS, 397, 1816

Pritzl, B. J., Venn, K. A., & Irwin, M. 2005, AJ, 130, 2140

Puzia, T. H., Paolillo, M., Goudfrooij, P., et al. 2014, ArXiv e-prints, arXiv:1402.6714

Puzia, T. H., Zepf, S. E., Kissler-Patig, M., et al. 2002, A&A, 391, 453

Rots, A. H. 1978, AJ, 83, 219

Sandoval, M. A., Vo, R. P., Romanowsky, A. J., et al. 2015, ApJ, 808, L32

Schlafly, E. F., & Finkbeiner, D. P. 2011, ApJ, 737, 103

Schlegel, D. J., Finkbeiner, D. P., & Davis, M. 1998, ApJ, 500, 525

Seth, A. C., van den Bosch, R., Mieske, S., et al. 2014, Nature, 513, 398

Sirianni, M., Jee, M. J., Benítez, N., et al. 2005, PASP, 117, 1049

Sivakoff, G. R., Jordán, A., Sarazin, C. L., et al. 2007, ApJ, 660, 1246

Spitler, L. R., Larsen, S. S., Strader, J., et al. 2006, AJ, 132, 1593

Strader, J., Beasley, M. A., & Brodie, J. P. 2007, AJ, 133, 2015

Strader, J., Brodie, J. P., Spitler, L., & Beasley, M. A. 2006, AJ, 132, 2333

Strader, J., Romanowsky, A. J., Brodie, J. P., et al. 2011, ApJS, 197, 33

Strader, J., Fabbiano, G., Luo, B., et al. 2012, ApJ, 760, 87

Taylor, M. A., Puzia, T. H., Harris, G. L., et al. 2010, ApJ, 712, 1191

Thomas, D., Maraston, C., & Bender, R. 2003, MNRAS, 339, 897

Thomas, D., Maraston, C., & Johansson, J. 2011, MNRAS, 412, 2183

Tonry, J. L., Dressler, A., Blakeslee, J. P., et al. 2001, ApJ, 546, 681

Usher, C., Forbes, D. A., Spitler, L. R., et al. 2013, MNRAS, 436, 1172

Usher, C., Forbes, D. A., Brodie, J. P., et al. 2012, MNRAS, 426, 1475

van den Bergh, S., Morbey, C., & Pazder, J. 1991, ApJ, 375, 594

Villanova, S., Geisler, D., Gratton, R. G., & Cassisi, S. 2014, ApJ, 791, 107

Villegas, D., Jordán, A., Peng, E. W., et al. 2010, ApJ, 717, 603

Weisz, D. R., Fouesneau, M., Hogg, D. W., et al. 2013, ApJ, 762, 123

Yoon, S.-J., Sohn, S. T., Lee, S.-Y., et al. 2011, ApJ, 743, 149

Yoon, S.-J., Yi, S. K., & Lee, Y.-W. 2006, Science, 311, 1129

Zepf, S. E., & Ashman, K. M. 1993, MNRAS, 264, 611

Zibetti, S. 2009, ArXiv e-prints, arXiv:0911.4956

Zibetti, S., Charlot, S., & Rix, H.-W. 2009, MNRAS, 400, 1181

Zwicky, F. 1956, Ergebnisse der exakten Naturwissenschaften, 29, 344